

Graphene Nanoribbons

From fume hood to transistor

Cover:

All types of graphene nanoribbons as well as polymers and a bisanthene dimer (**chapter 2**) that occur throughout this thesis. The nanoribbons are a 5-acGNR (**chapters 3, 5**), a 7-acGNR (**1, 5, 6**), a 3,1-cGNR (**1, 3, 6**) and a 5/7-acGNR heterostructure (**5**). The structures are on the gold(111) surface, silver(111) surface and copper(111) surface, as well as on sodium chloride (**6**). The 5/7-acGNR heterostructure is lifted off from the surface with the tip of a scanning tunneling microscope (**5**). The structures were rendered with *Mathematica* using the MathemaTB package developed by the author (**4**). The top region shows $E(k)$ band structures of 5-acGNR, 7-acGNR and 3,1-cGNR, as well as a tight-binding Hamiltonian (**4**). Additionally, an atomically resolved nc-AFM image and two differential conductance maps of the 3,1-cGNR are shown (**3, 6**), and a Suzuki coupling reaction (**2**).

ISBN:

978-90-393-7040-7

Printing:

Ridderprint BV

www.ridderprint.nl

Graphene Nanoribbons

From fume hood to transistor

Grafeen-nanodraden
Van zuurkast tot transistor
(met een samenvatting in het Nederlands)

Proefschrift

ter verkrijging van de graad van doctor aan de Universiteit Utrecht op gezag van de rector magnificus, prof. dr. H.R.B.M. Kummeling, ingevolge het besluit van het college voor promoties in het openbaar te verdedigen op vrijdag 30 november 2018 des middags te 2.30 uur.

door

Peter Herman Jacobse

geboren op 6 april 1990 te Emmen

Promotor:

Prof. dr. R. J. M. Klein Gebbink

Copromotoren:

Dr. I. Swart

Dr. M.-E. Moret

Dit proefschrift werd mede mogelijk gemaakt met financiële steun van de Nederlandse Organisatie voor Wetenschappelijk Onderzoek (NWO).

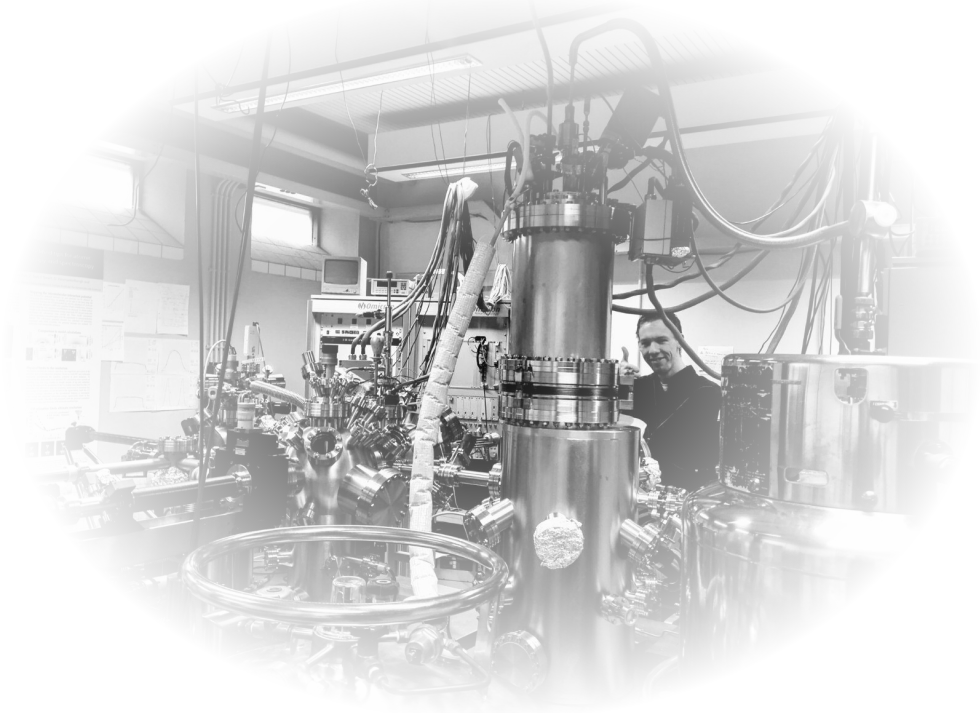
Contents

0.1	Summary of this thesis	xi
0.2	Scanning probe microscopy	xiv
0.2.1	Scanning tunneling microscopy	xiv
0.2.2	Atomic force microscopy	xvii
0.3	Graphene and graphene nanoribbons	xviii
0.3.1	The honeycomb lattice and its reciprocal lattice	xix
0.3.2	Electronic structure of graphene	xxi
0.3.3	Linear dispersion	xxiii
0.3.4	Graphene nanoribbons	xxvi
0.4	Synthesis	xxx
0.4.1	Solution-phase synthesis	xxxix
0.4.2	On-surface synthesis	xxxix
0.5	Conclusions	xxxiii
1	Tracking on-surface chemistry with atomic precision	1
1.1	On-surface synthesis	2
1.2	Scanning tunneling and atomic force microscopy	4
1.3	Graphene nanoribbons	6
1.4	Chiral nanoribbons	9
1.5	Conclusions	10
2	Aryl radical geometry determines nanographene formation on Au(111)	15
2.1	Introduction	16
2.2	Results	17
2.2.1	Dichlorobianthryl on Au(111)	17
2.2.2	Bianthryl on Au(111)	21
2.3	Conclusions	22
2.4	Experimental methods	23
2.4.1	Synthesis of 10,10'-dichloro-9,9'-bianthryl (DCBA)	23
2.4.2	Scanning probe experiments	25

3	Precursor geometry determines the growth mechanism in graphene nanoribbons	29
3.1	Introduction	30
3.2	Results	32
3.2.1	Identification of the 3,1-chiral graphene nanoribbon . .	32
3.2.2	Resolving the formation mechanism	34
3.2.3	Importance of precursor geometry	37
3.3	Conclusions	40
3.4	Experimental methods	41
3.4.1	Sample preparation	41
3.4.2	Scanning probe measurements	42
3.4.3	DFT calculations	42
3.4.4	nc-AFM simulations	43
4	MathemaTB: A Mathematica package for tight-binding calculations	47
4.1	Introduction	48
4.2	Results	51
4.2.1	Functions in the MathemaTB package	51
4.2.2	Molecular tight-binding	53
4.2.3	Symmetry and coupling	58
4.2.4	Tight-binding in two dimensions	62
4.2.5	Tight-binding with more dimensions and more atoms . .	65
4.2.6	One-dimensional tight-binding	67
4.3	Conclusions	71
5	Electronic components embedded in a single graphene nanoribbon	73
5.1	Introduction	74
5.2	Results	75
5.2.1	Synthesis of GNR heterojunctions	75
5.2.2	Electronic structure of the GNR heterojunctions	76
5.2.3	Electronic characterization of heterojunctions	80
5.2.4	Charge transport through GNR heterojunctions	82
5.3	Conclusions	86
5.4	Experimental methods	87
5.4.1	STM and AFM measurements	87
5.4.2	Conductance measurements	88
5.4.3	DFT calculations	88
5.4.4	Transport calculations	88

6	Mapping the conductance of electronically decoupled graphene nanoribbons	91
6.1	Introduction	92
6.2	Results	95
6.2.1	Characterization of 3,1-cGNR on NaCl	95
6.2.2	Conductance mapping of 7-acGNR	97
6.2.3	Conductance experiment simulations	100
6.2.4	Conductance mapping of 3,1-cGNR	103
6.2.5	Double modulation spectroscopy	105
6.3	Conclusions	107
6.4	Experimental methods	108
6.4.1	Conductance mapping	108
6.4.2	Double modulation spectroscopy	109
6.4.3	Tight-binding calculations	109
6.4.4	Conductance map simulations	109
7	Appendix	113
7.1	Samenvatting in het Nederlands	114
7.2	Publications	123
7.3	About the author	125
7.4	Acknowledgments	126

Introduction



This thesis describes the work on the fabrication and characterization of graphene nanoribbons, spanning the range from organic synthesis in the chemistry lab (the fume hood) to advanced measurements on electronic components comprised of single graphene nanoribbons (the transistor). A broad spectrum of subjects is presented, among which solution-based chemistry, on-surface synthesis, the formation mechanism of nanographenes, scanning probe microscopy, electronic structure calculations and conductance measurements. This thesis describes work both on elucidating formation mechanisms of graphene nanostructures as well as measurements of their electronic properties. The interplay between the geometric and electronic structure is examined and exploited by synthesizing ribbons of different widths and edge structures. The resulting structures, both pristine nanoribbons and segmented, heterojunction-type nanoribbons are subjected to extensive scanning tunneling spectroscopy and conductance measurements, and a marinade of theoretical calculations is added to top it all off.

Mankind's desire for smaller and faster electronics, for the storage of vast amounts of data, for smartphones and gadgets with an ever-increasing amount of capabilities seems insatiable. Satisfying the need for capacity and speed calls for the continued miniaturization of electronic devices such as logic gates and memory cells. As of today, microchips can already be manufactured in which the electronic components, like transistors and diodes, approach a staggeringly small length scale of below 10 nm. This has recently made it possible for USB flash drives to pass the terabyte limit in storage capacity, allowing the user to store the equivalent of more than 80 high-definition movies on a device no larger than three inches.

Unfortunately, the miniaturization of electronic components on silicon chips is likely to end soon, as some physical limits are approached. Importantly, the lithography process, in which light is used to etch the correct patterns into the silicon wafers, is becoming increasingly challenging as the small length scales set an upper limit to the wavelength of the light used. This diffraction limit requires that an ever-increasing energetic type of light is used, causing unwanted side-effects to the wafers (*e.g.* heating and associated thermal expansion) that need to be addressed properly. The inevitable question that has arisen and cannot be ignored much longer is: how long can we still carry on with the top-down, lithographic methods and silicon chips?[1]

Bottom-up methodologies - fabricating components by assembly from smaller structures - have the capacity to present a paradigm shift in the world of nanoelectronics. This is the aim of molecular electronics: to build electronic devices from molecules instead of bulk materials. To create chips from carbon instead of silicon. To assemble transistors and diodes from the tiniest

introduction

of structures instead of imprinting them into large wafers. Since the rather recent inception of this field of research, many molecules have been subjected to investigation by various techniques as potential candidates for functional elements in molecular electronic circuits.[2, 3]

Apart from the progress in investigating molecules, another extremely interesting material for nanoelectronic is graphene. Graphene is a single-atom thick honeycomb lattice of carbon atoms. Its inherent flatness already makes it a promising material for making stacks of electronic components. Even more interestingly, it has been shown that its conductivity and charge carrier velocity makes it outperform even materials like copper and gold, and recent investigations have also shown promising results in the direction of spintronics.[4, 5, 6, 7]

A drawback of graphene is that it is a zero-gap semiconductor. That is, no energy gap needs to be overcome in order for it to support a current. The material is therefore not switchable, unlike silicon, which can be made into field-effect transistors that lie on the basis of active components on microchips. However, it is possible to open up an electronic band gap in graphene by various methods. One of the most promising strategies involves quantum confinement of the bulk, two-dimensional material into narrow strips known as graphene nanoribbons (GNRs).[8]

Here we come back at the bottom-up methodology. Graphene nanoribbons can in principle be made from top-down methods such as lithographic etching of graphene sheets or unzipping of carbon nanotubes, but recently it has been shown that nanoribbons can be made in a much more controlled method by assembly from molecules. Here, chemical reactions are used to produce nanoribbons with an atomically precise geometry: something that cannot be achieved by any top-down strategy. More precisely, on-surface synthesis has recently been established as a methodology that utilizes the supporting and catalyzing role of a metal substrate to direct reactions between molecules on them towards atomically well-defined nanostructures. The ability to fine-tune the atomic structure by selecting the correct precursor molecule for the growth process even allows a precise control over the resulting electronic structure. This opens up the possibility to control properties like band gap size, charge-carrier mobility and Fermi level position in the fume hood. The ability to design GNRs by synthesizing the correct precursor molecules and then have them react on surface has recently become reality, establishing a true conjunction between the world of graphene-based electronics and molecular electronics.[9, 10, 11]

0.1 Summary of this thesis

Making graphene nanoribbons by bottom-up methods (specifically through on-surface synthesis) is what this thesis is about. The work described here involves the synthesis of both precursor molecules, in the fume hood, as well as graphene nanoribbons. Furthermore, heterojunctions of graphene nanoribbons are made, which contain segments with different electronic properties and which are shown to exhibit the behavior that lie at the basis of active components such as diodes and transistors. Scanning tunneling microscopy and atomic force microscopy are used to examine the formation of these graphene nanostructures on surface, and to study their geometric and electronic properties.

Most experiments presented in the following chapters use molecules known as dihalobianthryl: an organic compound with six benzene rings and two halogen atoms. The halogen atoms may either be bromine or chlorine atoms. The brominated molecules have been shown to produce 7-atom wide armchair type graphene nanoribbons when subjected to thermal assembly on an Au(111) surface. Interestingly, it was found that copper catalyzes a different kind of reaction than gold, with the 3,1-chiral graphene nanoribbon as the unexpected result. These nanoribbons feature a mixed armchair/zigzag edge structure - which we unambiguously resolved with non-contact atomic force microscopy - and have a much smaller band gap than armchair-type nanoribbons, which is mostly due to the localization of low-energy electronic states on the edges of the ribbon. A third type of GNR that can be produced in our lab is the 5-atom wide graphene nanoribbon. In contrast with the 7-atom wide nanoribbon, this structure has a vanishing band gap with increasing length and may therefore be considered as a metal.

Synthesis of graphene nanoribbons generally contains a stage where the precursor molecules are synthesized using conventional synthetic methods in the chemistry laboratory, and a stage where the molecules are entered into the vacuum system for carrying out on-surface synthesis. Here, the molecules are evaporated from an effusion cell onto a metal single crystal (copper, gold or silver in a specific surface orientation) after which thermal treatment of the crystal induces the desired reactions. The reactions of interest are (intermolecular) coupling reactions, that may result in the formation of polymeric structures of molecules, and (intramolecular) transformations such as cyclodehydrogenations, which flatten the molecules under the formation of carbon-carbon bonds and release of hydrogen. The first few chapters in this thesis have a stronger focus on on-surface mechanisms and tracking the processes in the synthesis of graphene nanoribbons with scanning tunneling and atomic force microscopy. However, from **chapter 5** we start to investigate the copolymerization of the molecules for 5-atom wide and 7-atom wide nanoribbons, which gives rise to

introduction

metal-semiconductor junctions. From this point on, the focus of the research shifts towards electronic structure.

The UHV set-up

Scanning tunneling- (STM) and atomic force microscopy (AFM) experiments are conducted in our laboratory in ultra high vacuum (UHV, $p \approx 10^{-10}$ mbar) at a temperature of 4.5 K (-268.5 °C). These cold, controlled conditions allow the AFM to be utilized in non-contact mode, which is necessary to elucidate the geometric structure of graphene nanoribbons with atomic precision. The same set-up houses a preparation chamber which is used for sample preparation and cleaning of metal single crystals (see Fig. 1). Cleaning of metal single crystals is performed by cycles of sputtering (removing the topmost layers by bombarding the crystal with a plasma of high energy argon ions) and annealing (heating the crystal to the point where the atoms at the surface become mobile enough to arrange in atomically flat terraces). After this has been done, a molecule evaporator (a tiny cup containing a few grains of the molecular precursor of interest) is heated to the point at which the molecules will start to sublime. Stable sublimation can be inferred from a pressure increase, roughly of the order of $5 \cdot 10^{-9}$ mbar from a base pressure that is lower by one order of magnitude. The molecules are deposited onto the metal crystal by evaporation after which the on-surface synthetic reactions can be carried out.

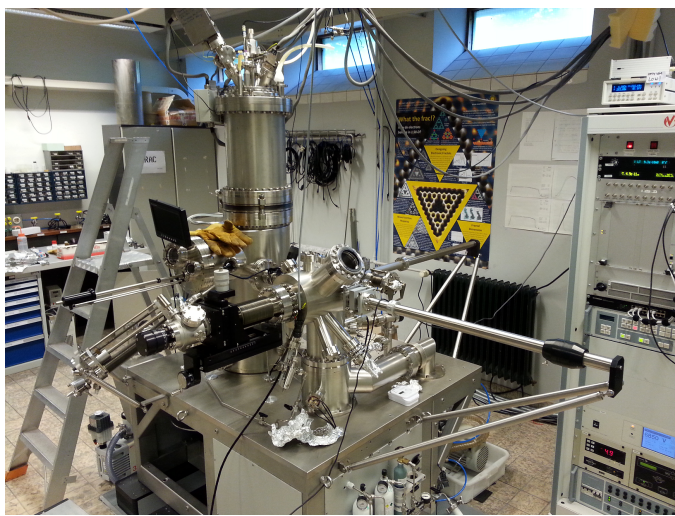


Fig. 1 Our UHV setup. In front one can see the preparation chamber, whereas the large, vertical cylinder houses the scanning tunneling- and atomic force microscope.

In addition to the geometric and electronic measurements, the conductance properties of GNRs can be probed by controlled lifting of the graphene nanoribbons with the tip of the STM. The electronic structure measurements are amended with calculations on the basis of density functional theory and tight-binding. The result is a blend of on-surface chemistry and organic syn-

thesis, a mixture of scanning probe measurements and calculations, a Wiener melange of chemistry and physics.

Chapters 1 to 3 focus on the on-surface chemistry involved in the fabrication of GNRs. The processes involved, the mechanisms, and importantly, the characterization of products and intermediates with STM and non-contact atomic force microscopy (nc-AFM). The on-surface reactions give rise to various types of graphene nanoribbons and other nanographenes depending on both the nature of the molecule and of the surface. **Chapter 1** gives a detailed introduction into nc-AFM, as well as the young field of on-surface chemistry. Recent advances in structure determination of single molecules on surfaces are reviewed, and the work described in **chapters 2 and 3** is introduced, where the mechanism of formation of different nanographenes and nanoribbons is described. **Chapter 2** describes the elucidation of the mechanism of nanographene formation from 10,10'-dichloro-9,9'-bianthryl (DCBA) on a gold surface. This molecule is a chlorine analog of 10,10'-dibromo-9,9'-bianthryl (DBBA). It was found that the nature of the halogen plays a key role in the order of different inter- and intramolecular reactions, and the brominated and chlorinated molecules give vastly different nanographenes. In **chapter 3**, the formation of nanoribbons on a copper surface is investigated. Surprisingly, the structure of the ribbons is completely unlike what would be expected on the basis of the design of the precursors. It turns out that the copper surface catalyzes a specific C-H cleavage and facilitates the formation of chiral nanoribbons, which have a mixed armchair-zigzag edge.

The subsequent chapters have a stronger focus on electronic structure rather than formation mechanism and it is in these chapters that more electronic measurements are presented. These measurements are corroborated with electronic structure calculations, on the basis of both density functional theory and tight-binding. First, **chapter 4** ventures into the quantum mechanical properties of GNRs as investigated by the tight-binding methodology. This chapter presents the *Mathematica* package that has been developed to perform the calculations: MathemaTB. This package is not only applicable to nanoribbons, but can be used for all types of molecular systems (Hückel-type calculations) as well as periodic structures. **Chapter 5** describes the synthesis and characterization of metal-semiconductor junctions in graphene nanoribbons, where copolymerization of two different precursor molecules is utilized to arrive at structures with metallic and semiconducting segments. Apart from the nc-AFM characterization of these junctions, a more detailed investigation into the electronic properties of the ribbons is presented by means of scanning tunneling spectroscopy. Not only are the ribbons characterized on the metal surface, but by controlled lift-off from the surface, the conductance properties could be explored. These conductance measurements form the basis for **chapter 6**, where the electronic properties of the ribbons are investigated in

introduction

even more detail, using an intercalating layer of sodium chloride to counteract interfering effects that the bare metal surface poses on these measurements.

The rest of this chapter is dedicated to introducing the background of graphene nanoribbons and techniques used throughout this thesis.

0.2 Scanning probe microscopy

Most experimental work described in this thesis involves scanning probe microscopy (SPM). In SPM, a surface is typically raster-scanned using a sharp tip to create an image of the topology. The motion of the tip is controlled using piezo-electric elements, allowing for a level of precision of imaging down to the atomic level - a scale that is impossible to achieve using optical microscopy.[12, 13, 14, 15, 16, 17]

Scanning probe microscopy techniques are subdivided into scanning tunneling microscopy (STM) and atomic force microscopy (AFM), and related spectroscopic techniques such as scanning tunneling spectroscopy (STS) and Kelvin probe force microscopy (KPFM).[18] The working principles behind STM and AFM are different, with STM being based on electron tunneling and AFM based on physical attraction and repulsion interactions between tip and sample. Nevertheless, these techniques have a lot in common and can even be used in conjunction.

0.2.1 Scanning tunneling microscopy

Scanning tunneling microscopy utilizes the quantum mechanical tunnel effect to raster scan a surface with the tip. When the tip and sample are in close proximity, application of a bias voltage results in a tunnel current - a current of electrons tunneling through the vacuum gap between the tip and sample.

The tunnel current can be written as the sum of contributions of tunneling from occupied (unoccupied) states in the tip to unoccupied (occupied) states in the sample.

$$I = \int_{-\infty}^{\infty} |\langle \psi_{\text{tip}} | \psi_{\text{sample}} \rangle|^2 (\rho_{\text{occ,tip}} \rho_{\text{unocc,sample}} - \rho_{\text{unocc,tip}} \rho_{\text{occ,sample}}) dE$$

where $\rho(E)$ is the density of states (DOS), $\psi(E)$ are the wave functions of the individual states and the overlap $|\langle \psi_{\text{tip}} | \psi_{\text{sample}} \rangle|^2$ follows from a perturbative approach to the interaction integral or *tunnel matrix element*, as put forward by Tersoff and Hamann.[19] Given equilibrium Fermi-Dirac statistics, one can write $\rho_{\text{occ}} = \rho(E)/(1 + e^{(E-\mu)/(k_B T)})$, where μ is the chemical potential of the tip/sample. Assuming a ground sample and biased tip gives $\mu_{\text{sample}} = 0$ and $\mu_{\text{tip}} = eV$. Furthermore, the Fermi-Dirac distributions become, to a good

approximation, step functions for the low temperatures in the experiments described in this thesis ($kT = k \cdot 4.5 \text{ K} = 0.4 \text{ meV}$), so that

$$I = \int_0^{eV} |\langle \psi_{\text{tip}} | \psi_{\text{sample}} \rangle|^2 \rho_{\text{tip}} \rho_{\text{sample}} dE$$

where $\{0, eV\}$ is called the bias window. If the tip is metallic and has a rather flat density of states inside the bias window, it is possible to approximate this equation as

$$\frac{dI}{dV} \propto |\langle \psi_{\text{tip}} | \psi_{\text{sample}}(eV) \rangle|^2 \rho_{\text{sample}}(eV) dV$$

Since the tunnel current in the STM is proportional to the total number of available states in the bias window, the derivative of the current is proportional to the density of states.

A feedback loop is commonly employed to regulate the tip height in such a way that the tunnel current is kept constant. This is called constant current mode, or STM feedback mode. Effectively, whenever the tip scans across a protrusion on the surface (which may for example be a molecule or metal cluster) the tip is retracted so as to maintain the same tunnel current, and conversely, an indent in the surface will cause the tip to extend towards the surface. Monitoring the tip height as a function of x - and y position then returns a map $z(x, y)$ of the topology of the surface.

In principle, the feedback mechanism can be switched off, allowing the mapping of the tunnel current $I(x, y)$ as a function of position. This is called constant height mode. However, since the tunnel current is sensitively dependent on tip-sample distance (through the overlap of the tip and sample wave functions) - with an appreciable tunnel current only obtainable at tip-sample separations of 1 nm or lower - it is difficult to image a surface in constant height mode without physically crashing the tip into any protrusions on the surface. Therefore, constant height mode is only relevant for small areas of the surface that have been verified to be flat beforehand, in constant current mode.

Measuring molecules or graphene nanoribbons physisorbed on a metal surface involves a two-step tunneling process: tunneling from tip to molecule and subsequently from molecule to metal. Whichever of the two steps is rate-limiting for the overall current, the current will be proportional to the local density of states of the molecule. One thing to keep in mind though is that the bias voltage may drop over both junctions, so that the molecule “resides” at a bias voltage different from both tip and sample. In principle, if C_{tip} is the capacitance experienced by the molecule due to electrostatic interaction with the tip, and $C_{\text{substrate}}$ is the capacitance with the substrate, the bias level of

introduction

the molecule can be found as

$$V_{\text{mol}} = \frac{C_{\text{tip}}}{C_{\text{tip}} + C_{\text{substrate}}} V_{\text{tip}}$$

where again the substrate is held at ground and the tip is biased. This capacitive voltage division plays an important role in chapter 6. Conveniently, for most measurements, it can safely be assumed that $C_{\text{tip}} \ll C_{\text{substrate}}$ so that the energy levels of the molecule are capacitively “tied” to the substrate.

0.2.1.1 Local density of states and the lock-in amplifier technique

A factor that plays a role in the differential conductance is how well the tip “connects” to each orbital corresponding to a certain energy level. This means that the density of states as observed in scanning tunneling microscopy or spectroscopy is modulated by the overlap of the tip with the wave functions of the states it is tunneling into. In other words, in STM the local, rather than total density of states is returned. The tunneling probability is reflected by the value of the tunnel matrix element of each state.

The fact that the local density of states can be probed both spatially and as a function of energy means that not only differential spectra can be recorded on certain points on the sample of interest, but also orbitals can be mapped spatially at a certain bias voltage by using the STM in differential conductance mapping mode.

$$\frac{dI}{dV}(x, y, V) \propto |\langle \psi_{\text{tip}} | \psi_{\text{sample}}(x, y, eV) \rangle|^2 \rho_{\text{sample}}(eV) dV$$

Here, the overlap integral may be approximated as $|\langle \psi_{\text{tip}} | \psi_{\text{sample}}(x, y, eV) \rangle|^2 \propto |\psi_{\text{sample}}(x, y, eV)|^2$ for a point-like tip, whereas a p -wave tip (one that is passivated with a molecule of carbon monoxide) may be approximated as [20]

$$|\langle \psi_{\text{tip}} | \psi_{\text{sample}}(x, y, eV) \rangle|^2 \propto \left| \frac{d\psi_{\text{sample}}(x, y, eV)}{dx} \right|^2 + \left| \frac{d\psi_{\text{sample}}(x, y, eV)}{dy} \right|^2$$

An effective way to measure the differential conductance dI/dV with much lower noise than would be possible by numerically integrating $I(V)$ spectra is by making use of the lock-in amplifier technique. Here, a voltage oscillation is superimposed on a constant bias ($V(t) = V_0 + V_{\text{osc}} \sin \omega t$), resulting in an oscillation in the tunnel current ($I(t) = I_0 + I_{\text{osc}} \sin(\omega t + \phi)$) that is proportional to the differential conductance at the probed bias voltage. By feeding the tunnel current signal back to the lock-in amplifier, the differential conductance can be obtained by comparing it to the signal that was given out in the first place.

In fact, the process can be understood as calculating the Fourier component of the tunnel current at the frequency of the output signal.

$$(X, Y) \propto \left(\int_0^\tau I(t) \sin(\omega t) dt, \int_0^\tau I(t) \cos(\omega t) dt \right) \propto I_{\text{osc}}(\cos \phi, \sin \phi)$$

where X and Y are the in-phase and out-of-phase (quadrature) components, respectively. The out of phase signal usually results from current lagging the voltage oscillation as a result of charging and discharging of the junction, but methods exist to cancel out these capacitive effects. The in-phase and out-of-phase components can be transformed to phase and magnitude signals simply by transforming to polar coordinates

$$(R, \theta) = \left(\sqrt{X^2 + Y^2}, \arctan Y/X \right)$$

0.2.1.2 Manipulation

The precise control of the STM tip down to the picometer level allows for more than imaging of the surface. It can also be exploited to manipulate structures on the surface. For example, it has been shown how xenon atoms and carbon monoxide molecules can be shifted over the surface or be absorbed onto the tip in a controlled fashion.[21] Molecules can be pushed, pulled or pulsed over the surface.[22] Voltage pulses can be used to induce chemical changes within molecules on surfaces.[23] Molecule manipulation can also be achieved on larger structures.

Highlights in the realm of graphene nanoribbons are the demonstration of controlled pick-up and lifting of a nanoribbon from a surface[24], bending of individual nanoribbons[25] and voltage-pulse induced dehydrogenation.[26] Initially, lifting of nanoribbons allowed for the determination of conductance through a nanoribbon as a function of tip height, but was later used to demonstrate graphene's superlubricity over an atomically flat surface[27] and to measure electroluminescence in GNR.[28] Finally, the pick-up technique has been used to deposit nanoribbons on top of sodium chloride monolayers to achieve electronic decoupling from the surface.[29, 30] These results will make a reappearance in this thesis in chapter 6, where exactly these techniques are exploited to perform conductance measurements on single graphene nanoribbons.

0.2.2 Atomic force microscopy

In atomic force microscopy, the surface is raster-scanned using a tip as in STM, but the imaging mechanism relies on the physical interactions between tip and substrate rather than tunnel current.

introduction

The specific AFM method used in this research is non-contact atomic force microscopy (nc-AFM). Here, the tip is actively oscillated at its resonance frequency, and this oscillation is maintained by carefully monitoring both the amplitude and the phase shift between the tip and the driving signal. The van der Waals attraction between surface and tip makes that the tip slightly “sticks” to the surface, resulting in a reduction in the resonance frequency (of the order of a few Hertz on a resonance frequency of the order of 20 kHz). However, in even closer proximity, the physical overlap between electrons of the ultimate tip atom and the substrate causes a repulsive force - the Pauli interaction - that gives an upshift of the resonance frequency. Therefore, when monitoring the frequency shift as a function of the tip-sample separation, a Lennard-Jones or Morse-type potential curve is obtained.

AFM can be used in feedback mode, where the tip is locked to a certain resonance frequency shift and an image of the tip height as a function of x and y is acquired. However, given the non-monotonic nature of the frequency shift and the large variations of the Morse potential profile as a function of whatever is on the surface, it can sometimes prove challenging to operate AFM in this mode. Most AFM images in this thesis are acquired in constant height mode, where the frequency shift is monitored as a function of x and y at a certain height above the surface.

A key difference between AFM and STM is that STM probes electronic states within a narrow bias window - close to the Fermi level - whereas the contrast in AFM implicitly depends on the total, rather than resonant, electron density. The result is that STM images basically give a convolution of the geometric and electronic structure of an adsorbate, whereas an AFM image returns images where the “electronic quirks” are basically integrated out and the contrast really relates to the geometric structure. In fact, nc-AFM images really show the individual bonds within single molecules. More information on how AFM can be utilized to obtain atomic contrast in organic molecules on surface can be found in [31, 32, 20, 17], and information on how atomic force microscopy can be applied to resolve molecular structures on surfaces down to the atomic level is given in chapter 2 of this thesis.

0.3 Graphene and graphene nanoribbons

In order to understand why graphene nanoribbons are a sought-after material in the first place, it is important to come to grips why its parent material graphene is so special. The following gives a brief introduction into the electronic structure of graphene and graphene nanoribbons, along the line of the derivations of [33] and [34, 35]. Fig. 2 shows a model of graphene, a single-atom thick honeycomb lattice of carbon atoms. The carbon atoms in the graphene

lattice are sp^2 -hybridized, meaning that their trigonal environment of adjacent carbon atoms forces their valence orbitals (the 2s shell and 2p shell) to mix in such a way that the resulting orbitals are best described in a basis of sp^2 hybrid orbitals. *E.g.*

$$\begin{pmatrix} |\phi_1\rangle \\ |\phi_2\rangle \\ |\phi_3\rangle \\ |\phi_4\rangle \end{pmatrix} = \begin{pmatrix} 1/\sqrt{3} & -\sqrt{2/3} & 0 & 0 \\ 1/\sqrt{3} & 1/\sqrt{6} & 1/\sqrt{2} & 0 \\ 1/\sqrt{3} & 1/\sqrt{6} & -1/\sqrt{2} & 0 \\ 0 & 0 & 0 & 1 \end{pmatrix} \begin{pmatrix} |2s\rangle \\ |2p_x\rangle \\ |2p_y\rangle \\ |2p_z\rangle \end{pmatrix}$$

The first three sp^2 hybrids are in the xy -plane (as can be inferred from the entries in the column that multiplies with $|2p_z\rangle$, which are all zero), bonding together to form the σ framework of the honeycomb lattice. The p_z orbital however remains unaffected by the in-plane field of carbon atoms and can contribute electrons to strongly delocalized orbitals at energies closer to the Fermi energy. It is these orbitals - the so-called π -system of the honeycomb lattice - that are responsible for the interesting physics of graphene.

0.3.1 The honeycomb lattice and its reciprocal lattice

The honeycomb lattice can be described as two interpenetrating hexagonal *sublattices*: the “A” sublattice and the “B” sublattice (indicated in the top right corner of Fig. 2 with blue and red, respectively). As indicated in the figure with green and orange, within the graphene sheet, one can distinguish two main directions: *armchair* and *zigzag*. The unit cell in the honeycomb lattice is the purple diamond in the bottom right corner of Fig. 2. If $\hat{\mathbf{x}}$ is a unit vector aligned with the armchair direction of the lattice and $\hat{\mathbf{y}}$ is a unit vector in the zigzag direction, the lattice vectors of the honeycomb lattice are

$$\begin{pmatrix} \mathbf{a}_1 \\ \mathbf{a}_2 \\ \mathbf{a}_3 \end{pmatrix} = a_0 \begin{pmatrix} -\frac{3}{2}\hat{\mathbf{x}} + \frac{\sqrt{3}}{2}\hat{\mathbf{y}} \\ \frac{3}{2}\hat{\mathbf{x}} + \frac{\sqrt{3}}{2}\hat{\mathbf{y}} \\ -\sqrt{3}\hat{\mathbf{y}} \end{pmatrix}$$

where $a_0 \approx 1.42 \text{ \AA}$ is the interatomic spacing and where the (redundant) auxiliary lattice vector $\mathbf{a}_3 = -\mathbf{a}_1 - \mathbf{a}_2$ was introduced. These are the brown vectors in Fig. 2, where it can be seen that \mathbf{a}_1 and \mathbf{a}_2 define the edges of the unit cell. The addition of \mathbf{a}_3 gives a basis of vectors that is three-fold symmetric: a clockwise rotation of 120 degree maps \mathbf{a}_1 onto \mathbf{a}_2 , \mathbf{a}_2 onto \mathbf{a}_3 and \mathbf{a}_3 onto \mathbf{a}_1 . One can label the unit cells with indices m and n , where unit cell $m+1, n$ is translated along \mathbf{a}_1 with respect to unit cell m, n and unit cell $m, n+1$ is translated along \mathbf{a}_2 .

In addition to the lattice vectors, the nearest-neighbor vectors from an

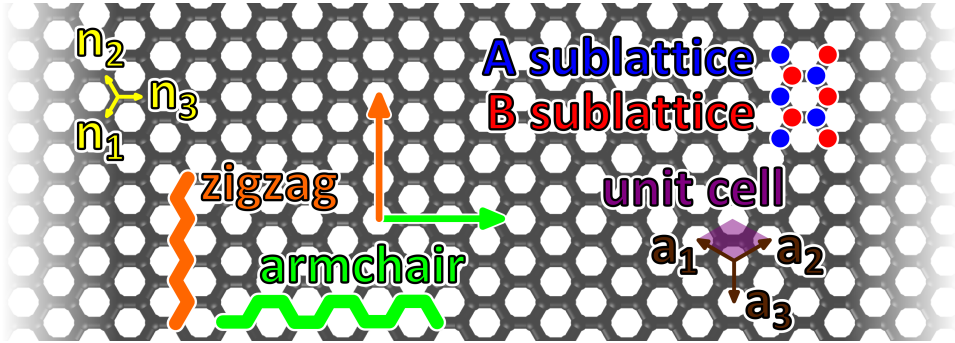


Fig. 2 Graphene. Indicated in orange (green) is the zigzag (armchair) direction of the honeycomb lattice. Blue (red) carbon atoms are on the A (B) sublattice. The purple diamond indicates a unit cell of the lattice. The brown arrows signify the lattice vectors of the honeycomb lattice. The yellow arrows are the nearest-neighbor vectors.

atom on sublattice B to its adjacent atoms on the A sublattice are

$$\begin{pmatrix} \mathbf{n}_1 \\ \mathbf{n}_2 \\ \mathbf{n}_3 \end{pmatrix} = a_0 \begin{pmatrix} -\frac{1}{2}\hat{x} - \frac{\sqrt{3}}{2}\hat{y} \\ -\frac{1}{2}\hat{x} + \frac{\sqrt{3}}{2}\hat{y} \\ \hat{x} \end{pmatrix}$$

where $\mathbf{n}_3 = -\mathbf{n}_1 - \mathbf{n}_2$. Similarly, the nearest-neighbor vectors from a site on sublattice A to its adjacent sites on B are $-\mathbf{n}_1$, $-\mathbf{n}_2$ and $-\mathbf{n}_3$. It can be verified that the nearest-neighbor vectors can be written in terms of the lattice vectors as $\mathbf{n}_i = (\mathbf{a}_{i+2} - \mathbf{a}_{i+1})/3$ where i is assumed modulo 3.

The reciprocal lattice vectors of the honeycomb lattice can be found as

$$\begin{pmatrix} \mathbf{b}_1 \\ \mathbf{b}_2 \\ \mathbf{b}_3 \end{pmatrix} = \frac{2\pi}{a_0} \begin{pmatrix} \frac{1}{3}\hat{x} + \frac{1}{\sqrt{3}}\hat{y} \\ \frac{1}{3}\hat{x} - \frac{1}{\sqrt{3}}\hat{y} \\ -\frac{2}{3}\hat{x} \end{pmatrix}$$

where in a similar fashion as to the real space vectors, $\mathbf{b}_3 = -\mathbf{b}_1 - \mathbf{b}_2$. These reciprocal lattice vectors are defined in such a way that the Kronecker product is

$$\mathbf{a} \otimes \mathbf{b} = 2\pi \begin{pmatrix} 0 & -1 & 1 \\ -1 & 0 & 1 \\ 1 & -1 & 0 \end{pmatrix}$$

Since the reciprocal lattice of the honeycomb lattice describes a basis for another honeycomb lattice, reciprocal nearest neighbor vectors can be defined for the reciprocal lattice in the same way as nearest neighbor vectors were defined for the real-space honeycomb lattice. This will turn out to be relevant in the description of the electronic structure. Setting $\mathbf{K}_i = (\mathbf{b}_{i+2} - \mathbf{b}_{i+1})/3$,

where i is assumed modulo 3, gives

$$\begin{pmatrix} \mathbf{K}_1 \\ \mathbf{K}_2 \\ \mathbf{K}_3 \end{pmatrix} = \frac{2\pi}{a_0} \begin{pmatrix} -\frac{1}{3}\hat{\mathbf{x}} + \frac{1}{3\sqrt{3}}\hat{\mathbf{y}} \\ \frac{1}{3}\hat{\mathbf{x}} + \frac{1}{3\sqrt{3}}\hat{\mathbf{y}} \\ \frac{2}{3\sqrt{3}}\hat{\mathbf{y}} \end{pmatrix}$$

$$\mathbf{n} \otimes \mathbf{K} = \frac{2\pi}{3} \begin{pmatrix} 0 & -1 & 1 \\ 1 & 0 & -1 \\ -1 & -1 & 0 \end{pmatrix} = \frac{1}{3} (\mathbf{a} \times \mathbf{b})$$

0.3.2 Electronic structure of graphene

The electronic structure of graphene can be described by a tight-binding model, where the wave functions of the low-energy electrons are expanded from the p_z atomic orbitals in the honeycomb lattice.[36, 37] The σ -type orbitals may be disregarded from symmetry considerations. A simple model may take into account interactions between adjacent carbon sites on the lattice, so that the Hamiltonian may be written as

$$\hat{H} = \sum_i^{atoms} \epsilon_i a_i^\dagger a_i + \sum_{\langle i,j \rangle}^{pairs} t (a_i^\dagger a_j + a_j^\dagger a_i)$$

The wave function on the honeycomb lattice can be written as

$$|\psi\rangle = \sum_{m,n}^{unit\ cells} |\psi\rangle_{m,n} = \sum_{m,n}^{unit\ cells} (x|A\rangle_{m,n} + y|B\rangle_{m,n}) e^{i\mathbf{k}\cdot\mathbf{r}}$$

where $|A\rangle$ ($|B\rangle$) describes a p_z orbital on the A (B) sublattice and x (y) is its expansion coefficient.

Within the nearest-neighbor tight-binding model, an electron can hop from site A in unit cell m, n to site B in the same unit cell, as well as to site B in cell $m, n + 1$ and unit cell $m - 1, n$, so that

$$\sum_{\langle i,j \rangle} a_j^\dagger a_i |A\rangle_{m,n} = |B\rangle_{m,n} + |B\rangle_{m-1,n} + |B\rangle_{m,n+1} = \gamma_0^*(\mathbf{k}) |B\rangle_{m,n}$$

where $\gamma_0(\mathbf{k}) = (1 + e^{i\mathbf{k}\cdot\mathbf{a}_1} + e^{-i\mathbf{k}\cdot\mathbf{a}_2})$ is a term describing the phase gained by hopping to adjacent unit cells. Similarly, $\sum_{\langle i,j \rangle} a_j^\dagger a_i |B\rangle_{m,n} = \gamma_0(\mathbf{k}) |A\rangle_{m,n}$. Therefore, we have

$$\begin{aligned} \hat{H}|\psi\rangle_{m,n} &= [(\epsilon_A x + t y \gamma_0(\mathbf{k})) |A\rangle_{m,n} + (\epsilon_B y + t x \gamma_0^*(\mathbf{k})) |B\rangle_{m,n}] e^{i\mathbf{k}\cdot\mathbf{r}} \\ &= E|\psi\rangle_{m,n} = [E x |A\rangle_{m,n} + E y |B\rangle_{m,n}] e^{i\mathbf{k}\cdot\mathbf{r}} \end{aligned}$$

introduction

so that

$$|A\rangle : (E - \epsilon_A)x = ty\gamma_0(\mathbf{k}) \quad \text{and} \quad |B\rangle : (E - \epsilon_B)y = tx\gamma_0^*(\mathbf{k})$$

Multiplication of the left- and right hand sides of the two equations gives

$$(E - \epsilon_A)(E - \epsilon_B)xy = t^2xy|\gamma_0(\mathbf{k})|^2$$

which can be solved (after removing the coefficients xy from both sides) to give the hyperbolic relation

$$E_{\pm} = \langle \epsilon \rangle \pm \sqrt{(\Delta\epsilon/2)^2 + t^2|\gamma_0(\mathbf{k})|^2}$$

where $\langle \epsilon \rangle = (\epsilon_A + \epsilon_B)/2$ is the average on-site energy that determines the center of the dispersion and $\Delta\epsilon = |\epsilon_A - \epsilon_B|$ is the difference in on-site energy. This $E(\mathbf{k})$ energy dispersion is plotted in Fig. 3.

Note that the energy dispersion of graphene has a degree of freedom in the phase factor in the sense that it is possible to write

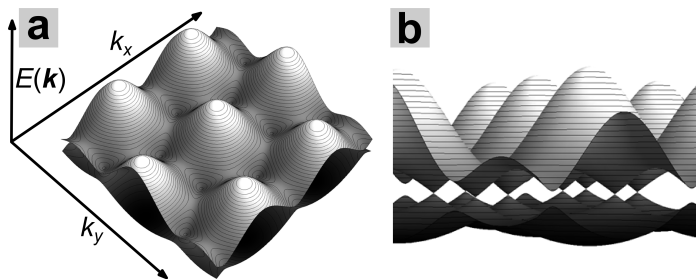
$$E_{\pm} = \langle \epsilon \rangle \pm \sqrt{(\Delta\epsilon/2)^2 + t^2|\gamma(\mathbf{k})|^2}$$

for an alternative phase factor $\gamma(\mathbf{k}) = \gamma_0(\mathbf{k})u(\mathbf{k})$ as long as $|\gamma(\mathbf{k})|^2 = \gamma^*(\mathbf{k})\gamma(\mathbf{k}) = [\gamma_0^*(\mathbf{k})u^*(\mathbf{k})][\gamma_0(\mathbf{k})u(\mathbf{k})] = [\gamma_0^*(\mathbf{k})\gamma_0(\mathbf{k})][u^*(\mathbf{k})u(\mathbf{k})] = |\gamma_0(\mathbf{k})|^2|u(\mathbf{k})|^2 = |\gamma_0(\mathbf{k})|^2$. This holds as long as $|u(\mathbf{k})|^2 = u^*(\mathbf{k})u(\mathbf{k}) = 1$, so that u is a complex phase factor. Setting $u(\mathbf{k}) = e^{i\mathbf{k}\cdot(\mathbf{a}_2 - \mathbf{a}_1)/3}$ gives

$$\begin{aligned} \gamma(\mathbf{k}) &= \gamma_0(\mathbf{k})u(\mathbf{k}) = \left(1 + e^{i\mathbf{k}\cdot\mathbf{a}_1} + e^{-i\mathbf{k}\cdot\mathbf{a}_2}\right) e^{i\mathbf{k}\cdot(\mathbf{a}_2 - \mathbf{a}_1)/3} \\ &= e^{i\mathbf{k}\cdot(\mathbf{a}_2 - \mathbf{a}_1)/3} + e^{i\mathbf{k}\cdot(\mathbf{a}_3 - \mathbf{a}_2)/3} + e^{i\mathbf{k}\cdot(\mathbf{a}_1 - \mathbf{a}_3)/3} = \sum_i e^{i\mathbf{k}\cdot\mathbf{n}_i} \end{aligned}$$

so that γ is conveniently the sum of complex phase factors corresponding to the nearest neighbors in the honeycomb lattice.

Fig. 3 Electronic (energy *versus* two-dimensional momentum) dispersion of graphene. a) $E(\mathbf{k})$ band structure of graphene b) Same as in a, but seen in the k_x, k_y -plane. Here, the emergence of Dirac cones is evident.



The largest energy separation - or band width - of the dispersion is given by the value of \mathbf{k} that maximizes $\gamma(\mathbf{k})$. Setting $\mathbf{k} = 0$ (the so-called Γ point)

reduces each of the three complex phase factors to unity, so that $|\gamma(\mathbf{k})| = 3$ and

$$E_{\pm}(\mathbf{\Gamma}) = \langle \epsilon \rangle \pm \sqrt{(\Delta\epsilon/2)^2 + (3t)^2}$$

which reduces to a band width of $6t$ for vanishing on-site energy difference. Furthermore, the on-site energy difference between the A sublattice sites and B sublattice sites immediately translates to the magnitude of the band gap since the smallest value that $|\gamma(\mathbf{k})|$ can obtain is 0, in which case $E_{\pm} = \langle \epsilon \rangle \pm \Delta\epsilon/2 \Rightarrow E_+ = \epsilon_A, E_- = \epsilon_B$.

In the case of graphene, however, the sublattices are identical, so that the on-site energies ϵ_A and ϵ_B are equal and the band gap vanishes. As a result, the electronic dispersion of graphene can be written as

$$E_{\pm}(\Delta\epsilon = 0) = \epsilon_0 \pm t|\gamma(\mathbf{k})| \quad \text{with} \quad \gamma(\mathbf{k}) = \sum_i e^{i\mathbf{k}\cdot\mathbf{n}_i}$$

where ϵ_0 is simply the carbon on-site energy.

It can be seen in the energy dispersion in Fig. 3b that the valence and conduction bands touch at certain points in reciprocal space. In fact, this occurs when the momentum \mathbf{k} of an electron in the honeycomb lattice happens to correspond to one of the six reciprocal nearest neighbor vectors $\pm\mathbf{K}_i$.

$$\gamma(\pm\mathbf{K}_i) = \sum_j e^{\pm i\mathbf{K}_i\cdot\mathbf{n}_j} = e^{\pm i\mathbf{K}_i\cdot\mathbf{n}_1} + e^{\pm i\mathbf{K}_i\cdot\mathbf{n}_2} + e^{\pm i\mathbf{K}_i\cdot\mathbf{n}_3}$$

Since each column in the Kronecker product $\pm\mathbf{n} \otimes \mathbf{K}$ contains the values 0, $2\pi/3$ and $-2\pi/3$, whatever nearest-neighbor vector $\pm\mathbf{K}_i$ is chosen, the sum will always return the three cube roots of unity (or their negative values) which trivially sum to zero.

$$\gamma(\pm\mathbf{K}_i) = \pm \left(1 + e^{i2\pi/3} + e^{-i2\pi/3} \right) = 0 \quad \forall i$$

As a result, the nearest neighbor vectors of the reciprocal lattice define the Dirac points, where the valence band E_+ and the conduction band E_- touch.

0.3.3 Linear dispersion

What happens to electrons or holes with momentum close to the Dirac points? This can be investigated by setting $\mathbf{k} = \mathbf{K}_3 + \delta\mathbf{k}$, which gives

$$\mathbf{k} \cdot \mathbf{n} = a_0 \left\{ -\frac{\delta k_x}{2} - \frac{\sqrt{3}\delta k_y}{2} + \frac{2\pi}{3}, -\frac{\delta k_x}{2} + \frac{\sqrt{3}\delta k_y}{2} - \frac{2\pi}{3}, \delta k_x \right\}$$

$$\frac{\gamma(\mathbf{k})}{a_0} = \left[e^{i\delta k_x} \right] + 2 \left[e^{-i\delta k_x/2} \right] \cos \left[\frac{2\pi}{3} - \frac{\sqrt{3}\delta k_y}{2} \right]$$

introduction

$$\begin{aligned} \frac{\gamma(\mathbf{k})}{a_0} &\approx [1 + i\delta k_x] + 2 \left[1 - \frac{i\delta k_x}{2} \right] \frac{1}{2} \left[\frac{3\delta k_y}{2} - 1 \right] \\ &\approx \frac{3}{2} \left(i\delta k_x + \delta k_y - \frac{1}{2} i\delta k_x \delta k_y \right) \approx \frac{3}{2} (i\delta k_x + \delta k_y) \end{aligned}$$

Therefore

$$E_{\pm}(\mathbf{K} + \delta\mathbf{k}) = \epsilon_0 \pm \frac{3}{2} a_0 t |i\delta k_x + \delta k_y|$$

This equation defines a Dirac cone: the dispersion around the Dirac points is locally linear ($E(\mathbf{K} + \delta\mathbf{k}) \propto |\delta\mathbf{k}|$). The same result is obtained by evaluating the eigenvalues of the Dirac Hamiltonian matrix.

$$\begin{aligned} \mathbf{H} &= \begin{pmatrix} \epsilon_0 & 3ta_0(-i\delta k_x + \delta k_y)/2 \\ 3ta_0(i\delta k_x + \delta k_y)/2 & \epsilon_0 \end{pmatrix} \\ &= \epsilon_0 \mathbf{I} + \frac{3ta_0}{2} \left(\delta k_x \begin{pmatrix} 0 & -i \\ i & 0 \end{pmatrix} + \delta k_y \begin{pmatrix} 0 & 1 \\ 1 & 0 \end{pmatrix} \right) = \epsilon_0 \mathbf{I} + \frac{3ta_0}{2} \delta\mathbf{k} \cdot \vec{\sigma} \end{aligned}$$

where $\vec{\sigma}$ is a vector containing the two Pauli spin matrices above. This result is equivalent to the dispersion for (massless) photons, which have

$$E = \hbar\omega = \hbar c|\mathbf{k}|$$

but with the proportionality of energy to momentum changed from $\hbar c$ to $\hbar v_F$, where $v_F = 3ta_0/2\hbar$ is the Fermi velocity of graphene (of the order of 10^6 ms^{-1}). This means, loosely speaking, that the electrons and holes in the graphene lattice have photon-like characteristics. It is this linear dispersion that makes graphene such an interesting material.[4, 38] Linear dispersion establishes that the charge carriers in the honeycomb lattice can travel in an almost unimpeded fashion. This is furthermore reflected in a vanishing effective mass and high charge carrier mobility.[39, 6]

Linear dispersion is not unique to the honeycomb lattice. In fact, Dirac cones can emerge in a number of lattices. The addition of a third hexagonal sublattice (“C”) could in principle exactly fill the voids of the honeycomb lattice and return a new hexagonal lattice. So in a sense, the honeycomb lattice is a hexagonal-depleted lattice with two instead of three sites per unit cell. Since not all nearest neighbor phase terms $e^{i\mathbf{k}\cdot\mathbf{a}_i}$ are “compensated” by opposite nearest neighbors $e^{-i\mathbf{k}\cdot\mathbf{a}_i}$, the band structure can deviate from “cosine-like” behavior ($e^{i\mathbf{k}\cdot\mathbf{a}_i} + e^{-i\mathbf{k}\cdot\mathbf{a}_i} = 2 \cos \mathbf{k} \cdot \mathbf{a}_i$), and this may result in a linear dispersion. A similar effect occurs in the Kagome lattice, which is a hexagonal-depleted lattice of three interpenetrating sublattices and one “missing sublattice”, and the Lieb lattice, which is a square-depleted lattice of three interpenetrating square sublattices and one missing sublattice. Of these, the

Lieb lattice is particularly relevant since it was the subject of some theoretical analysis by the author[40].

The Hamiltonian of the Lieb lattice can be written as

$$\mathbf{H} = \begin{pmatrix} \epsilon_0 & t\gamma_y^* & 0 \\ t\gamma_y & \epsilon_0 + \Delta\epsilon & t\gamma_x \\ 0 & t\gamma_x^* & \epsilon_0 \end{pmatrix}$$

where $\gamma_i^{(*)} = 1 + e^{(-)i\mathbf{k}\cdot\mathbf{a}_i}$, and $(\mathbf{a}_1, \mathbf{a}_2) = 2a_0(\hat{\mathbf{x}}, \hat{\mathbf{y}})$ are the lattice vectors. The Lieb lattice has a trivial flat band for vanishing density on the ‘‘square’’ sites (the remaining sites have no connectivity so zero dispersivity).

$$\mathbf{H}\mathbf{c}_0 = \begin{pmatrix} \epsilon_0 & t\gamma_y^* & 0 \\ t\gamma_y & \epsilon_0 + \Delta\epsilon & t\gamma_x \\ 0 & t\gamma_x^* & \epsilon_0 \end{pmatrix} \begin{pmatrix} x \\ 0 \\ z \end{pmatrix} = \begin{pmatrix} \epsilon_0 x \\ t(\gamma_y x + \gamma_x z) \\ \epsilon_0 z \end{pmatrix} = \epsilon_0 \begin{pmatrix} x \\ 0 \\ z \end{pmatrix}$$

for $(x, z) \propto (\gamma_x, -\gamma_y)$. The remaining energy bands can be obtained by evaluating the eigenvalues of the Hamiltonian.

$$E_{\pm} = \langle \epsilon \rangle \pm \sqrt{(\Delta\epsilon/2)^2 + t^2(|\gamma_x|^2 + |\gamma_y|^2)} = \langle \epsilon \rangle \pm \sqrt{(\Delta\epsilon/2)^2 + t^2|\vec{\gamma}|^2}$$

where $\langle \epsilon \rangle = \epsilon_0 + \Delta\epsilon$ is the average energy value of the top and bottom bands and $\vec{\gamma} = \gamma_x + i\gamma_y$. Like the honeycomb result, this is again a hyperbolic relation in the phase factors, even though the phase factor γ is different. Again, the top and bottom bands can touch if and only if the sites are all equivalent, so that $\Delta\epsilon = 0$ and the dispersion becomes

$$E_{\pm} = \epsilon_0 \pm t|\vec{\gamma}|$$

Since $|\gamma_x|^2 = (1 + e^{i\mathbf{k}\cdot\mathbf{a}_1})(1 + e^{-i\mathbf{k}\cdot\mathbf{a}_1}) = 2 + 2\cos\mathbf{k}\cdot\mathbf{a}_1 = 2 + 2\cos 2k_x a_0$ and equivalently for the y -direction, we have

$$|\gamma_x|^2 + |\gamma_y|^2 = 4 - 2\cos 2\delta k_x a_0 - 2\cos 2\delta k_y a_0$$

where $\mathbf{k} = \pi(\pm 1, \pm 1)/(2a_0) + \delta\mathbf{k}$ (close to the \mathbf{M} -points in reciprocal space). Expanding the cosines up to second order gives

$$|\gamma_x|^2 + |\gamma_y|^2 = (\delta k_x a_0)^2 + (\delta k_y a_0)^2 = a_0^2 |\delta\mathbf{k}|^2$$

so that

$$E_{\pm} = \epsilon_0 \pm a_0 t |\delta k_x + i\delta k_y| = \epsilon_0 \pm a_0 t |\delta\mathbf{k}|$$

meaning that the Lieb lattice has Dirac cone physics. Therefore, an effective low-energy Hamiltonian can be defined as

$$\mathbf{H} = \begin{pmatrix} \epsilon_0 & t\vec{\gamma} & 0 \\ t\vec{\gamma}^* & \epsilon_0 + \Delta\epsilon & 0 \\ 0 & 0 & \epsilon_0 \end{pmatrix} \approx \begin{pmatrix} \epsilon_0 & ta_0(\delta k_x - i\delta k_y) & 0 \\ ta_0(\delta k_x + i\delta k_y) & \epsilon_0 + \Delta\epsilon & 0 \\ 0 & 0 & \epsilon_0 \end{pmatrix}$$

introduction

where the block-diagonal shape reflects the presence of the dispersive, Dirac-cone-like bands ($E_{\pm}(\mathbf{k})$) while also maintaining a flat band solution ($E_0(\mathbf{k}) = \epsilon_0 \forall \mathbf{k}$).

In summary, lattices like the Lieb lattice and the Kagome lattice share the same recipe for Dirac cone physics as graphene. These are depleted lattices where the absence of opposite nearest-neighbor interaction integrals allows the band structure to deviate from cosine-like behavior. Then, the band structure turns out to be hyperbolic in some “composite” phase factor γ , and this hyperbolic relation turns into a linear one for equal on-site energies for the sublattice sites. Finally, points in reciprocal space can be found where γ becomes zero and around which γ becomes linearly proportional to $\delta\mathbf{k}$. These ingredients give rise to materials with amazing conductance properties. The fascinating world of Dirac materials and topological flat bands may very well play a large role in future electronics.

0.3.4 Graphene nanoribbons

Graphene nanoribbons are narrow strips of graphene and as such, share a lot of favorable electronic properties of their parent material, and their electronic structures can be derived by similar tight-binding methodologies.[41, 42, 34, 43, 44] Nevertheless, there are some fundamental differences between the bulk, two-dimensional material and the narrow one-dimensional structures. Most notably, the quantization of electron waves in the confined structure allows for the opening of a band gap - a sought-after property in the realm of nanoelectronics. This opening of the band gap is not necessarily monotonic with decreasing width. Moreover, the presence of topologically protected edge states makes the physics of graphene nanoribbons richer than one might initially expect.

In order to properly understand how electrons travel through graphene nanoribbons, one can envision a wave function in the graphene lattice, whose wave function is described by a momentum $\mathbf{k} = k_{ac}\hat{\mathbf{x}} + k_{zz}\hat{\mathbf{y}}$, where $\hat{\mathbf{x}}$ and $\hat{\mathbf{y}}$ are the perpendicular armchair and zigzag directions as in Fig. 2. Furthermore, this wave function has a certain coefficient vector $\mathbf{c} = (x, y)$. Elastic scattering of this electron onto an armchair edge of the graphene will invert its momentum in the zigzag direction, so that its final momentum becomes $\mathbf{k}' = k_{ac}\hat{\mathbf{x}} - k_{zz}\hat{\mathbf{y}}$. As this process unfolds, the wave function can be described as the superposition

$$\psi = \frac{\psi(\mathbf{k}) - \psi(\mathbf{k}')}{\sqrt{2}} = \frac{1}{\sqrt{2}} \sum_{m,n}^{unit\ cells} (x|A\rangle_{m,n} + y|B\rangle_{m,n}) \left(e^{i\mathbf{k}\cdot\mathbf{r}} - e^{i\mathbf{k}'\cdot\mathbf{r}} \right)$$

$$= \frac{2}{\sqrt{2}} \sum_{m,n}^{\text{unit cells}} (x|A\rangle_{m,n} + y|B\rangle_{m,n}) \left(e^{ik_{ac}x} \sin k_{zz}y \right) = \sqrt{2}\psi(k_{ac}, 0) \sin k_{zz}y$$

This wave function describes a plane wave in the armchair direction with a standing wave pattern in the zigzag direction.

Now consider an armchair-type graphene nanoribbon. An n -atom wide ribbon will be able to host the above wave functions provided the density vanishes to 0 at the 0'th and $(n + 1)$ 'th row. This means that whenever $y = (n + 1)a_0\sqrt{3}/2$, $\sin k_{zz}y = 0$ so that

$$k_{zz} = \pm \frac{2m\pi}{\sqrt{3}(n + 1)a_0}$$

where the quantum number m is referred to as the band index. This means that n -atom wide graphene nanoribbons can be envisioned as graphene wave guides with wave functions

$$\psi_{n\text{-acGNR}}(k_{ac}, m) = \psi_{\text{graphene}}(k_{ac}, 0) \sin \frac{\pm 2m\pi y}{\sqrt{3}(n + 1)a_0}$$

and their energies are given by cross-sections of the graphene dispersion relation for the k_{zz} -values that correlate with the different band indices m .

$$E_{ac,m}(k_{ac}) = \epsilon_0 \pm t \left| \gamma \left(k_{ac}, k_{zz} = \frac{2m\pi}{\sqrt{3}(n + 1)a_0} \right) \right|$$

This treatment is exact within the nearest-neighbor tight-binding model as atomic rows 0 and $n + 1$ have zero orbital density for all orbitals and hence no ‘‘cross-talk’’ exists between the nanoribbon and its periodic images.

Fig. 4 shows the band structures of armchair nanoribbons of widths $n = 3$ to $n = 8$. Surprisingly, although the general trend is a decrease of the band gap due to the emergence of an increasing number of bands, ribbons with width $n = 5$ and $n = 8$ can be seen to have bands crossing through the Fermi energy. The reason can easily be deduced to the fact that there is a \mathbf{K} -point in graphene in reciprocal space at $\mathbf{K} = \pm 4\pi\hat{\mathbf{y}}/(3\sqrt{3}a_0)$. Comparing this to the allowed k_{zz} values in armchair nanoribbons shows that the dispersion may cross this Dirac point

$$k_{zz} = \frac{2m\pi}{\sqrt{3}(n + 1)a_0} = \pm \frac{4\pi}{3\sqrt{3}a_0}$$

whenever the band index $m = \pm 2(n + 1)/3$. Since the band index is integer, this can only happen whenever $2(n + 1)/3$ is integer, which is the case if and only if $n = 3N + 2$ where N is an integer. So, whenever the width n of an armchair-type graphene nanoribbon is an integer multiple of three plus two,

introduction

the nanoribbon belongs to the “quasi-metallic” class of armchair ribbons as the band structure contains the Dirac point of graphene.

A similar zone-folding argument may be used to derive the electronic structure of zigzag-type graphene nanoribbons (Fig. 5) but the result obtained is not exact, as can be seen in Fig. 5b. Here, the band structure of a 6-zzGNR is calculated using the method above (red curves), as well as by a tight-binding calculation starting from a complete unit cell of the zigzag nanoribbon (black curves). The reason why the zone-folding method does not give the same exact answer is because of the fact that the nodal planes “miss” the sites on the zigzag edge that should have vanishing density: The zigzag sites “wobble” around any nodal plane positioned at a certain x -value. As a result, the edge is not taken into account well. It can clearly be seen that the correct treatment of the zigzag edges immediately gives rise to electronic states that constitute a local flat band at the Fermi energy. The spatial profile of the corresponding wave functions shows a localization on the zigzag edges (see Fig. 5c,d).

It is these topological zigzag-edge localized states near the Fermi energy that make the physics of graphene nanoribbons even richer.[41, 45] In particular, the tight-binding here does not take into account magnetic interactions, and it is thought that the degeneracy of the edge-localized bands at

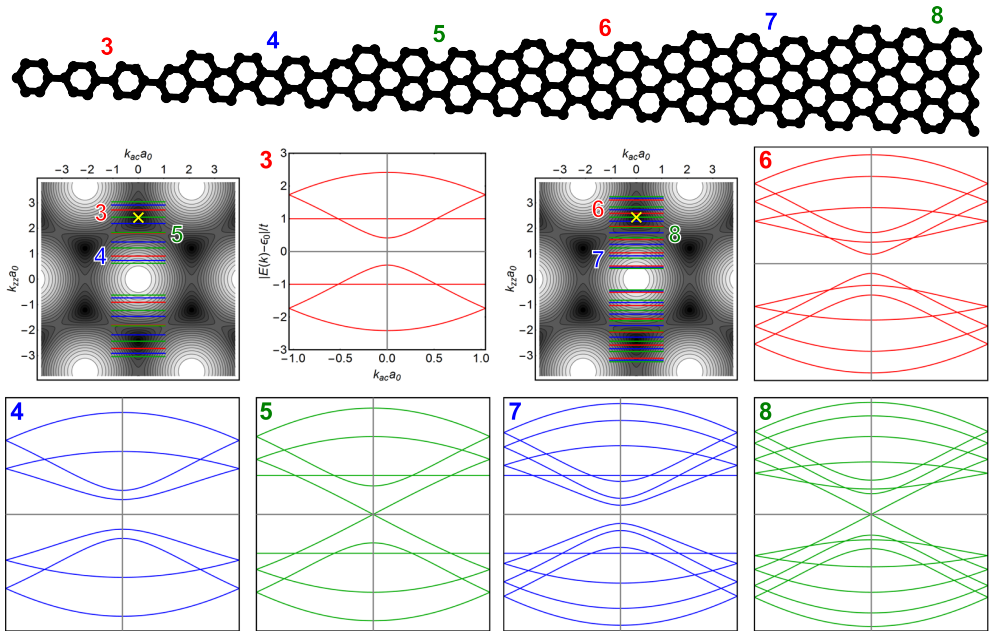


Fig. 4 Structure and energy dispersions of armchair-type graphene nanoribbons as obtained from the zone-folding method. The numbers indicate the width in atoms of the nanoribbons. The red and blue dispersions indicate the large gap families, whereas the green dispersions indicate the quasi-metallic family.

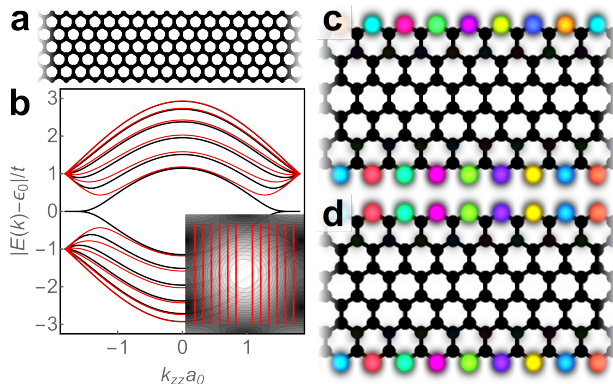


Fig. 5 Electronic structure of a zigzag graphene nanoribbon. a) Geometric structure and b) dispersion of the 6-zzGNR. The black curves are the results from a tight-binding calculation from the entire unit cell, whereas the red curves are the result from the zone-folding approach. The inset shows the slices of the zone folding calculation on the graphene dispersion. c) Lowest unoccupied and d) highest occupied crystal orbitals of the 6-zzGNR at the \mathbf{K} -point ($k = \pi/(2a_0)$).

the Fermi energy may in reality be lifted to accommodate electrons in opposite edges with opposite spins through antiferromagnetic coupling. Therefore, zigzag-type nanoribbons hold additional promise as functional structures in future spintronics.[46, 47, 48, 49]

Different types (shapes, edge structures) of graphene nanoribbons may be analyzed through the tight-binding methods above or through density-functional theory based methods.[50] In general, it will be the case that the zigzag edges of nanoribbons feature low-energy states. For example, the 3,1-chiral graphene nanoribbon - which is of significance for this thesis - features a mixed armchair/zigzag edge. Fig. 6 shows the dispersion of this nanoribbon in comparison with the metallic 5-acGNR and semiconducting 7-acGNR. Here, the green (red) color denotes the localization of the wave function on the edge (bulk) of the nanoribbon. In comparison with the 7-acGNR, low-energy states are present with significant localization on the edges, due to the partial zigzag character of the edges.

In summary, graphene nanoribbons can, to a first approximation, be understood as wave guides of graphene, and as such their electronic structure is closely related to their parent material. In particular, the decreasing band gap with increasing width and the $3n + 2$ -rule for metallicity in armchair type graphene nanoribbons are easily derived from applying a simple zone folding argument to the graphene electronic structure. However, zigzag type graphene nanoribbons feature topological edge states which cannot be obtained in a zone folding model. Chiral nanoribbons can be understood as having properties intermediate of those of armchair-type nanoribbons and zigzag nanoribbons.

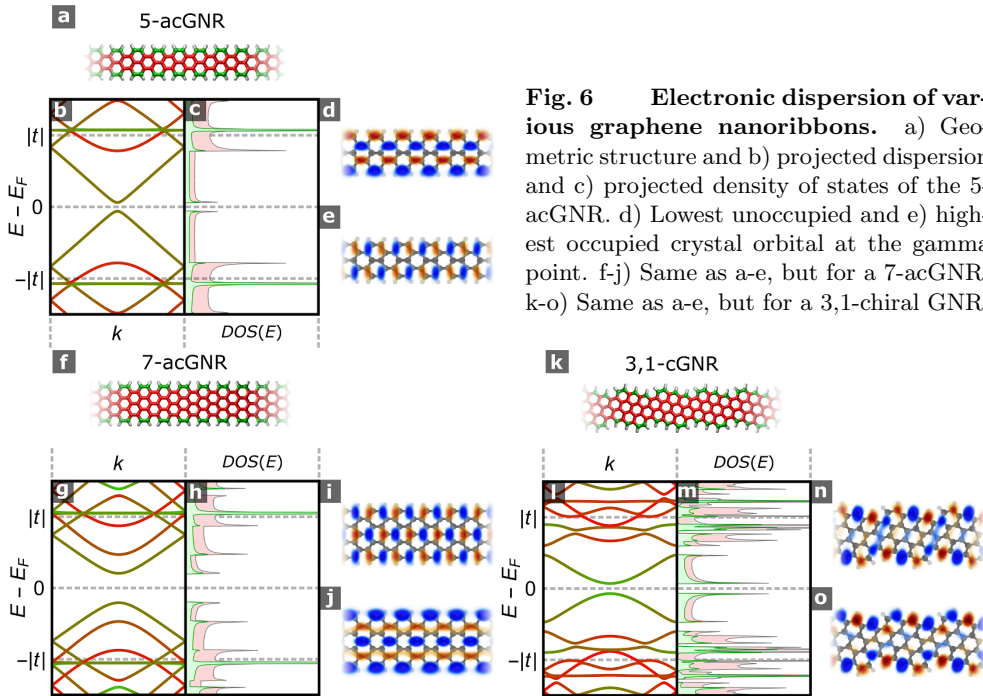


Fig. 6 Electronic dispersion of various graphene nanoribbons. a) Geometric structure and b) projected dispersion and c) projected density of states of the 5-acGNR. d) Lowest unoccupied and e) highest occupied crystal orbital at the gamma point. f-j) Same as a-e, but for a 7-acGNR. k-o) Same as a-e, but for a 3,1-chiral GNR.

0.4 Synthesis

In this last section of the introduction, we address the question of how graphene nanoribbons can be made. In principle, there are two fundamental approaches to arrive at these structures. The first and oldest one is the top-down approach, where nanoribbons are fabricated by processing larger materials into these small structures. Fabrication methods include lithography and unzipping of nanotubes.[51, 52, 53] A completely different approach involves bottom-up methodologies. Here, the nanostructures are obtained by assembly from smaller precursors.

As is clear from the previous section, the electronic structure of graphene nanoribbons is extremely sensitive on their atomic structure. Therefore, it is of utmost importance to control the structure of the molecules in the bottom-up process so that they allow for well-defined graphene nanoribbons to be formed. These molecules must first be designed to give the correct nanoribbon structure and allow for growth to occur successfully. Then they should be synthesized using conventional chemical synthesis, after which the molecules are introduced into the vacuum to complete nanoribbon fabrication by means of on-surface chemistry.

0.4.1 Solution-phase synthesis

Precursor molecules for graphene nanoribbons are commonly large, polycyclic aromatic hydrocarbons (PAHs) that are usually decorated with halogen atoms at the positions where intermolecular carbon-carbon coupling reactions are desired. For example, the archetypical 10,10'-dibromo-9,9'-bianthryl that is used in the synthesis of 7-atom wide armchair GNR contains two bromine atoms that are removed during the course of on-surface reactions to allow for the formation of polyanthrylene chains. By their nature, crafting these molecules therefore chiefly relies on ring-closure or cyclization reactions (extending the PAH system), halogenations (decorating the benzene rings to functionalize them for coupling reactions) and coupling reactions (stitching together smaller molecules to arrive at a larger precursor molecule).

Typical aryl-aryl cross-coupling reactions are the Kumada coupling (using an arylmagnesium compound and an aryl halide), the Stille coupling (using an aryltin compound and an aryl halide), the Negishi coupling (using an arylzinc compound and aryl halide), and the Suzuki coupling (using an arylboronic acid (or ester) and an aryl halide). Aryl-aryl cross-coupling of PAHs into larger, composed structures can sometimes prove to be challenging. Challenges that should be overcome are generally the low solubility of PAHs in most laboratory solvents as well as increasing steric demand of various coupling reactions as the molecules become more bulky. Nevertheless, as will be shown in chapter 2, we have succeeded in synthesizing 9,9'-bianthryl through palladium-catalyzed Suzuki cross coupling of 9-anthrylboronic acid with 9-bromoanthracene, despite the steric demand imposed by the PAH molecules. This molecule could subsequently be chlorinated to yield 10,10'-dichloro-9,9'-bianthryl.

Various heterocycles have been used in precursor molecules for graphene nanoribbons, and graphene nanoribbons with heteroatoms have been synthesized in this way. First, employing pyridine[54, 55] resulted in the formation of electron-poor graphene nanoribbons. By fusing together segments with pyrimidine rings with pristine, carbon-containing segments, staggered gap heterojunctions could be made.[56] More examples of heteroatom-substituted graphene nanoribbons include the boron-containing graphene nanoribbon made simultaneously in the groups of Crommie[57] and Fasel[58], as well as the sulfur-containing graphene nanoribbon by Nguyen *et al.*[59]

0.4.2 On-surface synthesis

The last step in the bottom-up process of building graphene nanostructures involves on-surface synthesis. To this end, molecular precursors as synthesized in the chemistry laboratory are deposited onto a clean metal surface and thermally induced (coupling) reactions are carried out. For example,

introduction

in the case of 10,10'-dibromo-9,9'-bianthryl - a molecule that will make numerous appearances throughout this thesis and the brominated analogue of the 10,10'-dichloro-9,9'-bianthryl mentioned in the previous section - deposition onto an atomically flat gold surface and subsequent heat-induced reactions result in the formation of 7-atom wide graphene nanoribbons (see Fig. 7a).[60] Similarly, a U-shaped molecule has been used on gold to create zigzag-type nanoribbons[30] (Fig. 7b) and chiral nanoribbons (which will also make a number of appearances throughout this thesis) can be synthesized by depositing 9,9'-bianthryl onto copper (Fig. 7c).[61, 62] On-surface synthesis employing 3,9-dibromoperylene results in 5-atom wide armchair nanoribbons (Fig. 7d).[63] More types of graphene nanoribbons that can be accessed by means of on-surface chemistry are described in [64].

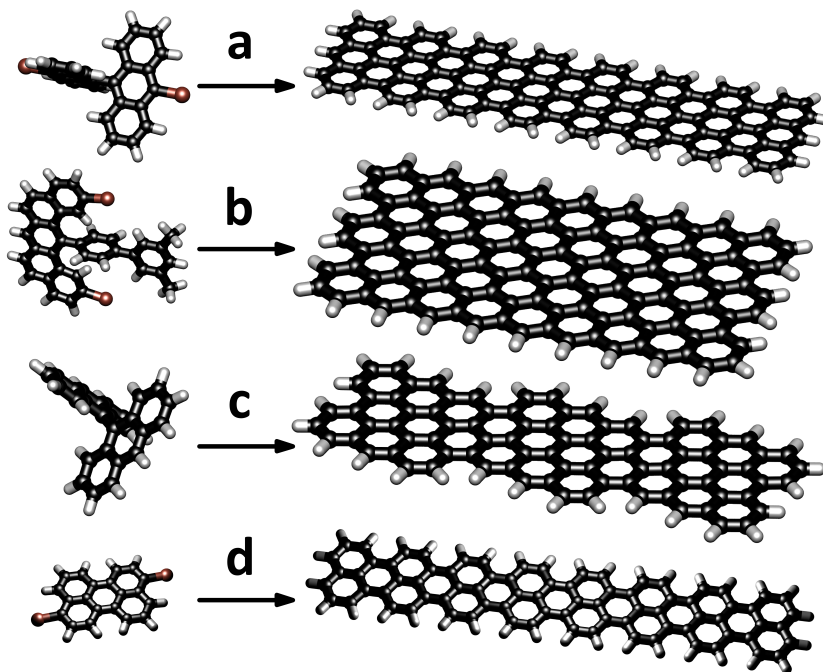


Fig. 7 Different types of graphene nanoribbons that can be synthesized by means of on-surface synthesis. a) armchair-type nanoribbons from 10,10'-dibromo-9,9'-bianthryl.[60] b) zigzag-type nanoribbons from 1-(3,5-dimethylphenyl)-4-(di-(3-bromo)benz[a,]j-9'-anthracenyl)benzene.[30] c) chiral nanoribbons from 9,9'-bianthryl.[61, 62] d) narrow armchair-type nanoribbons from 3,9-dibromoperylene.[63]

The following chapter gives an introduction into on-surface synthesis, and how atomic force microscopy can be applied to determine the geometric structure of molecules and structures such as graphene nanoribbons. This chapter serves as an introduction to the on-surface chemistry presented later in this thesis.

0.5 Conclusions

In summary, this PhD thesis presents a body of work on the synthesis and characterization of various types of graphene nanoribbons. In order to fulfill their promise as candidates for tomorrow's molecular electronics, controlling their structure down to the atomic level is of utmost importance. This is achieved using the bottom-up methodology, which comprises organic synthesis of precursor molecules and subsequent on-surface synthesis into graphene nanostructures. The processes and intermediates in the on-surface synthesis are studied using STM and AFM, and the thus-obtained graphene nanoribbons are subjected to extensive electronic characterization. This characterization is furthermore supported with electronic structure calculations on the basis of density functional theory and tight-binding calculations. In order to carry out the latter, a *Mathematica* package was developed. The research presented in this thesis has led to the synthesis of various types of GNR, understanding about their formation and properties, and synthesis and characterization of heterostructures of graphene nanoribbons containing electronic functionality. As a result, the work in this thesis presents significant steps forward in GNR-based nanoelectronics as well as in the development of methodologies related to electronic structure characterization and on-surface synthesis, which is of considerable interest in the communal progression towards tomorrow's electronics.

Bibliography

- [1] S. E. Thompson and S. Parthasarathy, *Materials Today* **9**, pp. 20–25 (2006).
- [2] R. J. Nichols and S. J. Higgins, *Annual Review of Analytical Chemistry* **8**, pp. 389–417 (2015).
- [3] D. Xiang, X. Wang, C. Jia, T. Lee, and X. Guo, *Chemical Reviews* **116**, pp. 4318–4440 (2016).
- [4] A. K. Geim and K. S. Novoselov, *Nature Materials* **6**, pp. 183–191 (2007).
- [5] F. Schwierz, *Nature Nanotechnology* **5**, pp. 487–496 (2010).
- [6] S. Das Sarma, S. Adam, E. H. Hwang, and E. Rossi, *Reviews of Modern Physics* **83**, pp. 407–470 (2011).
- [7] W. Han, R. K. Kawakami, M. Gmitra, and J. Fabian, *Nature Nanotechnology* **9**, pp. 794 (2014).
- [8] M. Terrones, A. R. Botello-Méndez, J. Campos-Delgado, F. López-Urías, Y. I. Vega-Cantú, F. J. Rodríguez-Macías, A. L. Elías, E. Muñoz-Sandoval, A. G. Cano-Márquez, J. C. Charlier, and H. Terrones, *Nano Today* **5**, pp. 351–372 (2010).
- [9] A. Narita, X. Feng, Y. Hernandez, S. A. Jensen, M. Bonn, H. Yang, I. A. Verzhbitskiy, C. Casiraghi, M. R. Hansen, A. H. Koch, G. Fytas, O. Ivasenko, B. Li, K. S. Mali, T. Balandina, S. Mahesh, S. De Feyter, and K. Müllen, *Nature Chemistry* **6**, pp. 126–132 (2014).
- [10] A. Narita, X.-Y. Wang, X. Feng, and K. Müllen, *Chem. Soc. Rev.* **44**, pp. 6616–6643 (2015).

introduction

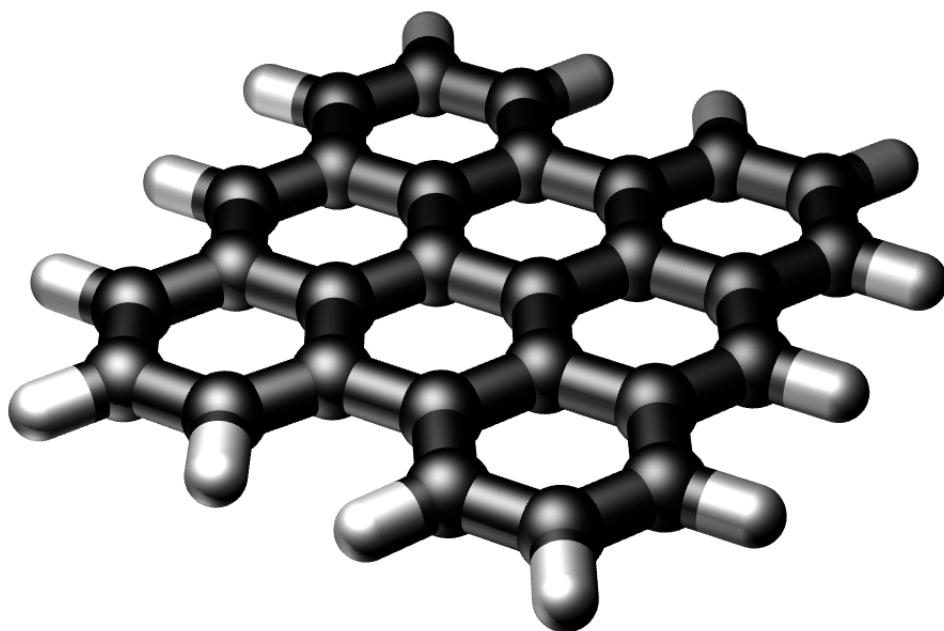
- [11] A. Narita, X. Feng, and K. Müllen, *Chemical Record* **15**, pp. 295–309 (2015).
- [12] G. Binnig, H. Rohrer, C. Gerber, and E. Weibel, *Applied Physics Letters* **40**, pp. 178–180 (1982).
- [13] G. Binnig, H. Rohrer, C. Gerber, and E. Weibel, *Physical Review Letters* **49**, pp. 57–61 (1982).
- [14] G. Binnig, C. F. Quate, and C. Gerber, *Physical Review Letters* **56**, pp. 930–933 (1986).
- [15] G. Binnig and H. Rohrer, *Reviews of Modern Physics* **59**, pp. 615–625 (1987).
- [16] F. J. Giessibl, H. Bielefeldt, S. Hembacher, and J. Mannhart, *Annalen Der Physik* **10**, pp. 887–910 (2001).
- [17] F. J. Giessibl, *Reviews of Modern Physics* **75**, pp. 1–35 (2003).
- [18] M. Nonnenmacher, M. P. O’Boyle, and H. K. Wickramasinghe, *Applied Physics Letters* **58**, pp. 2921–2923 (1991).
- [19] J. Tersoff and D. R. Hamann, *Physical Review B* **31**, pp. 805–813 (1985).
- [20] L. Gross, *Nature Chemistry* **3**, pp. 273–278 (2011).
- [21] L. Grill, M. Dyer, L. Lafferentz, M. Persson, M. V. Peters, and S. Hecht, *Nature Nanotechnology* **2**, pp. 687–691 (2007).
- [22] G. Meyer, L. Bartels, and K.-H. Rieder, *Computational Materials Science* **20**, pp. 443–450 (2001).
- [23] S.-W. Hla, L. Bartels, G. Meyer, and K.-H. Rieder, *Physical Review Letters* **85**, pp. 2777–2780 (2000).
- [24] M. Koch, F. Ample, C. Joachim, and L. Grill, *Nature Nanotechnology* **7**, pp. 713–717 (2012).
- [25] J. van der Lit, P. H. Jacobse, D. A. M. Vanmaekelbergh, and I. Swart, *New Journal of Physics* **17**, pp. 53013 (2015).
- [26] J. van der Lit, M. P. Boneschanscher, D. Vanmaekelbergh, M. Ijäs, A. Uppstu, M. Ervasti, A. Harju, P. Liljeroth, and I. Swart, *Nature Communications* **4**, pp. 2023 (2013).
- [27] S. Kawai, S. Saito, S. Osumi, S. Yamaguchi, A. S. Foster, P. Spijker, and E. Meyer, *Nature Communications* **6**, pp. 8098 (2015).
- [28] M. C. Chong, N. Afshar-Imani, F. Scheurer, C. Cardoso, A. Ferretti, D. Prezzi, and G. Schull, *Nano Letters* **18**, pp. 175–181 (2018).
- [29] S. Wang, L. Talirz, C. A. Pignedoli, X. Feng, K. Müllen, R. Fasel, and P. Ruffieux, *Nature Communications* **7**, pp. 11507 (2016).
- [30] P. Ruffieux, S. Wang, B. Yang, C. Sanchez-Sanchez, J. Liu, T. Dienel, L. Talirz, P. Shinde, C. A. Pignedoli, D. Passerone, T. Dumslaff, X. Feng, K. Müllen, and R. Fasel, *Nature* **531**, pp. 489–492 (2016).
- [31] F. J. Giessibl, *Physical Review B* **56**, pp. 16010–16015 (1997).
- [32] L. Gross, F. Mohn, N. Moll, P. Liljeroth, and G. Meyer, *Science* **325**, pp. 1110–1114 (2009).
- [33] C. B. Mallah, F. Ducastelle, and T, *Journal of Physics: Condensed Matter* **29**, pp. 465302 (2017).
- [34] Y. W. Son, M. L. Cohen, and S. G. Louie, *Physical Review Letters* **97**, pp. 216803 (2006).
- [35] K. Wakabayashi, K.-I. Sasaki, T. Nakanishi, and T. Enoki, *Science and Technology of Advanced Materials* **11**, pp. 054504 (2010).
- [36] P. R. Wallace, *Phys. Rev.* **71**, pp. 622–634 (1947).
- [37] J. C. Slonczewski and P. R. Weiss, *Physical Review* **109**, pp. 272–279 (1958).
- [38] M. I. Katsnelson, *Materials Today* **10**, pp. 20–27 (2007).
- [39] A. K. Geim, *Science* **324**, pp. 1530–1534 (2009).
- [40] M. R. Slot, T. S. Gardenier, P. H. Jacobse, G. C. Van Miert, S. N. Kempkes, S. J. Zevenhuizen, C. M. Smith, D. Vanmaekelbergh, and I. Swart, *Nature Physics* **13**, pp. 672–676 (2017).

- [41] K. Nakada, M. Fujita, G. Dresselhaus, and M. S. Dresselhaus, *Physical Review B* **54**, pp. 17954–17961 (1996).
- [42] M. Fujita, K. Wakabayashi, K. Nakada, and K. Kusakabe, *Journal of the Physical Society of Japan* **65**, pp. 1920–1923 (1996).
- [43] Y. Hancock, A. Uppstu, K. Saloritta, A. Harju, and M. J. Puska, *Physical Review B - Condensed Matter and Materials Physics* **81**, pp. 245402 (2010).
- [44] M. Ijäs, M. Ervasti, A. Uppstu, P. Liljeroth, J. van der Lit, I. Swart, and A. Harju, *Physical Review B - Condensed Matter and Materials Physics* **88**, pp. 75429 (2013).
- [45] H. Raza, *Journal of Physics Condensed Matter* **23**, pp. 382203 (2011).
- [46] Y. W. Son, M. L. Cohen, and S. G. Louie, *Nature* **444**, pp. 347–349 (2006).
- [47] S. Lakshmi, S. Roche, and G. Cuniberti, *Materials Science*, p. 4 (2009).
- [48] E. S. Grichuk and E. A. Manykin, *JETP Letters* **93**, pp. 372–376 (2011).
- [49] D. Kang, B. Wang, C. Xia, and H. Li, *Nanoscale Research Letters* **12**, pp. 357 (2017).
- [50] O. V. Yazyev, *Accounts of Chemical Research* **46**, pp. 2319–2328 (2013).
- [51] M. Y. Han, B. Özyilmaz, Y. Zhang, and P. Kim, *Physical Review Letters* **98**, pp. 206805 (2007).
- [52] L. Jiao, L. Zhang, X. Wang, G. Diankov, and H. Dai, *Nature* **458**, pp. 877–880 (2009).
- [53] D. V. Kosynkin, A. L. Higginbotham, A. Sinitskii, J. R. Lomeda, A. Dimiev, B. K. Price, and J. M. Tour, *Nature* **458**, pp. 872–876 (2009).
- [54] C. Bronner, S. Strelau, M. Gille, F. Brauße, A. Haase, S. Hecht, and P. Tegeder, *Angewandte Chemie - International Edition* **52**, pp. 4422–4425 (2013).
- [55] Y. Zhang, Y. Zhang, G. Li, J. Lu, X. Lin, S. Du, R. Berger, X. Feng, K. Müllen, and H. J. Gao, *Applied Physics Letters* **105**, pp. 023101 (2014).
- [56] J. Cai, C. A. Pignedoli, L. Talirz, P. Ruffieux, H. Söde, L. Liang, V. Meunier, R. Berger, R. Li, X. Feng, K. Müllen, and R. Fasel, *Nature Nanotechnology* **9**, pp. 896–900 (2014).
- [57] R. R. Cloke, T. Marangoni, G. D. Nguyen, T. Joshi, D. J. Rizzo, C. Bronner, T. Cao, S. G. Louie, M. F. Crommie, and F. R. Fischer, *Journal of the American Chemical Society* **137**, pp. 8872–8875 (2015).
- [58] S. Kawai, V. Haapasilta, B. D. Lindner, K. Tahara, P. Spijker, J. A. Buitendijk, R. Pawlak, T. Meier, Y. Tobe, A. S. Foster, and E. Meyer, *Nature Communications* **7**, pp. 12711 (2016).
- [59] G. D. Nguyen, F. M. Toma, T. Cao, Z. Pedramrazi, C. Chen, D. J. Rizzo, T. Joshi, C. Bronner, Y. C. Chen, M. Favaro, S. G. Louie, F. R. Fischer, and M. F. Crommie, *Journal of Physical Chemistry C* **120**, pp. 2684–2687 (2016).
- [60] J. Cai, P. Ruffieux, R. Jaafar, M. Bieri, T. Braun, S. Blankenburg, M. Muoth, A. P. Seitsonen, M. Saleh, X. Feng, K. Müllen, and R. Fasel, *Nature* **466**, pp. 470–473 (2010).
- [61] C. Sánchez-Sánchez, T. Dienel, O. Deniz, P. Ruffieux, R. Berger, X. Feng, K. Müllen, and R. Fasel, *ACS Nano* **10**, pp. 8006–8011 (2016).
- [62] F. Schulz, P. H. Jacobse, F. F. Canova, J. Van Der Lit, D. Z. Gao, A. Van Den Hoogenband, P. Han, R. J. Klein Gebbink, M. E. Moret, P. M. Joensuu, I. Swart, and P. Liljeroth, *Journal of Physical Chemistry C* **121**, pp. 2896–2904 (2017).
- [63] A. Kimouche, M. M. Ervasti, R. Drost, S. Halonen, A. Harju, P. M. Joensuu, J. Sainio, and P. Liljeroth, *Nature Communications* **6**, pp. 10177 (2015).
- [64] L. Talirz, P. Ruffieux, and R. Fasel, *Advanced Materials* **28**, pp. 6222–6231 (2016).

introduction

Chapter 1

Tracking on-surface chemistry with atomic precision

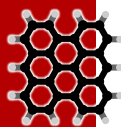


This chapter is based on

Tracking on-surface chemistry with atomic precision

Peter H. Jacobse, Marc-Etienne Moret, Robertus J. M. Klein Gebbink,
Ingmar Swart

Synlett **28** (19), pp. 2509-2516 (2017)



The field of on-surface synthesis has seen a tremendous development in the past decade as an exciting new methodology towards atomically well-defined nanostructures. A strong driving force in this respect is its inherent compatibility with scanning probe techniques, which allows one to view the reactants and products at the single-molecule level. In this chapter, we review the ability of non-contact atomic force microscopy to study on-surface chemical reactions with atomic precision. We highlight recent advances in using noncontact atomic force microscopy to obtain mechanistic insight into reactions and focus on the recently elaborated mechanisms in the formation of different types of graphene nanoribbons.

1.1 On-surface synthesis

Surface chemistry has played a prominent role in organic synthesis for centuries, most notably in the form of heterogeneous catalysis. The discovery of platinum-catalyzed combustion of gaseous mixtures by Davy[1] was only the beginning of a rich history of surface chemistry that would prove to have a tremendous impact on chemistry at large. Although the chemical transformations themselves take place at the surface, the way in which heterogeneous catalysis is employed is most often three-dimensional, with the catalyst dispersed in the reaction medium or the medium being passed through a catalyst bed. Furthermore, the rugged and often ill-defined surface of the catalyst can hardly be considered two-dimensional. With the advent of on-surface synthesis, however, reactions have started to become truly two-dimensional. Here, molecules are deposited onto an atomically flat surface under typically ultrahigh vacuum (UHV) conditions. The reactants can move laterally over the surface but have no freedom to jump off the surface: this would imply desorption, which, under UHV conditions, is permanent. Reactions between molecules therefore take place in-plane. The rules of the game of on-surface synthesis therefore allow for a distinct type of chemistry that facilitates the controlled synthesis of new types of nanostructures. Another powerful aspect of this technique is its synergy with conventional chemical methods: The precursor molecules for on-surface reactions can be prepared by solution-based methods before being transferred to the UHV setup. Indeed, on-surface reactions can be applied to a large proportion of molecules that can be tailored in the chemistry lab. Therefore, on-surface synthesis can be particularly powerful when used in conjunction with solution-phase synthesis.

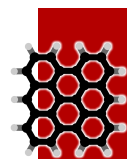
In on-surface synthesis, precursor molecules are commonly deposited onto a surface by evaporation from an effusion cell followed by adsorption, after which heating or irradiation may be carried out to induce chemical reactions. These

reactions may be intramolecular, but in the quest for extended nanostructures, intermolecular coupling reactions are particularly desirable. On-surface chemistry has proven to be a valuable technique to obtain high-quality one- or two-dimensional materials like graphenes, polyphenylenes, fullerenes, and graphene nanoribbons (GNRs).[2, 3, 4, 5, 6, 7, 8] Restriction of adsorbates to the surface effectively eliminates nonselective out-of-plane reactions, facilitating the creation of atomically well-defined low-dimensional nanostructures.

Despite its virtues, on-surface synthesis could only take off as a new emerging field with the advent of sensitive surface-probing techniques. Traditional chemical synthesis mostly relies on spectroscopic techniques and other bulk characterization methods, which are ill-suited for the typically obtained sub-monolayer coverages on single crystals. Therefore, it was not until the development of highly sensitive methods such as scanning probe microscopy that on-surface chemistry could really develop into a field of its own.

The most used scanning probe technique in on-surface chemistry is scanning tunneling microscopy. Here, a bias voltage is applied between a conductive tip and sample. When the tip-sample distance is on the order of a (few) nanometer(s), electrons can tunnel across the vacuum gap between tip and surface, creating a current which may be used as a feedback parameter to control the tip height.[9] When scanning the tip across a surface littered with molecular adsorbates, the tunnel current depends on both the physical height as well as the available electronic energy levels that may contribute to the tunneling process. An STM topograph of an absorbed species may thus be regarded as a convolution of its geometric and electronic structure. As far as electronic structure is concerned, STM probes the low-energy states, which in large aromatic systems, such as polycyclic aromatic hydrocarbons (PAHs) and nanographenes, typically arises from π -orbitals. STM is a powerful technique in identifying molecules and nanostructures on surfaces, and has the additional advantage that the bias voltage can be used as an extra degree of freedom to facilitate a detailed electronic analysis.[10] However, the pure geometric structure the framework of bonds and atoms cannot be identified as it is clouded by electrons from frontier orbitals, as well as non-resonant tunneling processes.

In contrast, noncontact atomic force microscopy is a more recently established technique and admittedly, a much more demanding one that is capable of imaging the chemical structure of molecules with atomic resolution.[11] In nc-AFM, an AFM cantilever with high stiffness (typically $1,800 \text{ N m}^{-1}$) is driven at its resonance frequency. Upon approaching the tip to the surface, the resonance frequency shifts due to electrostatic, van der Waals, and Pauli interactions with the sample. This landscape of interactions is established by the total electron density, rather than the resonant electron density, and therefore includes all covalent bonds. As a result, an nc-AFM scan can actu-





ally uncover the molecular framework of bonds and atoms, and allows to peek inside a single molecule.[12] The remarkable capability of nc-AFM to really reveal the molecular skeleton with atomic resolution is unprecedented.

1.2 Scanning tunneling and atomic force microscopy

The first realization of intramolecular contrast with nc-AFM came with the seminal visualization of the individual benzene rings in the backbone of pentacene.[11] Soon after, a plethora of other, mostly aromatic molecules were examined, each time revealing images of their respective backbones of bonds and rings in a way that closely resembled the structural models from chemistry textbooks.[13, 14, 15, 16, 17, 18, 19] Noteworthy is the extensive effort in elucidating the structure of asphaltene molecules.[20] Like snowflakes, no two of these large PAHs are alike, and therefore, their structure cannot be identified with ensemble techniques. On the contrary, by using nc-AFM, each single asphaltene could be identified by the atoms and rings displayed in the respective images.

Nc-AFM is a powerful tool to uncover the structure of known or unknown molecules and becomes even more interesting when the molecules themselves engage in chemistry. Reactions on surfaces can be induced by means of heating[2, 3, 21, 22], irradiation[23], or even by employing voltage pulses with an STM tip.[24, 25] In each case, nc-AFM can be used to directly compare the structure of the molecular adsorbates before and after the transformation. The unique insight that this provides is particularly useful in reactions with multiple steps, multiple products, or products that cannot be unambiguously identified with other methods.

A beautiful example of a reaction with multiple steps is the tip-induced debromination and reversible Bergman cyclization of 9,10-dibromoanthracene.[26] By application of a voltage pulse, Schuler *et al.* succeeded in selectively cleaving off the bromine atoms, yielding the 9-bromo-10-anthryl radical and subsequently the 9,10-anthrylene diradical. Both the reactant and the two individual radicals were visualized with nc-AFM, as can be seen in Fig. 1.1a. Surprisingly, it was found that further application of voltage pulses induced reversible switching of the molecule into three different isomeric states. The isomers turned out to be the diradical and two equivalent retro-Bergman products, with the outermost ring cleaved internally to give an expanded, ten-membered ring. By using nc-AFM, the team was able to visualize the ring-expanded molecules, clearly revealing the cleaved bond and giving indisputable evidence of the transformation.

Other elegant examples of isomers and intramolecular transformations an-

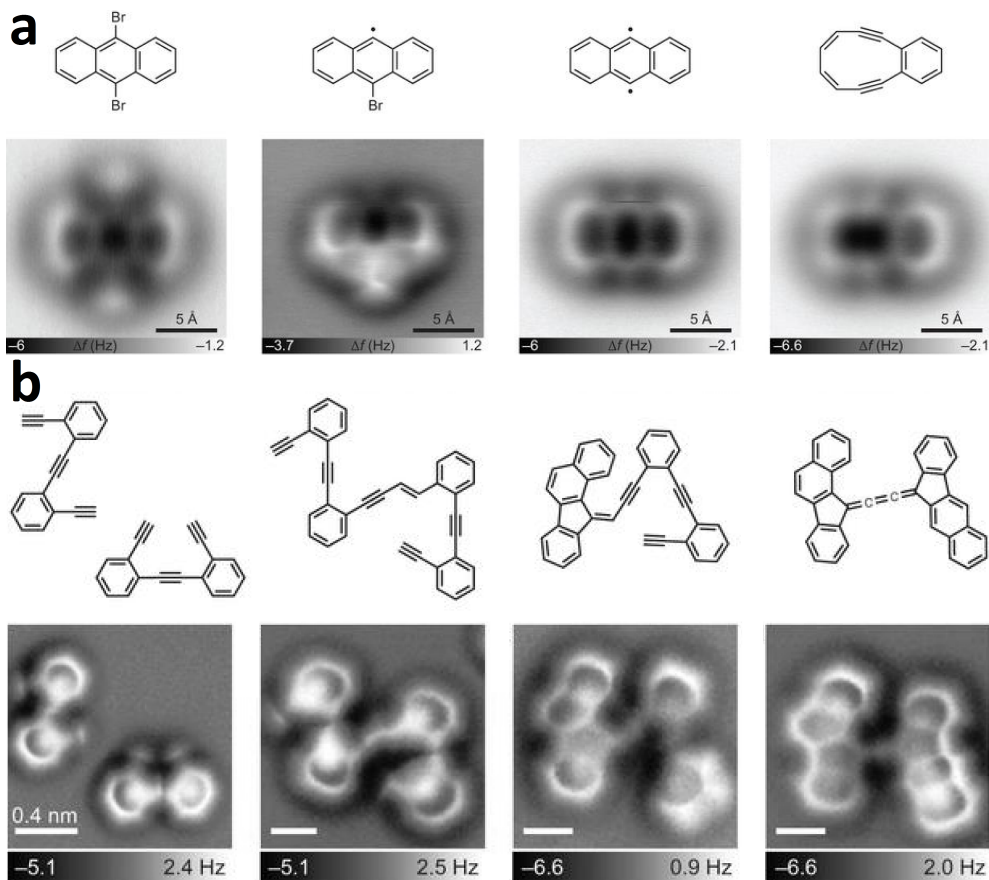


Fig. 1.1 a) Products and intermediates of the Bergman cyclization, identified with nc-AFM. Adapted by permission from Macmillan Publishers Ltd: Nature Communications, ref. [26], Copyright (2016). b) Coupling and cyclization reactions of oligo-(phenylene-1,2-ethynylenes). Adapted by permission from Macmillan Publishers Ltd: Nature Chemistry, ref. [27], Copyright (2016).

alyzed with nc-AFM include the subtle differentiation of cumulene and aryne tautomers in a PAH[28], cyclization of triangular dehydrobenzoannulene[22], reactions of oligo-(phenylene-1,2-ethynylenes)[27, 29] (see Fig. 1.1b), sulfur elimination from diphenanthrothiophene[30], and conformational changes in tetraphenylporphyrins[31] and dibenzo[a,h]thianthrene.[32] The last three examples show that nc-AFM can even be used on molecules that are not completely planar, although at the expense of losing contrast in regions that are closer to the surface. All examples mentioned above are elegant instances of using AFM in visualizing different products, reactants, and intermediates within single molecules. In the rest of this article, we will review its application to intermolecular reactions.

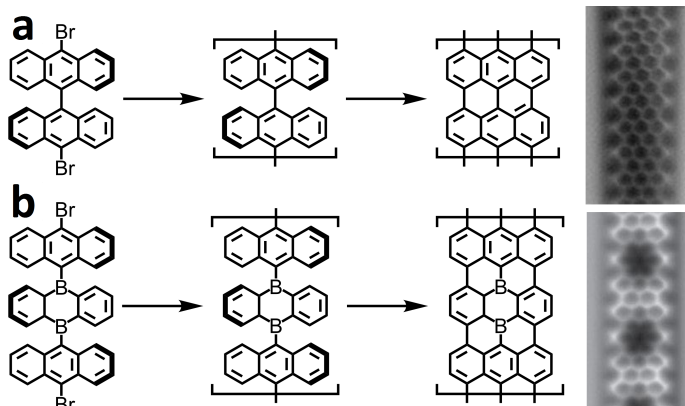


In the context of intermolecular on-surface reactions tracked with AFM, the dimerization and polymerization of enediynes[29], the formation of a metal-organic framework from 4,9-diaminoperylene-quinone-3,10-diimine[35], and coupling of porphine onto a graphene sheet[36] are noteworthy examples. Coupling reactions also play an important role in the bottom-up assembly of potentially extremely useful nanostructures: GNRs. GNRs are particularly promising structures as they are based on the parent material graphene, which features unprecedented electronic properties such as high-charge carrier mobility and low effective mass. Their one-dimensional, quantum-confined nature allows for additional advantageous properties such as a finite and tunable band gap, where fine-tuning of the electronic structure can be achieved through tailoring the width, edge structure, and doping.[37, 38, 39, 40, 41, 42, 43, 44, 45, 46, 47] As such, they hold promise for use in future nanoelectronics. In their pioneering work, Cai *et al.* presented the first bottom-up synthesis of atomically well-defined GNR on surface.[48] The ribbons were fabricated in a two-step process from 10,10-dibromo-9,9-bianthryl (DBBA) on an Au(111) surface. As shown in Fig. 1.2a, the first step is a thermally induced debromination, giving rise to surface-stabilized radicals that couple to form staggered polyanthrylene chains.[49][50][51] The subsequent annealing step takes place at higher temperature and induces cyclodehydrogenation of the polyanthrylene into seven-atom wide nanoribbons with armchair-type edges (7-AGNR). Indeed, STM images obtained from samples prepared with omission of the annealing step show a characteristic pattern of protrusions as expected from the staggered anthryl units in polyanthrylene chains. Furthermore, the 7-AGNR were unambiguously resolved as such with nc-AFM (see Fig. 1.2a).[33] In the subsequent development of more types of nanoribbons, on-surface synthesis has played a dominant role.[52] Not only does it facilitate the fabrication of atomically defect-free structures that are difficult to obtain with solution-based methods, but is also inherently compatible with scanning probe techniques that allow for detailed characterization.[4, 5, 53, 54, 55, 56]

1.3 Graphene nanoribbons

Further tailoring of the electronic properties of graphene nanoribbons can be performed by making use of heteroatom doping. For example, nitrogen can be incorporated by substituting phenyl groups with pyridyl groups in the precursor molecules.[57, 58, 42] Both Cloke *et al.* and Kawai *et al.* showed that the bottom-up assembly could also be used to produce boron-doped 7-AGNR, by making use of a precursor that can be thought of as a functionalized analogue of DBBA.[22, 59] This molecule has a single diboraanthracene moiety

Fig. 1.2 a) Synthesis of 7-AGNR from DBBA. b) Synthesis of boron-doped 7-AGNR from 9,10"-dibromo-9',10'-diborateranthryl. Adapted by permission from Macmillan Publishers Ltd: Nature Communications, refs. [33, 34]. Copyright (2013, 2015).



sandwiched between two bromoanthryl extremities (Fig. 1.2b). The radical coupling takes place at the bromoanthryl groups in the same exact way as in DBBA, and may thus be thought to be blind for the embedded diboraaanthracene. However, when the subsequent cyclodehydrogenation step forces the previously unnoticed boron-substituted anthryl units to enter the lattice, it is not difficult to notice an analogy with the Trojan horse. Nc-AFM images of the product show the same structure as the undoped 7-AGNR, but with characteristic variations in σ -bond contrast due to the substitutional boron atoms.

The boron-doped 7-AGNR is just one of many different GNRs that were produced by cleverly designing and modifying precursor molecules.[57, 60, 61, 62] The preparation requires, in each case, a number of solution-phase synthesis steps. Importantly, aryl-aryl coupling reactions similar to those used on surface may already play an important role in the fume hood, before the molecules are ready to enter the UHV setup. For example, DBBA itself has been produced by Kumada and Suzuki cross-coupling reactions of anthryl bromides.[33, 63] Suzuki coupling has also been used in the preparation of the precursors for the 13-atom-wide GNR, by attaching biphenylboronic acid and thiophenylphenylboronic acid onto the bianthryl core.[60, 64] In the latter case, a tetrabromo coupling partner was used, but fortunately the coupling turned out to be selective towards the desired disubstituted product. The Ullmann coupling on the surface, on the other hand, is a homocoupling, and does not permit the same level of selectivity as can be achieved in solution. These results highlight the importance to control the different possible coupling steps, so that they can be carried out in the right sequence. Since the large majority of aryl-aryl cross-coupling reactions rely on aryl halides, the greatest synthetic flexibility can in principle be achieved by carrying out the on-surface coupling with the most strongly bound halogen. This recognition led us to pursue the question whether aryl chlorides could be used instead of aryl bromides in the

synthesis of GNR.[63]

We started by synthesizing 10,10'-dichloro-9,9'-dibromobianthryl (DCBA): the dichloro analogue of DBBA. Interestingly, when thermally treated in a similar way as with DBBA, DCBA was found to give rise to extensive planar aromatic networks, rather than 7-AGNRs. Nc-AFM clearly revealed these networks to consist of randomly interconnected bisanthene units (bisanthene being the cyclodehydrogenation product of bianthryl (see Fig. 1.3). To figure out why these disordered structures were obtained, we tried to identify mechanistic intermediates by conducting the experiment at a range of different temperatures. At 200 °C, we observed a large number of bisanthene molecules as well as coupled bisanthenes. Once again, we used nc-AFM to reveal their structure, allowing us to discover that the coupling products almost exclusively feature interconnecting bonds from the 'middle' C(10) position to the 'corner' CH(3) position, as can be seen in Fig. 1.3 (where we use the numbering of the parent bianthryl molecules). What could be the reason that the usual radical-radical coupling is blocked, and intercepted by this alternative pathway?

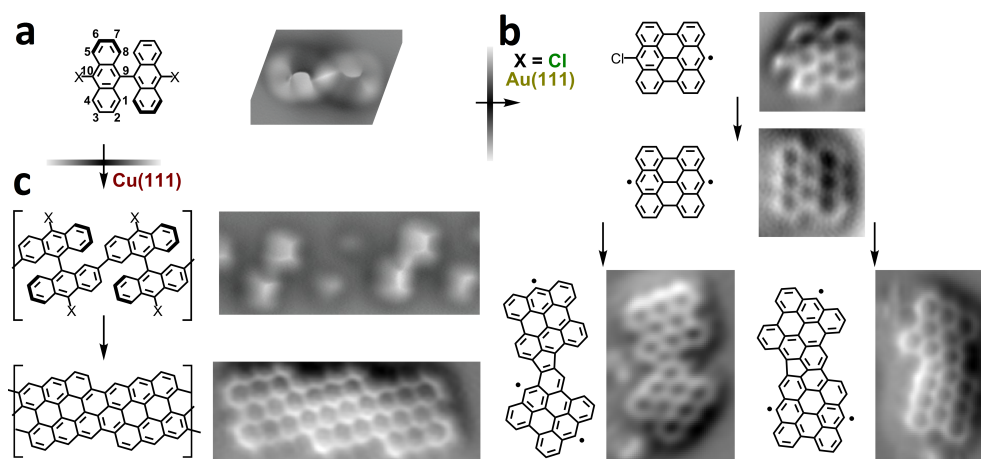


Fig. 1.3 a) Structure of dihalobianthryl, and an AFM scan of dibromobianthryl (X = Br) on Cu(111). b) Formation mechanism of oligo- and polybisanthenes from DCBA on Au(111). Reprinted (adapted) by permission from Jacobse, P. H. *et al.* *Angew. Chem. Int. Ed.* 2016, 55, 13052-13055[63], Copyright (2017) American Chemical Society. The AFM images show the products of hydrogenation (passivation) of the corresponding radical intermediates. c) Formation mechanism of 3,1-chiral graphene nanoribbons on Cu(111). The substituent X = H, Cl, Br. Reprinted (adapted) by permission from Schulz, F. *et al.* *J. Phys. Chem. C* 2017, 121, 2896-2904 [71], Copyright (2017) American Chemical Society.

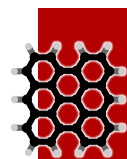
The final piece of the puzzle was found by preparing a sample at the even lower temperature of 120 °C, where the vast majority of DCBA molecules

remain unaffected and only a few undergo chemical transformations. Instead of coupling together, we found isolated molecules of monochlorobisanthene (see Fig. 1.3), with the chlorine clearly distinguishable from the nc-AFM images. These images proved that cyclodehydrogenation can actually precede dechlorination, effectively reversing the order of Ullmann coupling and cyclodehydrogenation as compared to DBBA. This result can be ascribed to the increased aryl halide bond strength in DCBA compared to DBBA, causing the dehalogenation temperature to surpass the cyclodehydrogenation temperature. Since the radicals in the reaction mechanism are planar bisanthene radicals, rather than the staggered bianthryl radicals, the natural coupling behavior is suddenly severely impeded by steric effects. The least sterically hindered position, the corner, then remains as the most likely candidate for coupling, and indeed, bisanthene radicals couple radical-to-corner, or from CH(3) to C(10). In conclusion, although we established that GNRs could not be obtained from DCBA, our analysis of mechanistic intermediates using nc-AFM allowed us to fully reveal their behavior on a surface.

1.4 Chiral nanoribbons

Another reaction mechanism that we were interested in was the formation of nanoribbons from bianthryls on Cu(111). Intuitively, one may think that the Ullmann coupling and cyclodehydrogenation should take place in the exact same way as on Au(111). However, in STM the edges of the ribbons were found to exhibit a notable sawtooth-like appearance. This peculiar feature was initially ignored by Simonov *et al.*[65], but at the same time prompted Han *et al.* to claim the product to be the counterintuitive 3,1-chiral GNR (see Fig. 1.3c).[66] The dispute that followed between the two groups could not be settled by STM imaging.[67, 68, 69, 70]

In order to solve the controversy, we started by growing GNRs from DBBA on Cu(111) in the same way as Han and Simonov, and performed nc-AFM experiments to indisputably reveal the product to be the 3,1-chiral GNR.[71] A simultaneous effort by Sánchez-Sánchez *et al.* corroborated these results.[72] The inevitable conclusion is that the Ullmann coupling, which should interconnect the C(10) positions of bianthryls, is compromised; in contrast, the chiral nanoribbons feature bonds between the CH(2) positions of adjacent monomers. We continued the experiments by attempting the synthesis with both DCBA and unsubstituted bianthryl. Surprisingly, in all three cases we obtained the 3,1-chiral nanoribbon. Evidently, the halogen at the C(10) position does not play an important role in the reaction. Therefore, we concluded that bianthryls could be activated directly at the CH(2) positions by the copper surface.





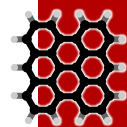
We decided to delve more deeply into this problem by attempting to identify intermediates in the mechanism. As noted by Simonov, the GNR formation from DBBA on Cu(111) is a three-step process, with an additional intermediate as compared to the two-step process on Au(111). Instead of going through a single polyanthrylene stage - or rather its chiral GNR counterpart - two different staggered polymer structures appear in successive stages with DBBA. The first polymer, with large spacing, was thought to originate from an organometallic chain containing copper atoms in between the adjacent monomers. Unfortunately, due to the staggered nature of the chains, the hypothetical interstitial copper atoms are hidden away from view as far as nc-AFM is concerned. We noted that the long-periodicity intermediate could only be obtained using DBBA and not for either DCBA or bianthryl, suggesting that the nature of the intermediate is indeed related to a debrominated product, and may therefore be the C(10)-coupled product. By performing nc-AFM, we could determine the orientation of the monomers in both chains. This allowed us to conclude that the short-periodicity chain is the CH(2)-CH(2) coupled polymer. The long-periodicity chain appeared to be connected in the regular Ullmann-type fashion, with extra spacing between the monomers likely originating from the copper atoms.

We completed our analysis by tip-manipulation experiments, and by looking into the analogous 5-AGNR formation from dibromoperylene.[71] This reaction only involves planar products, and indeed allowed us to identify both organometallic and covalent stages in the reaction. By combining all the information, we could establish the mechanism by which the nanoribbons form on Cu(111). Even though DBBA debrominates and takes the first step to assemble into the usual polyanthrylene chain and subsequent 7-AGNR, the Ullmann coupling is still intercepted by activation of CH(2) and covalent coupling at this position. On the other hand, activation at the C(10) position plays no role in bianthryl nor in DCBA. In these cases, the organometallic Ullmann intermediate is absent and coupling at the CH(2) positions produces the covalent polymer directly. Subsequent cyclodehydrogenation produces the 3,1-chiral nanoribbon in all three cases.

1.5 Conclusions

The elucidation of the formation mechanism of chiral nanoribbons on Cu(111), as well as that of the oligo- and polybisanthrenes on Au(111) are cases where uncovering the structure of products and intermediates provides a unique insight into the processes occurring in on-surface chemistry. As nanostructures continue to grow more sophisticated and complex, nc-AFM will prove to be an important tool to elucidate molecular frameworks of products and inter-

mediates, providing a unique understanding that cannot be obtained with any other method.

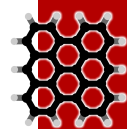


Bibliography

- [1] H. Davy, *Philos Trans R Soc Lond* **107**, pp. 77–85 (1817).
- [2] R. Lindner and A. Kühnle, *ChemPhysChem* **16**, pp. 1582–1592 (2015).
- [3] J. Björk, *Journal of Physics Condensed Matter* **28**, pp. 083002 (2016).
- [4] A. Narita, X.-Y. Wang, X. Feng, and K. Müllen, *Chem. Soc. Rev.* **44**, pp. 6616–6643 (2015).
- [5] A. Narita, X. Feng, and K. Müllen, *Chemical Record* **15**, pp. 295–309 (2015).
- [6] J. Méndez, M. F. López, and J. A. Martín-Gago, *Chemical Society Reviews* **40**, pp. 4578 (2011).
- [7] J. A. Martín-Gago, *Nat Chem* **3**, pp. 11–12 (2011).
- [8] G. Otero, G. Biddau, C. Sánchez-Sánchez, R. Caillard, M. F. López, C. Rogero, F. J. Palomares, N. Cabello, M. A. Basanta, J. Ortega, J. Méndez, A. M. Echavarren, R. Pérez, B. Gómez-Lor, and J. A. Martín-Gago, *Nature* **454**, pp. 865–868 (2008).
- [9] C. J. Chen, *Introduction to Scanning Tunneling Microscopy*, Introduction to Scanning Tunneling Microscopy. OUP Oxford (2007).
- [10] J. Repp, G. Meyer, S. M. Stojković, A. Gourdon, and C. Joachim, *Physical Review Letters* **94**, pp. 26803 (2005).
- [11] L. Gross, F. Mohn, N. Moll, P. Liljeroth, and G. Meyer, *Science* **325**, pp. 1110–1114 (2009).
- [12] L. Gross, *Nature Chemistry* **3**, pp. 273–278 (2011).
- [13] S. P. Jarvis, *International Journal of Molecular Sciences* **16**, pp. 19936–19959 (2015).
- [14] E. I. Altman, M. Z. Baykara, and U. D. Schwarz, *Accounts of Chemical Research* **48**, pp. 2640–2648 (2015).
- [15] L. Gross, F. Mohn, N. Moll, B. Schuler, A. Criado, E. Guitián, D. Peña, A. Gourdon, and G. Meyer, *Science* **337**, pp. 1326–1329 (2012).
- [16] S. Kawai, A. Sadeghi, X. Feng, P. Lifan, R. Pawlak, T. Glatzel, A. Willand, A. Orita, J. Otera, S. Goedecker, and E. Meyer, *ACS Nano* **7**, pp. 9098–9105 (2013).
- [17] J. Zhang, P. Chen, B. Yuan, W. Ji, Z. Cheng, and X. Qiu, *Science* **342**, pp. 611–614 (2013).
- [18] S. K. Hämmäläinen, N. van der Heijden, J. van der Lit, S. den Hartog, P. Liljeroth, and I. Swart, *Physical Review Letters* **113**, pp. 186102 (2014).
- [19] P. Hapala, M. Švec, O. Stetsovyh, N. Van Der Heijden, M. Ondráček, J. Van Der Lit, P. Mutombo, I. Swart, and P. Jelínek, *Nature Communications* **7**, pp. 11560 (2016).
- [20] B. Schuler, G. Meyer, D. Peña, O. C. Mullins, and L. Gross, *Journal of the American Chemical Society* **137**, pp. 9870–9876 (2015).
- [21] L. Lafferentz, V. Eberhardt, C. Dri, C. Africh, G. Comelli, F. Esch, S. Hecht, and L. Grill, *Nature Chemistry* **4**, pp. 215–220 (2012).
- [22] S. Kawai, V. Haapasilta, B. D. Lindner, K. Tahara, P. Spijker, J. A. Buitendijk, R. Pawlak, T. Meier, Y. Tobe, A. S. Foster, and E. Meyer, *Nature Communications* **7**, pp. 12711 (2016).
- [23] D. Wang, Q. Chen, and L.-J. Wan, *Physical chemistry chemical physics : PCCP* **10**, pp. 6467–78 (2008).
- [24] S.-W. Hla, L. Bartels, G. Meyer, and K.-H. Rieder, *Physical Review Letters* **85**, pp. 2777–2780 (2000).
- [25] S.-W. Hla and K.-H. Rieder, *Annual Review of Physical Chemistry* **54**, pp. 307–330 (2003).

- 
- [26] B. Schuler, S. Fatayer, F. Mohn, N. Moll, N. Pavliček, G. Meyer, D. Penã, and L. Gross, *Nature Chemistry* **8**, pp. 220–224 (2016).
- [27] A. Riss, A. P. Paz, S. Wickenburg, H. Z. Tsai, D. G. De Oteyza, A. J. Bradley, M. M. Ugeda, P. Gorman, H. S. Jung, M. F. Crommie, A. Rubio, and F. R. Fischer, *Nature Chemistry* **8**, pp. 678–683 (2016).
- [28] N. Pavliček, B. Schuler, S. Collazos, N. Moll, D. Pérez, G. Meyer, D. Peña, L. Gross, and E. Guitián, *Nat Chem* **7**, pp. 1–12 (2015).
- [29] D. G. D. Oteyza, *Science* **340**, pp. 1434 LP – 1437 (2013).
- [30] F. Albrecht, N. Pavliček, C. Herranz-Lancho, M. Ruben, and J. Repp, *Journal of the American Chemical Society* **137**, pp. 7424–7428 (2015).
- [31] F. Albrecht, F. Bischoff, W. Auwärter, J. V. Barth, and J. Repp, *Nano Letters* **16**, pp. 7703–7709 (2016).
- [32] N. Pavliček, B. Fleury, M. Neu, J. Niedenführ, C. Herranz-Lancho, M. Ruben, and J. Repp, *Physical Review Letters* **108**, pp. 86101 (2012).
- [33] J. van der Lit, M. P. Boneschanscher, D. Vanmaekelbergh, M. Ijäs, A. Uppstu, M. Ervasti, A. Harju, P. Liljeroth, and I. Swart, *Nature Communications* **4**, pp. 2023 (2013).
- [34] S. Kawai, S. Saito, S. Osumi, S. Yamaguchi, A. S. Foster, P. Spijker, and E. Meyer, *Nature Communications* **6**, pp. 8098 (2015).
- [35] S. Kawai, A. S. Foster, T. Björkman, S. Nowakowska, J. Björk, F. F. Canova, L. H. Gade, T. A. Jung, and E. Meyer, *Nature Communications* **7**, pp. 11559 (2016).
- [36] Y. He, M. Garnica, F. Bischoff, J. Ducke, M. L. Bocquet, M. Batzill, W. Auwärter, and J. V. Barth, *Nature Chemistry* **9**, pp. 33–38 (2017).
- [37] A. Celis, M. N. Nair, A. Taleb-Ibrahimi, E. H. Conrad, C. Berger, W. A. de Heer, and A. Tejada, *Journal of Physics D: Applied Physics* **49**, pp. 143001 (2016).
- [38] H. Terrones, R. Lv, M. Terrones, and M. S. Dresselhaus, *Reports on Progress in Physics* **75**, pp. 62501 (2012).
- [39] M. Ezawa, *AIP Conference Proceedings* **893**, pp. 1015–1016 (2007).
- [40] V. Barone, O. Hod, and G. E. Scuseria, *Nano Letters* **6**, pp. 2748–2754 (2006).
- [41] A. H. Castro Neto, F. Guinea, N. M. R. Peres, K. S. Novoselov, and A. K. Geim, *Reviews of Modern Physics* **81**, pp. 109–162 (2009).
- [42] J. Cai, C. A. Pignedoli, L. Talirz, P. Ruffieux, H. Söde, L. Liang, V. Meunier, R. Berger, R. Li, X. Feng, K. Müllen, and R. Fasel, *Nature Nanotechnology* **9**, pp. 896–900 (2014).
- [43] X. Wang, Y. Ouyang, L. Jiao, H. Wang, L. Xie, J. Wu, J. Guo, and H. Dai, *Nature Nanotechnology* **6**, pp. 563–567 (2011).
- [44] W. Liao, H. Bao, J. Guo, and H. Zhao, *Applied Physics A: Materials Science and Processing* **120**, pp. 657–662 (2015).
- [45] L. Talirz, H. Söde, T. Dumsclaff, S. Wang, J. R. Sanchez-Valencia, J. Liu, P. Shinde, C. A. Pignedoli, L. Liang, V. Meunier, N. C. Plumb, M. Shi, X. Feng, A. Narita, K. Müllen, R. Fasel, and P. Ruffieux, *ACS Nano* **11**, pp. 1380–1388 (2017).
- [46] H. Söde, L. Talirz, O. Gröning, C. A. Pignedoli, R. Berger, X. Feng, K. Müllen, R. Fasel, and P. Ruffieux, *Physical Review B - Condensed Matter and Materials Physics* **91**, pp. 045429 (2015).
- [47] S. Wang, L. Talirz, C. A. Pignedoli, X. Feng, K. Müllen, R. Fasel, and P. Ruffieux, *Nature Communications* **7**, pp. 11507 (2016).
- [48] J. Cai, P. Ruffieux, R. Jaafar, M. Bieri, T. Braun, S. Blankenburg, M. Muoth, A. P. Seitsonen, M. Saleh, X. Feng, K. Müllen, and R. Fasel, *Nature* **466**, pp. 470–473 (2010).
- [49] A. Batra, D. Cvetko, G. Kladnik, O. Adak, C. Cardoso, A. Ferretti, D. Prezzi, E. Molinari, A. Morgante, and L. Venkataraman, *Chem. Sci.* **5**, pp. 4419–4423 (2014).
- [50] C. Bronner, J. Björk, and P. Tegeder, *Journal of Physical Chemistry C* **119**, pp. 486–493 (2015).
- [51] J. Björk, S. Stafström, and F. Hanke, *J. Am. Chem. Soc.* **133**, pp. 14884–14887 (2011).

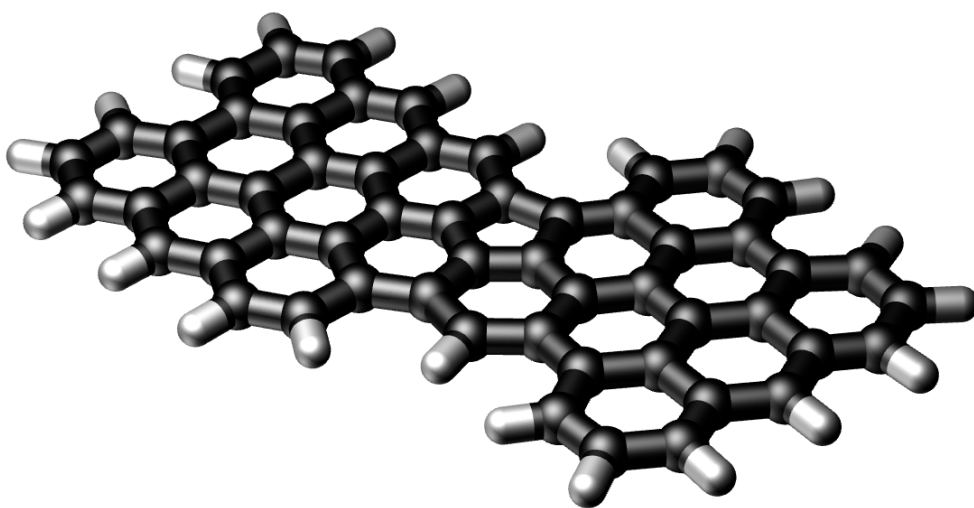
- [52] L. Talirz, P. Ruffieux, and R. Fasel, *Advanced Materials* **28**, pp. 6222–6231 (2016).
- [53] X. Yang, X. Dou, A. Rouhanipour, L. Zhi, H. J. Räder, and K. Müllen, *Journal of the American Chemical Society* **130**, pp. 4216–4217 (2008).
- [54] A. Narita, X. Feng, Y. Hernandez, S. A. Jensen, M. Bonn, H. Yang, I. A. Verzhbitskiy, C. Casiraghi, M. R. Hansen, A. H. Koch, G. Fytas, O. Ivasenko, B. Li, K. S. Mali, T. Balandina, S. Mahesh, S. De Feyter, and K. Müllen, *Nature Chemistry* **6**, pp. 126–132 (2014).
- [55] D. K. James and J. M. Tour, *Macromolecular Chemistry and Physics* **213**, pp. 1033–1050 (2012).
- [56] O. V. Yazyev, *Accounts of Chemical Research* **46**, pp. 2319–2328 (2013).
- [57] C. Bronner, S. Stremlau, M. Gille, F. Brauße, A. Haase, S. Hecht, and P. Tegeder, *Angewandte Chemie - International Edition* **52**, pp. 4422–4425 (2013).
- [58] Y. Zhang, Y. Zhang, G. Li, J. Lu, X. Lin, S. Du, R. Berger, X. Feng, K. Müllen, and H. J. Gao, *Applied Physics Letters* **105**, pp. 023101 (2014).
- [59] R. R. Cloke, T. Marangoni, G. D. Nguyen, T. Joshi, D. J. Rizzo, C. Bronner, T. Cao, S. G. Louie, M. F. Crommie, and F. R. Fischer, *Journal of the American Chemical Society* **137**, pp. 8872–8875 (2015).
- [60] G. D. Nguyen, F. M. Toma, T. Cao, Z. Pedramrazi, C. Chen, D. J. Rizzo, T. Joshi, C. Bronner, Y. C. Chen, M. Favaro, S. G. Louie, F. R. Fischer, and M. F. Crommie, *Journal of Physical Chemistry C* **120**, pp. 2684–2687 (2016).
- [61] A. Kimouche, M. M. Ervasti, R. Drost, S. Halonen, A. Harju, P. M. Joensuu, J. Sainio, and P. Liljeroth, *Nature Communications* **6**, pp. 10177 (2015).
- [62] J. Liu, B.-W. Li, Y.-Z. Tan, A. Giannakopoulos, C. Sanchez-Sanchez, D. Beljonne, P. Ruffieux, R. Fasel, X. Feng, and K. Müllen, *Journal of the American Chemical Society* **137**, pp. 6097–6103 (2015).
- [63] P. H. Jacobse, A. van den Hoogenband, M. E. Moret, R. J. Klein Gebbink, and I. Swart, *Angewandte Chemie - International Edition* **55**, pp. 13052–13055 (2016).
- [64] Y. C. Chen, D. G. De Oteyza, Z. Pedramrazi, C. Chen, F. R. Fischer, and M. F. Crommie, *ACS Nano* **7**, pp. 6123–6128 (2013).
- [65] K. A. Simonov, N. A. Vinogradov, A. S. Vinogradov, A. V. Generalov, E. M. Zagrebina, N. Mårtensson, A. A. Cafolla, T. Carpy, J. P. Cunniffe, and A. B. Preobrajenski, *Journal of Physical Chemistry C* **118**, pp. 12532–12540 (2014).
- [66] P. Han, K. Akagi, F. Federici Canova, H. Mutoh, S. Shiraki, K. Iwaya, P. S. Weiss, N. Asao, and T. Hitosugi, *ACS Nano* **8**, pp. 9181–9187 (2014).
- [67] K. A. Simonov, N. A. Vinogradov, A. S. Vinogradov, A. V. Generalov, E. M. Zagrebina, G. I. Svirskiy, A. A. Cafolla, T. Carpy, J. P. Cunniffe, T. Taketsugu, A. Lyalin, N. Mårtensson, and A. B. Preobrajenski, *ACS Nano* **9**, pp. 8997–9011 (2015).
- [68] P. Han, K. Akagi, F. Federici Canova, H. Mutoh, S. Shiraki, K. Iwaya, P. S. Weiss, N. Asao, and T. Hitosugi, *ACS Nano* **9**, pp. 3404–3405 (2015).
- [69] K. A. Simonov, N. A. Vinogradov, A. S. Vinogradov, A. V. Generalov, E. M. Zagrebina, N. Mårtensson, A. A. Cafolla, T. Carpy, J. P. Cunniffe, and A. B. Preobrajenski, *ACS Nano* **9**, pp. 3399–3403 (2015).
- [70] P. Han, K. Akagi, F. Federici Canova, R. Shimizu, H. Oguchi, S. Shiraki, P. S. Weiss, N. Asao, and T. Hitosugi, *ACS Nano* **9**, pp. 12035–12044 (2015).
- [71] F. Schulz, P. H. Jacobse, F. F. Canova, J. Van Der Lit, D. Z. Gao, A. Van Den Hoogenband, P. Han, R. J. Klein Gebbink, M. E. Moret, P. M. Joensuu, I. Swart, and P. Liljeroth, *Journal of Physical Chemistry C* **121**, pp. 2896–2904 (2017).
- [72] C. Sánchez-Sánchez, T. Dienel, O. Deniz, P. Ruffieux, R. Berger, X. Feng, K. Müllen, and R. Fasel, *ACS Nano* **10**, pp. 8006–8011 (2016).





Chapter 2

Aryl radical geometry determines nanographene formation on Au(111)



This chapter is based on

Aryl radical geometry determines nanographene formation on Au(111)

Peter H. Jacobse, Adrianus van den Hoogenband, Marc-Etienne Moret,
Robertus J. M. Klein Gebbink, Ingmar Swart

Angewandte Chemie International Edition **55** (42), pp. 13052-13055
(2016)



The Ullmann coupling has been used extensively as a synthetic tool for the formation of C-C bonds on surfaces. Thus far, most syntheses made use of aryl bromides or aryl iodides. We investigated the applicability of an aryl chloride in the bottom-up assembly of graphene nanoribbons. Specifically, the reactions of 10,10'-dichloro-9,9'-bianthryl (DCBA) on Au(111) were studied. Using atomic resolution non-contact AFM, the structure of various coupling products and intermediates were resolved, allowing us to reveal the important role of the geometry of the intermediate aryl radicals in the formation mechanism. For the aryl chloride, cyclodehydrogenation occurs before dehalogenation and polymerization. Due to their geometry, the planar bisanthene radicals display a different coupling behavior compared to the staggered bianthryl radicals formed when aryl bromides are used. This results in oligo- and polybisanthenes with predominantly fluoranthene-type connections.

2.1 Introduction

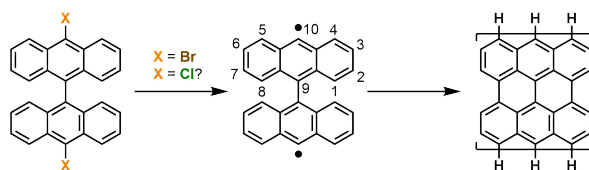
The Ullmann coupling has proven to be an indispensable tool for the bottom-up assembly of graphene nanostructures and covalent organic frameworks on surfaces.[1, 2, 3, 4, 5, 6, 7, 8] Numerous structures can be accessed with aryl chlorides[9, 10, 11, 12], aryl bromides[13, 14, 15, 16, 17, 18] and aryl iodides.[19, 20, 21, 22] The combination of different halogen substituents in a single molecule has been used to provide an extra degree of freedom as individual Ullmann couplings can be carried out in sequence.[23, 24, 25, 26, 27] This hierarchical approach is also useful in the preparation of precursor molecules, which are typically synthesized by means of solution-based coupling methods. The presence of two different halogens then allows for solution-phase coupling on the heaviest halogen, followed by surface-mediated Ullmann coupling on the lightest one, providing increased synthetic freedom.

Among the most fascinating structures produced with the Ullmann coupling are graphene nanoribbons (GNR). The archetypical synthesis, pioneered by Cai *et al.*, uses the precursor molecule 10,10'-dibromo-9,9'-bianthryl (DBBA).[28] The coupling is a two-step process, in which first the carbon-halogen bonds are dissociated thermally and the resulting (surface-bound) bianthryl radicals polymerize to give polyanthrylene.[29, 30] By heating the polyanthrylene chains to over 250 °C, cyclodehydrogenation (CDH) is induced, transforming the staggered polyanthrylenes into flat, conjugated nanoribbons.[31, 32, 33] CDH releases hydrogen atoms onto the surface, which has been shown to passivate leftover radicals.[34]

Nanoribbons of various widths, edge structures, and heteroatom-

functionalized GNRs have been synthesized.[35, 36, 37, 38, 39] Interestingly, all of the precursor molecules were synthesized by means of aryl halide coupling chemistry. The subsequent on-surface synthesis has so far also always employed the aryl bromide Ullmann coupling. Investigating the feasibility of aryl chloride Ullmann coupling in the on-surface synthesis of GNR is highly desirable as it may increase the flexibility and selectivity of the solution-phase synthesis of the precursor molecules.

Here, we report on our investigation of the applicability of the aryl chloride Ullmann coupling in the thermal assembly of graphene nanostructures. Specifically, the precursor 10,10'-dichloro-9,9'-bianthryl (DCBA) was used, which is the chloro analogue of the DBBA used by Cai to synthesize 7-armchair graphene nanoribbons (7-acGNR), as shown in Scheme 2.1. We find that changing the halogen strongly impacts the course of the reaction: instead of the expected graphene nanoribbons, we observe the formation of fused oligo- and polybisanthenes (bisanthene being the cyclodehydrogenated form of bianthryl) with varying degrees of atomic order. This difference is proposed to stem from the stronger C-Cl bond allowing for cyclodehydrogenation prior to radical formation.



Scheme 2.1 Synthesis of 7-acGNR from bianthryl halides through subsequent Ullmann coupling and cyclodehydrogenation. Numbering is shown for a single anthryl unit.

2.2 Results

2.2.1 Dichlorobianthryl on Au(111)

First, DCBA molecules were evaporated onto an Au(111) crystal held at room temperature. As is evident from the STM image shown in Fig. 2.1a, a well-ordered self-assembled layer was observed. The apparent height ($4.0 \pm 0.5 \text{ \AA}$) and periodicity ($1.2 \pm 0.2 \text{ nm}$) are consistent with a close packing of DCBA molecules. Interestingly, multiple crystal structures were identified within the monolayer, which we ascribe to variations in the three-dimensional orientation of DCBA molecules relative to each other. The structures could be interconverted by applying voltage pulses.

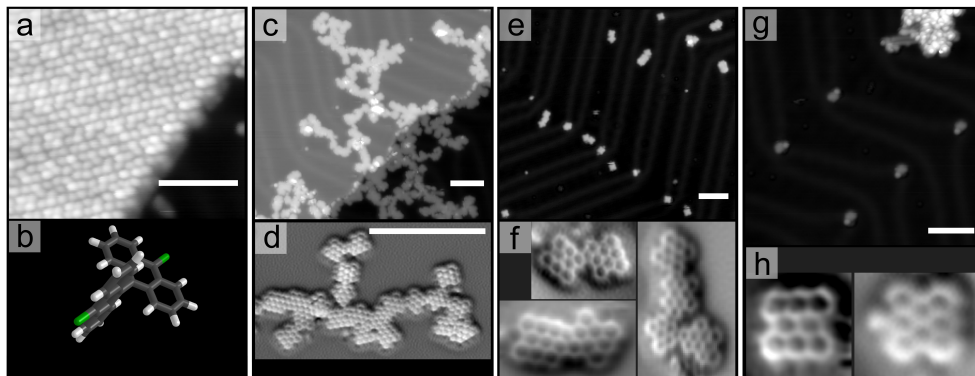


Fig. 2.1 STM and AFM images of DCBA on the Au(111) surface treated at different temperatures. a) Room temperature. b) Model of the DCBA molecule. c) Heated to 360 °C. d) AFM of structures in c. e) Heated to 200 °C. f) AFM on structures in e. g) Heated to 120 °C. h) AFM on structures in g. All scale bars are 5nm.

Subsequent slow heating of the sample from room temperature to 360 °C over the course of 1 h results in a large decrease of adsorbate concentration. The remaining molecules formed extensive disordered polymer-like chains, near the Au(111) step edges, as seen in Fig. 2.1c. These chains have a different conjugation than graphene nanoribbons.[40] The formation of disordered chains implies that the orientation and coupling of subsequent bisanthenes is random and that branching of the chains is prevalent. This is confirmed using sub-molecular resolution AFM images (Fig. 2.1d). This is in obvious contrast with the linear structures that result from radicalradical coupling of staggered bianthryl radical intermediates, as is the case for DBBA.

By having performed the assembly of DCBA in a slow-heating experiment, we rule out a possible temperature quenching effect: the hypothetical case that molecules are heated too quickly to a temperature at which they may undergo intramolecular reactions before having the chance to couple.[41] Hence, the rationale behind slow heating is that it maximizes the probability that all steps in the mechanism are traversed in the order of increasing activation energy while giving every single one of them enough time to occur before possibly being quenched by reactions that happen at higher temperature. Since both coupling and cyclodehydrogenation reactions must have occurred for the poly-bisanthene chains to form, it was decided to carry out the next experiments at lower temperatures, closer to the onset of various reactions.

When evaporating molecules onto Au(111) maintained at 200 °C, smaller, planar structures are observed. In AFM these were found to correspond to mostly monomers, dimers and oligomers of bisanthene (Fig. 2.1e). In the STM images, the vast majority of dimers appear as a structure where the two

monomers are attached at a 34 ± 5 degree angle (based on 11 measurements). A few dimers feature a different angle and appear to be fused even more intricately. AFM (Fig. 2.1f) reveals both of these structures to be fused bisanthrene dimers, both featuring the non-alternant fluoranthene-type motif, containing a single pentagon sandwiched between the two moieties. Similar attachments are seen in oligomers (Fig. 2.1d).

Evaporating molecules onto Au(111) heated to 120 °C results mostly in agglomerates of staggered molecules. In addition, some flat molecules were observed, particularly near the kink sites of the Au(111) herringbone reconstruction (Fig. 2.1g). Most of these flat species were identified as bisanthrene, with a smaller fraction of monochlorobisanthrene (Fig. 2.1h). At even lower temperatures, no flat molecules were observed, indicating that cyclodehydrogenation of bianthryl species does not take place.

The observation of monochlorobisanthrene implies that the DBCA molecules first undergo cyclodehydrogenation and only then dehalogenation and polymerization. This order is reversed with respect to the order found for the bromo-analog (DBBA)[28, 29] (see Fig. 2.2). This can be rationalized from the fact that the carbon-chlorine bond is stronger than the carbon-bromine bond.

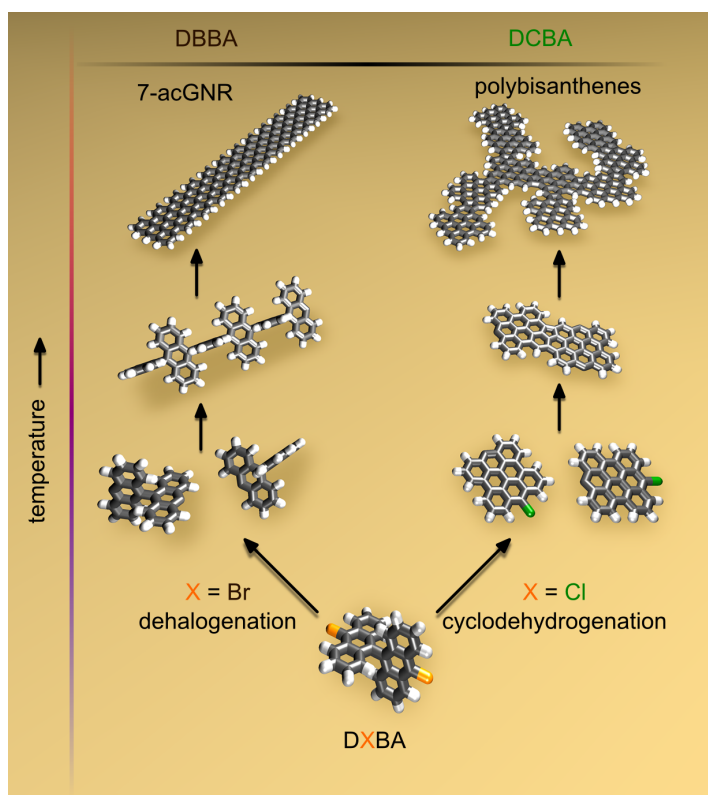
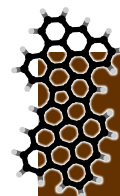
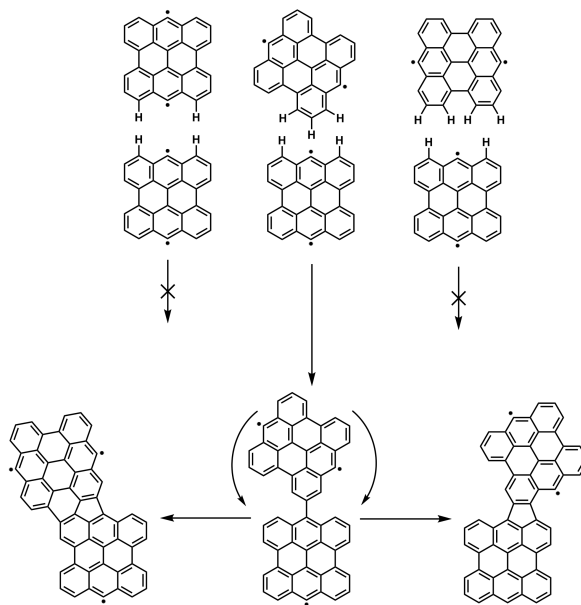


Fig. 2.2 Mechanisms for the nanographene formation from dibromobianthryl (left) and dichlorobianthryl (right).



Scheme 2.2 Coupling mechanism for bisanthrene radicals.

Only hydrogens that play a role in the steric effect are shown explicitly. Radical-to-corner attack may create a bisanthenylbisanthene intermediate, which then cyclizes into either fused dimeric structure after pivoting to the left or to the right around this bond (as denoted by the curved arrows).



When dehalogenation precedes cyclodehydrogenation, that is, the case of DBBA, bianthryl radicals are formed. The staggered geometry of bianthryl radicals is essential to alleviate the steric repulsion between the peri hydrogen atoms and allow for carbon-carbon coupling at the 10 and 10' positions. Only this coupling will result in well-defined graphene nanoribbons. When the order of the reaction is reversed, radical polymerization can only occur between planar species that are lying flat on the surface. Here the radical carbon atom is flanked by two peri-hydrogens, which pose a significant steric difficulty for the radical to approach another molecule - particularly another radical. For the planar radical, the most accessible position is now the corner, as shown in Scheme 2.2. C-C bond formation at this position gives an intermediate bisanthenylbisanthene, which, when followed by cyclization, gives the dimeric structures that were resolved with AFM (Fig. 2.1f). The present data do not, however, allow us to resolve the exact mechanism of coupling. It may be that the hydrogen at the corner is lost during the bisanthenylbisanthene formation in a single step. Alternatively, the hydrogen may be removed from the corner by an initial abstraction through a first-generation radical, followed by radical-radical coupling to another bisanthene radical. Both hypothetical couplings will give rise to the same type of dimers. The dimer radicals may be passivated by H atoms or participate in further coupling steps to give oligo- and polybisanthenes. Since coupling can occur at every corner, ill-defined polybisanthene chains are formed. Upon increasing the temperature, also more indistinct radical coupling reactions can take place. Nevertheless, a significant amount of fluoranthene-type connections can be distinguished in the

polybisanthenes. A number of different structures was resolved, as shown in Fig. 2.3. We conclude that the three-dimensional geometry of the intermediate radicals determines the regioselectivity in aryl-aryl bond formation.

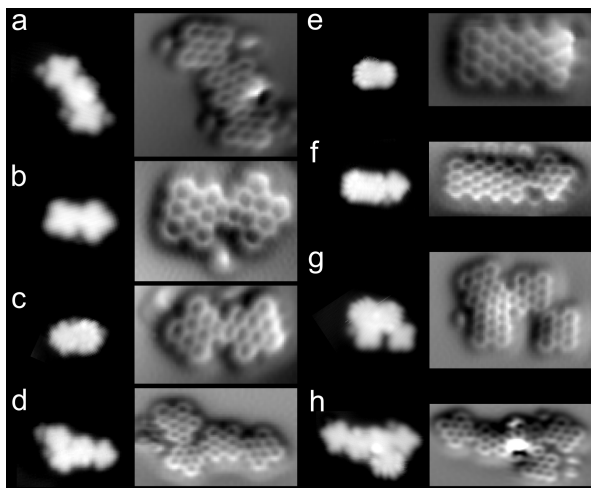
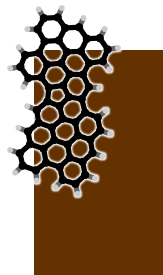


Fig. 2.3 STM (left columns) and AFM (right columns) topographies of various bisanthene oligomers. a) A trimer. b) A dimer. c) A dimer with Stone-Wales defect. d) An oligomer featuring multiple Stone-Wales type attachments. e) A 7-acGNR tetramer. f) A 7-acGNR tetramer with fused bisanthene. g) An ill-defined oligomer. h) An ill-defined oligomer.



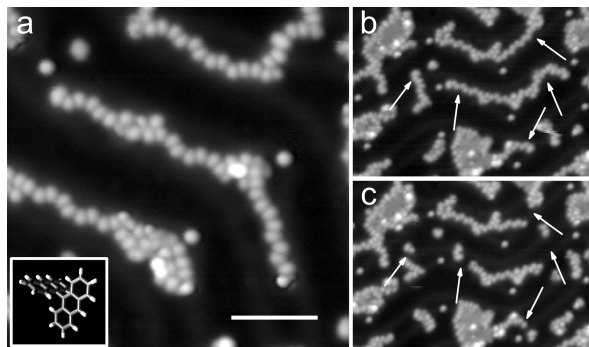
2.2.2 Bianthryl on Au(111)

Further evidence of the necessity of radical species in the coupling reactions was obtained from experiments with the non-halogenated 9,9'-bianthryl. This molecule, which was obtained as an intermediate in the synthesis of DCBA, is the non-halogenated equivalent of dihalobianthryl. Since it contains no halogens, it cannot dehalogenate to give radical species. Therefore, bianthryl may undergo cyclodehydrogenation to bisanthene, but it is passive with regard to radical coupling reactions.

In the first experiment, bianthryl was evaporated onto a sample held at room temperature. In contrast with the large, two-dimensional patches that were observed for the DCBA, bianthryl molecules were found to self-assemble into one-dimensional chains, aligned along the Au(111) herringbone reconstruction, as seen in Fig. 2.4. To verify that these are non-covalently bonded assemblies of bianthryl molecules, STM tip manipulation of the chains was performed. A manipulation consisted of disconnecting the feedback loop from the STM feedback setpoint of 500 mV, 10 pA, lowering the tip towards the surface by 400 pm, moving the tip over the surface, and retracting it by the same distance before reconnecting the feedback. As can be seen in Fig. 2.4, where panel b and c show the situation before and after manipulation, the chains break up when sweeping the tip through them. This suggests that the BA molecules within the chains are not covalently bonded.

This sample was heated to 360 °C using the same slow-heating experi-

Fig. 2.4 Bianthryl on Au(111). a) Bianthryl adsorbed onto the Au(111) surface. Scale bar = 5 nm. Inset: model of the bianthryl molecule. b) bianthryl assemblies before manipulation. c) Same area as in b, after manipulation.



ment as described for the DCBA. When observing the surface in STM, it is found to be completely empty. This means that the structures obtained in the slow-heating experiment have a binding energy so small that they completely desorb from the surface at the temperature obtained in the experiment. To make sure that this result is not caused by the hypothetical situation that desorption outcompetes coupling, two more experiments were performed. In one experiment, after evaporating bianthryl at room temperature, the sample was heated to 360 °C at once. In the last experiment, bianthryl was evaporated onto a sample held at 360 °C. In both cases, no BA molecules were observed on the Au(111) surface. These experiments show that non-radical coupling is absent at the temperatures used in our experiments. Therefore, we conclude that the bisanthene oligomers and polybisanthene structures that were identified in the experiments with DCBA can only be generated from bisanthene radicals.

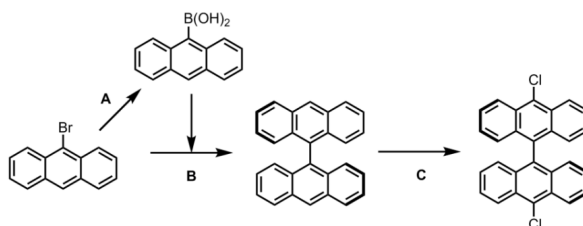
2.3 Conclusions

In summary, we investigated the Ullmann coupling of DCBA, an aryl chloride, on Au(111). In contrast to the coupling of the analogous bromide, highly branched structures were formed, which is due to an inversion of dehalogenation and cyclodehydrogenation steps. This changes the intermediate radicals from staggered bianthryl-type to planar bisanthene-type. Because of steric effects these undergo an alternative coupling reaction, giving rise predominantly to fluoranthene-type connections. We conclude that the geometry of the aryl radical, in combination with surface confinement determines the regioselectivity of C-C bond formation on surfaces. The notion that the reaction sequence in on-surface synthesis can be tuned by proper choice of halogen, combined with the importance of the geometry of reaction intermediates establishes new design criteria for the preparation of nanographenes and covalent organic frameworks. Specifically, the strong aryl chloride bond may be used to allow

for intramolecular reactions before intermolecular couplings in cases where the analogous bromide gives the reverse order. Proper design of monomers may furthermore exploit the steric effects to generate the desired products in future syntheses.

2.4 Experimental methods

2.4.1 Synthesis of 10,10'-dichloro-9,9'-bianthryl (DCBA)



Scheme 2.3 Synthesis of DCBA through lithiation/borylation (A), Suzuki coupling (B) and chlorination (C).

DCBA was obtained by Suzuki coupling of 9-anthrylborynic acid with 9-bromoanthracene, followed by chlorination of the 9,9'-bianthryl (BA) intermediate (see Scheme 2.3). Although the anthryl-anthryl coupling suffers from high steric demand and significant protideborylation, it was optimized to give a yield of 20 %. Our synthesis may be extended to more complex anthracene derivatives. As such, it allows for better control over regioselectivity than the literature procedure involving the reductive dimerization of anthraquinone.[42, 43] Reagents were used as purchased from Acros and Sigma Aldrich. All reactions were carried out in oven-dried glassware under a nitrogen atmosphere. Flash column chromatography was performed using silicagel 60 (0.040–0.063 mm, Merck). ^1H NMR spectra were recorded on an Agilent MRF400 or Varian VNMR-S400 spectrometer at 25 °C. Chemical shifts are reported in ppm relative to TMS. UV-Vis spectra were recorded using a Perkin Elmer spectrometer Lambda 950.

2.4.1.1 9-anthrylborynic acid

The synthesis of 9-anthrylborynic acid was performed in a similar way as described in literature. [44, 45] A 100 mL three-necked reaction vessel was charged with anhydrous THF (20 mL) and 9-bromoanthracene (2.57 g, 10 mmol). The resulting magnetically stirred solution was cooled to -78 °C followed by dropwise addition of n-BuLi (6.9 mL, 1.6 M in n-hexane, 11 mmol)



resulting in an orange suspension. After the reaction mixture was stirred for an additional 30 min, a solution of trimethylborate (3.12 g, 30 mmol) in anhydrous THF (10 mL) was added dropwise and the reaction mixture was further stirred for 3 h allowing the temperature to rise to room temperature. Then, it was quenched with a saturated aqueous solution of NH_4Cl and ethyl acetate was added. The organic layer was successively separated, washed with brine, dried over MgSO_4 , filtered and concentrated *in vacuo*. TLC of the crude 9-anthrylboronic acid with petroleum ether-ethyl acetate 9:1 (v/v) showed 9-bromoanthracene and anthracene as impurities, which were removed by stirring the crude boronic acid in some petroleum ether (bp 40-60 °C), followed by filtration over a glass-filter under *vacuo* to give 1.55 g 9-anthrylboronic acid (70 %) as a pale yellowish-brown solid which was used without further characterization in the next step.

2.4.1.2 9,9'-bianthryl

A 50 mL Schlenk tube was charged with anhydrous degassed toluene (10 mL), followed by addition of 9-bromoanthracene (128.5 mg, 0.5 mmol), 9-anthrylboronic acid (133 mg, 0.6 mmol), $\text{K}_3\text{PO}_4 \cdot \text{H}_2\text{O}$ (207 mg, 0.9 mmol), Pd_2dba_3 (13.7 mg, 0.015 mol) and 2-dicyclohexylphosphino-2',6'-dimethoxybiphenyl (SPhos, 24.6 mg, 0.06 mmol). The Schlenk tube was capped with a stopper and the mixture was stirred for 19 h in a pre-heated oil bath at 100 °C. After cooling to room temperature, the reaction mixture was diluted with ethyl acetate, filtered and evaporated *in vacuo*. The crude product was dissolved in a minimum amount of dichloromethane and further purified by flash chromatography with petroleum ether (bp 40 - 60 °C). First, some unreacted 9-bromoanthracene and anthracene were eluted, after which the solvent was changed to dichloromethane-petroleum ether 3:1 (v/v) to obtain the title compound as a yellow solid with blue fluorescence in 20 % yield (35 mg). $^1\text{H NMR}$ (400 MHz, CD_3CN) δ (ppm): 8.84 (s, 2H), 8.26 (d, $J = 8.5$ Hz, 4H), 7.51 (m, 4H), 7.22 (m, 4H), 6.99 (dd, $J_1 = 8.5$ Hz, $J_2 = 1.0$ Hz, 4H). UV-Vis was recorded in CH_3CN .

2.4.1.3 10,10'-dichloro-9,9'-bianthryl (DCBA)

A three-necked flask was provided with reflux condenser and charged with CCl_4 (5 ml), 9,9'-bianthryl (40 mg, 0.113 mmol), N-chlorosuccinimide (43 mg, 0.34 mmol) and two drops of aqueous hydrochloric acid (36 %). The resulting mixture was stirred in a pre-heated oil bath at 80 °C. TLC showed no full conversion. Additional N-chlorosuccinimide (16 mg, 0.11 mmol) and one drop of aqueous HCl were added and the mixture was stirred for another 6 h. After cooling to room temperature, the reaction was concentrated *in*

vacuo. The obtained crude 10,10'-dichloro-9,9'-bianthryl was dissolved in a minimum amount of dichloromethane and further purified by flash column chromatography with petroleum ether. DCBA was obtained as a yellow solid with blue fluorescence in 63 % yield (30 mg). ^1H NMR (400 MHz, CDCl_3) δ (ppm): 8.68 (d, $J = 8.5$ Hz, 4H), 7.58 (m, 4H), 7.19 (m, 4H), 7.08 (d, $J = 8.5$ Hz, 4H). ^{13}C NMR (100 MHz, CDCl_3 , 25 °C) δ (ppm): 132.1, 131.9, 129.7, 129.7, 128.7, 127.0, 126.8, 126.3, 125.1. UV-Vis was recorded in CH_3CN . Data are in accordance with literature.[46]

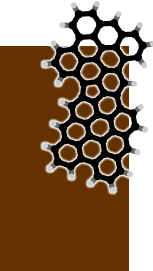
2.4.2 Scanning probe experiments

The scanning probe experiments were carried out with a Scienta-Omicron LT STM/AFM with a commercially available qPlus sensor (quality factor of $Q \approx 30000$, a resonance frequency of $f_0 = 19500$ Hz and a peak-to-peak oscillation amplitude of approximately 2 Å), operating at 4.6 K. The molecules were thermally evaporated onto an Au(111) surface cleaned by several sputter and annealing cycles. All AFM images were acquired in constant height mode with CO terminated tips prepared using standard procedures.[47]

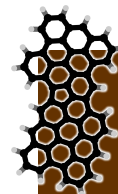
Bibliography

- [1] Q. Fan, J. M. Gottfried, and J. Zhu, *Accounts of Chemical Research* **48**, pp. 2484–2494 (2015).
- [2] M. El Garah, J. M. Macleod, and F. Rosei, *Surface Science* **613**, pp. 6–14 (2013).
- [3] X. Zhang, Q. Zeng, and C. Wang, *Nanoscale* **5**, pp. 8269 (2013).
- [4] L. Dong, P. N. Liu, and N. Lin, *Accounts of Chemical Research* **48**, pp. 2765–2774 (2015).
- [5] G. Franc and A. Gourdon, *Physical Chemistry Chemical Physics* **13**, pp. 14283 (2011).
- [6] J. Méndez, M. F. López, and J. A. Martín-Gago, *Chemical Society Reviews* **40**, pp. 4578 (2011).
- [7] J. Björk, *Journal of Physics Condensed Matter* **28**, pp. 083002 (2016).
- [8] M. Lackinger and W. M. Heckl, *Journal of Physics D: Applied Physics* **44**, pp. 464011 (2011).
- [9] K. J. Shi, D. W. Yuan, C. X. Wang, C. H. Shu, D. Y. Li, Z. L. Shi, X. Y. Wu, and P. N. Liu, *Organic Letters* **18**, pp. 1282–1285 (2016).
- [10] M. Kittelmann, M. Nimmrich, R. Lindner, A. Gourdon, and A. Kühnle, *ACS Nano* **7**, pp. 5614–5620 (2013).
- [11] H. Zhang, J. H. Franke, D. Zhong, Y. Li, A. Timmer, O. D. Arado, H. Mönig, H. Wang, L. Chi, Z. Wang, K. Müllen, and H. Fuchs, *Small* **10**, pp. 1361–1368 (2014).
- [12] M. Kittelmann, P. Rahe, M. Nimmrich, C. M. Hauke, A. Gourdon, and A. Kühnle, *ACS Nano* **5**, pp. 8420–8425 (2011).
- [13] C. Zhang, Q. Sun, H. Chen, Q. Tan, and W. Xu, *Chem. Commun.* **51**, pp. 495–498 (2015).
- [14] L. Grill, M. Dyer, L. Lafferentz, M. Persson, M. V. Peters, and S. Hecht, *Nature Nanotechnology* **2**, pp. 687–691 (2007).

chapter 2

- 
- [15] Q. Fan, C. Wang, Y. Han, J. Zhu, J. Kuttner, G. Hilt, and J. M. Gottfried, *ACS Nano* **8**, pp. 709–718 (2014).
- [16] C. Sánchez-Sánchez, S. Brüller, H. Sachdev, K. Müllen, M. Krieg, H. F. Bettinger, A. Nicolai, V. Meunier, L. Talirz, R. Fasel, and P. Ruffieux, *ACS Nano* **9**, pp. 9228–9235 (2015).
- [17] L. Lafferentz, F. Ample, H. B. Yu, S. Hecht, C. Joachim, and L. Grill, *Science* **323**, pp. 1193–1197 (2009).
- [18] R. Gutzler, L. Cardenas, J. Lipton-Duffin, M. El Garah, L. E. Dinca, C. E. Szakacs, C. Fu, M. Gallagher, M. Vondráček, M. Rybachuk, D. F. Perepichka, and F. Rosei, *Nanoscale* **6**, pp. 2660–2668 (2014).
- [19] J. A. Lipton-Duffin, O. Ivasenko, D. F. Perepichka, and F. Rosei, *Small* **5**, pp. 592–597 (2009).
- [20] M. Bieri, M. T. Nguyen, O. Gröning, J. Cai, M. Treier, K. Ait-Mansour, P. Ruffieux, C. A. Pignedoli, D. Passerone, M. Kastler, K. Müllen, and R. Fasel, *Journal of the American Chemical Society* **132**, pp. 16669–16676 (2010).
- [21] G. Eder, E. F. Smith, I. Cebula, W. M. Heckl, P. H. Beton, and M. Lackinger, *ACS Nano* **7**, pp. 3014–3021 (2013).
- [22] S. Schlögl, W. M. Heckl, and M. Lackinger, *Surface Science* **606**, pp. 999–1004 (2012).
- [23] L. Lafferentz, V. Eberhardt, C. Dri, C. Africh, G. Comelli, F. Esch, S. Hecht, and L. Grill, *Nature Chemistry* **4**, pp. 215–220 (2012).
- [24] J. Eichhorn, T. Strunskus, A. Rastgoo-Lahrood, D. Samanta, M. Schmittel, and M. Lackinger, *Chem. Commun.* **50**, pp. 7680–7682 (2014).
- [25] J. Eichhorn, D. Nieckarz, O. Ochs, D. Samanta, M. Schmittel, P. J. Szabelski, and M. Lackinger, *ACS Nano* **8**, pp. 7880–7889 (2014).
- [26] J. Björk, F. Hanke, and S. Stafström, *Journal of the American Chemical Society* **135**, pp. 5768–5775 (2013).
- [27] K. J. Shi, X. Zhang, C. H. Shu, D. Y. Li, X. Y. Wu, and P. N. Liu, *Chem. Commun.* **52**, pp. 8726–8729 (2016).
- [28] J. Cai, P. Ruffieux, R. Jaafar, M. Bieri, T. Braun, S. Blankenburg, M. Muoth, A. P. Seitsonen, M. Saleh, X. Feng, K. Müllen, and R. Fasel, *Nature* **466**, pp. 470–473 (2010).
- [29] A. Batra, D. Cvetko, G. Kladnik, O. Adak, C. Cardoso, A. Ferretti, D. Prezzi, E. Molinari, A. Morgante, and L. Venkataraman, *Chem. Sci.* **5**, pp. 4419–4423 (2014).
- [30] L. Massimi, O. Ourdjini, L. Lafferentz, M. Koch, L. Grill, E. Cavaliere, L. Gavioli, C. Cardoso, D. Prezzi, E. Molinari, A. Ferretti, C. Mariani, and M. G. Betti, *Journal of Physical Chemistry C* **119**, pp. 2427–2437 (2015).
- [31] C. Bronner, J. Björk, and P. Tegeder, *Journal of Physical Chemistry C* **119**, pp. 486–493 (2015).
- [32] S. Blankenburg, J. Cai, P. Ruffieux, R. Jaafar, D. Passerone, X. Feng, K. Müllen, R. Fasel, and C. A. Pignedoli, *ACS Nano* **6**, pp. 2020–2025 (2012).
- [33] J. Björk, S. Stafström, and F. Hanke, *J. Am. Chem. Soc.* **133**, pp. 14884–14887 (2011).
- [34] L. Talirz, H. Söde, J. Cai, P. Ruffieux, S. Blankenburg, R. Jafaar, R. Berger, X. Feng, K. Müllen, D. Passerone, R. Fasel, and C. A. Pignedoli, *Journal of the American Chemical Society* **135**, pp. 2060–2063 (2013).
- [35] Y. C. Chen, D. G. De Oteyza, Z. Pedramrazi, C. Chen, F. R. Fischer, and M. F. Crommie, *ACS Nano* **7**, pp. 6123–6128 (2013).
- [36] R. R. Cloke, T. Marangoni, G. D. Nguyen, T. Joshi, D. J. Rizzo, C. Bronner, T. Cao, S. G. Louie, M. F. Crommie, and F. R. Fischer, *Journal of the American Chemical Society* **137**, pp. 8872–8875 (2015).
- [37] S. Kawai, S. Saito, S. Osumi, S. Yamaguchi, A. S. Foster, P. Spijker, and E. Meyer, *Nature Communications* **6**, pp. 8098 (2015).

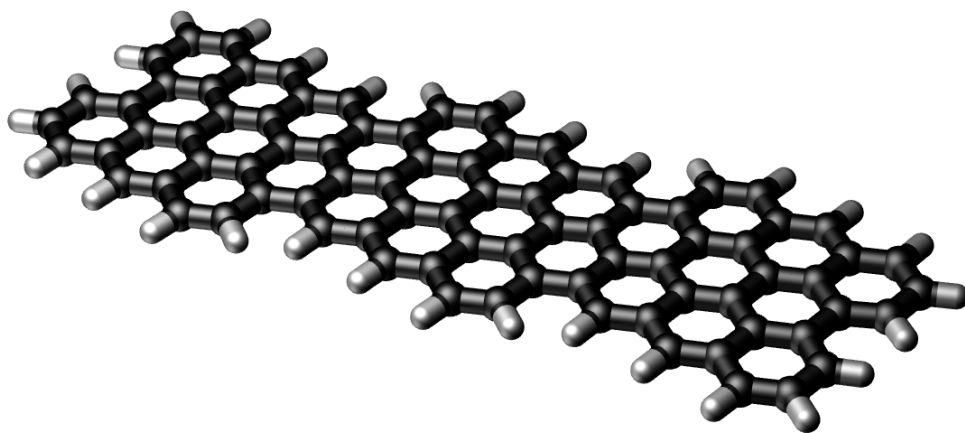
-
- [38] A. Kimouche, M. M. Ervasti, R. Drost, S. Halonen, A. Harju, P. M. Joensuu, J. Sainio, and P. Liljeroth, *Nature Communications* **6**, pp. 10177 (2015).
- [39] P. Ruffieux, S. Wang, B. Yang, C. Sanchez-Sanchez, J. Liu, T. Dienel, L. Talirz, P. Shinde, C. A. Pignedoli, D. Passerone, T. Dumslaff, X. Feng, K. Müllen, and R. Fasel, *Nature* **531**, pp. 489–492 (2016).
- [40] M. Koch, F. Ample, C. Joachim, and L. Grill, *Nature Nanotechnology* **7**, pp. 713–717 (2012).
- [41] B. Cirera, N. Giménez-Agulló, J. Björk, F. Martínez-Peña, A. Martín-Jimenez, J. Rodríguez-Fernandez, A. M. Pizarro, R. Otero, J. M. Gallego, P. Ballester, J. R. Galan-Mascaros, and D. Ecija, *Nature Communications* **7** (2016).
- [42] E. Clar, *Berichte der deutschen chemischen Gesellschaft (A and B Series)* **72**, pp. 1645–1649 (1939).
- [43] S. K. Talapatra, S. Chakrabarti, A. K. Mallik, and B. Talapatra, *Tetrahedron* **46**, pp. 6047–6052 (1990).
- [44] M. Filthaus, I. M. Oppel, and H. F. Bettinger, *Organic & Biomolecular Chemistry* **6**, pp. 1201 (2008).
- [45] P. Natarajan and M. Schmittel, *Inorganic Chemistry* **52**, pp. 8579–8590 (2013).
- [46] R. Herges and H. Neumann, *Liebigs Annalen* **1995**, pp. 1283–1289 (1995).
- [47] L. Gross, F. Mohn, N. Moll, P. Liljeroth, and G. Meyer, *Science* **325**, pp. 1110–1114 (2009).





Chapter 3

Precursor geometry determines the growth mechanism in graphene nanoribbons



This chapter is based on

Precursor Geometry Determines the Growth Mechanism in Graphene Nanoribbons

Fabian Schulz, Peter H. Jacobse, Filippo Federici Canova, Joost van der Lit, David Z. Gao, Adrianus van den Hoogenband, Patrick Han, Robertus J. M. Klein Gebbink, Marc-Etienne Moret, Pekka M. Joensuu, Ingmar Swart, Peter Liljeroth

The Journal of Physical Chemistry C **121** (5), pp. 2896-2904 (2017)



On-surface synthesis with molecular precursors has emerged as the de facto route to atomically well-defined graphene nanoribbons (GNRs) with controlled zigzag and armchair edges. On Au(111) and Ag(111) surfaces, the prototypical precursor 10,10-dibromo-9,9-bianthryl (DBBA) polymerizes through an Ullmann reaction to form straight GNRs with armchair edges. However, on Cu(111), irrespective of the bianthryl precursor (dibromo-, dichloro-, or halogen-free bianthryl), the Ullmann route is inactive, and instead, identical chiral GNRs are formed. Using atomically resolved non-contact atomic force microscopy (nc-AFM), we studied the growth mechanism in detail. In contrast to the nonplanar BA-derived precursors, planar dibromoperylene (DBP) molecules do form armchair GNRs by Ullmann coupling on Cu(111), as they do on Au(111). These results highlight the role of the substrate, precursor shape, and molecule-molecule interactions as decisive factors in determining the reaction pathway. Our findings establish a new design paradigm for molecular precursors and opens a route to the realization of previously unattainable covalently bonded nanostructures.

3.1 Introduction

Graphene nanoribbons (GNRs) are narrow, one-dimensional structures derived from two-dimensional graphene. GNRs have been proposed as a means for introducing a tunable band gap into graphene while preserving its favorable electronic properties.[1, 2] Such a band gap is a prerequisite to electronic applications of graphene and, together with the predicted spin-polarized flat-band edge states for certain edge terminations, gives GNRs enormous potential for use in next-generation nanoelectronics.[2] As a result, tremendous efforts have been devoted to the top-down fabrication of nanoribbons, for example, through the lithographic etching of graphene[3, 4] or the unzipping of carbon nanotubes.[5, 6] However, using these methods, it is not possible to produce nanoribbons with atomically well-defined edges. As the electronic properties of GNRs are intricately linked to their edge structure[2, 7], methods for synthesizing GNRs with atomically precise widths and edge structures need to be developed for actual applications.

On-surface synthesis has emerged as a complementary approach for obtaining covalently bonded nanostructures.[8] Using suitable precursor molecules, this bottom-up approach yields atomically well-defined graphene nanoribbons with either the armchair[9] or zigzag[10] edge topology. The beauty of this approach is that, by changing the precursor molecule, the resulting nanoribbon structure can be precisely selected. Since the initial demonstration of

seven-atom-wide armchair GNRs (7-AGNRs) synthesized by coupling 10,10'-dibromo-9,9'-bianthryl (DBBA) on a Au(111) surface[9], the field has progressed rapidly. Addition of biphenyl and (thiophenyl)phenyl moieties to DBBA molecules results in the formation of 13-AGNRs[11] and sulfur-doped GNRs[12], respectively, whereas incorporation of a diboraanthracene moiety into the molecule allows for the synthesis of boron-doped 7-AGNRs.[13, 14] The versatility of the bottom-up method is further illustrated by the numerous examples of GNRs that have been established recently, such as chevron-type GNRs[9] and their nitrogen-doped counterparts[15, 16], ultranarrow 5-AGNRs[17, 18], and zigzag GNRs with modified edges.[10, 19, 20]

Typically, the synthesis is carried out on gold (occasionally silver[21]) substrates, and it has been proposed to proceed through the metal-catalyzed Ullmann coupling of aryl halides.[8, 22, 23] The reaction mechanism is not completely known, but the first step involves metal-substrate-catalyzed cleavage of the carbon-halogen bond, resulting in a radical species[24], followed by aryl-aryl coupling to form polymer chains (protoribbons) at elevated temperatures. These protoribbons are converted to fully aromatic GNRs through cyclodehydrogenation at an even higher temperature (Fig. 3.1a).[9, 23]

It would be of interest to extend GNR synthesis to the technologically more relevant copper surfaces, for which large-scale graphene growth and reliable transfer techniques have been developed with great success in recent years.[25, 26, 27] Simonov *et al.*[28] described the synthesis of GNRs on Cu(111) from DBBA precursors. Based on the earlier experiments on Au(111) and Ag(111)[9, 21] and the assumption that the molecules follow the same Ullmann-coupling mechanism on Cu(111), the resulting structures were assigned to be 7-AGNRs. However, when the same experiments were performed by Han *et al.*[29], a characteristic corrugation of the nanoribbon edges was observed, which was ascribed to the formation of 3,1-chiral GNRs (Fig. 3.1a). The controversy over the actual structure of these ribbons on Cu(111)[30, 31, 32, 33] shows the difficulties in assessing the atomic structures of synthesis products by scanning tunneling microscopy (STM). Structure identification by STM is limited, as STM is sensitive to only electronic states near the Fermi energy[34], which, for polyaromatic hydrocarbons, are usually highly delocalized. A possible solution is offered by frequency-modulation noncontact atomic force microscopy (nc-AFM)[35]: nc-AFM images acquired with a passivated tip (*e.g.*, after deliberate attachment of a carbon monoxide molecule) provide a means of visualizing the chemical structure of single molecules[36], including graphene nanoribbons.[37, 38]

In this work, we used atomically resolved nc-AFM images to confirm that DBBA forms 3,1-chiral GNRs on Cu(111) surfaces, in stark contrast to the results obtained on Au(111)[9] and Ag(111)[39], as suggested by Han *et al.*[29] and verified by Sánchez-Sánchez *et al.*[40] This implies that the polymerization





on Cu(111) does not proceed by the Ullmann coupling route as on Au(111). To establish the reaction mechanism and determine the factors governing it, we repeated the experiments with chlorinated (dichlorobianthryl) and halogen-free (bianthryl) precursors. The nc-AFM images revealed that, in all cases, the same 3,1-chiral GNRs were formed. We investigated the reaction mechanism with further nc-AFM/STM experiments and followed the evolution of the reaction products from self-assembled molecular chains to linear polymers and eventually to fully aromatic graphene nanoribbons upon controlled annealing to higher temperatures. The importance of molecule-molecule interactions is highlighted by experiments with flat precursors (dibromoperylene, DBP)[17] that do form armchair GNRs on Cu(111) through Ullmann coupling. Our findings suggest a new paradigm for the synthesis of graphene nanoribbons in which the coupling of the precursor molecules is controlled by their geometry rather than their chemical functionality. This break from prototypical Ullmann coupling will allow for the realization of previously unattainable covalently bonded nanostructures.

3.2 Results

3.2.1 Identification of the 3,1-chiral graphene nanoribbon

We begin by confirming that DBBA[1] on Cu(111) forms 3,1-chiral GNRs, as proposed by Han *et al.*[29] and recently verified by Sánchez-Sánchez *et al.*[40] Fig. 3.1b shows an nc-AFM constant-height image of a GNR obtained after annealing submonolayer coverages of DBBA on Cu(111) to 620 K. The image shows the chemical structure of the GNR and clearly reveals its chiral symmetry, with a periodic arrangement of three zigzag units and one armchair unit comprising the GNR edge. We observed only these chiral GNRs on Cu(111), implying that the formation does not proceed by Ullmann coupling. The general coupling scheme resulting in such ribbons is outlined in Fig. 3.1a.

Surprisingly, the same chiral GNRs can also be synthesized from 10,10'-dichloro-9,9'-bianthryl (DCBA, Fig. 3.1c), that is, when the bromines in the precursor molecule are replaced by chlorines, and by 9,9'-bianthryl (BA, Fig. 3.1d), which does not contain any halogen atoms thought to be required for Ullmann-type couplings. DBBA and BA represent extreme cases, where the radical is expected to form either at the very beginning of the GNR formation process[1] or not at all[3]. Because the C-Cl bond in DCBA is stronger than the C-Br bond in DBBA[41, 42, 43], the radical is formed at a higher temperature, that is, at a later stage in the reaction. Yet the outcome is the same covalently bonded nanostructure with all of the precursors. This confirms that the aryl-aryl coupling is of non-Ullmann type and suggests that the entire GNR formation is insensitive to radical formation by dehalogenation.

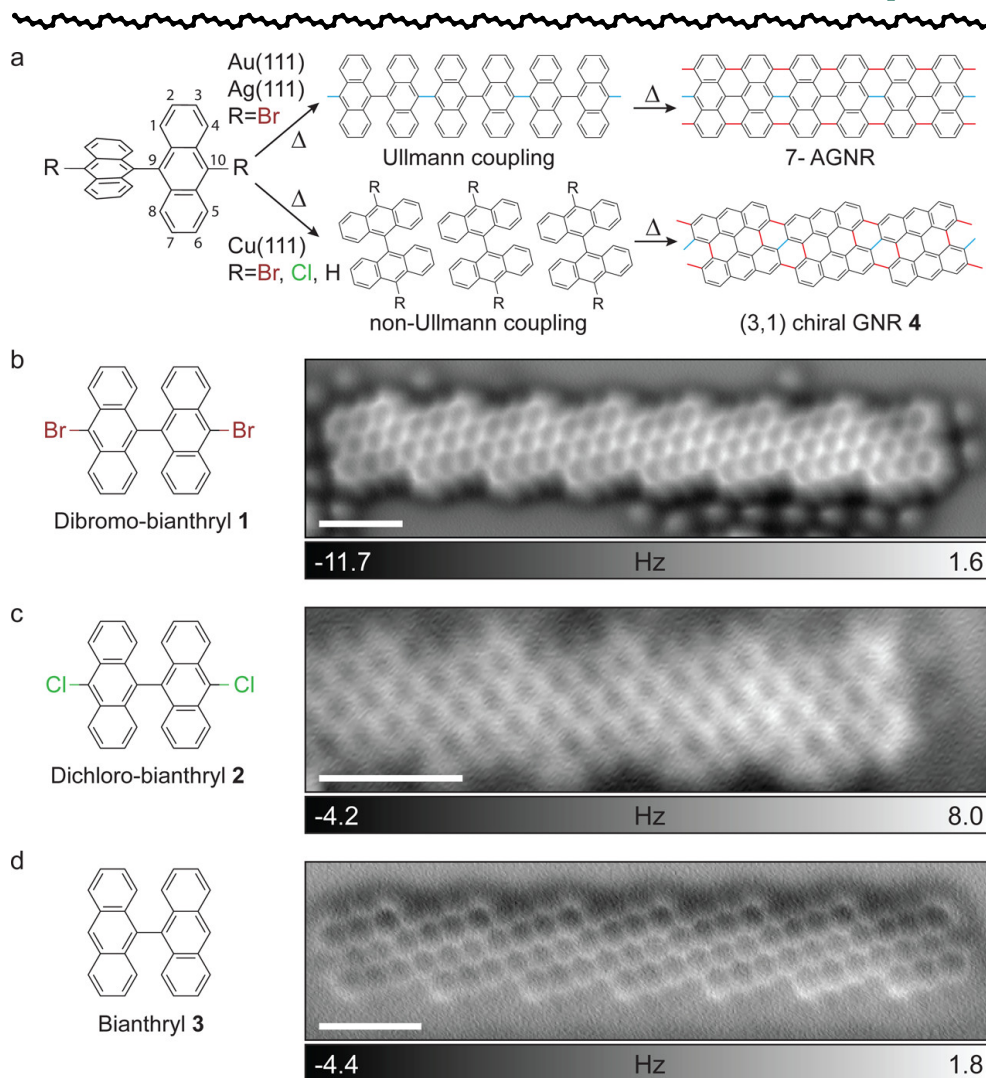


Fig. 3.1 Synthesis of chiral graphene nanoribbons on Cu(111) from different bianthryl precursors. a) Three-dimensional wireframe representation of the bianthryl precursor with different functionalizations ($R = \text{Br, Cl, or H}$) and two-dimensional schematics of the molecular coupling on Au(111) and Ag(111) (top, following Ullmann coupling) and on Cu(111) resulting in the observed 3,1-chiral nanoribbons (bottom). Bonds in red result from intramolecular cyclodehydrogenation, and those in blue result from intermolecular arylaryl coupling. b-d) Two-dimensional wireframe representations of the precursor and nc-AFM images of the resulting nanoribbons for b) DBBA/Cu(111) annealed to 620 K, c) DCBA/Cu(111) annealed to 550 K, and d) BA/Cu(111) annealed to 510 K. All scale bars represent 1 nm.

3.2.2 Resolving the formation mechanism



We unravel the chemical mechanism behind the deviation from Ullmann coupling[29, 31] and explain why this synthesis proceeds even without aryl halides by performing the synthesis step by step, for all three precursors. Fig. 3.2a shows an STM image of a single DBBA molecule after evaporation onto Cu(111) at (200 ± 50) K, which results in mostly isolated molecules and dimers. The molecule shows the typical dumbbell-like protrusions due to the nonplanar geometry of the bianthryl core, caused by steric hindrance between the inner hydrogen atoms at C1, C1' and C8, C8' (Fig. 3.1a). Constant-height nc-AFM images of the same molecule, recorded at different tip-sample distances, are depicted in Fig. 3.2c. When the tip is far away, the molecule is imaged as two repulsive arcs. Because their positions coincide with the two lobes in the STM images, we assign them to the edges of the topmost carbon ring of each of the two anthracene units of DBBA. The tilting of the CO at the tip apex significantly influences the image contrast at closer distances.[44, 45] This results in a sharp line diagonally through the center of the molecule and unrelated to any actual bond in the molecule.[46] This feature can be identified based on simulated nc-AFM images including the effect of CO flexibility through a molecular-mechanics model of the tip-sample junction [34, 45] with the DFT-optimized geometry of the molecule on the surface. We calculated the adsorption configuration for both the intact DBBA molecule and the debrominated biradical. Upon adsorption on Cu(111), the nonplanar shape of the bianthryl core in both cases is mostly conserved, although the symmetry in comparison to the gas phase is reduced. The two carbon rings closest to the copper tend to adsorb flat on the surface, inducing considerable distortion in the anthracene moieties. In the case of the biradical (Fig. 3.2b), the debrominated C10 and C10' bend down toward the copper substrate, causing additional strain. Our subsequent nc-AFM simulations reproduced the filament-like feature appearing at small tip-sample distances for both species. This feature is due to the CO bending as a response to a saddle point in the potential energy surface over the molecule[34], thereby connecting the two upper benzene rings of the two anthracene units. However, the arc-like features at large tip-sample distances were reproduced only in the nc-AFM simulation of the biradical shown in Fig. 3.2d. This is in agreement with the earlier experiments, suggesting that bromine-carbon bond cleavage occurs already below room temperature.[32]

As a next step, we heated the DBBA/Cu(111) system to room temperature, giving the results shown in Fig. 3.3. The molecules self-assemble into wiggly, disordered chain structures with rare and only short straight sections with periodicities between 10 and 11 Å (Fig. 3.3c). STM images with a CO tip reveal cleaved bromine atoms next to the chains (Fig. 3.3b). This assign-

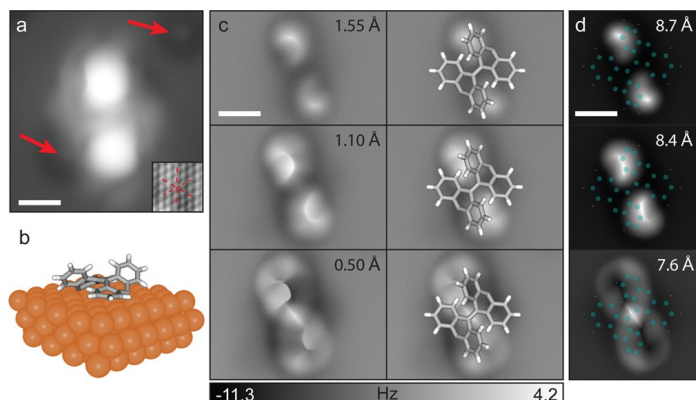


Fig. 3.2 Characterization of the DBBA precursor molecule. a) STM image of an individual DBBA molecule evaporated onto Cu(111) below room temperature. Red arrows mark adsorbed CO molecules. Inset: Atomically resolved STM image of the Cu(111) substrate. b) Adsorption configuration for debrominated DBBA as calculated by DFT. c) Constant-height nc-AFM images at different tipsample distances, given as offsets with respect to the tunneling set point (left) and overlaid with a structural model of debrominated DBBA (right). d) Simulated nc-AFM images based on the DFT-optimized geometry. Tip heights are given as distances between the CO carbon atom and the plane of the topmost copper layer. All scale bars represent 5 Å.

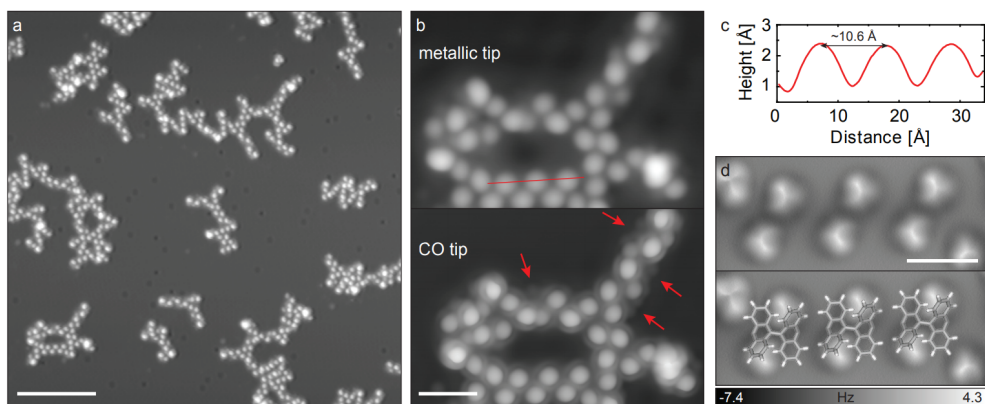
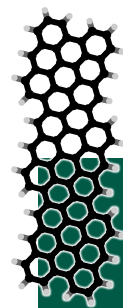


Fig. 3.3 DBBA on Cu(111) after annealing to room temperature. a) STM overview image. Scale bar is 10 nm. b) Zoom-in into one of the disordered chain assemblies, with a metallic (upper panel) and CO-functionalized (lower panel) tip. The red arrows in the lower panel mark additional protrusions, visible only with a CO tip, which are interpreted as cleaved bromines. Scale bar is 2 nm. c) STM profile along the red line shown in panel b, indicating the long periodicity of the chains at this stage. d) AFM image of the same chain as in panel c, overlaid with the structural model of the bi-radical. Scale bar is 1 nm.



ment is supported by the asymmetric appearance of some of the molecules, likely caused by the scission of only one of the two CBr bonds of DBBA or asymmetric subsequent stabilization/passivation of the radical. The nc-AFM image shown in Fig. 3.3d suggests that the structure does not deviate significantly from what would be expected for an Ullmann pathway, with the radical sites of adjacent monomers pointing toward each other. Although this cannot be directly verified from the STM or nc-AFM images, the distance between the monomers agrees with the incorporation of copper atoms into the chains, which could stabilize the bianthryl radicals.[30]

Fig. 3.4a presents an STM image of the DBBA/Cu(111) sample after it had been annealed to 470 K. The wiggly, disordered structures have transformed into long, straight molecular chains. Interestingly, the periodicity of the chains is also reduced to about 8.5–9 Å, as confirmed by the STM line profile in Fig. 3.4b. Such a reduction in periodicity was observed previously and was interpreted as a transition from an organometallic chain of surface-stabilized radicals to a polymer.[30] We obtained analogous molecular chains for DCBA and BA after they had been annealed to 500 and 440 K, respectively, with similar periodicities between 8.5 and 9 Å, as shown in Fig. 3.4c–f. Within the experimental uncertainty, these values are identical to the periodicity of the final 3,1-chiral ribbons of ≈ 9 Å calculated from purely geometrical considerations. Interestingly, we observed chains with long periodicity for neither DCBA nor BA, despite testing a wide range of annealing temperatures.

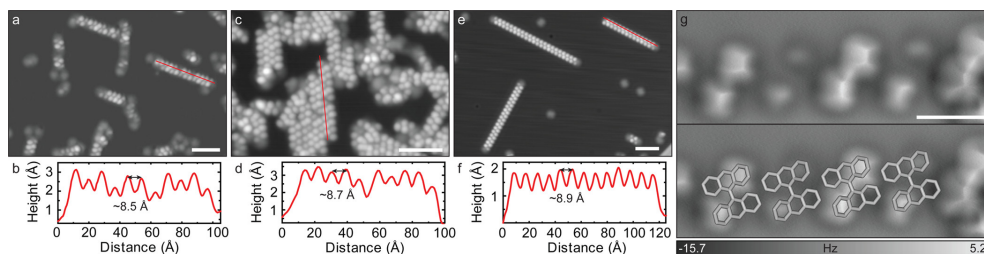


Fig. 3.4 Formation of molecular chains. a–f) STM images and line profiles of molecular chains formed after annealing a, b) DBBA/Cu(111) to 470 K, c, d) DCBA/Cu(111) to 500 K, and e, f) BA/Cu(111) to 440 K. Scale bars represent 5 nm. g) nc-AFM image with overlaid structural models (only BA core for clarity) for a chain with short periodicity formed from DBBA precursors. Scale bar represents 1 nm.

Within the chains shown in Fig. 3.4, some monomers exhibit a greatly reduced apparent height in the STM images, which is an indication of the onset of cyclodehydrogenation of the bianthryl cores. Indeed, the STM images in Fig. 3.4a, c, e also show individual molecules that are already fully cyclodehydrogenated, similarly to many of the chain ends. The energy barrier for cyclodehydrogenation seems to be considerably higher for molecules within

the chains. This might be due to the intermolecular interactions favoring a three-dimensional shape of the bianthryl core or the fact that the cyclodehydrogenation reaction in the middle of a chain would involve the formation of more bonds than that at the chain end. Fig. 3.4g shows an nc-AFM image of a DBBA chain with short periodicity. Even though not all monomers look alike because of the partial cyclodehydrogenation, we used the filament-like feature exhibited by some of them to obtain their orientation. Assuming that the remaining monomers have comparable positions, we found a structure that is radically different from that of the chains with longer periodicity. Instead, it is very close to the orientation of the monomers in the final 3,1-chiral GNRs (see Fig. 3.1a), with the C10 and C10' sites pointing away from each other and toward the sites of the chain.

The question arises whether the molecules in these chains are already polymerized, which we addressed by STM lateral manipulation experiments.[47] Fig. 3.5a shows a sequence of four STM images. The topmost depicts a straight BA chain, whereas the other three were recorded after subsequent manipulation attempts, in which the tip was positioned on one side of the chain, the tip-sample distance was reduced, and the tip was moved across the chain. As can be seen, the chain did not break, nor were individual molecules extracted. Instead, the chain bent in the direction of tip movement while remaining connected. This is a clear indication that intermolecular bonds have been established at this point of the growth process.[31] These chains are thus the chiral analogues of the so-called protoribbons (polymer chains with a single chemical bond between the monomers) formed on Au(111) and Ag(111).[9] Considering the AFM image in Fig. 3.4g, the most likely covalent bond formation is through C2-C2' coupling, as depicted in Fig. 3.5b. For the DBBA and DCBA precursors, this could be explained by radical hopping from C10 (C10') to C2 (C2'). However, in the case of BA, no halogen-carbon bond can be cleaved to give rise to a radical. Thus, the unusual C2-C2' bond formation is most likely due to activation of the corresponding C-H bonds by the catalytic activity of the Cu(111) surface, followed by polymerization into the chains shown in Fig. 3.4 through homocoupling. Formation of these protoribbons subsequently facilitates the ring-closure reaction by cyclodehydrogenation, which is the final step to achieve graphene nanoribbons. Indeed, further annealing leads to the chiral GNRs shown in Fig. 3.1.

3.2.3 Importance of precursor geometry

The importance of the nonplanar shape of the precursor molecules is emphasized by another set of experiments, depicted in Fig. 3.5c-e. The STM image in panel c shows BA molecules evaporated onto Cu(111) at room temperature, exhibiting their typical dumbbell shape. Fig. 3.5d shows the same sample after



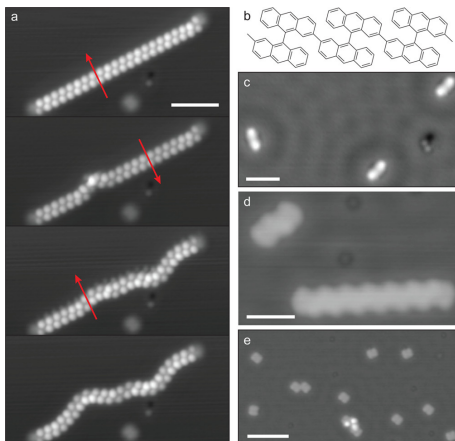


Fig. 3.5 Chain manipulation and quenching of GNR formation by cyclodehydrogenation. a) Stepwise STM lateral manipulation of a BA chain, starting from the top-most image. Scale bar represents 5 nm. b) Schematic of a protoribbon in which a single bond connects the BA monomers. c) STM image of BA molecules evaporated onto Cu(111) at room temperature. Scale bar represents 2 nm. d) STM image of chiral GNRs formed after the sample in panel c had been annealed to 510 K. Scale bar represents 2 nm. e) STM image of cyclodehydrogenated BA molecules after evaporation onto a Cu sample held at 510 K. Scale bar represents 5 nm.

it had been annealed to 510 K, resulting in the formation of chiral ribbons. The same evaporation procedure as in panel c was repeated for the sample shown in Fig. 3.5e, except that the Cu(111) substrate was already held at 510 K during the evaporation. As can be seen, no GNRs formed, but the surface is covered by cyclodehydrogenated BA molecules, namely, bisanthenes. Because they were evaporated onto the hot copper surface, the BA molecules cyclodehydrogenated immediately, before they could diffuse around to self-assemble into chains and polymerize, thus efficiently quenching GNR formation.

Thus far, we have established that the surface (Cu vs Au and Ag) has a significant influence on the coupling mechanism. In the following discussion, we further describe how the molecular shape (planar vs nonplanar) affects GNR formation. In Fig. 3.6, we follow, step by step, the GNR formation from planar 3,9-dibromoperylene and 3,10-dibromoperylene (DBP) precursors[17] on Cu(111), in a manner similar to that described above for the different BA-derived precursors. Fig. 3.6a shows a schematic of DBP and an STM image and the corresponding nc-AFM image of DBP evaporated onto Cu(111) at (200 ± 50) K. Three DBP molecules have assembled into a trimer with the bromines most likely still attached to the perylene core. In contrast, when evaporated onto the Cu(111) sample held at room temperature (Fig. 3.6b), the molecules form long, wiggly chains. Additional circular protrusions are visible next to the chain in both the STM and nc-AFM images, corresponding to the bromines from cleaved carbon-halogen bonds. The nc-AFM image at first suggests the formation of covalent bonds between C3 and C9' (C10') of adjacent perylene units (where primed and unprimed carbon atoms indicate the two different perylene units), that is, between radical sites formed by C-Br bond cleavage. However, closer inspection reveals that these apparent bonds have lengths of about 3-4 Å, much too long for a covalent carbon-carbon bond. In addition, the STM image shows bright, circular protrusions at the

positions of the peryleneperylene links (indicated by the arrows in Fig. 3.6b). This is likely caused by the inclusion of individual copper atoms into the structure [18, 47], indicating the formation of organometallic chains to stabilize the perylene biradicals after C-Br bond scission. The exact nature of the copper atoms cannot be identified from our experiments, with both adatoms and surface atoms pulled out of the plane of the top layer of the substrate being plausible.

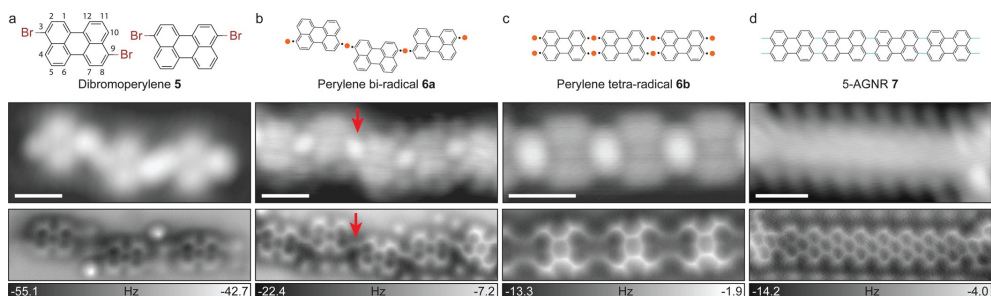


Fig. 3.6 Formation of armchair GNRs from dibromoperylene through on-surface Ullmann coupling on Cu(111). a-d) Structural model, STM image, and AFM image of DBP evaporated onto Cu(111) at a) 200 K and b) room temperature and of DBP on Cu(111) annealed to c) 470 and d) 570 K. The two very bright protrusions in the AFM image in panel a are CO molecules. All scale bars represent 1 nm.

Fig. 3.6c shows the sample after it had been annealed to 470 K. The appearance of the chains has changed markedly, as they have become straighter and shorter. An analysis similar to that applied to the wiggly chains can be carried out: The apparent bonds in the nc-AFM image between C3 (C4) and C10' (C9') of adjacent perylene units are too long for covalent carbon-carbon bonds, and the STM image shows an oblong bright feature at the same position. Because the four carbon atoms C3, C4, C9, and C10 all look alike in the nc-AFM image, with reduced intensity indicating a slight downward bending, we conclude that these features indicate the formation of perylene tetraradicals due to CH activation, stabilized through formation of organometallic chains connected by copper-atom dimers. We completed the formation of the GNRs by further annealing the sample to 570 K, as highlighted in Fig. 3.6c. The obtained ribbon is a five-atom-wide armchair GNR (5-AGNR), undoubtedly formed by an on-surface Ullmann coupling reaction and thus identical to the results for DBP on Au(111). [17] This confirms that radical coupling is effective in the case of the DBP precursor and points to the nonplanar molecular geometry being responsible for the departure from the Ullmann coupling scheme in the case of the BA-derived precursor molecules.

When performing such a step-by-step synthesis, it is important to differentiate between actual reaction intermediates and self-assembled structures

formed upon cooling to the imaging temperature after the heating step. The two types of organometallic chains formed by DBP at different temperatures and the long-periodicity DBBA chains probably represent the latter. Nevertheless, these structures yield important information about the sequence of the different steps along the reaction path. The formation of the perylene tetraradicals indicates that, on Cu(111), the energy barrier for CH bond activation at C4 and C10 (C9) is significantly lower than that for arylaryl homocoupling between C3 and C9' (C10'), in stark contrast to Au(111), where arylaryl coupling precedes CH bond activation and cyclodehydrogenation.[9, 17, 48] This also explains the reduced quality of the 5-AGNRs on Cu(111): The higher number of radical sites compared to Au(111) increases the coupling rate and reduces the diffusion rate, which leads to less-ordered structures.[49]

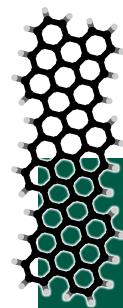
Applying these findings to the chiral ribbons completes our picture of their unusual formation mechanism: Initially, radicals are formed at C10 and C10' by dehalogenation in the case of DBBA, which form long-periodicity organometallic chains after cooling. Such chains are not observed for DCBA and BA, indicating that dechlorination occurs at similar temperatures as homocoupling or cyclodehydrogenation. The next step occurs analogously for all three precursors, which is CH activation at the C2 atoms. On Cu(111), this process has a reduced energy barrier compared to that on Au(111), allowing for deviation from the Ullmann route through C2-C2' homocoupling. This step is likely driven by π - π interactions, which can significantly influence adsorption structures[50] and would favor an arrangement of the bianthryl cores in which the C2 and C2' radical sites point toward each other because of the three-dimensional shape of the precursors.[29] Potential passivation of the C10 and C10' radical sites for DBBA and DCBA could also facilitate this step. Once the covalent bond between the monomers is established, further heating induces the cyclodehydrogenation of the remaining bianthryl core to form the fully aromatic chiral ribbon.

3.3 Conclusions

Using STM and atomically resolved nc-AFM imaging, we have followed the synthesis of chiral GNRs on Cu(111) from three different BA-derived precursors step by step. Despite radical formation through dehalogenation of the DBBA precursors, the formation of armchair nanoribbons through Ullmann coupling does not occur. This is due to the stronger interaction of the molecule with the surface on Cu(111), which stabilizes the radical after halogen-carbon bond scission and reduces the energy barrier for C-H bond activation. Consequently, C-H bond activation at C2 and C2' atoms occurs at a lower temperature than C10-C10' aryl-aryl coupling, resulting in similar intermolecular

carbon-carbon bond formation for DBBA, DCBA, and BA. The ring-closure reaction through cyclodehydrogenation yields as the final product the fully aromatic chiral GNR.

The situation is quite different for the planar DBP precursor. Although the observed organometallic chains show that the formed radicals are stabilized by interaction with native substrate atoms, further CH bond activation and intermolecular carbon-carbon bond formation still results in armchair GNRs. The main difference between these two cases is the three-dimensional shape of the BA-derived precursors that favors molecular chains along the chiral direction. On the fairly inert Au(111) surface, the C-H bond activation at the C2 and C2' atoms occurs only in the final cyclodehydrogenation step, the difference in the precursor shape is insignificant, and both DBBA and DBP follow the Ullmann coupling pathway. On Cu(111), however, the strong interaction of the precursors with the surface decisively influences the reaction pathway and results in GNR formation being controlled by the precursor shape rather than by the chemical functional groups. This opens up new possibilities for on-surface synthesis in which the precursor shape determines the coupling reaction, thus allowing for the realization of previously unattainable covalently bonded nanostructures.



3.4 Experimental methods

3.4.1 Sample preparation

10,10'-Dibromo-9,9'-bianthryl was synthesized according to the method reported in ref [37], 9,9'-bianthryl and 10,10'-dichloro-9,9'-bianthryl according to the method reported in ref [41], and 3,9-dibromoperylene and 3,10-dibromoperylene according to the method reported in ref [17]. The two isomers of dibromoperylene form in a roughly 1:1 ratio during the synthesis for symmetry reasons. Although the isomers could be separated with some effort, the publication of Kimouche *et al.*[17] showed that the mixture of the two isomers does not seem to affect the GNR formation, as straight GNRs are obtained.

Samples were prepared by evaporating the precursor molecules from Knudsen-cell-type evaporators onto Cu(111) single crystals, cleaned by sputtering/annealing cycles. Low-temperature evaporation for DBBA and DBP was performed by removing the cold Cu substrate from the STM/AFM instrument (≈ 5 K), positioning it for short time in front of the evaporator, and inserting it immediately back into the STM/AFM instrument. The total time outside the cold microscope was between 2 and 3 min, yielding a conservative estimated temperature (and error margin) of (200 ± 50) K. Thus, the difference in debromination after low-temperature evaporation between DBBA and

DBP (see below) is more likely to reflect the variation in sample temperature than different energy barriers for C-Br bond cleavage.

For the experiments on DBBA and DBP, annealing temperatures were monitored using a pyrometer, which is sensitive to the optical alignment with the sample, the way it is calibrated, and potential stray light. For the experiments on DCBA and BA, sample temperatures during annealing were deduced from the filament power and a calibration curve recorded with a pyrometer. A reasonable error estimation for the temperatures reported in this article is ± 30 K for each setup. Comparing absolute sample temperatures between different ultrahigh-vacuum systems is generally difficult. While temperature measurements are repeatable as such, large systematic differences between different setups can easily exist.

3.4.2 Scanning probe measurements

After preparation, the sample was inserted into a low-temperature STM/AFM instrument, housed within the same ultrahigh-vacuum system (base pressure $\approx 10^{-10}$ mbar). The experiments on DBBA and DBP precursors were carried out with a Createc LT-STM/AFM system (with a qPlus sensor resonance frequency f_0 of ≈ 30.7 kHz, a quality factor of $\approx 100k$, a spring constant k of ≈ 1.8 kN/m, and an oscillation amplitude of 50 pm). The experiments on DCBA and BA precursors were carried out with an Omicron LT-STM/qPlus AFM system (with a qPlus sensor resonance frequency f_0 of ≈ 19.5 kHz, a quality factor of $\approx 30k$, a spring constant k of ≈ 1.8 kN/m, and an oscillation amplitude of 85 pm).

Carbon monoxide for nc-AFM imaging with functionalized tips was dosed onto the surface through a leak valve. Picking up an individual carbon monoxide molecule on the tip apex was carried out as described previously.[36, 51] nc-AFM images were acquired at a bias voltage of 0 V.

3.4.3 DFT calculations

Density functional theory (DFT) simulations to examine the adsorption geometries and interactions between molecules on the surface were performed with the CP2K code using the Perdew-Burke-Ernzerhof (PBE) generalized gradient approximation (GGA) density functional and a mixed Gaussian and plane wave (GPW) basis set.[52, 53] These calculations included geometry minimizations of various molecular variants on the surface. The Cu(111) surface was represented using three atomic layers; the lowermost layer was fixed, whereas the other two layers were allowed to relax to reproduce the atomic and electronic structure of the system. We employed semiempirical long-range dispersion corrections[54] to represent van der Waals (vdW) interactions in the

system. Finally, the molecularly optimized (MOLOPT)[55] basis set was used to minimize basis set superposition error (BSSE), and the plane-wave cutoff was selected to be 400 Ry, as, above this value, the results did not change. The lowest-energy configuration of each molecule was computed by placing the molecule onto the surface in various positions and optimizing the geometry. The starting positions were obtained by rotating the molecule by 2° increments on the surface.

3.4.4 nc-AFM simulations

AFM simulations were performed with the MechAFM code, based on the probe particle model[44, 45], as implemented by Spijker and co-workers.[56] The probe consists of a fixed C atom connected to an O atom restrained in the xy plane by a harmonic spring with a stiffness of 0.5 N/m. The tipsample interactions were calculated by placing the tip in several locations above the DFT-optimized structures of the molecules and relaxing the tip O termination. For simplicity, the interatomic interactions between O and the atomic species of the sample were described by Lennard-Jones potentials. At this stage, electrostatic interactions were disregarded. The atomic parameters for the potentials were taken from the CHARMM force field.[57] Parameters for pair potentials were obtained from the atomic parameters using arithmetic mixing rules. Frequency shift images were calculated from the tipsample interaction maps using the method described in ref [58], assuming that the AFM cantilever had a stiffness of 1.8 kN/m and an oscillation amplitude of 50 pm at a resonance frequency of 25 kHz.



Bibliography

- [1] P. Ruffieux, J. Cai, N. C. Plumb, L. Patthey, D. Prezzi, A. Ferretti, E. Molinari, X. Feng, K. Müllen, C. A. Pignedoli, and R. Fasel, *ACS Nano* **6**, pp. 6930–6935 (2012).
- [2] A. H. Castro Neto, F. Guinea, N. M. R. Peres, K. S. Novoselov, and A. K. Geim, *Reviews of Modern Physics* **81**, pp. 109–162 (2009).
- [3] M. Y. Han, B. Özyilmaz, Y. Zhang, and P. Kim, *Physical Review Letters* **98**, pp. 206805 (2007).
- [4] J. Bai, X. Duan, and Y. Huang, *Nano Letters* **9**, pp. 2083–2087 (2009).
- [5] L. Jiao, L. Zhang, X. Wang, G. Diankov, and H. Dai, *Nature* **458**, pp. 877–880 (2009).
- [6] D. V. Kosynkin, A. L. Higginbotham, A. Sinitskii, J. R. Lomeda, A. Dimiev, B. K. Price, and J. M. Tour, *Nature* **458**, pp. 872–876 (2009).
- [7] O. V. Yazyev, *Accounts of Chemical Research* **46**, pp. 2319–2328 (2013).
- [8] L. Grill, M. Dyer, L. Lafferentz, M. Persson, M. V. Peters, and S. Hecht, *Nature Nanotechnology* **2**, pp. 687–691 (2007).
- [9] J. Cai, P. Ruffieux, R. Jaafar, M. Bieri, T. Braun, S. Blankenburg, M. Muoth, A. P. Seitsonen, M. Saleh, X. Feng, K. Müllen, and R. Fasel, *Nature* **466**, pp. 470–473 (2010).

- 
- [10] P. Ruffieux, S. Wang, B. Yang, C. Sanchez-Sanchez, J. Liu, T. Dienel, L. Talirz, P. Shinde, C. A. Pignedoli, D. Passerone, T. Dumslaff, X. Feng, K. Müllen, and R. Fasel, *Nature* **531**, pp. 489–492 (2016).
- [11] Y. C. Chen, D. G. De Oteyza, Z. Pedramrazi, C. Chen, F. R. Fischer, and M. F. Crommie, *ACS Nano* **7**, pp. 6123–6128 (2013).
- [12] G. D. Nguyen, F. M. Toma, T. Cao, Z. Pedramrazi, C. Chen, D. J. Rizzo, T. Joshi, C. Bronner, Y. C. Chen, M. Favaro, S. G. Louie, F. R. Fischer, and M. F. Crommie, *Journal of Physical Chemistry C* **120**, pp. 2684–2687 (2016).
- [13] S. Kawai, S. Saito, S. Osumi, S. Yamaguchi, A. S. Foster, P. Spijker, and E. Meyer, *Nature Communications* **6**, pp. 8098 (2015).
- [14] R. R. Cloke, T. Marangoni, G. D. Nguyen, T. Joshi, D. J. Rizzo, C. Bronner, T. Cao, S. G. Louie, M. F. Crommie, and F. R. Fischer, *Journal of the American Chemical Society* **137**, pp. 8872–8875 (2015).
- [15] C. Bronner, S. Stremlau, M. Gille, F. Brauße, A. Haase, S. Hecht, and P. Tegeder, *Angewandte Chemie - International Edition* **52**, pp. 4422–4425 (2013).
- [16] J. Cai, C. A. Pignedoli, L. Talirz, P. Ruffieux, H. Söde, L. Liang, V. Meunier, R. Berger, R. Li, X. Feng, K. Müllen, and R. Fasel, *Nature Nanotechnology* **9**, pp. 896–900 (2014).
- [17] A. Kimouche, M. M. Ervasti, R. Drost, S. Halonen, A. Harju, P. M. Joensuu, J. Sainio, and P. Liljeroth, *Nature Communications* **6**, pp. 10177 (2015).
- [18] H. Zhang, H. Lin, K. Sun, L. Chen, Y. Zagranyski, N. Aghdassi, S. Duhm, Q. Li, D. Zhong, Y. Li, K. Müllen, H. Fuchs, and L. Chi, *Journal of the American Chemical Society* **137**, pp. 4022–4025 (2015).
- [19] J. Liu, B.-W. Li, Y.-Z. Tan, A. Giannakopoulos, C. Sanchez-Sanchez, D. Beljonne, P. Ruffieux, R. Fasel, X. Feng, and K. Müllen, *Journal of the American Chemical Society* **137**, pp. 6097–6103 (2015).
- [20] D. G. De Oteyza, A. García-Lekue, M. Vilas-Varela, N. Merino-Díez, E. Carbonell-Sanromà, M. Corso, G. Vasseur, C. Rogero, E. Guitián, J. I. Pascual, J. E. Ortega, Y. Wakayama, and D. Peña, *ACS Nano* **10**, pp. 9000–9008 (2016).
- [21] H. Huang, D. Wei, J. Sun, S. L. Wong, Y. P. Feng, A. H. C. Neto, and A. T. S. Wee, *Scientific Reports* **2**, pp. 983 (2012).
- [22] F. Ullmann and J. Bielecki, *Berichte der deutschen chemischen Gesellschaft* **34**, pp. 2174–2185 (1901).
- [23] L. Talirz, P. Ruffieux, and R. Fasel, *Advanced Materials* **28**, pp. 6222–6231 (2016).
- [24] J. Björk, F. Hanke, and S. Stafström, *Journal of the American Chemical Society* **135**, pp. 5768–5775 (2013).
- [25] X. Li, W. Cai, J. An, S. Kim, J. Nah, D. Yang, R. Piner, A. Velamakanni, I. Jung, E. Tutuc, S. K. Banerjee, L. Colombo, and R. S. Ruoff, *Science* **324**, pp. 1312–1314 (2009).
- [26] X. Li, Y. Zhu, W. Cai, M. Borysiak, B. Han, D. Chen, R. D. Piner, L. Colomba, and R. S. Ruoff, *Nano Letters* **9**, pp. 4359–4363 (2009).
- [27] S. Bae, H. Kim, Y. Lee, X. Xu, J.-S. Park, Y. Zheng, J. Balakrishnan, T. Lei, H. Ri Kim, Y. I. Song, Y.-J. Kim, K. S. Kim, B. Özyilmaz, J.-H. Ahn, B. H. Hong, and S. Iijima, *Nature Nanotechnology* **5**, pp. 574 (2010).
- [28] K. A. Simonov, N. A. Vinogradov, A. S. Vinogradov, A. V. Generalov, E. M. Zagrebina, N. Mårtensson, A. A. Cafolla, T. Carpy, J. P. Cunniffe, and A. B. Preobrajenski, *Journal of Physical Chemistry C* **118**, pp. 12532–12540 (2014).
- [29] P. Han, K. Akagi, F. Federici Canova, H. Mutoh, S. Shiraki, K. Iwaya, P. S. Weiss, N. Asao, and T. Hitosugi, *ACS Nano* **8**, pp. 9181–9187 (2014).
- [30] K. A. Simonov, N. A. Vinogradov, A. S. Vinogradov, A. V. Generalov, E. M. Zagrebina, N. Mårtensson, A. A. Cafolla, T. Carpy, J. P. Cunniffe, and A. B. Preobrajenski, *ACS Nano* **9**, pp. 3399–3403 (2015).

- [31] P. Han, K. Akagi, F. Federici Canova, H. Mutoh, S. Shiraki, K. Iwaya, P. S. Weiss, N. Asao, and T. Hitosugi, *ACS Nano* **9**, pp. 3404–3405 (2015).
- [32] K. A. Simonov, N. A. Vinogradov, A. S. Vinogradov, A. V. Generalov, E. M. Zagrebina, G. I. Svirskiy, A. A. Cafolla, T. Carpy, J. P. Cunniffe, T. Taketsugu, A. Lyalin, N. Mårtensson, and A. B. Preobrajenski, *ACS Nano* **9**, pp. 8997–9011 (2015).
- [33] P. Han, K. Akagi, F. Federici Canova, R. Shimizu, H. Oguchi, S. Shiraki, P. S. Weiss, N. Asao, and T. Hitosugi, *ACS Nano* **9**, pp. 12035–12044 (2015).
- [34] F. Schulz, S. Hämäläinen, and P. Liljeroth, “Atomic-Scale Contrast Formation in AFM Images on Molecular Systems BT - Noncontact Atomic Force Microscopy: Volume 3”, pp. 173–194. Springer International Publishing Cham (2015).
- [35] T. R. Albrecht, P. Grütter, D. Horne, and D. Rugar, *Journal of Applied Physics* **69**, pp. 668–673 (1991).
- [36] L. Gross, F. Mohn, N. Moll, P. Liljeroth, and G. Meyer, *Science* **325**, pp. 1110–1114 (2009).
- [37] J. van der Lit, M. P. Boneschanscher, D. Vanmaekelbergh, M. Ijäs, A. Uppstu, M. Ervasti, A. Harju, P. Liljeroth, and I. Swart, *Nature Communications* **4**, pp. 2023 (2013).
- [38] T. Dienel, S. Kawai, H. Söde, X. Feng, K. Müllen, P. Ruffieux, R. Fasel, and O. Gröning, *Nano Letters* **15**, pp. 5185–5190 (2015).
- [39] Y. Y. Huang and E. M. Terentjev, *Polymers* **4**, pp. 275–295 (2012).
- [40] C. Sánchez-Sánchez, T. Dienel, O. Deniz, P. Ruffieux, R. Berger, X. Feng, K. Müllen, and R. Fasel, *ACS Nano* **10**, pp. 8006–8011 (2016).
- [41] P. H. Jacobse, A. van den Hoogenband, M. E. Moret, R. J. Klein Gebbink, and I. Swart, *Angewandte Chemie - International Edition* **55**, pp. 13052–13055 (2016).
- [42] D. F. McMillen and D. M. Golden, *Annual Review of Physical Chemistry* **33**, pp. 493–532 (1982).
- [43] K. J. Shi, X. Zhang, C. H. Shu, D. Y. Li, X. Y. Wu, and P. N. Liu, *Chem. Commun.* **52**, pp. 8726–8729 (2016).
- [44] P. Hapala, M. Švec, O. Stetsovyh, N. Van Der Heijden, M. Ondráček, J. Van Der Lit, P. Mutombo, I. Swart, and P. Jelínek, *Nature Communications* **7**, pp. 11560 (2016).
- [45] S. K. Hämäläinen, N. van der Heijden, J. van der Lit, S. den Hartog, P. Liljeroth, and I. Swart, *Physical Review Letters* **113**, pp. 186102 (2014).
- [46] N. Pavliček, B. Fleury, M. Neu, J. Niedenführ, C. Herranz-Lancho, M. Ruben, and J. Repp, *Physical Review Letters* **108**, pp. 86101 (2012).
- [47] J. Park, K. Y. Kim, K.-H. Chung, J. K. Yoon, H. Kim, S. Han, and S.-J. Kahng, *The Journal of Physical Chemistry C* **115**, pp. 14834–14838 (2011).
- [48] A. Basagni, F. Sedona, C. A. Pignedoli, M. Cattelan, L. Nicolas, M. Casarin, and M. Sambi, *Journal of the American Chemical Society* **137**, pp. 1802–1808 (2015).
- [49] M. Bieri, M. T. Nguyen, O. Gröning, J. Cai, M. Treier, K. Ait-Mansour, P. Ruffieux, C. A. Pignedoli, D. Passerone, M. Kastler, K. Müllen, and R. Fasel, *Journal of the American Chemical Society* **132**, pp. 16669–16676 (2010).
- [50] Q. S. Stöckl, Y.-C. Hsieh, A. Mairena, Y.-T. Wu, and K.-H. Ernst, *Journal of the American Chemical Society* **138**, pp. 6111–6114 (2016).
- [51] L. Bartels, G. Meyer, and K. H. Rieder, *Applied Physics Letters* **71**, pp. 213–215 (1997).
- [52] G. Lippert, J. Hutter, and M. Parrinello, *Molecular Physics* **92**, pp. 477–488 (1997).
- [53] J. Vandevondele, M. Krack, F. Mohamed, M. Parrinello, T. Chassaing, and J. Hutter, *Computer Physics Communications* **167**, pp. 103–128 (2005).
- [54] S. Grimme, *Journal of Computational Chemistry* **27**, pp. 1787–1799 (2006).
- [55] J. VandeVondele and J. Hutter, *The Journal of Chemical Physics* **127**, pp. 114105 (2007).
- [56] J. Tracey, F. Federici Canova, O. Keisanen, D. Z. Gao, P. Spijker, B. Reischl, and A. S. Foster, *Computer Physics Communications* **196**, pp. 429–438 (2015).



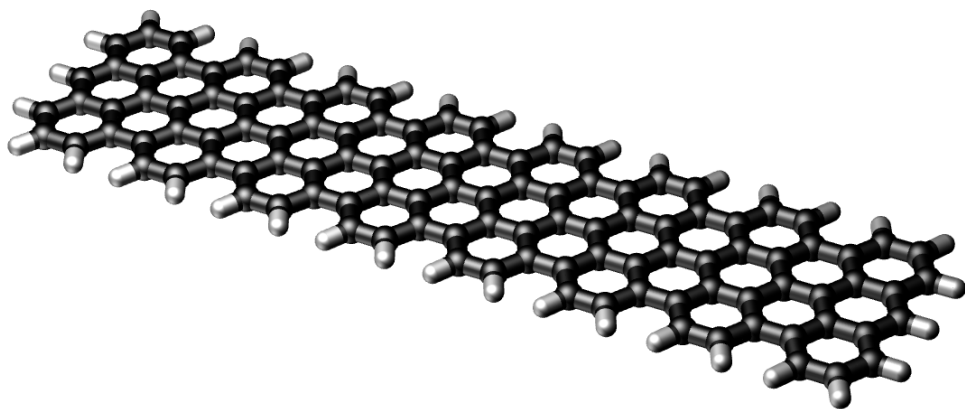
chapter 3

- [57] K. Vanommeslaeghe and A. D. MacKerell, *Journal of Chemical Information and Modeling* **52**, pp. 3144–3154 (2012).
- [58] F. J. Giessibl, *Reviews of Modern Physics* **75**, pp. 1–35 (2013).



Chapter 4

MathemaTB: A Mathematica package for tight-binding calculations



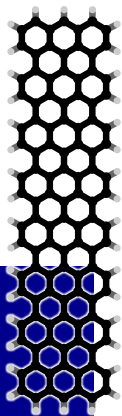
This chapter is based on

MathemaTB: A Mathematica package for tight-binding calculations

Peter H. Jacobse

Manuscript in preparation

The MathemaTB package is a package developed to enable tight-binding calculations within *Mathematica*. The package presents 49 functions dedicated to facilitating these quantum mechanical computations. MathemaTB offers functionalities to carry out matrix manipulation, data analysis and visualizations on molecules, wave functions, Hamiltonians, coefficient matrices, and energy spectra, providing a unique insight into the interplay between geometric and electronic structure. Crystal orbitals, projected dispersions and densities of states can be obtained with only a few lines of code. The effect of different structures, heteroatoms and tight-binding parameters can easily be explored. Calculations can be carried out on molecules (Hückel-type calculations) or on systems with periodicities in one, two or three dimensions. Particularly powerful features are the possibility to plot band structures both along paths (one-dimensional) and over planes (two-dimensional) in reciprocal space, where in each case the localization of the wave function onto different sites, symmetries or basis functions can be visualized with color coding. Further features involve crystal orbital plotting with color coding of the complex phase and manipulation of the Hamiltonian matrix with numerical and symbolic elements. The conjunction of tight-binding functions, matrix algebra functions for symmetry, overlap and change of basis, wave function- and dispersion functions and a high degree of interactivity and flexibility makes MathemaTB a useful package for electronic structure calculations.



4.1 Introduction

The tight-binding, or Hückel method is a popular tool in quantum chemistry and solid state physics to determine the electronic structure of molecules and extended structures. The methodology allows the quantum mechanical nature of different condensed matter systems to be determined by relatively (computationally) simple means, and in a much more translucent manner than *ab initio* methods such as density functional theory (DFT). The following gives a brief introduction in the basic concepts of tight-binding as used in the MathemaTB package. More background information can be found in refs. [1, 2, 3].

Tight-binding is usually presented in the second quantization formalism as

$$\hat{H}|\psi\rangle = E|\psi\rangle$$

$$\hat{H} = \sum_i^{\text{atoms}} \epsilon_i a_i^\dagger a_i + \sum_{\langle i,j \rangle}^{\text{pairs}} t(a_i^\dagger a_j + a_j^\dagger a_i)$$

Here, \hat{H} is the Hamiltonian operator, which operates on the electronic wave function. a^\dagger and a are the creation and annihilation operators, respectively, which are defined through

$$a_i^\dagger a_j |k\rangle = |i\rangle \delta_{jk}$$

The wave function is linearly expanded as

$$|\psi\rangle = \mathbf{c} \cdot |\vec{\chi}\rangle$$

where $|\vec{\chi}\rangle$ is the basis set and \mathbf{c} is the expansion coefficient vector. Wave functions that are eigenfunctions of the Hamiltonian are allowed single-particle solutions, and the set of these (molecular/crystal) orbitals defines the electronic structure of the molecule or lattice.

Molecular wave functions are commonly approximated as a linear combination of atomic orbitals (LCAO approach), or in a more general case, from *sites*. Application of the tight-binding Hamiltonian on a n -site linearly expanded wave function results in the emergence of n linearly coupled equations. These are conveniently written in matrix form as

$$\mathbf{HC} = \mathbf{CE}$$

where \mathbf{C} is the coefficient matrix, whose columns are the coefficient vectors of the individual single-electron orbitals, and \mathbf{E} is the diagonal eigenenergy matrix. It turns out that the diagonal elements of the Hamiltonian are the on-site energies: the energies associated with the electron remaining on a specific atom. The off-diagonal element \mathbf{H}_{ij} signify the energy that an electron has to “pay” to hop from site i to site j . In the more general case, where the basis functions are not orthogonal but feature a finite overlap, the matrix form of the Schrödinger equation becomes

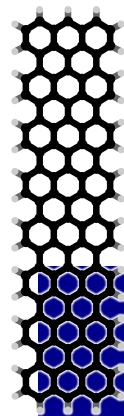
$$\mathbf{HC} = \mathbf{SCE}$$

where \mathbf{S} is the overlap matrix. This is an example of a generalized eigenvalue equation. The most convenient way to solve this equation is to first cast it into the special eigenvalue equation form by means of the Löwdin orthogonalization procedure.[2]

$$\mathbf{H}'\mathbf{C}' = \mathbf{C}'\mathbf{E}$$

with $\mathbf{H}' = \mathbf{S}^{-1/2}\mathbf{HS}^{-1/2}$ and $\mathbf{C}' = \mathbf{S}^{1/2}\mathbf{C}$. After diagonalizing \mathbf{H}' , the coefficient matrices can be brought back to the original basis by backtransformation as $\mathbf{C} = \mathbf{S}^{-1/2}\mathbf{C}'$. The off-diagonal element \mathbf{S}_{ij} in the overlap matrix signify the physical overlap between the orbitals on site i and site j .

The first challenge in tight-binding is to parametrize the Hamiltonian matrix elements as to give an accurate description of the potential energy landscape of the molecule or lattice to which the electron is subjected. These



matrix elements are usually chosen semi-empirically, and are normally defined for interactions between sites that are in close proximity (always nearest neighbors, often next-nearest neighbors, maybe second-next nearest neighbors, *etc.*). The second challenge is to diagonalize the Hamiltonian to obtain the electronic energy spectrum \mathbf{E} and wave function coefficient matrix \mathbf{C} . For periodic structures, the wave function may be expanded from Bloch-type wave functions. In this case, the Hamiltonian matrix is a function of the momentum vector \mathbf{k} , and diagonalization needs to be performed at different points in reciprocal space to find the electronic dispersion and density of states. Finally, the last challenge is to interpret and visualize the results.

Some tight-binding calculations can be performed relatively easily, even analytically, but the level of complexity of a tight-binding calculation correlates with the complexity of the system under investigation. Therefore, to obtain useful results on various structures, it is helpful to have a software implementation of the tight-binding method at hand. Notably, the development of packages such as PythTB, Pybinding and Kwant has made make tight-binding accessible to a wider audience than before.[4, 5, 6]

Mathematica is a powerful computer program that contains numerous functionalities to carry out matrix manipulation, molecular visualization and much more.[7] With sufficient knowledge of the program, it is possible to script and carry out tight-binding calculations. However, going all the way from parametrization to analysis and visualization requires a significant amount of coding. Therefore, to be able to perform quantum chemical computations in *Mathematica* in a more accessible fashion, it is helpful to have a standard implementation of tight-binding functionalities. The MathemaTB package was developed to provide exactly this. The package provides an implementation of *Mathematica*'s elementary functions into functions that are tailored towards electronic structure calculations, allowing tight-binding calculations to be executed in an easy, comprehensible way. MathemaTB was made in such a way that carrying out a tight-binding calculation can in principle be as easy as evaluating a single line of code

```
In[1]:= Diagonalize[BuildHamiltonian[
        XYZImport[]["Geometry"]]["Hamiltonian"]]
```

but more functions and options can be used as desired to perform more elaborate calculations.

In comparison with available tight-binding implementations, MathemaTB is flexible and provides a high degree of interactivity and a focus on translucency and comprehensibility. `BuildHamiltonian` and `Diagonalize` are just two of the 49 functions that MathemaTB provides, and all functionalities can be used in conjunction with all possibilities already provided by default in *Mathematica*. MathemaTB has some unusual features not found in other packages.

Notably, the site- or basis function-projected dispersion, energy diagram or density of states can be calculated easily, and the (projected) band structure can be plotted in one (along a path) or two (on a plane) dimensions of reciprocal space. Also, molecular or crystal orbitals are plotted easily, and the hue of the orbitals signifies the complex phase of the wave function. Atoms, sites, lattices and parameters are easily defined and redefined, and the Hamiltonian can even be diagonalized analytically or be used with symbolical values.

The MathemaTB package comes with a manual which describes all functions and their options, but also contains a tutorial section. The following sections give an overview of what can be achieved with MathemaTB by highlighting a few specific case studies, which are also treated in the respective sections of the tutorial. The highlights here give a good synopsis of the capabilities of the package. For more background information on how the results presented here are generated, the reader is referred to the manual. Finally, some concluding remarks will be given.

4.2 Results

4.2.1 Functions in the MathemaTB package

We start by listing all functions available in the package. These are listed alphabetically in Table 4.1 and Table 4.2. Functions whose use is explicitly described in this paper contain a reference to the corresponding section. Information on functions whose use is not described here can be found in the manual. Most functions have optional arguments (which are passed to a function as `OptionalArgument → <value>`), and these are listed in the manual. For example, `MoleculePlot[R]` will produce a plot of the geometry `R` with default settings. `MoleculePlot[R, AtomSize → .5]` will produce a plot of the geometry `R`, but with the atoms drawn at 0.5 times their van der Waals radii (the default value is 0.3).

In addition to functions, MathemaTB also contains three associations, `Atoms`, `Lattices` and `TBParameters`. These store the information on different elements, lattices (bases and lattice vectors) and the tight-binding parameters. The data in the associations can be manipulated with the functions `SetAtom`, `DeleteAtom`, `SetLattice`, `DeleteLattice`, `SetParameter` and `DeleteParameter`. Furthermore, the package contains the pre-defined constants `Hartree`, `Avogadro` and `Bohr`, which give the numerical values of the Hartree energy in eV, the number of particles in one mole, and the Bohr radius in multiples of Å, respectively.

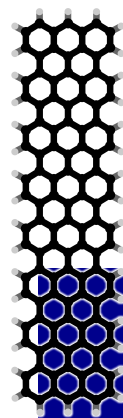


Table 4.1 List of functions (A-L) in the MathemaTB package. Optional arguments are listed in the MathemaTB manual.

function name	explanation	section
AdjustGeometry	Centers and aligns a geometry interactively	4.2.2
BuildHamiltonian	Constructs the Hamiltonian and overlap matrices	4.2.2
BuildLattice	Constructs a periodic geometry	4.2.4
BlockCombine	Constructs a block-diagonal matrix from blocks	4.2.3
BlockSeparate	Extracts the blocks from a block-diagonal matrix	4.2.3
ChangeBasis	Brings the Hamiltonian into a different basis	4.2.3
ChargesFrom-KPointSampling	Calculates the Mulliken charges for a periodic structure	4.2.4
CleanGeometry	Centers and aligns a geometry	4.2.2
CopyGeometry	Copies a geometry	4.2.4
CropGeometry	Crops a geometry	4.2.4
DeleteAtom	Deletes an atom	
DeleteLattice	Deletes a lattice	
DeleteParameter	Deletes tight-binding parameters	
DensityMatrix	Calculates the density matrix	4.2.2
DensityOfStates	Calculates the density of states	4.2.2
Diagonalize	Diagonalizes the Hamiltonian	4.2.2
Differential-ConductanceMaps	Simulates STM differential conductance maps	4.2.3
Dispersion	Calculates the electronic dispersion	
DispersionPlot	Visualizes the electronic dispersion	4.2.5
Dispersion2D	Calculates the electronic dispersion	
Dispersion2DPlot	Visualizes the electronic dispersion	4.2.4
DOSFromEnergyList	Calculates the density of states	4.2.2
DOSFrom-KPointSampling	Calculates the density of states for a periodic structure	4.2.4
DOSFromSelfEnergy	Calculates the density of states	4.2.3
FileSelector	Selects a file	
FindPlaneVector	Finds the plane vector for a geometry	
FindSALCs	Calculates symmetry-adapted linear combinations	
IsoSurfacePlot	Makes an isosurface plot	4.2.2
LevelsPlot	Generates an energy level diagram	4.2.2
LowdinTransform	Carries out the Löwdin orthogonalization	4.2.2
LowdinBackTransform	Carries out the Löwdin backtransformation	4.2.2

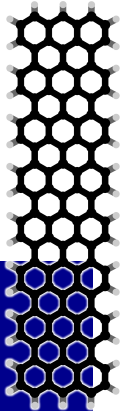


Table 4.2 List of functions (M-Z) in the MathemaTB package. Optional arguments are listed in the MathemaTB manual.

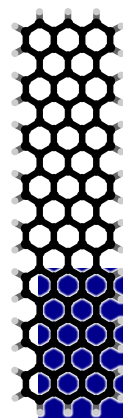
function name	explanation	section
<code>MoleculePlot</code>	Draws the molecule, lattice or structure	4.2.2
<code>MullikenCharges</code>	Calculates the Mulliken charges	4.2.2
<code>Maximize-AspectRatio</code>	Aligns the geometry along its long and short axes	
<code>OrbitalCompare</code>	Compares an orbital vector and matrix	
<code>OrbitalGenerate</code>	Makes an orbital plot	
<code>OrbitalPlot</code>	Makes an orbital plot	4.2.2
<code>Reciprocal-LatticeVectors</code>	Finds the reciprocal lattice vectors from a set of lattice vectors	4.2.4
<code>RotateTranslate</code>	Rotates and translates a geometry	
<code>SALCProjection-Matrix</code>	Calculates symmetry-adapted linear combinations and constructs a change-of-basis matrix	4.2.3
<code>SetAtom</code>	Sets an atom	
<code>SetLattice</code>	Sets a lattice	
<code>SetParameter</code>	Sets tight-binding parameters	4.2.2
<code>ToCoefficient-Vector</code>	Selects or extracts a coefficient vector from a (Hamiltonian) matrix	
<code>VoigtConvolve</code>	Convolve a spectrum with a Voigt profile	
<code>WaveFunction</code>	Calculates the wave function	4.2.3
<code>XYZImport</code>	Imports an xyz file	4.2.2
<code>XYZExport</code>	Exports an xyz file	4.2.2

4.2.2 Molecular tight-binding

The starting point for all types of calculations is molecular tight-binding: application of the tight-binding methodology to zero-dimensional structures.[8] These systems provide a sand box to explore the effects of different tight-binding parametrizations, inclusion of overlap, different basis functions and so forth. It is easy to carry out zero-dimensional tight-binding, or Hückel calculations with MathemaTB.

Molecular tight-binding is the first subject treated in the tutorial that is included in the manual. The ability to tinker with the molecular structure and the on-site-, coupling and heteroatom parameters lays a foundation for less trivial calculations later on, where different periodicities are invoked and aspects like symmetry and self-energies are explored. This section treats basic functionalities not only with regard to the calculations themselves, but also those aimed at setting up, visualizing and manipulating the molecular geometry in the first place.

The first step in most tight-binding calculations is to set up the geometry. `XYZImport` can be used to import a geometry from an xyz file. For example, an xyz file of the molecule anthracene (provided with the package), is loaded as follows



```
In[1]:= R = AdjustGeometry[
        XYZImport["skewedanthracene.xyz"]["Geometry"]]
        XYZExport[R]
```

`AdjustGeometry` opens a window that allows the user to planarize and straighten the geometry. `XYZExport` allows the geometry to be exported. The molecule is readily visualized with `MoleculePlot`.

A different approach, which is particularly useful when treating periodic geometries, is to evaluate `BuildLattice`. This function also provides lattice vectors and reciprocal lattice vectors that are essential for periodic calculations. `CopyGeometry`, `CropGeometry` and `RotateTranslate` are functions that allow the geometry to be manipulated as desired. Planarizing and straightening of the geometry can be achieved by the functions `CleanGeometry` and `AdjustGeometry`, the latter being an interactive variant of `CleanGeometry`.

The second step in the calculation is to set up the molecular Hamiltonian matrix. Here, the diagonal entries reflect the on-site energies of the different sites (orbitals localized on the individual atoms), whereas the off-diagonal elements are the interaction-, transfer- or hopping parameters. The on-site energies for different atoms, and hopping and overlap parameters for pairs of atoms can be set by `SetParameter`. The parameters thus defined (on-site energy "e", hopping terms "t", overlap terms "s" and site occupation terms "n") are stored globally in `TBParameters` and used when `BuildHamiltonian` is evaluated. `BuildHamiltonian` assigns the nearest neighbor hopping term "t" to the Hamiltonian matrix elements corresponding to nearest neighbors (pairs of sites whose distance d is smaller than the value of the optional argument `MaxNNDistance`). The next-nearest neighbor term "t2" is assigned to next nearest-neighbors (`MaxNNDistance < d < MaxNNNDistance`) and "t3" to second-next nearest neighbors (`MaxNNNDistance < d < MaxNNNNDistance`), if defined. Similarly, "s", "s2" and "s3" are assigned to the corresponding elements of the overlap matrix. The correct values are not only based on the inter-site distances, but also on the nature of the atoms - again, they can be set as desired through `SetParameter`.

A rather unusual feature of `MathematicaTB` is that the program allows the Hamiltonian and overlap matrices to contain symbolic quantities, such as strings or symbols. This enables the subsequent diagonalization to be carried out analytically, if so desired. Another added advantage is that these symbolic quantities can later on be substituted for numerical ones by means of a replacement rule. This enables the user, for example, to work with (partly) symbolic matrices and provide a range of substitutional values inside a `Do` or `Table` environment, so that the effect of different parametrizations can be investigated.

The following example shows how first a symbolic Hamiltonian matrix is

given for the anthracene molecule, and subsequently a numerical matrix is defined.

```
In[2]:= Clear[e, t, t2, t3, s, s2, s3];
SetParameter[6 → <|"e" → e, "t" → t, "t2" → t2,
  "t3" → t3, "s" → s, "s2" → s2, "s3" → s3|>]
{H, S} = BuildHamiltonian[R] // Values;
H // MatrixForm
```

Out[5]//MatrixForm=

$$\begin{pmatrix} e & t & t2 & 0 & \dots \\ t & e & t & t2 & \dots \\ t2 & t & e & t & \dots \\ 0 & t2 & t & e & \dots \\ \vdots & \vdots & \vdots & \vdots & \ddots \end{pmatrix}$$

```
In[7]:= SetParameter[6 → <|"e" → -4., "t" → -2.8,
  "t2" → -0.2, "s" → 0.1|>]
{H, S} = BuildHamiltonian[R] // Values;
H // MatrixForm
```

Out[9]//MatrixForm=

$$\begin{pmatrix} -4. & -2.8 & -0.2 & 0 & \dots \\ -2.8 & -4. & -2.8 & -0.2 & \dots \\ -0.2 & -2.8 & -4. & -2.8 & \dots \\ 0 & -0.2 & -2.8 & -4. & \dots \\ \vdots & \vdots & \vdots & \vdots & \ddots \end{pmatrix}$$

Note that *Mathematica* functions like `MatrixForm` and `MatrixPlot` are useful to inspect Hamiltonian, overlap or coefficient matrices.

The third step is the diagonalization of the Hamiltonian matrix. This is performed using `Diagonalize`. `Diagonalize` returns a list, the first element of which is the list of (sorted) eigenenergies and the second element of which is the coefficient matrix. For numerical Hamiltonians, the procedure is usually very quick. Analytical diagonalization may be possible in some cases, but generally requires a significant computational effort. Diagonalization in the presence of overlap is also supported. To this end, the Hamiltonian is first transformed to a Löwdin-orthogonalized basis using `LowdinTransform`. The resulting coefficients in the Löwdin basis are transformed to the site-localized basis using `LowdinBackTransform`. A typical procedure to include overlap in tight-binding calculations is as follows.

```
In[10]:= {Sqrt, Sinvsqrt, Hortho} = LowdinTransform[S,
  ApplyToMatrix → H] // Values;
{en, Co} = Diagonalize[Hortho];
Co = LowdinBackTransform[Co, Sinvsqrt];
```



chapter 4

where `Ssqrt`, `Sinvsqrt` and `Hortho` refer to the square root overlap matrix, its inverse and the orthogonalized Hamiltonian matrix, respectively.

Remarkably, in the case of the symbolic anthracene Hamiltonian above, it can be shown that, for vanishing next-nearest and second-next nearest neighbor interactions, diagonalization can be performed analytically. This is shown below, where "t2" and "t3" are "switched off" *a posteriori* by means of a replacement rule.

```
In[11]:= Hnn = H /. {t2 -> 0, t3 -> 0};
energies = Diagonalize[Hnn][[1]];
Row[energies, Spacer[10]]
```

```
Out[11]= e - 2 t, e - t, e - t, e + t, e + t, e + 2 t, ...
```

Analytical diagonalization can also be achieved in some other simple cases. For example, the final section of the tutorial shows how the analytical form of the band structure of graphene

$$E_+(\mathbf{k}) = t \frac{|f|}{1 + s|f|}$$

$$E_-(\mathbf{k}) = -t \frac{|f|}{1 - s|f|}$$

with

$$f = 1 + e^{i\mathbf{k}\cdot\mathbf{a}_1} + e^{-i\mathbf{k}\cdot\mathbf{a}_2}$$

and with wave functions described by the (unnormalized) expansion vectors

$$\mathbf{c}_+ = \left(\sqrt{f/f^*}, 1 \right) = \left(e^{2i\text{Arg}(f)}, 1 \right)$$

$$\mathbf{c}_- = \left(-\sqrt{f/f^*}, 1 \right) = \left(-e^{2i\text{Arg}(f)}, 1 \right)$$

can be achieved simply by using `BuildHamiltonian` and `Diagonalize`. [9, 10, 11, 12] The only requirement is to use symbolic values rather than numerical quantities for the hopping parameter "t" and overlap parameter "s" in `SetParameter`.

The final step in a tight-binding calculation is to analyze or visualize the results. Fig. 4.1a shows the result for a Hückel calculation on anthracene. Here, the energy levels are plotted in a diagram using `LevelsPlot`, and the density of states is obtained by Lorentzian-broadening all energy levels through `DensityOfStates` (or equivalently in this case: `DOSFromEnergyList`).

```
In[12]:= {en, Co} = Diagonalize[Hortho];
enocc = Select[en, # < TParameters[6, "e"]&];
enunocc = Select[en, # > TParameters[6, "e"]&];
Co = LowdinBackTransform[Co, Sinvsqrt];
```

```

LevelsPlot[enocc, enunocc]

dosoptions = Sequence[Points → 1000, FWHM → .2,
  EnergyRange → {-11, 4}, CutOff → 1.6];
DOSocc = DensityOfStates[enocc, dosoptions];
DOSunocc = DensityOfStates[enunocc, dosoptions];
ListPlot[{DOSocc, DOSunocc}]

```

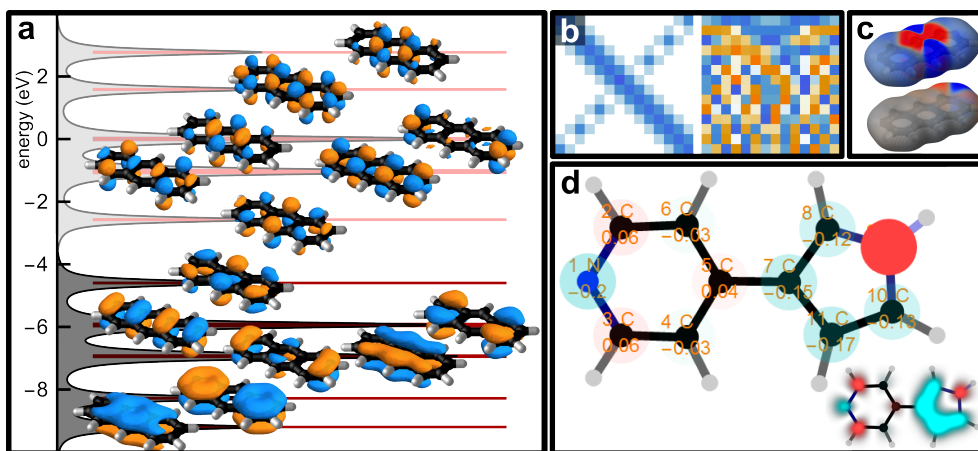


Fig. 4.1 Molecular tight-binding. a) Energy level diagram with density of states of anthracene (darker gray: occupied states; lighter gray: virtual states). The molecular orbitals of anthracene are shown on top of their corresponding energy levels. b) Visualization of the molecular Hamiltonian matrix (left) and expansion coefficient matrix (right) for azaanthracene. c) Isosurface plot of the (Mulliken) charge distribution of anthracene (top) and azaanthracene (bottom). d) Electron density visualization of pyridylpyrrole. The large image has the Mulliken charges added as labels to the atoms. The bottom right shows a molecular-orbital style visualization of the charge distribution.

The insets of Fig. 4.1a show some molecular orbitals as plotted by the function `OrbitalPlot`. The input of `OrbitalPlot` is a wave function expansion coefficient vector which is a row of the coefficient matrix (visualized on the right side of Fig. 4.1b through `MatrixPlot`) that is obtained by diagonalization of the Hamiltonian matrix (visualized on the left side of Fig. 4.1b). Orbitals can be drawn in two dimensions (at a height above the xy -plane given by the argument `ZValue`), or in three dimensions (for 'all' z -values, by setting `ZValue` → "All").

```

In[13]:= Table[OrbitalPlot[R, Co[[orb]], ZValue → "All"],
  {orb, Length[Co]}]

```

Orbital plots can be tailored or stylized with optional arguments such as `GridPoints`, `Transparency`, *etc.* to create the desired appearance. The reader is referred to the manual for all options available for all functions.

The coefficient matrices can be translated into electron populations on the different sites. To this end, the functions `DensityMatrix` and `MullikenCharges` have been implemented. Fig. 4.1c shows a rendering of the charge distribution thus obtained on anthracene and azaanthracene - latter molecule featuring a nitrogen atom on the place of a CH group. The following code generates the charge distribution and visualizes the result with the function `IsoSurfacePlot`.

```
In[14]:= Dens = DensityMatrix[R, en, Co,
          InverseSquareRootOverlapMatrix → Sinvsqrt];
mull = MullikenCharges[R, Dens];
IsoSurfacePlot[R, mull, Transparency → .1]
```

It can clearly be seen in the resulting plots (Fig. 4.1c) that the electron density is largest on the center sites of the anthracene (blue). This results in a relatively large nucleophilic reactivity of the respective atoms, an observation that can also be rephrased in the language of Clar aromaticity.[13] The nitrogen-substituted molecule has a high electron density on the pyridinic nitrogen atom, whereas the ortho positions of the pyridinic nitrogen are positive (red).

Another result of a calculation where the charge distribution was calculated through `DensityMatrix` and `MullikenCharges` is shown in Fig. 4.1d, where pyridylpyrrole is investigated. In contrast with the pyridinic nitrogen, the pyrrolic nitrogen is electron donating.[14]

4.2.3 Symmetry and coupling

MathemaTB offers functions for calculations involving symmetry and coupling. Although the implementation of symmetry is elementary, with only point group D_{2h} being supported, the spirit of its inclusion is mostly to provide some rudiments that could become a starting point for future developments. Its presence allows the user to explore some key concepts in the realm of basis changes.

D_{2h} is a point group that features three perpendicular symmetry planes, each of them containing a rotation axis and all crossing through an inversion point. Tetraazaperylene is a molecule that satisfies these symmetries, and it is shown together with the symmetry elements in Fig. 4.2a.

First, to detect symmetry, MathemaTB contains the functions `FindSALCs` and `SALCProjectionMatrix`. Latter returns a matrix that allows the Hamiltonian to be transformed to a symmetry-adapted basis by means of a similarity transformation through `ChangeBasis`.

```
In[15]:= {P, irreps} = SALCProjectionMatrix[R] // Values;
         irreps
         Hsym = ChangeBasis[H, P];
         Ssym = ChangeBasis[S, P];
```

```
Out[16]= <|B1u → 6, B2g → 6, B3g → 4, Au → 4|>
```

In the new basis, the different rows/columns of the Hamiltonian now refer to symmetry-adapted linear combinations of site-localized functions (SALCs). The SALCs belonging to different irreducible representations are mutually orthogonal, which translates into a block-diagonal shape of the Hamiltonian matrix. This is shown in Fig. 4.2b, where a visual representation of the Hamiltonian \mathbf{H} and the block-diagonalized Hamiltonian \mathbf{H}_{sym} are shown. Changing to a symmetry-adapted basis is also possible in the case of a non-orthogonal basis. Here, the Löwdin transformation is used in conjunction with `ChangeBasis`.

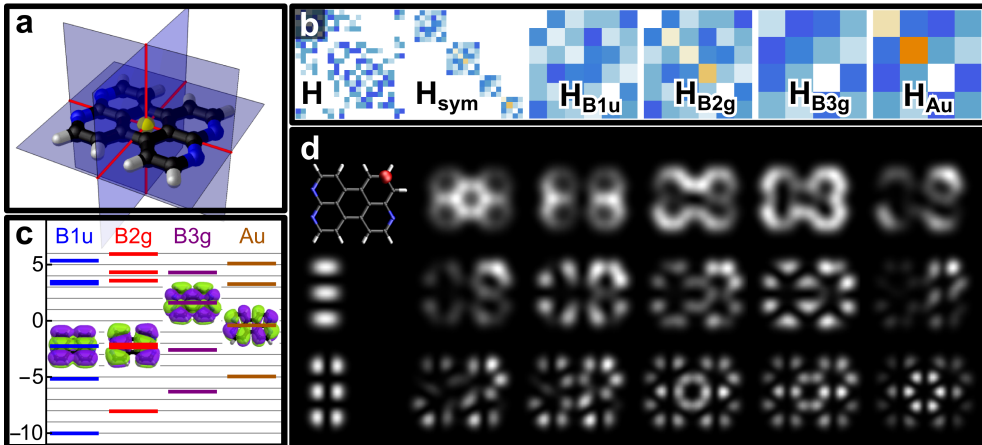


Fig. 4.2 Symmetry and coupling in MathemaTB. a) Tetraazaperylene, with its symmetry elements (blue: mirror planes, red: rotation axes and yellow: inversion center) indicated. b) Visualization of the block-diagonalization of the tetraazaperylene Hamiltonian matrix and subsequent separation of the subhamiltonians. c) Energy level diagram of tetraazaperylene, where the energies are sorted according to irreducible representation (irrep) in the D_{2h} point group. d) Simulated density of states arising from coupling a self-energy to a specific atom in triazaperylene. The top left image shows the molecule, where the position at which the molecule is coupled to a reservoir is indicated in red.

```
In[17]:= {Ssqrt, Sinvsqrt, Hortho} = LowdinTransform[S,
         ApplyToMatrix → H] // Values;
         {Sqrtsym, Sinvsqrtsym, Horthosym} = LowdinTransform[Ssym,
         ApplyToMatrix → Hsym] // Values;

         {en, SsqrtCo} = Diagonalize[Hortho];
         {ensym, SsqrtCosym} = Diagonalize[Horthosym];
```

```

Co = LowdinBackTransform[SqrtCo, Sinvsqrt];
Cosym = LowdinBackTransform[SqrtCosym, Sinvsqrtsym];
Co2 = Cosym.P

```

The coefficient matrices `Co` and `Co2` can now be compared, and it can be verified that they are equivalent. The following equations show why this combined change-of-basis and Löwdin orthogonalization procedure works.

$$\mathbf{HC} = \mathbf{SCE}$$

$$\begin{aligned}
[\mathbf{P}^{-1}\mathbf{HP}] [\mathbf{P}^{-1}\mathbf{C}] &= [\mathbf{P}^{-1}\mathbf{SP}] [\mathbf{P}^{-1}\mathbf{C}] \mathbf{E} \\
[\mathbf{H}_{\text{new}}] [\mathbf{C}_{\text{new}}] &= [\mathbf{S}_{\text{new}}] [\mathbf{C}_{\text{new}}] \mathbf{E} \\
\left(\mathbf{S}_{\text{new}}^{-1/2} [\mathbf{H}_{\text{new}}] \mathbf{S}_{\text{new}}^{-1/2}\right) \left(\mathbf{S}_{\text{new}}^{1/2} [\mathbf{C}_{\text{new}}]\right) &= \left(\mathbf{S}_{\text{new}}^{1/2} [\mathbf{C}_{\text{new}}]\right) \mathbf{E} \\
(\mathbf{H}'_{\text{new}}) (\mathbf{C}'_{\text{new}}) &= (\mathbf{C}'_{\text{new}}) \mathbf{E}
\end{aligned}$$

Here, the second line signifies the change of basis of the Hamiltonian through the matrix `P`, and the fourth line shows the Löwdin transformation.

The function `BlockSeparate` exploits the block-diagonal shape of a Hamiltonian to decouple the tight-binding calculations of the different irreducible representations (irreps) of the point group. A visualization of the block separation of a symmetrized Hamiltonian is shown in Fig. 4.2b. The subhamiltonians can be diagonalized individually, and the coefficient matrix can be reconstructed by merging the coefficient matrices together with `BlockCombine`.

```

In[18]:= {HB1u, HB2g, HB3g, HAu} = BlockSeparate[Hsym];

{{enB1u, CoB1u}, {enB2g, CoB2g}, {enB3g, CoB3g},
 {enAu, CoAu}} = Diagonalize /@ %;
en = Flatten[{enB1u, enB2g, enB3g, enAu}];

Cosym = BlockCombine[{CoB1u, CoB2g, CoB3g, CoAu}];
Co = Cosym.P;

```

The different eigenenergy lists corresponding to the individual irreps for tetraazaperylene are visualized using `LevelsPlot` in Fig. 4.2c.

The fact that the Hamiltonian rows/columns after the change of basis refer to the energies of, and interactions between SALCs means that, whenever functions with projections are used (for example the calculation of the local density of states), the projections onto the SALCs are obtained rather than onto the individual sites. This feature is exploited in the manual in calculations with triazaperylene, where the broken symmetry in comparison to tetraazaperylene does not disallow the user to project the density of states in the different irreducible representations of the D_{2h} point group.

Finally, the subject of coupling is investigated. The manual presents a calculation of a molecule on a metal slab. Rather than including the substrate explicitly, the net effect of coupling can more efficiently be induced in the subspace of the molecular Hamiltonian by using the self-energy method. Mapping of reservoir coupling onto the molecular Hamiltonian is achieved as follows:[15] The Green's function matrix of the coupled system described by the block Hamiltonian

$$\mathbf{H} = \begin{pmatrix} \mathbf{H}_{\text{res}} & \mathbf{H}_{\text{coupling}} \\ \mathbf{H}_{\text{coupling}}^\dagger & \mathbf{H}_{\text{mol}} \end{pmatrix}$$

can be written as

$$\begin{aligned} \mathbf{G}(E) &= (EI - \mathbf{H})^{-1} = \begin{pmatrix} EI - \mathbf{H}_{\text{res}} & -\mathbf{H}_{\text{coupling}} \\ -\mathbf{H}_{\text{coupling}}^\dagger & EI - \mathbf{H}_{\text{mol}} \end{pmatrix}^{-1} \\ &= \begin{pmatrix} \mathbf{G}_{0,\text{res}}^{-1} & -\mathbf{H}_{\text{coupling}} \\ -\mathbf{H}_{\text{coupling}}^\dagger & \mathbf{G}_{0,\text{mol}}^{-1} \end{pmatrix}^{-1} = \begin{pmatrix} \mathbf{G}_{\text{res}} & \mathbf{G}_{\text{coupling}} \\ \mathbf{G}_{\text{coupling}}^\dagger & \mathbf{G}_{\text{mol}} \end{pmatrix} \end{aligned}$$

where $\mathbf{G}_{0,\text{res}} = (EI - \mathbf{H}_{\text{res}})^{-1}$ and $\mathbf{G}_{0,\text{mol}} = (EI - \mathbf{H}_{\text{mol}})^{-1}$ are the Green's function matrices of the isolated reservoir and the isolated molecule, respectively. Explicit inversion of the block diagonal matrix gives

$$\mathbf{G}_{\text{mol}} = (\mathbf{G}_{0,\text{mol}}^{-1} - \mathbf{H}_{\text{coupling}} \mathbf{G}_{0,\text{res}} \mathbf{H}_{\text{coupling}}^\dagger)^{-1} = (EI - \mathbf{H}_{\text{mol}} - \Sigma)^{-1}$$

where $\Sigma = \mathbf{H}_{\text{coupling}} \mathbf{G}_{0,\text{res}} \mathbf{H}_{\text{coupling}}^\dagger$. This means that - provided it is possible to find an appropriate expression of the self-energy matrix Σ - the effective Hamiltonian of the molecule can be found as $\mathbf{H}_{\text{mol}} = \mathbf{H}_{0,\text{mol}} + \Sigma$. The self-energy matrix makes the Hamiltonian non-Hermitian.

When a non-Hermitian Hamiltonian is diagonalized, the complex eigenenergies $\tilde{\epsilon}_m = \epsilon_m + i\gamma_m$ thus obtained contain information on the energetic positions (real parts) as well as Lorentzian energy broadenings (imaginary parts). Application of `DensityOfStates` on a complex energy list or complex Hamiltonian automatically takes this into account, and calculates the density of states from the spectral function that is the imaginary part of the diagonal molecular Green's function matrix.[15, 16] This works as follows:

$$\begin{aligned} \Im(\mathbf{G}_{\text{mn}}(E)) &= \Im\left(\frac{\delta_{mn}}{E - (\epsilon_m + i\gamma_m)}\right) = -\frac{\gamma_m}{(E - \epsilon_m)^2 + \gamma_m^2} \\ \Rightarrow \text{DOS}(E) &= -\frac{1}{\pi} \text{Tr} \Im(\mathbf{G}(E)) \end{aligned}$$

In case a complex Hamiltonian, or an explicit self-energy matrix is supplied, `DensityOfStates` works through the function `DOSFromSelfEnergy`, which can be used equivalently.



Another function that takes complex eigenenergies into account is `DifferentialConductanceMaps`, which basically combines orbitals as obtained through `WaveFunction` to simulate scans that can be measured experimentally using scanning tunneling microscopy.[17, 18, 19, 20] Fig. 4.2d shows simulated differential conductance maps on triazaperylene, where a coupling to a reservoir was described through a self-energy. The maps can be generated using the following code.

```
In[19]:= orbitals = Table[
  psi = WaveFunction[R, Co[[orb]]];
  density = Abs[psi]^2;
  {en[[orb]], density},
  {orb, Length[Co]}
] // Transpose
DifferentialConductanceMaps[orbitals[[1]], orbitals[[2]],
  EnergyRange → {-8, 8}, EnergySpacing → 1]
```

4.2.4 Tight-binding in two dimensions

MathemaTB offers functionalities to perform tight-binding calculations in any number of dimensions. This section highlights some results that can be obtained in two dimensions. The corresponding section in the tutorial treats the Kagome-honeycomb lattice, a two-dimensional lattice that is of interest due to the presence of Dirac cones and flat bands in its electronic structure, and which lies at the basis of recent efforts with regard to two-dimensional metal-organic frameworks.[21, 22, 23, 24, 25, 26, 27]

An important function that allows the user to set up periodic geometries is `BuildLattice`. This function extracts the requested lattice information as stored in `Lattices`, maps specific atoms onto the positions of the basis and sets the lattice size. The reciprocal lattice vectors are also returned, but can equivalently be computed by providing the lattice vectors to the function `ReciprocalLatticeVectors`. Mapping red and yellow atoms onto the honeycomb- and Kagome sublattice sites results in the structure shown in Fig. 4.3a, where it is visualized by `MoleculePlot`. The lattice is built as

```
In[1]:= {R, latticevectors, kvectors} = BuildLattice["KagomeHoneycomb",
  AtomValues → {16, 16, 16, 8, 8}, Size → 1.4] // Values;
lattice = CropGeometry[
  CopyGeometry[R,
    LatticeVectors → latticevectors, Copies → {10, 10}
  ], {{-9, 9}, {-10, 10}}
];

MoleculePlot[lattice, Quality → 50, BondSize → .3]
```

The periodicity of a system is reflected in the form of the Hamiltonian. Passing a periodic structure to `BuildHamiltonian` - that is, a geometry to-

gether with its lattice vectors - returns a Hamiltonian matrix containing elements (phase factors) that are a function of the wave vector \mathbf{k} of the electron in the lattice. Therefore, for each value of the wave vector \mathbf{k} the Hamiltonian will be different, giving rise to wave vector-dependent energies (dispersion) and expansion coefficients. The Hamiltonian can be diagonalized at specific points in reciprocal space, but can also be diagonalized along a continuous path through reciprocal space, returning the electronic dispersion along this path. This is achieved using the functions `Dispersion` and `DispersionPlot`. Diagonalization over a plane in k -space results in a two-dimensional dispersion, which can be calculated with `Dispersion2D` and `Dispersion2DPlot`. The following shows an example of `Dispersion2DPlot`, where the dispersion is projected onto the honeycomb and Kagome sublattice sites using the optional argument `Projections`.

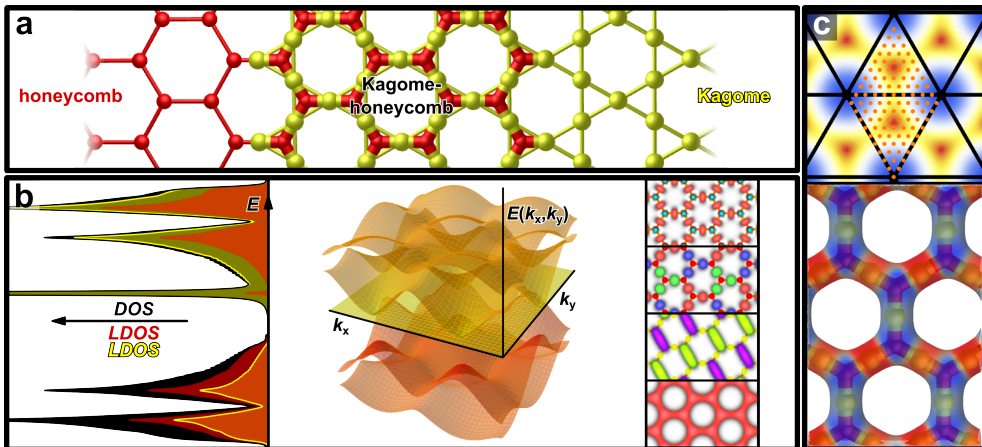


Fig. 4.3 Two-dimensional tight-binding calculations. a) Visualization of the Kagome-honeycomb lattice, with the honeycomb sublattice indicated by the red sites and the Kagome sublattice indicated by the yellow sites. The thick bonds indicate nearest-neighbor couplings, and the thin bonds indicate next-nearest neighbor couplings. b) Electronic structure of the Kagome-honeycomb lattice, with sublattice on-site energy asymmetry. The left subpanel shows the (local) density of states projected onto the Kagome (yellow) and honeycomb (red) sublattice sites, whereas the black area indicates the total density of states. The middle subpanel shows a three-dimensional plot of the band structure $(k_x, k_y, E(k_x, k_y))$. The projection onto the Kagome (honeycomb) sites is indicated by the yellow (red) color of the bands. The right subpanel shows a few crystal orbitals plotted at the high-symmetry points of the Brillouin zone. c) Top subpanel: a density plot rendering of one of the dispersive Kagome-honeycomb bands, with the reciprocal lattice and a k -point grid superimposed. This grid is used to sample the charge distribution, which is plotted on an isosurface in the bottom subpanel. Here, the on-site energies of the different Kagome sites were shifted to break symmetry.

```
In[2]:= kvectors = ReciprocalLatticeVectors[latticevectors];
```

```

BZ = k vectors / 2;
kpath = {"Γ", BZ[[1]], 2 BZ[[1]] / 3 + 2 BZ[[2]] / 3,
        - 2 BZ[[1]] / 3 + 4 BZ[[2]] / 3, "Γ"} /. "Γ" → {0, 0, 0};
kplane = Norm[kvectors[[1]]] {{-1, -1, 0},
        {-1, 1, 0}, {1, -1, 0}};

SetParameter[8 → <|"e" → -1., "t2" → -0.2, "s" → 0.2,
        16 → <|"t" → -1, "s" → 0.2|>|>]
SetParameter[16 → <|"e" → 0, "t2" → -0.2, "s" → 0.2|>]

{H, S} = BuildHamiltonian[R, LatticeVectors → latticevectors,
        MaxNNNDistance → 3] // Values;

Dispersion2DPlot[H, OverlapMatrix → S, KPoints → {40, 40},
        LatticeVectors → latticevectors[ ; 2]], KPlane → kplane,
        Projections → {{1, 2, 3} → Yellow, {4, 5} → Red}
] ["ProjectedPlot"]

```

The resulting band structure - color-coded to show the degree of localization of the wave functions on the Kagome (yellow) and honeycomb (red) sublattice sites - is shown in Fig. 4.3b.

Diagonalizing the Hamiltonian over an entire wedge of the entire reciprocal space (k -point sampling) is necessary for calculations of the density of states through `DOSFromKPointSampling` and of the charge distribution through `ChargesFromKPointSampling`. The following shows a calculation of the local density of states on the Kagome and honeycomb sublattices, by using `DensityOfStates` (which, upon detecting a periodic Hamiltonian, reverts to `DOSFromKPointSampling`).

```

In[3]:= dosoptions = Sequence[EnergyRange → {-2.6, 2.6},
        KPoints → {60, 60, 1}, Points → 1600,
        LatticeVectors → latticevectors, OverlapMatrix → S];

DOS = DensityOfStates[H, dosoptions];
LDOSKagome = DensityOfStates[H, dosoptions,
        Projections → {1, 2, 3}];
LDOShoneycomb = DensityOfStates[H, dosoptions,
        Projections → {4, 5}];

```

The respective (local) densities of states can be visualized with `ListPlot`, as shown in the left of Fig. 4.3b. An example of `ChargesFromKPointSampling` is shown in Fig. 4.3c, where the electron density is calculated through k -point sampling on the grid in reciprocal space as shown in the top subpanel, resulting in the charge distribution as shown in the periodic isosurface plot in the bottom subpanel. This is achieved with the following code.

```

In[4]:= mull = ChargesFromKPointSampling[R, H, OverlapMatrix → S,
        LatticeVectors → latticevectors,
        KPoints → {9, 9, 1}, FermiLevel → .262]

IsoSurfacePlot[R, mull, LatticeVectors → latticevectors,
        GridPoints → 40, Transparency → .4, ContourValue → .5]

```

As shown in the right subpanel of Fig. 4.3b, crystal orbitals can be plotted using `OrbitalPlot` for any desired band and any desired value of \mathbf{k} . Here, the hue of the orbital indicates the complex phase of the wave function. These plots were generated by passing the geometry `R`, and Hamiltonian `H` to `OrbitalPlot`, together with the appropriate values for the optional elements `LatticeVectors`, `OrbitalNumber` and `KVector`.

The Kagome-honeycomb lattice presented in the tutorial is particularly interesting, as a symbolic parametrization of the Hamiltonian matrix allows it to later be decomposed into the block-diagonal sublattice Hamiltonians and the block-antidiagonal nearest-neighbor Hamiltonians. Furthermore, along the lines of ref. [27], the energy dispersion is calculated by diagonalizing the square of the Hamiltonian (which also obtains a block-diagonal shape) and taking the square root of the energy dispersions. Procedures like these are highly unusual in comparison to the standard procedure of simply numerically diagonalizing the Hamiltonian. This underlines the flexibility of MathemaTB in matrix manipulations.

4.2.5 Tight-binding with more dimensions and more atoms

MathemaTB allows calculations to be performed in three dimensions. The corresponding section of the tutorial deals with graphite, a stacking of graphene layers. Fig. 4.4a shows the dispersion and density of states for AA-stacked graphite and ABC-stacked graphite, which are in agreement with literature results.[28, 29, 30] The dispersion is calculated through `DispersionPlot` along a path through reciprocal space. The Hamiltonian and overlap matrices `H` and `S` are obtained in the standard way, by building the geometry (`BuildLattice`), setting the parameters (`SetParameter`), and constructing the matrices (`BuildHamiltonian`). Now, the following code can be used to generate the dispersion and density of states.

```

In[5]:= BZ = kvectors / 2;
inplanesymmetrypoints = {"Γ" → {0, 0, 0},
        "K" → 2 BZ[[1]] / 3 + 2 BZ[[2]] / 3, "M" → BZ[[1]]};
outofplanesymmetrypoints = Table[
        Switch[point, 1, "A", 2, "H", 3, "L"] →
        inplanesymmetrypoints[[point, 2]] + BZ[[3]],
        {point, 3}
];
highsymmetrypoints = Join[inplanesymmetrypoints,

```



```

outofplanesymmetrypoints];
kpath = {"K", "Γ", "M", "K", "H", "L", "A", "H"}
/. highsymmetrypoints

DispersionPlot[H, OverlapMatrix → S, KPath → kpath,
  LatticeVectors → latticevectors, KPoints → 20] ["Plot"]
DensityOfStates[H, OverlapMatrix → S, Points → 400
  LatticeVectors → latticevectors, KPoints →
  {50, 50, Floor[50 Norm[kvectors[[3]]] / Norm[kvectors[[1]]]}],
  EnergyRange → {-2, 2}, ] // ListPlot

```

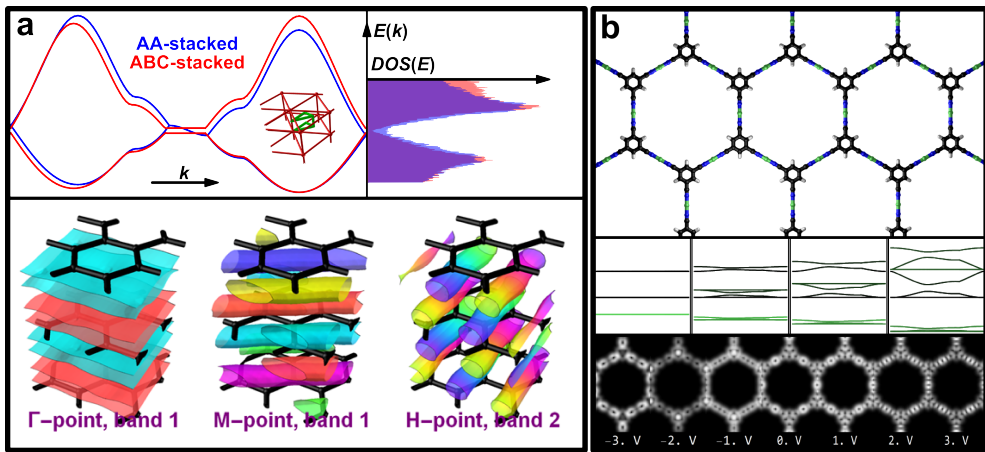


Fig. 4.4 tight-binding calculations on systems with more dimensions and more atoms. a) Results from tight-binding calculations on (three-dimensional) graphite. The blue energy dispersion corresponds to AA-stacked graphite, whereas red bands show the result for ABC-stacked graphite. The insets shows the reciprocal lattice of AA-stacked graphite, with the path along which the dispersion is drawn in green. The density of states for ABC-stacked (red) and AA-stacked (blue) graphite are shown. The bottom subpanel shows crystal orbitals at the high-symmetry points of the Brillouin zone of ABC-stacked graphite. b) Results from tight-binding calculations on a metal-organic framework, which forms a Kagome-honeycomb lattice. The middle subpanel shows the band structure, where the green color indicates the projection onto the metal sites and the metal-ligand coupling is increased from left to right. The bottom subpanel shows simulated differential conductance maps with a p -wave tip.

In three dimensions, the user may again be interested in crystal orbitals. Three-dimensional rendering of crystal orbitals, with periodicity and color-coding of the complex phase, although computationally intensive, is within the possibilities of the MathemaTB package. The bottom subpanel of Fig. 4.4a displays three crystal orbitals of ABC-stacked graphite at the high symmetry points in the Brillouin zone. The following code generates the orbital plot with the required styling.

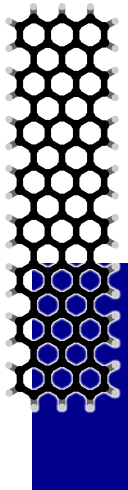
```

In[26]:=  $\delta\mathbf{k} = .0001 \{1, 1, 1\};$ 
         {kpoint, band} = {"K", 2};
         OrbitalPlot[R, H, KVector  $\rightarrow$  (kpoint /. highsymmetrypoints)
           +  $\delta\mathbf{k}$ , OverlapMatrix  $\rightarrow$  S, OrbitalNumber  $\rightarrow$  band, GridPoints
            $\rightarrow$  12, LatticeVectors  $\rightarrow$  latticevectors, Copies  $\rightarrow$  {3, 3, 3},
           ZValue  $\rightarrow$  "All", Basis  $\rightarrow$  "pz", Quality  $\rightarrow$  50,
           Transparency  $\rightarrow$  .3, BondSize  $\rightarrow$  .1, AtomSize  $\rightarrow$  .1,
           RenderLarger  $\rightarrow$  5, ContourValue  $\rightarrow$  .7]

```

Here, $\delta\mathbf{k}$ is used to slightly “nudge” the k -vector away from the high-symmetry points of the Brillouin zone, in order to avoid unwanted hybridization of wave functions that become degenerate at these points in reciprocal space. In this example, a large number of optional arguments are passed to `OrbitalPlot` to generate the plot in the correct styling. The functions of these argument is documented in the manual.

The manual also presents some calculations on a hypothetical molecular Kagome-honeycomb lattice, where the honeycomb sites contain tricyanobenzene molecules and the Kagome sites are decorated with nickel atoms. This is an example of a metal-organic framework. “Switching on” the dispersion is as simple as defining a symbolic nickel-nitrogen interaction integral in the Hamiltonian matrix and manipulating this value as desired. When switched on, the nickel-projected dispersion shows that the bands close in energy to the nickel become dispersive and attain a Kagome-honeycomb-like dispersion. This is shown in the middle subpanel of Fig. 4.4b, where from left to right the nickel-nitrogen hopping parameter is increased from 0 to t (where t is the hopping parameter for all other nearest-neighbor interactions). The bottom subpanel of Fig. 4.4b shows simulated differential conductance maps with a CO-passivated tip (using `DifferentialConductanceMaps` on a set of wave functions generated at different k -points through `WaveFunction`), that reveal the orbital shapes of these bands. The metal atoms are particularly visible at the maps simulated at 0 V and 1 V, close to the on-site energy of 1 eV that was chosen for the contributing metal orbital.



4.2.6 One-dimensional tight-binding

Finally, this last section highlights some results that can be obtained on one-dimensional structures. Here, results of tight-binding calculations on different types of graphene nanoribbons are shown, utilizing the periodic functions (with the optional argument `LatticeVectors`) as shown in the previous sections. In general, tight-binding methods are well applicable to graphene nanoribbons.[31, 32]

Graphene nanoribbons with zigzag edges are known to host edge-localized states.[33, 34] This can easily be verified with `MathemaTB` by calculating the dispersion and density of states. Fig. 4.5a shows a `DispersionPlot` calculation

chapter 4

on a 4-atom wide zigzag nanoribbon (4-zzGNR), where the edge atoms are colored red to distinguish them from the (black) bulk atoms. The colors of the band structure reflect the localization of the wave function on the edge (red) and bulk (black) sites. The density of states, as shown on the right and calculated with `DensityOfStates`, is projected onto the bulk sites (black curve) and red sites (red curve). This is achieved *via* the following code:

```
In[27]:= dosoptions = Sequence[OverlapMatrix → S,
    KPoints → {400, 1, 1},
    LatticeVectors → latticevectors, EnergyRange → {-7, 11}]

edgeDOS = DensityOfStates[H, dosoptions,
    Projections → {1, 8}];
bulkDOS = DensityOfStates[H, dosoptions,
    Projections → Range[2, 7]];
```

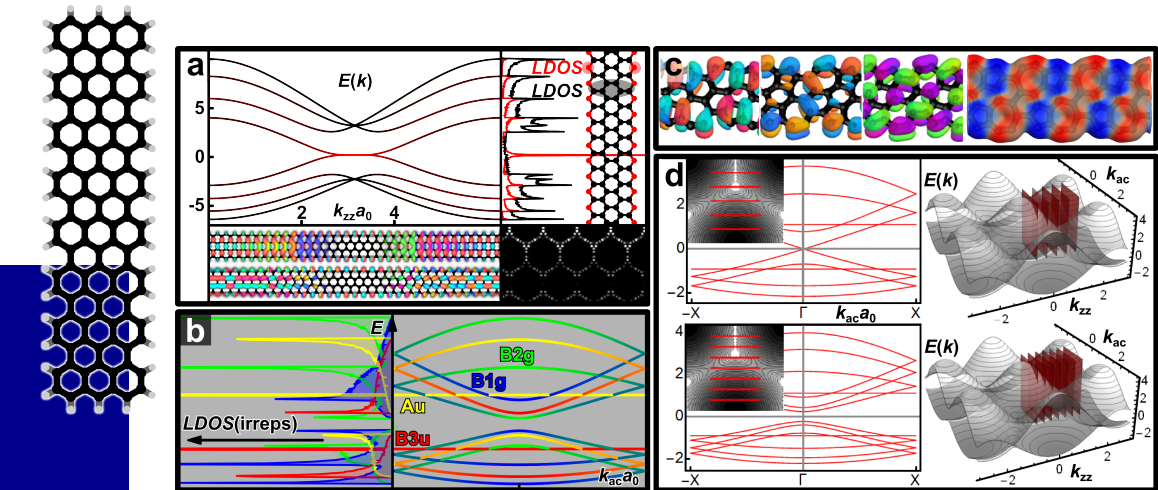


Fig. 4.5 One-dimensional tight-binding. a) Results from tight-binding calculations on zigzag-type nanoribbons. The upper left subpanel shows the $E(k)$ electronic dispersion, where the projection onto the bulk (edges) is indicated by a black (red) color. The corresponding zigzag graphene nanoribbon is shown in the top right subpanel, with bulk (edge) sites indicated in black (red). Here, also the local density of states on the bulk (black) and edge (red) sites is shown. The bottom left subpanel shows the crystal orbitals of the two middle bands plotted as a function of wavenumber k . The bottom right subpanel shows an edge-localized state that emerges in a zigzag-type nanoribbon constructed from the Kagome-honeycomb MOF introduced in the previous section. b) Irrep-projected electronic dispersion for a 7-atom wide armchair graphene nanoribbon. c) Crystal orbitals (HOCO) and charge distribution in a 5/7-Haeckelite graphene nanoribbon. Red areas are positive, whereas blue areas are negative. d) Energy dispersion diagrams for the 5-atom wide (top) and 7-atom wide (bottom) armchair graphene nanoribbon, as obtained by the zone folding approximation. The right images show the slicing of the graphene dispersion in 3 dimensions.

```
DispersionPlot[H, OverlapMatrix → S,
  KPath → {{0, 0, 0}, {2 Pi, 0, 0}}, KPoints → 120,
  Projections → {{1, 8} → Red}]["Plot"]
```

Here, atoms 1 and 8 of the geometry were previously verified to be the edge atoms. The bottom of Fig. 4.5a shows the crystal orbitals of the two bands closest to the Fermi level, with k ranging from 0 to $2\pi/a_0$, using the same scale as the dispersion plot above (where a_0 is the length of the lattice vector). This is achieved through the following.

```
In[28]:= Table[
  OrbitalPlot[R, H,
    OverlapMatrix → S, KVector → x kvector[[1]],
    LatticeVectors → latticevectors[[1]],
    OrbitalNumber → Length[H] / 2 + state
  ], {state, 1, 0, -1}, {x, 0, 1, .03}
] // ImageAssemble
```

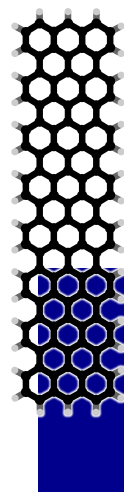
For values near $k = \pi/a_0$ the crystal orbitals are seen to diverge away from the bulk and localize on the edges exclusively. Interestingly, the emergence of edge-localized states is also observed in zigzag-type nanoribbons made by properly cropping the metal-organic framework of the previous section. This is evident from the wave function density image on the bottom right of Fig. 4.5a. This example shows how the local density of states, wave functions or crystal orbitals and the projected dispersion can all provide complementary information on the nature of the electronic structure (in this case the presence of edge states).

It is possible to project the density of states and the dispersion not only on sites, but also on other basis functions that are combinations of sites. In the case of the 7-atom wide armchair graphene nanoribbon, it is possible to utilize the D_{2h} symmetry of the unit cell *via* SALCProjectionMatrix and ChangeBasis to bring the Hamiltonian into a basis of symmetry-adapted wave functions. This allows the projection of dispersion and density of states onto the different irreducible representations (irreps) of the D_{2h} point group.

```
In[29]:= Hsym = ChangeBasis[H, P];
  Ssym = ChangeBasis[S, P];
  projectionlist = {Range[4] → Blue, Range[5, 8] → Green,
    Range[9, 11] → Red, Range[12, 14] → Yellow}
  DispersionPlot[Hsym, OverlapMatrix → Ssym,
    KPoints → 100, KPath → {{-Pi, 0, 0}, {Pi, 0, 0}},
    Projections → projectionlist]["Plot"];
```

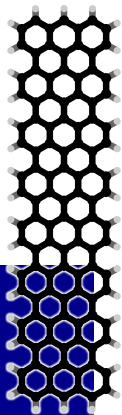
The SALC-projected dispersion (and projected density of states) is shown in Fig. 4.5b.

Another example of a one-dimensional system entails the hypothetical Haeckelite nanoribbon containing five-membered rings and seven-membered rings. This geometry is obtained by application of CopyGeometry and



CropGeometry on the graphene allotrope stored in Lattices as "57Graphene". The property of interest in this system is the charge distribution on the different sized rings. Fig. 4.5c shows the crystal orbitals of the highest occupied crystal orbital (HOCO) and lowest unoccupied crystal orbital (LUCO), as well as the HOCO-1. The rightmost plot is a periodic isosurface plot of the charge distribution of this 5/7-graphene nanoribbon. This plot was obtained in the same way as shown for the Kagome-honeycomb lattice, using ChargesFromKPointSampling and IsoSurfacePlot. As can readily be seen, the five-membered rings have an excess electron density (the blue color indicates a negative charge) whereas the seven-membered rings are partially positive. This is in line with what should be expected from Hückels rule: aromatic systems strive towards a number of electrons that equals $4n + 2$, with excess electrons (in this case, seven in one ring) resulting in the system donating electron density and an insufficient number of electrons (five in one ring) making the system electron accepting.[35, 36] Therefore, to increase the aromaticity of the system, electron density is relocated from the larger rings to the smaller rings.

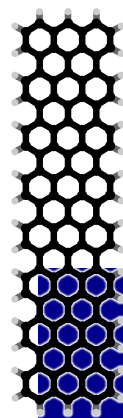
As a final example, the zone-folding approach for graphene nanoribbons is presented. This approach comprises the derivation of the $E(k_{ac})$ dispersion of armchair nanoribbons in terms of the two-dimensional graphene dispersion by "slicing" it at specific k_{zz} values of the perpendicular component of the momentum (in the zigzag direction). The k_{zz} values correspond to quantized standing waves of the graphene lattice in the confined direction of the nanoribbon.[37, 38, 39, 40, 41, 42] This method works because of the fact that for every wave vector, a superposition of graphene wave functions can be found that casts nodal planes onto parallel rows of carbon atoms. This superposition wave function - plane in the periodic direction but quantized in the lateral direction - satisfies the criteria of being an acceptable basis state for a graphene nanoribbon in the nearest neighbor tight-binding model. Fig. 4.5d shows examples of this zone-folding approach applied to the graphene dispersion (obtained previously through Diagonalize as the function $\text{energy}[k_x, k_y]$). The left images show the dispersion thus calculated for the 5-atom wide armchair graphene nanoribbon (top) and 7-atom wide armchair nanoribbon (bottom). The right images show a three-dimensional rendering of the dispersion plot of graphene, with planes intersecting the dispersion at the specified k_{zz} values. The insets in the dispersion show the same thing, but as lines on top of a density plot rendering of the dispersion. Here, it can readily be seen that, in the case of the 5-atom wide ribbon, the lines slice through the Dirac point, whereas in the 7-atom wide case the Dirac point is missed. This translates into a metallic dispersion for the narrow ribbon and semiconducting scenario for the wide ribbon. It can be verified that, in general, for armchair graphene nanoribbons that have a width of $(3n + 2)$ atoms, the Dirac cone enters the



one-dimensional band structure and quasimetallic behavior is obtained - a peculiar but well-established result.[37, 38, 38, 43] These results were created by defining a custom function (`ArmchairDispersionGenerator`) which takes as an argument the nanoribbon width, slices the graphene dispersion and returns the requested plots.

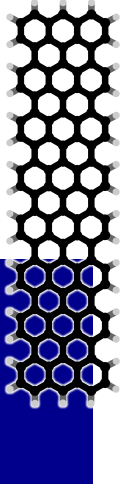
4.3 Conclusions

The MathemaTB package is a powerful yet easy tool to perform electronic structure calculations on the level of tight-binding theory on various types of systems. The sections above have highlighted some of the capabilities of the package. It is easy to manipulate matrices, wave functions, geometries and energy spectra in MathemaTB so as to achieve the desired calculation and desired presentation. Molecular or crystal orbitals, dispersion diagrams and densities of states can be produced with very little effort. Some unusual features of the package include the color-coding of orbitals to reflect the complex phase of the wave function, the projection and color-coding of band structures and densities of states to reflect the localization of the wave function on different sites, symmetries or basis functions, and the possibility to work with analytical or symbolic Hamiltonians. The MathemaTB package will prove to be a versatile tool for many different kinds of tight-binding calculations, on symmetric or antisymmetric systems, in the gas phase or coupled to reservoirs, and on systems with periodicities in zero, one, two or three dimensions.



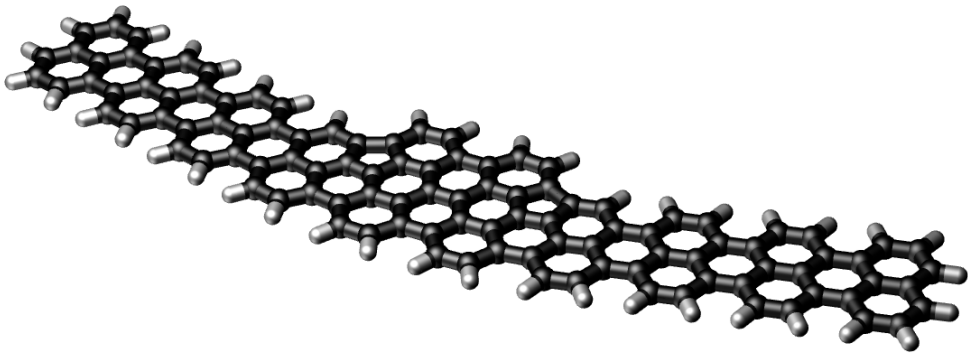
Bibliography

- [1] J. C. Slater and G. F. Koster, *Physical Review* **94**, pp. 1498–1524 (1954).
- [2] P. Löwdin, *The Journal of Chemical Physics* **18**, pp. 365–375 (1950).
- [3] C. M. Goringe, D. R. Bowler, and E. Hernández, *Reports on Progress in Physics* **60**, pp. 1447–1512 (1997).
- [4] S. Coh and D. Vanderbilt, “Python Tight Binding (PythTB)” (2010).
- [5] D. Moldovan, M. Anelković, and F. Peeters, “Pybinding v0.9.4: a Python package for tight-binding calculations” (2017).
- [6] C. W. G. Waintal, M. Wimmer, A. R. Akhmerov, and Xavier, *New Journal of Physics* **16**, pp. 63065 (2014).
- [7] Wolfram Research, “Mathematica, Version 11.3” (2018).
- [8] E. Hückel, *Zeitschrift für Physik* **72**, pp. 310–337 (1931).
- [9] P. R. Wallace, *Phys. Rev.* **71**, pp. 622–634 (1947).
- [10] J. C. Slonczewski and P. R. Weiss, *Physical Review* **109**, pp. 272–279 (1958).
- [11] S. Reich, J. Maultzsch, C. Thomsen, and P. Ordejón, *Physical Review B - Condensed Matter and Materials Physics* **66**, pp. 354121–354125 (2002).
- [12] M. I. Katsnelson, *Materials Today* **10**, pp. 20–27 (2007).
- [13] C. Glidewell and D. Lloyd, *Tetrahedron* **40**, pp. 4455–4472 (1984).

- 
- [14] G. W. Wheland and L. Pauling, *Journal of the American Chemical Society* **57**, pp. 2086–2095 (1935).
- [15] S. Datta, *Superlattices and Microstructures* **28**, pp. 253–278 (2000).
- [16] Y. Xue, S. Datta, and M. A. Ratner, *Chemical Physics* **281**, pp. 151–170 (2002).
- [17] J. Repp, G. Meyer, S. M. Stojković, A. Gourdon, and C. Joachim, *Physical Review Letters* **94**, pp. 26803 (2005).
- [18] I. Swart, L. Gross, and P. Liljeroth, *Chemical Communications* **47**, pp. 9011 (2011).
- [19] L. Gross, N. Moll, F. Mohn, A. Curioni, G. Meyer, F. Hanke, and M. Persson, *Physical Review Letters* **107**, pp. 086101 (2011).
- [20] G. Reecht, B. W. Heinrich, H. Bulou, F. Scheurer, L. Limot, and G. Schull, *New Journal of Physics* **19**, pp. 113033 (2017).
- [21] Z. Lan, N. Goldman, and P. Öhberg, *Physical Review B* **85**, pp. 155451 (2012).
- [22] Y. C. Chen, T. Cao, C. Chen, Z. Pedramrazi, D. Haberer, D. G. De Oteyza, F. R. Fischer, S. G. Louie, and M. F. Crommie, *Nature Nanotechnology* **10**, pp. 156–160 (2015).
- [23] O. J. Silveira, S. S. Alexandre, and H. Chacham, *Journal of Physical Chemistry C* **120**, pp. 19796–19803 (2016).
- [24] M. Maruyama and S. Okada, *Carbon* **125**, pp. 530–535 (2017).
- [25] O. J. S. Chacham and Helio, *Journal of Physics: Condensed Matter* **29**, pp. 09LT01 (2017).
- [26] M. W. Li, Z. Wang, J. Liu, W. Li, H. Fu, L. Sun, X. Liu, M. Pan, H. Weng, M. Dinc, L. Fu, and Ju, *2D Materials* **4**, pp. 15015 (2017).
- [27] C. B. Mallah, F. Ducastelle, and T, *Journal of Physics: Condensed Matter* **29**, pp. 465302 (2017).
- [28] R. R. Haering and M. S, *Progress in Semiconductors* **5**, pp. 273 (1960).
- [29] J. W. McClure, *IBM Journal of Research and Development* **8**, pp. 255–261 (1964).
- [30] C. W. Chiu, S. H. Lee, S. C. Chen, F. L. Shyu, and M. F. Lin, *New Journal of Physics* **12**, pp. 83060 (2010).
- [31] Y. Hancock, A. Uppstu, K. Saloriutta, A. Harju, and M. J. Puska, *Physical Review B - Condensed Matter and Materials Physics* **81**, pp. 245402 (2010).
- [32] M. Ijäs, M. Ervasti, A. Uppstu, P. Liljeroth, J. van der Lit, I. Swart, and A. Harju, *Physical Review B - Condensed Matter and Materials Physics* **88**, pp. 75429 (2013).
- [33] K. Nakada, M. Fujita, G. Dresselhaus, and M. S. Dresselhaus, *Physical Review B* **54**, pp. 17954–17961 (1996).
- [34] M. Fujita, K. Wakabayashi, K. Nakada, and K. Kusakabe, *Journal of the Physical Society of Japan* **65**, pp. 1920–1923 (1996).
- [35] J. Michl and E. W. Thulstrup, *Tetrahedron* **32**, pp. 205–209 (1976).
- [36] R. Mattohti and A. Kerim, *RSC Advances* **6**, pp. 108538–108544 (2016).
- [37] Y. W. Son, M. L. Cohen, and S. G. Louie, *Physical Review Letters* **97**, pp. 216803 (2006).
- [38] H. Zheng, Z. F. Wang, T. Luo, Q. W. Shi, and J. Chen, *Physical Review B - Condensed Matter and Materials Physics* **75**, pp. 165414 (2007).
- [39] H. Raza and E. C. Kan, *Physical Review B - Condensed Matter and Materials Physics* **77**, pp. 1–5 (2008).
- [40] K. Wakabayashi, Y. Takane, M. Yamamoto, and M. Sigrist, *New Journal of Physics* **11**, pp. 095016 (2009).
- [41] K. Wakabayashi, K.-I. Sasaki, T. Nakanishi, and T. Enoki, *Science and Technology of Advanced Materials* **11**, pp. 054504 (2010).
- [42] T. Cao, F. Zhao, and S. G. Louie, *Physical Review Letters* **119**, pp. 76401 (2017).
- [43] P. H. Jacobse, A. Kimouche, T. Gebraad, M. M. Ervasti, J. M. Thijssen, P. Liljeroth, and I. Swart, *Nature Communications* **8**, pp. 119 (2017).

Chapter 5

Electronic components embedded in a single graphene nanoribbon



This chapter is based on

Electronic components embedded in a single graphene nanoribbon

Peter H. Jacobse, Amina Kimouche, Tim Gebraad, Mikko M. Ervasti,
Joseph M. Thijssen, Peter Liljeroth, Ingmar Swart

Nature Communications **8** (1), p. 119 (2017)

The use of graphene in electronic devices requires a band gap, which can be achieved by creating nanostructures such as graphene nanoribbons. A wide variety of atomically precise graphene nanoribbons can be prepared through on-surface synthesis, bringing the concept of graphene nanoribbon electronics closer to reality. For future applications it is beneficial to integrate contacts and more functionality directly into single ribbons by using heterostructures. Here, we use the on-surface synthesis approach to fabricate a metal-semiconductor junction and a tunnel barrier in a single graphene nanoribbon consisting of 5- and 7-atom wide segments. We characterize the atomic scale geometry and electronic structure by combined atomic force microscopy, scanning tunneling microscopy, and conductance measurements complemented by density functional theory and transport calculations. These junctions are relevant for developing contacts in all-graphene nanoribbon devices and creating diodes and transistors, and act as a first step toward complete electronic devices built into a single graphene nanoribbon.

5.1 Introduction



Rapid progress has been made in high-performance graphene devices for the study of new physical phenomena.[1, 2, 3, 4, 5] Mainstream applications, however, require a nonzero band gap.[6, 7] This effect can be introduced in a variety of ways, one of the most prominent being the preparation of narrow strips of graphene known as graphene nanoribbons (GNRs).[8, 9, 10] The properties of these GNRs sensitively depends on width, orientation, and edge geometry.[5, 9, 11, 12, 13] Armchair-terminated GNRs are either metallic or semiconducting, depending on their exact atomic width: $3N$ or $3N + 1$ (where N is an integer) atom wide armchair GNRs are semiconductors, and those in the $3N + 2$ family are metallic.[5, 9, 14, 15, 16, 17, 18] This extreme sensitivity to the detailed atomic structure also implies that traditional fabrication methods, such as e-beam lithography, are not precise enough to fabricate structures of sufficient quality. This limitation has been overcome with the on-surface, bottom-up synthesis of atomically precise GNRs. In this route, precursor molecules containing halogen atoms are evaporated onto a metal substrate, typically Au(111), and heated to form polymeric chains *via* Ullmann coupling. These chains are converted into fully aromatic GNRs through a cyclodehydrogenation step occurring at a higher temperature than the initial polymerization step.[9]

The wide variety of atomically precise GNRs that can be prepared through on-surface synthesis[10] has brought the concept of GNR electronics closer

to reality with the first prototype transistors having been demonstrated.[19] For future applications, direct integration of electrical contacts and functional electronic components such as diodes and tunnel barriers into a single ribbon would be highly advantageous. This can be realized by synthesizing GNR heterostructures using a combination of different precursor molecules. For example, semiconductor-semiconductor heterostructures in single GNRs have been demonstrated through synthesis from precursors that give rise to segments of different widths[20] or segments with substitutional nitrogen doping.[21]

Here, we use the bottom-up approach to fabricate a metal-semiconductor junction and a tunnel barrier in a single GNR by utilizing atomically perfect connections between 5- and 7-atom wide segments (denoted as 5-GNR and 7-GNR, respectively). Not only are such junctions relevant for developing contacts in all-GNR devices, they also provide an additional route to create diodes and transistors.[10, 19, 20, 21]. We characterize the atomic scale geometry and electronic structure by combined atomic force microscopy (AFM), scanning tunneling microscopy (STM), and conductance measurements. The GNR equivalent of a tunnel barrier constitutes a first step toward complete electronic devices built into a single GNR.

5.2 Results

5.2.1 Synthesis of GNR heterojunctions

Fig. 5.1a shows the precursors used in this study: 10,10'-dibromo-9,9'-bianthryl (DBBA) and 3,9-dibromoperylene (DBP). These precursors can be used to grow semiconducting (band gap of 2.7 eV) and metallic GNRs, respectively.[9, 17] Co-deposition of both precursors on Au(111) was used to prepare heterojunctions, as well as heterostructures (ribbons with more than one junction). The overview STM scan shown in Fig. 5.1b displays nanoribbons with a clear width modulation, corresponding to 5-GNR and 7-GNR segments, indicating successful copolymerization. A higher resolution AFM image of a longer ribbon with several 5-GNR and 7-GNR segments is shown in Fig. 5.1c. A heterojunction consisting of n monomers of the 5-GNR precursor connected to m monomers of the 7-GNR precursor is referred to as 5/7-GNR(n,m).

Two distinct types of junctions (labeled I and II) were found, images of which are shown in Fig. 5.1d, e, respectively. The type I junction consists of a single six-membered ring between the collinear 5-GNR and 7-GNR segments. The enhanced contrast on one side of the anthracene moiety of the junction in the AFM image (Fig. 5.1d), as well as the increased apparent height at that location in the STM image, show that this junction is non-planar.[22] This non-planarity is caused by the steric repulsion between the inner hydrogen of



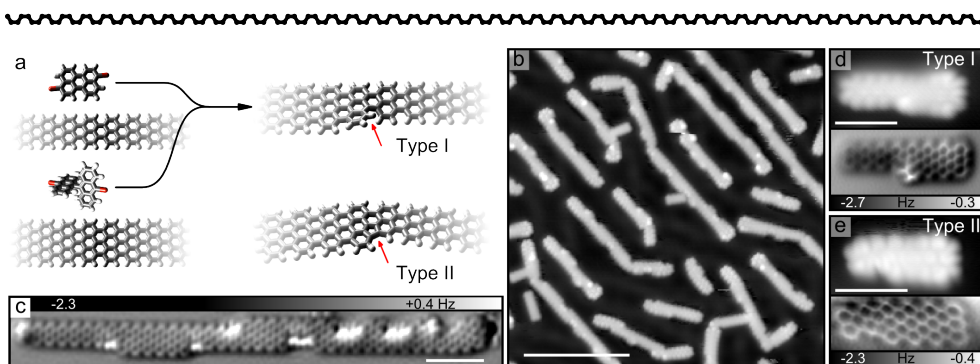


Fig. 5.1 Fabrication and characterization of metal-semiconductor heterojunctions and heterostructures. a) Chemical structure of 10,10'-dibromo-9,9'-bianthryl (DBBA) and dibromoperylene (DBP), and of a 5/7-GNR heterojunction. The red arrows indicate a type I (top) and type II (bottom) junction. b) Overview STM image of 5/7-GNR heterostructures on Au(111). $V = 0.1$ V, $I = 20$ pA, scale bar is 10 nm. c) AFM image of a heterostructure. d) Small-scale STM (top) and AFM (bottom) images of junction type I. z -offset for AFM image: -40 pm w.r.t. an STM set-point of $V = 0.1$ V, $I = 20$ pA. e) Small-scale STM (top) and AFM (bottom) images of junction type II. z -offset: -40 pm w.r.t. an STM set-point of $V = 0.1$ V, $I = 100$ pA. Scale bars in c-e are 2nm

the cove-edged helicene motif.[23, 24, 25]. Junction II (Fig. 5.1e) consists of a hexagon and a pentagon (red arrow in Fig. 5.1a, bottom). The formation of the additional C-C bond results in a planarization of the junction and the introduction of an angle of 15 degree between the 5- and 7-GNR segments. Junction I can be converted to junction II by an additional cyclodehydrogenation reaction.[26] Post-annealing to $T = 600$ K results in a sample showing predominantly type II junctions. In the following, only ribbons with junctions of type II are considered.

5.2.2 Electronic structure of the GNR heterojunctions

5.2.2.1 DFT calculations on heterojunctions

We now turn to the electronic structure of the heterojunctions. The results of density functional theory (DFT) calculations on three types of gas-phase GNRs are shown in Fig. 5.2. To the left of the vertical dotted line in Fig. 5.2a, the orbital energies of a pure 7-GNR are given as a function of the number of repeating bisanthene units. The states at approx. -3.4 and -3.8 eV correspond to states localized on the two zigzag termini of the ribbon. Because of this localization, the energy of these states is virtually independent of the length of the $N = 7$ segment. The states on the zigzag termini exhibit a significant spin-splitting, *i.e.*, one spin-channel is significantly lower in energy than the opposite channel.[27] In a pure $N = 7$ ribbon the states localized on opposite

termini are degenerate. However, upon connecting a single monomer of the 5-GNR, the degeneracy of the spin-polarized states is lifted (the two spin channels are represented by purple and green lines). As can be seen in Fig. 5.2b, the frontier orbitals of the perylene unit hybridize with the spin-split states localized on the zigzag end to which it is connected. Due to this hybridization, the spatial extent of these states increases, resulting in a lowering of the energy. In contrast, the spin states localized on the opposite zigzag end are unaffected. The spin splitting does not sensitively depend on the length of the 5-GNR part. Note that upon increasing the number of 5-GNR monomers, the energy gap between the bulk states decreases. As evidenced by the molecu-

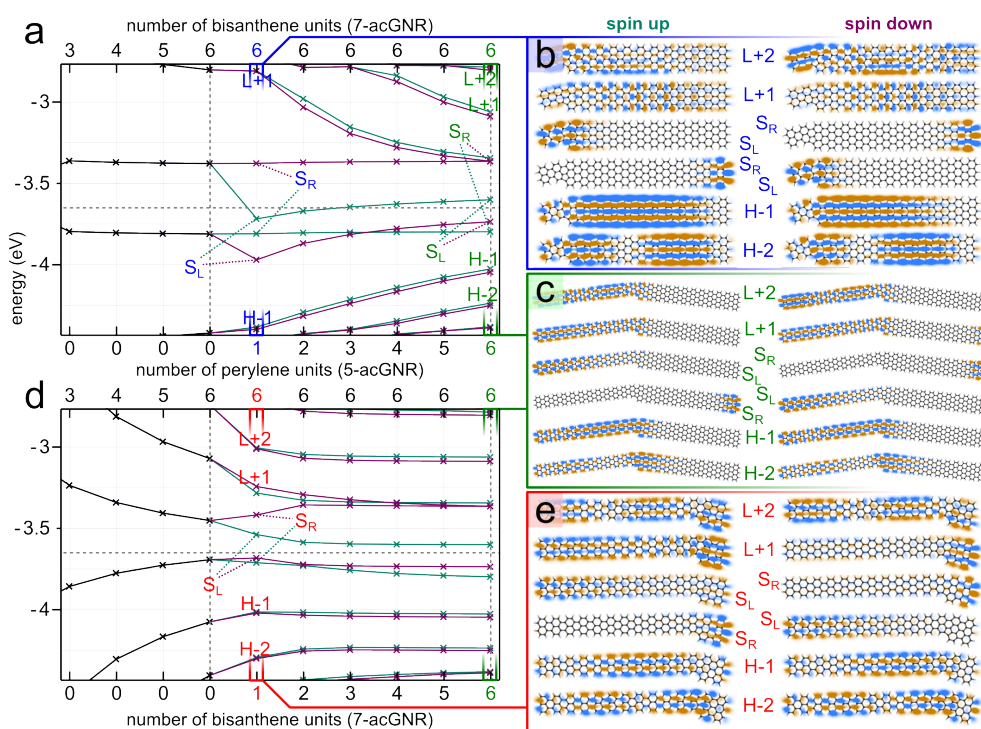


Fig. 5.2 Electronic structure of 5/7-GNR heterojunctions calculated by DFT. a) Evolution of the energy levels of pure 7-GNR as a function of length (left of the vertical dotted line), and of 5/7-GNR as a function of the number of 5-GNR monomers connected to a 7-GNR 6-mer. b, c) Orbital plots of the six frontier molecular orbitals of the b) 5/7-GNR(1,6) and c) 5/7-GNR(6,6). “H” denotes the highest occupied molecular orbital (HOMO), “L” denotes the lowest unoccupied molecular orbital (LUMO), and “S(L/R)” denotes a singly occupied molecular orbital localized on the left/right side (SOMO). c) Same as b) but for 5/7-GNR(6,6). Abbreviations as in b). d) Evolution of the energy levels of pure 5-GNR (left of the vertical dotted line) as a function of length, and of 5/7-GNR as a function of the number of 7-GNR monomers connected to a 5-GNR 6-mer. e) Orbital plots of the six frontier molecular orbitals of the 5/7-GNR(6,1). Abbreviations as in b).

lar orbitals of the 5/7-GNR(6,6) heterojunction, (Fig. 5.2c), these states are mostly localized on the narrow part of the heterojunction. States localized on the semiconductor segment of the ribbon are only found at higher and lower energy. Hence, the heterojunction can be characterized as a metal-semiconductor junction. The same picture emerges when connecting 7-GNR monomers to a pure 5-GNR nanoribbon (Fig. 5.2d, e). Upon attaching a bisanthrene unit, the spin-degeneracy of the lowest unoccupied molecular orbital of the 5-GNR ribbon is lifted. The spin-splitting of these states rapidly converges to a constant value. The localization of low-energy electronic states on the narrow segments and hybridization with end-localized states is also obtained in calculations on heterostructures containing multiple junctions (Fig. 5.3). We note that the splitting of the 7-GNR end states can also be explained in the framework of breaking of the bipartite symmetry of the lattice, as explained in the following subsection.

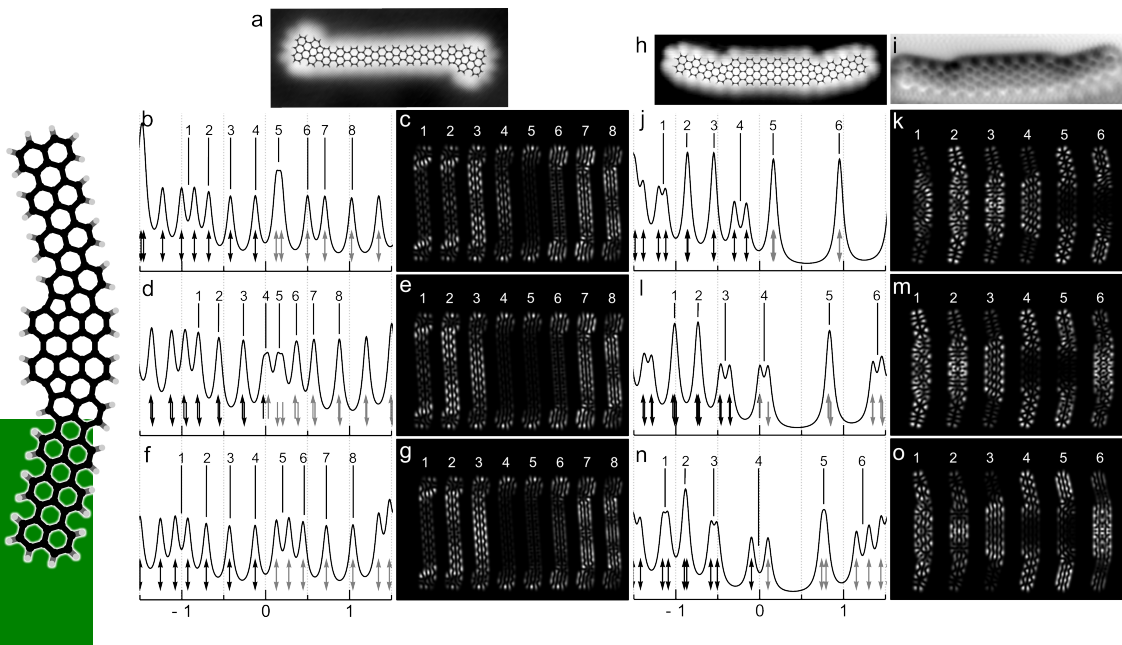


Fig. 5.3 Calculated spectra and simulated differential conductance maps of the 7/5/7-GNR(1,5,1) and 5/7/5-GNR(2,3,2) junctions. a) Model of the 7/5/7-GNR(1,5,1) junction. b, d, f) Calculated DOS for $q = +2e, +1e$ and $0e$, respectively. c, e, g) Simulated differential conductance maps at the energies indicated in b, d, f respectively. h) Model of the 5/7/5-GNR(2,3,2) junction. i) corresponding constant height AFM image. j, l, n) Calculated DOS for $q = +2e, +1e$ and $0e$, respectively. k, m, o) Simulated differential conductance maps at the energies indicated in j, l, n respectively.

5.2.2.2 Effect of the five-membered ring

In order to investigate the effect of the five-membered ring, we have performed a tight-binding calculation on a type I junction and type II junction, both of a 5/7-GNR(6,6). The results are shown in Fig. 5.4. Note that these calculations do not take electron-electron interactions into account, so they do not return the characteristic spin-splitting of the edge states that we find in DFT. Also, overlap has been switched off here in order to assess the symmetry of the energy spectrum.

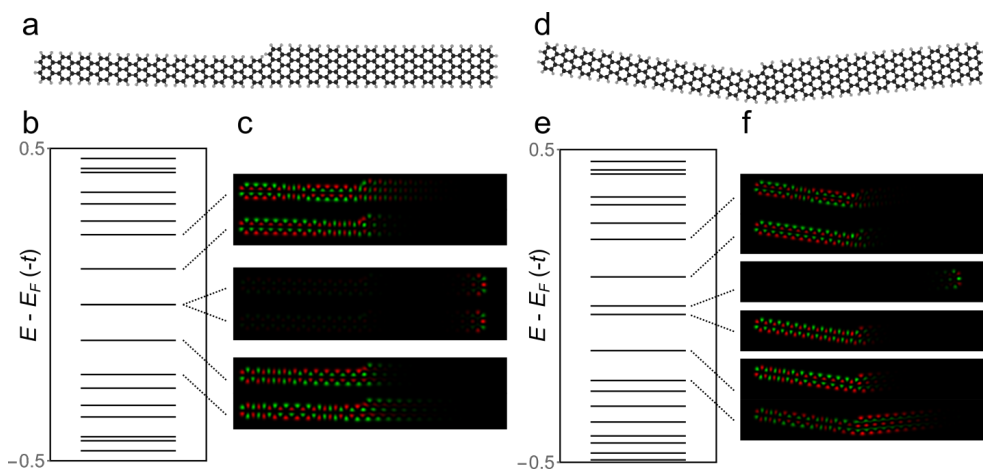


Fig. 5.4 Calculated energy levels and molecular orbitals for the 5/7-GNR(6,6). a) Model of the junction of type I. b) Calculated energy level spectrum for the junction of type I. c) Calculated frontier orbitals for the junction of type I. d) Model of the junction of type II. e) Calculated energy level spectrum for the junction of type II. f) Calculated frontier orbitals for the junction of type II.

As can be seen in the cove-edge case (geometry in Fig. 5.4a), the spectrum is completely symmetric around the Fermi energy (Fig. 5.4b). The two end-localized states are degenerate at exactly the Fermi level. The orbitals corresponding to the end-localized states show a strongly localized feature on the 7-GNR end and a feature delocalized over the 5-GNR segment (Fig. 5.4c). The frontier orbitals show a predominant localization on the 5-GNR segments in the same way as obtained from DFT calculations discussed in the manuscript.

The MO diagram of the 6,6 ribbon with type II junction (Fig. 5.4d), shows a significant asymmetry (Fig. 5.4e). The end state localized on the 7-GNR end remains unperturbed at the Fermi energy, whereas the other end state now resides at lower energy due to the extended delocalization (Fig. 5.4f). Apparently, the extra bond improves the electronic coupling of the 7-GNR end state with the 5-GNR bulk states and the corresponding breaking of the

bipartite symmetry of the lattice allows the newly formed end state to lower its energy.

We conclude that the result from DFT that the energy of the “connecting” end state is lowered upon contacting a 5-GNR segment can in fact be cast into the framework of breaking of the bipartite lattice through introduction of the five-membered ring.

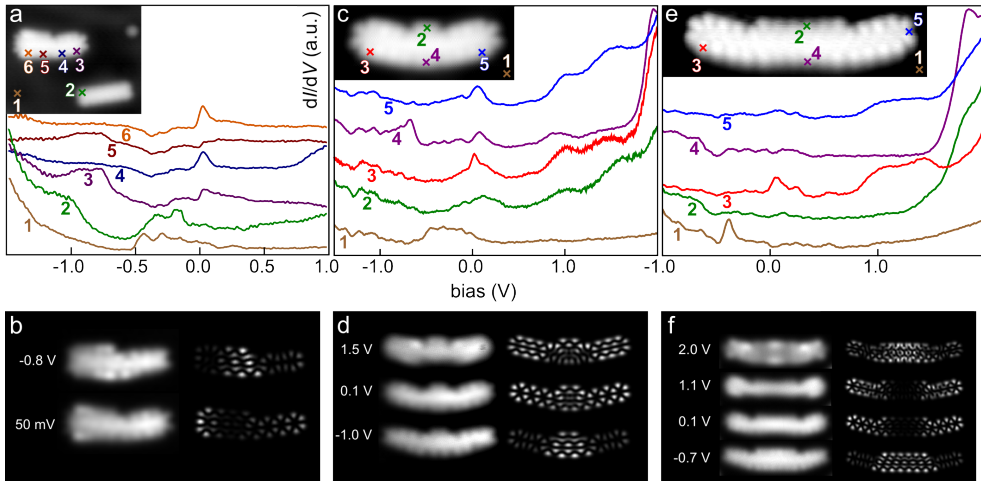


Fig. 5.5 STS experiments and differential conductance maps of 5/7-GNR heterojunctions. a) dI/dV spectra acquired on a 5-GNR and 7-GNR segment of a 5/7-GNR(2,2) heterojunction. For comparison, a spectrum on a three monomer long pure 5-GNR is shown in green. Curves are vertically offset for clarity. Inset: STM topograph of the 5/7-GNR(2,2) heterojunction and neighboring pure 5-GNR ($V = 0.1$ V, $I = 200$ pA). b) Experimental (left) and simulated (right) constant height dI/dV maps recorded at $V = -0.8$ V (top) and 50 mV (bottom), respectively. c) dI/dV spectra acquired on a 5/7/5-GNR(2,1,2) heterostructure. Curves are vertically offset for clarity. Inset: STM topograph of the 5/7/5-GNR(2,1,2) heterojunction ($V = 0.1$ V, $I = 500$ pA). d) Experimental (left) and simulated (right) constant-height dI/dV maps at $V = 1.5$ V (top), $V = 0.1$ V (middle), and $V = 1.0$ V (bottom), respectively. e) dI/dV spectra acquired on a 5/7/5-GNR(2,3,2) heterostructure. Curves are vertically offset for clarity. Inset: STM topograph of the 5/7/5-GNR(2,3,2) heterojunction ($V = 0.1$ V, $I = 100$ pA). f) Experimental (left) and simulated (right) constant-height dI/dV maps at $V = 2.0$ V, 1.1 V, 0.1 V, and -0.7 V, respectively

5.2.3 Electronic characterization of heterojunctions

Now, we turn our attention to the characterization of the junctions with scanning tunneling spectroscopy (STS) and differential conductance mapping. DFT calculations have been performed for all experimentally analyzed GNRs. The calculations do not take substrate effects into account. This should not affect the energetic order of the frontier orbitals. Fig. 5.5a shows an STM to-

pograph of a single junction 5/7-GNR(2,2) and a homogeneous ribbon segment 5-GNR(3). At low bias (0.1 V), there is enhanced contrast on the heterojunction compared to the pure 5-GNR (note the orbital structure and increased apparent height of the heterojunction). This indicates that the state originally localized at the zigzag edge of the 7-GNR hybridizes with states of the 5-GNR, in agreement with the DFT results. The differential conductance spectrum taken at the free zigzag end of the 7-atom wide part of the junction (Fig. 5.5a, spectrum 6, position indicated in the inset) shows a peak close to zero bias (≈ 30 mV), similar to pure 7-GNRs.[16] A state at this energy is also observed on the 5-GNR segment (spectra 3 and 4). DFT calculations show that this peak originates from near-degenerate orbitals on the 7-GNR end and 5-GNR segment, the latter showing hybridization with the 7-GNR end state on the interface. A spectrum acquired at the interface only exhibits a feature at approximately -0.8 V. Experimental and simulated constant-height differential conductance maps corresponding to these voltages are shown in Fig. 5.5b. The molecular orbitals are not reproduced as such in the dI/dV maps due to the finite size of the tip and the presence of background non-resonant tunneling. Nevertheless, the individual states can still be clearly recognized in the density variations over the ribbons, and are in good agreement with the results from theory.

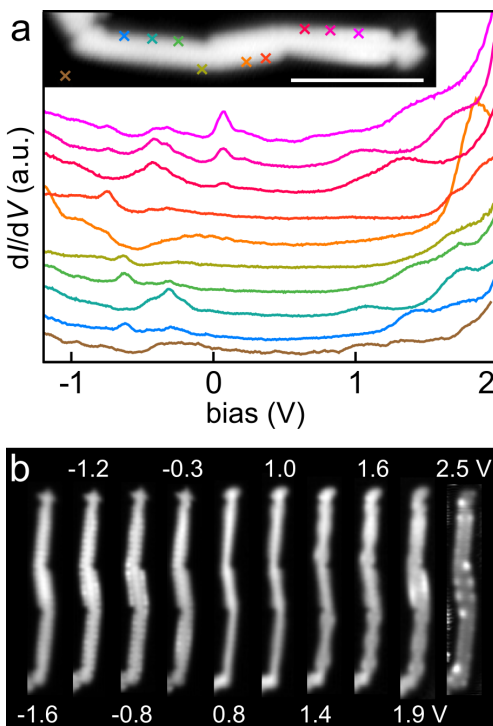
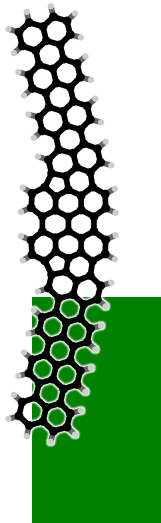


Fig. 5.6 Spectroscopy and differential conductance mapping on a longer heterostructure. a) dI/dV spectra acquired on different positions on a longer heterostructure. The inset shows an STM scan of the nanoribbon, and the colored crosses indicate the positions of the spectra. b) Differential conductance maps acquired on the heterostructure. Bias voltages are given above/underneath the different maps.



Experiments on longer heterostructures, as well as DFT calculations on the experimentally characterized junctions support the same general picture: the low-bias states are mainly localized on the 5-GNR segment, whereas the 7-GNR part of the ribbon retains its semiconducting character. Additionally, the 7-GNR end state at the interface hybridizes with the 5-GNR bulk states.

In addition to single junctions, we studied ribbons with two junctions. Fig. 5.5c, e show STM topographs of a 5/7/5-GNR(2,1,2) (short double junction) and a 5/7/5-GNR(2,3,2) (long double junction) heterostructures, respectively, and a set of dI/dV spectra acquired at various positions above the ribbons. These structures represent a GNR equivalent of a tunnel barrier, where the semiconducting 7-GNR “channel” is sandwiched between metallic 5-GNR segments. Similar to the 5/7-GNR(2,2) junction, there is pronounced orbital character visible in the STM images taken at $V = 0.1$ V. Indeed, all differential conductance spectra show a feature near 70 mV, except those recorded on the middle of the 7-GNR segment of the long double junction. This is also seen in the dI/dV maps: in the short double junction (Fig. 5.5d, 0.1 V) the corresponding state is delocalized over the entire structure, while in the long double junction (Fig. 5.5f, 0.1 and 1.1 V), it is localized on the 5-GNR leads. For both ribbons, the first resonance at negative bias is localized on the 7-GNR segment (Fig. 5.5d, -1.0 V and Fig. 5.5f, 0.7 V). At positive bias, the first two states for the short ribbon (≈ 1 V and 1.5 V) are delocalized over the entire ribbon, whereas for the long ribbon these states are predominantly localized at the 5-GNR leads. We conclude that the low-bias, lead-localized states in the short double junction have too much overlap for the structure to be considered a tunnel barrier. The longer double junction has states localized on the leads with vanishing density in the 7-GNR segment, and this ribbon should, therefore, act as a tunnel barrier for low energy charge carriers. Additional STS experiments again support this picture (Fig. 5.6).

5.2.4 Charge transport through GNR heterojunctions

We now discuss the conductance of these heterostructures. Conductance measurements on single GNRs were performed by picking up a nanoribbon with the STM tip and recording the current while retracting the tip. The measurements were corroborated by transport calculations. Fig. 5.7a shows experimental and simulated lifting curves for a pure 7-GNR(10). For 7-GNRs, pure exponential decay is observed: $I = I_0 e^{-\beta \Delta z}$, with $\beta = 4.2 \text{ nm}^{-1}$, in agreement with the result by Koch *et al.*[28] Fig. 5.7b shows a conductance measurement on pure 5-GNR(6). In all cases, there is an initial increase in the current before the current drops off again with $\beta \approx 1 \text{ nm}^{-1}$. The decay constant β is proportional to the square root of the energy difference between the Fermi level (set by the bias voltage) and the frontier orbitals. As the gap

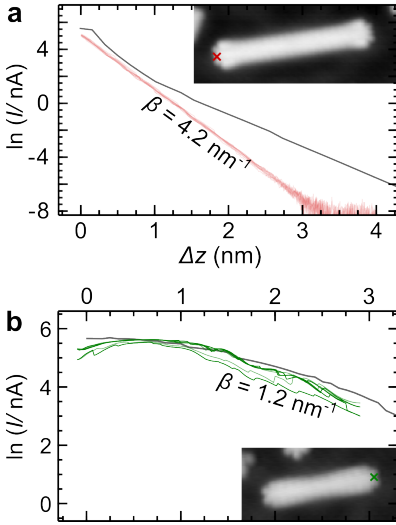
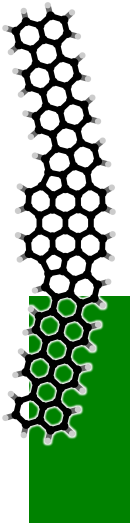


Fig. 5.7 Conductance measurements on mono-component ribbons and single junctions. a) Experimental (red) and theoretical (gray) $\ln(I/nA)(z)$ curves for the 7-GNR(10) shown in the inset. The position from which the GNR was lifted is indicated by a red cross. b) Experimental (green) and theoretical (gray) $\ln(I/nA)(z)$ curves for 5-GNR(6) shown in the inset. The position from which the GNR was lifted is indicated by a green cross

for the 5-GNR segment is much smaller than that of the 7-GNR segment, the frontier orbitals of that segment will be closer to the Fermi level, resulting in a much smaller value of β .^[28] The cause of the initial increase in the current with increasing tip-sample distance is unknown. One possible explanation is that the electronic coupling with the substrate decreases as the ribbon is lifted from the surface. This decrease in the coupling strength could result in a shift of the energy of an orbital, *i.e.*, a transport channel, toward the bias voltage at which the lifting experiments were performed. For both types of GNRs, the results from the transport calculations are in good agreement with the experimental data. Slight differences between the experimental and simulated curves can be due to the limitations of the underlying tight-binding model.

Fig. 5.8a shows the current decay as a 5/7-GNR(2,3) heterojunction is lifted from the 5-GNR and 7-GNR terminus (green and red, positions indicated in the inset images by crosses), respectively. Fig. 5.8b shows the calculated $\ln(I/nA)(z)$ curves. Fig. 5.8c shows the same experiment conducted on two different 5/7-GNR(3,2) heterojunctions (the atomic geometry is shown in Fig. 5.8e as resolved with nc-AFM), and Fig. 5.8d again shows the calculated current decays. In each case, when the ribbon is lifted starting with the 5-GNR segment, the current initially increases with increasing tip-sample distance, as observed for pure 5-GNRs. At larger distances the current decays exponentially, suggesting non-resonant (in-gap) electron transport. In these specific nanoribbons, the 5-GNR segment is so short that the fast current decay through the 7-GNR already appears before the characteristic initial increase is completed. Therefore, we cannot identify a mono-exponential regime of the 5-GNR segment from which we can extract a value of β . When the ribbon is lifted from the 7-GNR side, the current first decays with $\beta \approx 4 \text{ nm}^{-1}$, followed



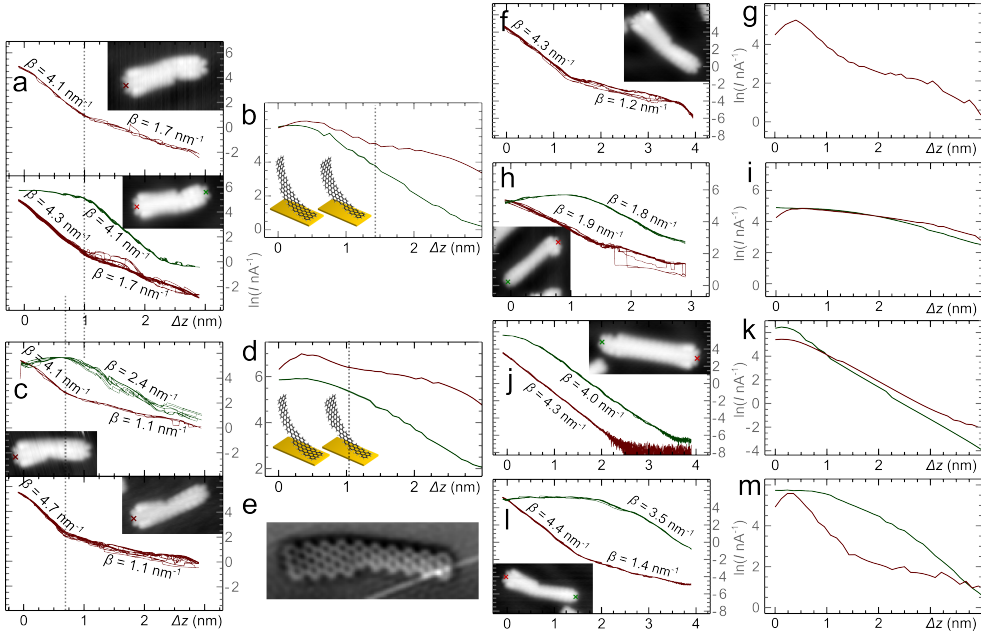


Fig. 5.8 Conductance measurements on single GNR heterojunctions. a) $\ln(I/nA)(\Delta z)$ curves obtained while lifting the 5/7-GNR(2,3) from the 7-GNR side (red) and from the 7-GNR side (green). b) Simulated $\ln(I/nA)(\Delta z)$ for the ribbons in panel a. c) $\ln(I/nA)(\Delta z)$ curves obtained while lifting the 5/7-GNR(3,2) from the 7-GNR side (red) and from the 7-GNR side (green). d) Simulated $\ln(I/nA)(\Delta z)$ for the ribbons in panel c. e) AFM image acquired on the ribbon in panel c. f, h, j, l) $\ln(I/nA)(\Delta z)$ spectra obtained while lifting single junctions from the 7-GNR side (red curves) and the 5-GNR side (green curves). g, i, k, m) Simulated $\ln(I/nA)(\Delta z)$ spectra on the ribbons of panels f, h, j, l. All insets show STM topographs of the respective ribbons ($V = 0.1$ V, $I = 40$ pA) with tip position for lifting experiment indicated by crosses (except panel b and d, which show simulated lifting geometries).

by a regime with $\beta \approx 1 \text{ nm}^{-1}$. These values are close to those of the pure 7- and 5-GNRs, respectively. This result suggests that, as soon as the entire 7-GNR segment is lifted from the surface, the further reduction in the current with distance is dominated by the detachment of the 5-GNR segment. The experimentally observed behavior is qualitatively reproduced by the transport calculations (Fig. 5.9a, bottom panel). This current decay behavior is found in all single junctions (as can be seen in Fig. 5.8f-m and Fig. 5.9a).

Conductance measurements on a 5/7/5-GNR(2,1,3) (short double junction) and 5/7/5-GNR(2,4,2) (long double junction) are shown in Fig. 5.9b, c. All double junctions show a signature of fast decay during the 7-GNR segment lift-off. For the short double junction, the length of the two 5-GNR segments differs by one 5-GNR monomer. As a result, the fast decay due to

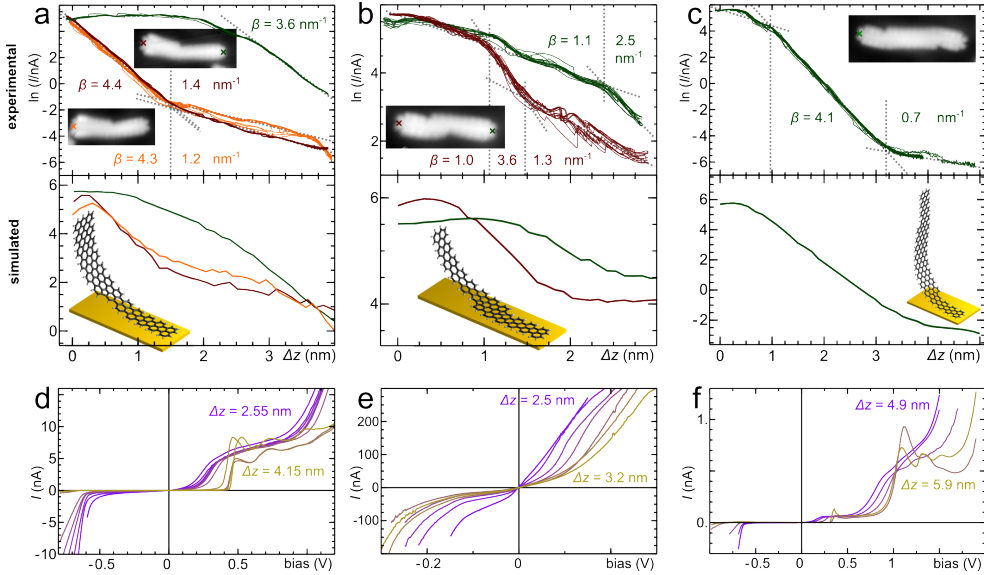


Fig. 5.9 Conductance spectroscopy on single GNR heterojunctions and heterostructures. a) Experimental (top) and simulated (bottom) $\ln(I/nA)(\Delta z)$ curves obtained while lifting the 5/7-GNR(3,3) from the 7-GNR side (orange) and while lifting the 5/7-GNR(4,3) from the 5-GNR side (green) and 7-GNR side (red). The insets in the top panels show STM topographs of the respective ribbons ($V = 0.1$ V, $I = 40$ pA) with tip position for lifting experiment indicated by crosses, whereas the inset in the bottom image shows a calculated lifting geometry of the 5/7-GNR(3,3). b) Same as a, but for lifting a 5/7/5-GNR(2,1,3) from the long 5-GNR side (green) and the short 5-GNR side (red). c) Same as a, but for lifting a 5/7/5-GNR(2,4,2). d-f) Experimental $I(V)$ curves recorded with increasing tip heights Δz for 5/7-GNR(3,3) and 5/7/5-GNR(2,1,3) and 5/7/5-GNR(2,4,2) heterojunctions, respectively

the lift-off of the 7-GNR segment occurs early when the ribbon is lifted from the short 5-GNR lead ($1 \text{ nm} < \Delta z < 1.5 \text{ nm}$) and late when the ribbon is lifted from the long 5-GNR lead ($\Delta z > 2.3 \text{ nm}$). The long double junction (5/7/5-GNR(2,4,2)) has a very clear signature of slow decay during the 5-GNR lift-off ($\Delta z < 1 \text{ nm}$ and $\Delta z > 3 \text{ nm}$) and fast decay during the 7-GNR lift-off ($1 \text{ nm} < \Delta z < 3 \text{ nm}$). Again, the experimentally observed features are qualitatively reproduced in the transport calculations. The lift-off experiments were complemented by recording $I(V)$ curves for a number of increasing tip heights (Fig. 5.9d-f), up to the point where the nanoribbon completely detached from the surface (evidenced by a sudden drop in the current and failure to relocate the nanoribbon on the surface in subsequent STM scans). The $I(V)$ curves for the single junction (Fig. 5.9d) show an onset of resonant tunneling at both sides of the bias window, as well as a relatively small peak in the current at low bias (around 500 mV). Since this peak occurs at energies that are in-gap



with respect to the 7-GNR segment, it can be ascribed to tunneling from the tip through the 7-GNR segment into orbitals localized on the 5-GNR segment. The $I(V)$ curves of long and short double junctions (Fig. 5.9e, f) show a striking difference. The short junction has no gap, demonstrating that the states from the 5-GNR segments couple through the short 7-GNR segment. In contrast, the long double junction exhibits a wide bias range (-0.6 V to 0.1 V) where the current is nearly zero, *i.e.*, it operates as a tunnel barrier. The spectra show a clear low-bias resonance at $\approx 0.2 - 0.4$ V and two resonances at $\approx 0.8 - 1.4$ V, which result from the low-bias lead-localized states as described above. The final two spectra ($\Delta z = 5.8$ and 5.9 nm) exhibit negative differential conductance. At these heights, the coupling of the heterostructure to the surface is small and comparable to the coupling to the STM tip, restoring the degeneracy of the lead-localized states. At low bias, electrons can tunnel resonantly between the 5-GNR leads, resulting in an enhanced tunnel current. However, at higher bias, the degeneracy of the orbitals on 5-GNR segments will be lifted, resulting in a suppression of resonant tunneling and, therefore, in negative differential conductance. This result provides conclusive evidence that the 5/7/5-GNR(2,4,2) functions as a tunnel barrier.

5.3 Conclusions

The motivation for synthesizing GNRs through on-surface covalent coupling of molecular precursors is to develop atomically precise components that could be the key enabling component in next-generation nanoelectronics. We build on this idea by encoding a complete electrical device (*e.g.*, a tunnel barrier or a diode) in a single GNR with a feature size of *ca.* 1 nm with atomic precision and directly test its function through a transport measurement.

We fabricated GNR heterostructures consisting of segments of two different widths with totally different electronic properties: 7-atom wide semiconducting and 5-atom wide metallic GNR-segments. This allowed us to realize metal-semiconductor and metal-semiconductor-metal junctions embedded in a single GNR. We characterized the geometry of these heterostructures with atomically resolved AFM and probed their local density of states with STM and STS. We find that the electronic structure close to the Fermi level arises from hybridization of the 5-GNR states with the localized zigzag end states of the 7-GNR segments. This picture remains valid in more complicated heterostructures consisting of multiple junctions.

The electrical performance of the GNRs can only be properly understood based on transport measurements. We have taken steps towards this by carrying out STM-based two-terminal transport experiments on GNR heterostructures with a known atomic structure. These experiments demonstrate that

the segments of different widths have strongly differing tunneling decay constants that are directly linked to their energy band gaps. Characterization of GNR heterostructures demonstrated that already four monomer units of 7-GNR can act as a tunnel barrier and effectively decouple 5-GNR leads from each other. STS measurements corroborated with DFT calculations further showed that this heterojunction with a semiconducting channel composed of four bisanthene units has low transmission in the energy window between -0.8 V and 1.8 V, where the electron density is exclusively localized on the leads. As a result, this junction represents a true tunnel barrier between leads.

Before real-life applications can be realized, our methods need to be further refined. Most importantly, the lengths of the different segments have to be controlled precisely and deterministically. This can conceivably be achieved through consecutive precursor supply, as a 1D analogue of the epitaxy in two-dimensional space.[29, 30, 31] An alternative method would be to use a hierarchical synthesis using different halogen atoms, where the Ullmann coupling reactions of the different monomers take place at different temperatures.[32] In addition, in order to contact the active parts of the GNR heterostructures with macroscopic leads, structures should be complemented by metallic parts. This could be achieved either through growth of longer metallic segments, or by incorporating 2D graphene islands.[33] Finally, methods for large-scale transfer of the GNR heterostructures from the growth substrate into device structures with positional control must be developed.

In conclusion, we demonstrated a complete electrical device contained in a single GNR, which represents a significant step toward all graphene nanostructure-based electronics. Moreover, the integration of metal-semiconductor heterojunctions in a single nanoribbon provides a seamless platform for realizing a broad range of multifunctional nanoscale electronic devices. The tunability of the on-surface synthesis through utilizing different molecular building blocks allows near-unlimited incorporation of atomically sharp interfaces and doping profiles into the GNR heterostructures.

5.4 Experimental methods

5.4.1 STM and AFM measurements

Samples were prepared by simultaneously evaporating the precursor molecules from two effusion cells onto a clean Au(111) single crystal held at $T = 480$ K. After maintaining the sample at this temperature for 10-30 min, it was annealed at $T = 570$ K for 5 min to induce cyclodehydrogenation reactions. The sample was then inserted into a Scienta-Omicron low-temperature ($T = 4.5$ K) STM/AFM, housed within the same ultrahigh vacuum system (base pressure $< 5 \cdot 10^{-10}$ mbar). The qPlus sensor had a resonance frequency f_0



chapter 5

of 19.5 kHz, a quality factor of 30000 and a spring constant $k = 1800$ N/m, and an oscillation amplitude of approximately 100 pm. CO terminated tips were prepared by picking up a CO molecule from the Au(111) surface using a method developed for Cu(111).[34, 35] AFM images were acquired at $V = 0$ V. dI/dV signals were recorded by a lock-in amplifier (frequency = 273 Hz, amplitude = 50 mV (r.m.s.) and 100 mV (r.m.s.) for the dI/dV maps on the heterostructures).

5.4.2 Conductance measurements

The nanoribbon to be lifted was scanned in STM feedback mode, after which the tip was positioned above clean Au(111) next to the ribbon. The feedback setpoint was set to 400 pA at $V = 100$ mV. After switching the feedback off, the voltage was decreased to 10 mV and the tip was repositioned on the terminus of the ribbon. While monitoring the current in real time, the tip was slowly lowered toward the surface in 1 pm decrements. Successful attachment is evident from a sudden jump in the current from tens of pA to 200 - 300 pA, and typically occurs when the tip is lowered to $\Delta z = (-100 \pm 50)$ pm with respect to the feedback setpoint. From this position, the ribbon was lifted and $I(\Delta z)$ was recorded, or the tip was retracted to the desired height for $I(V)$ experiments. For most $I(\Delta z)$ experiments, the ribbon was lifted and lowered a number of times, until the nanoribbon detached or it was deemed that enough data were acquired.

5.4.3 DFT calculations

All DFT calculations were performed on free nanoribbons using ORCA, Program Version 3.0.2.[36] The Perdew-Burke-Ernzerhof exchange-correlation functional was used, together with a 6-31g* basis set. Geometry optimizations were considered to be converged when the change in energy was smaller than $5 \cdot 10^{-6}$ a.u. and the forces on all atoms were below $3 \cdot 10^{-4}$ a.u.

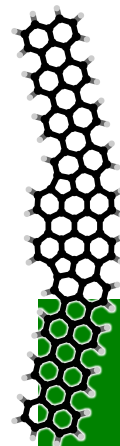
5.4.4 Transport calculations

The electronic structure of the nanoribbon was modeled by a tight-binding model with on-site energy $\epsilon_0 = -5$ eV, nearest-neighbor hopping of $t = 2.8$ eV and nearest-neighbor overlap parameter $s = 0.15$.[37, 38]. The coupling to the metallic surface and tip was modeled by the self-energy method, where the C-Au coupling constants were weighed according to the C-Au distances. The geometry of the nanoribbons was computed by minimizing the mechanical energy as a function of curvature for ribbons attached to the tip. Finally, the current was calculated by the Landauer formula.[39]



Bibliography

- [1] B. Hunt, T. Taniguchi, P. Moon, M. Koshino, and R. C. Ashoori, *Science* **340**, pp. 1427–1431 (2013).
- [2] J. R. Wallbank, D. Ghazaryan, A. Misra, Y. Cao, J. S. Tu, B. A. Piot, M. Potemski, S. Pezzini, S. Wiedmann, U. Zeitler, T. L. Lane, S. V. Morozov, M. T. Greenaway, L. Eaves, A. K. Geim, V. I. Fal’ko, K. S. Novoselov, and A. Mishchenko, *Science* **353**, pp. 575–579 (2016).
- [3] M. Yankowitz, J. Xue, D. Cormode, J. D. Sanchez-Yamagishi, K. Watanabe, T. Taniguchi, P. Jarillo-Herrero, P. Jacquod, and B. J. Leroy, *Nature Physics* **8**, pp. 382–386 (2012).
- [4] A. K. Geim and I. V. Grigorieva, *Nature* **499**, pp. 419–425 (2013).
- [5] A. H. Castro Neto, F. Guinea, N. M. R. Peres, K. S. Novoselov, and A. K. Geim, *Reviews of Modern Physics* **81**, pp. 109–162 (2009).
- [6] P. Avouris, “Graphene: Electronic and photonic properties and devices” (2010).
- [7] F. Schwierz, *Nature Nanotechnology* **5**, pp. 487–496 (2010).
- [8] M. Y. Han, B. Özyilmaz, Y. Zhang, and P. Kim, *Physical Review Letters* **98**, pp. 206805 (2007).
- [9] J. Cai, P. Ruffieux, R. Jaafar, M. Bieri, T. Braun, S. Blankenburg, M. Muoth, A. P. Seitsonen, M. Saleh, X. Feng, K. Müllen, and R. Fasel, *Nature* **466**, pp. 470–473 (2010).
- [10] L. Talirz, P. Ruffieux, and R. Fasel, *Advanced Materials* **28**, pp. 6222–6231 (2016).
- [11] K. Nakada, M. Fujita, G. Dresselhaus, and M. S. Dresselhaus, *Physical Review B* **54**, pp. 17954–17961 (1996).
- [12] Y. W. Son, M. L. Cohen, and S. G. Louie, *Nature* **444**, pp. 347–349 (2006).
- [13] O. V. Yazyev, *Accounts of Chemical Research* **46**, pp. 2319–2328 (2013).
- [14] Y. W. Son, M. L. Cohen, and S. G. Louie, *Physical Review Letters* **97**, pp. 216803 (2006).
- [15] P. Ruffieux, J. Cai, N. C. Plumb, L. Patthey, D. Prezzi, A. Ferretti, E. Molinari, X. Feng, K. Müllen, C. A. Pignedoli, and R. Fasel, *ACS Nano* **6**, pp. 6930–6935 (2012).
- [16] J. van der Lit, M. P. Boneschanscher, D. Vanmaekelbergh, M. Ijäs, A. Uppstu, M. Ervasti, A. Harju, P. Liljeroth, and I. Swart, *Nature Communications* **4**, pp. 2023 (2013).
- [17] A. Kimouche, M. M. Ervasti, R. Drost, S. Halonen, A. Harju, P. M. Joensuu, J. Sainio, and P. Liljeroth, *Nature Communications* **6**, pp. 10177 (2015).
- [18] P. Ruffieux, S. Wang, B. Yang, C. Sanchez-Sanchez, J. Liu, T. Dienel, L. Talirz, P. Shinde, C. A. Pignedoli, D. Passerone, T. Dumslaff, X. Feng, K. Müllen, and R. Fasel, *Nature* **531**, pp. 489–492 (2016).
- [19] J. P. Llinas, A. Fairbrother, G. Borin Barin, W. Shi, K. Lee, S. Wu, B. Yong Choi, R. Braganza, J. Lear, N. Kau, W. Choi, C. Chen, Z. Pedramrazi, T. Dumslaff, A. Narita, X. Feng, K. Müllen, F. Fischer, A. Zettl, P. Ruffieux, E. Yablonovitch, M. Crommie, R. Fasel, and J. Bokor, *Nature Communications* **8**, pp. 1–15 (2017).
- [20] Y. C. Chen, T. Cao, C. Chen, Z. Pedramrazi, D. Haberer, D. G. De Oteyza, F. R. Fischer, S. G. Louie, and M. F. Crommie, *Nature Nanotechnology* **10**, pp. 156–160 (2015).
- [21] J. Cai, C. A. Pignedoli, L. Talirz, P. Ruffieux, H. Söde, L. Liang, V. Meunier, R. Berger, R. Li, X. Feng, K. Müllen, and R. Fasel, *Nature Nanotechnology* **9**, pp. 896–900 (2014).
- [22] N. Pavliček, B. Fleury, M. Neu, J. Niedenführ, C. Herranz-Lancho, M. Ruben, and J. Repp, *Physical Review Letters* **108**, pp. 86101 (2012).
- [23] E. Clar and J. F. Stephen, *Tetrahedron* **21**, pp. 467–470 (1965).
- [24] S. Xiao, M. Myers, Q. Miao, S. Sanaur, K. Pang, M. L. Steigerwald, and C. Nuckolls, *Angewandte Chemie - International Edition* **44**, pp. 7390–7394 (2005).
- [25] T. A. Chen and R. S. Liu, *Organic Letters* **13**, pp. 4644–4647 (2011).



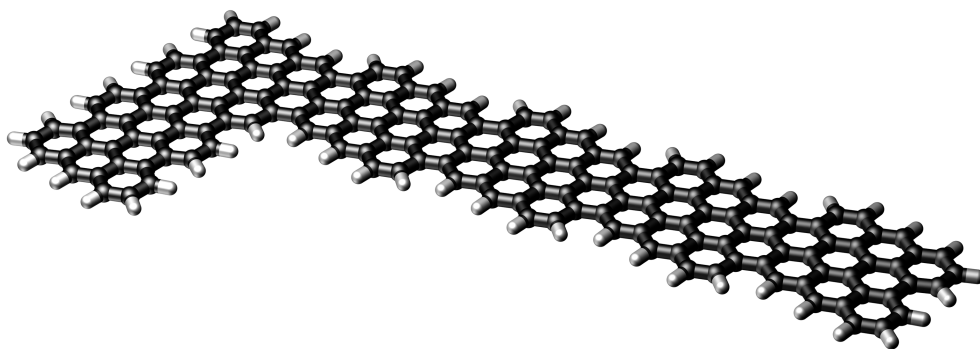
chapter 5

- [26] L. Peng and L. T. Scott, *Journal of the American Chemical Society* **127**, pp. 16518–16521 (2005).
- [27] S. Wang, L. Talirz, C. A. Pignedoli, X. Feng, K. Müllen, R. Fasel, and P. Ruffieux, *Nature Communications* **7**, pp. 11507 (2016).
- [28] M. Koch, F. Ample, C. Joachim, and L. Grill, *Nature Nanotechnology* **7**, pp. 713–717 (2012).
- [29] L. Liu, J. Park, D. A. Siegel, K. F. McCarty, K. W. Clark, W. Deng, L. Basile, J. C. Idrobo, A.-P. Li, and G. Gu, *Science* **343**, pp. 163 LP – 167 (2014).
- [30] P. Sutter, Y. Huang, and E. Sutter, *Nano Letters* **14**, pp. 4846–4851 (2014).
- [31] R. Drost, S. Kezilebieke, M. M. Ervasti, S. K. Hämäläinen, F. Schulz, A. Harju, and P. Liljeroth, *Scientific Reports* **5**, pp. 197–200 (2015).
- [32] L. Lafferentz, V. Eberhardt, C. Dri, C. Africh, G. Comelli, F. Esch, S. Hecht, and L. Grill, *Nature Chemistry* **4**, pp. 215–220 (2012).
- [33] Y. He, M. Garnica, F. Bischoff, J. Ducke, M. L. Bocquet, M. Batzill, W. Auwärter, and J. V. Barth, *Nature Chemistry* **9**, pp. 33–38 (2017).
- [34] L. Gross, F. Mohn, N. Moll, P. Liljeroth, and G. Meyer, *Science* **325**, pp. 1110–1114 (2009).
- [35] L. Bartels, G. Meyer, and K. H. Rieder, *Applied Physics Letters* **71**, pp. 213–215 (1997).
- [36] F. Neese, *Wiley Interdisciplinary Reviews: Computational Molecular Science* **2**, pp. 73–78 (2012).
- [37] R. Kundu, *Modern Physics Letters B* **25**, pp. 163–173 (2011).
- [38] Y. Hancock, A. Uppstu, K. Saloriutta, A. Harju, and M. J. Puska, *Physical Review B - Condensed Matter and Materials Physics* **81**, pp. 245402 (2010).
- [39] H. Haug and A.-P. Jauho, “Quantum kinetics in transport and optics of semiconductors, Volume 6” (2008).



Chapter 6

Mapping the conductance of electronically decoupled graphene nanoribbons



This chapter is based on

Mapping the Conductance of Electronically Decoupled Graphene Nanoribbons

Peter H. Jacobse, Mark J. J. Mangnus, Stephan J. M. Zevenhuizen, Ingmar Swart

ACS Nano **12** (7), pp. 7048-7056 (2018)



With the advent of atomically precise synthesis and consequent precise tailoring of their electronic properties, graphene nanoribbons (GNRs) have emerged as promising building blocks for nanoelectronics. Before being applied as such, it is imperative that their charge transport properties are investigated. Recently, formation of a molecular junction through the controlled attachment of nanoribbons to the probe of a scanning tunneling microscope (STM) and subsequent lifting allowed for the first conductance measurements. Drawbacks are the perturbation of the intrinsic electronic properties through interaction with the metal surface, as well as the risk of current-induced defect formation which largely restricts the measurements to low bias voltages. Here, we show that resonant transport - essential for device applications - can be measured by lifting electronically decoupled GNRs from an ultrathin layer of NaCl. By varying the applied voltage and tip-sample distance, we can probe resonant transport through frontier orbitals and its dependence on junction length. This technique is used for two distinct types of GNR: the 7-atom wide armchair GNR and the 3,1-chiral GNR. The features in the conductance maps can be understood and modelled in terms of the intrinsic electronic properties of the ribbons as well as capacitive coupling to tip and substrate. We demonstrate that we can simultaneously measure the current decay with increasing junction length and bias voltage by using a double modulation spectroscopy technique. The strategy described in this work is widely applicable and will lead to a better understanding of electronic transport through molecular junctions in general.

6.1 Introduction



The discovery of graphene's exceptional electronic properties [1, 2, 3] has initiated a quest for a new generation of graphene-based electronic devices. The absence of a band gap, however, has impeded the application of the two-dimensional material in electronics. A band gap can be introduced into graphene through quantum confinement in one of its lateral dimensions, forming graphene nanoribbons (GNRs). [4, 5, 6, 7] Since the electronic properties of graphene nanoribbons are sensitively dependent on their width and edge structure, it is important to control fabrication down to the atomic level, a degree of precision that currently cannot be obtained through top-down methods. [8, 9] Recently established bottom-up techniques based on on-surface synthesis [10, 11] have facilitated the fabrication of atomically well-defined graphene nanoribbons of various widths and edge structures. Notably, nu-



merous types of armchair edge nanoribbons[12, 13, 14, 15, 16, 17, 18, 19, 20] (acGNR) have been produced, as well as ribbons with zigzag[21, 22] or chiral[23, 24, 25, 26, 27] edges, which host low-energy edge-localized states.[3, 4, 7, 28, 29, 30, 31, 32] The high degree of control obtained so far has not only facilitated fabrication of atomically precise GNRs of a single type, but also heterojunctions, such as metal-semiconductor junctions[33], type-I (straddling gap) junctions[34, 35, 36, 37] and type-II (staggered gap) junctions.[38, 39] These developments signify a trend of incorporating more functionality into graphene nanoribbons, and indicate a maturing of the field towards electronics applications.[36, 40]

For applications in molecular electronic devices, it is essential to understand current transport through individual GNRs, and how it is impacted by their geometry. Field-effect transistor behaviour has been investigated in graphene nanoribbons[41, 42], but for a proper understanding of transport through individual GNRs, non-ensemble techniques are required. In a pioneering study by Koch *et al.*, single 7-acGNRs were lifted off a metal substrate with an STM tip and the voltage-dependent conductance was measured in this lifting geometry.[43] This STM-based conductance measurement methodology was developed earlier for conjugated polymers[44] and has later been used to demonstrate high conductance and resonant charge transport in different molecular wires.[45, 46] This technique has subsequently been used to measure the conductance through metal-semiconductor junctions in GNRs, composed of 5-acGNR and 7-acGNR segments.[33] When a low bias voltage is applied to the tip-GNR-substrate junction, off-resonant transport can be measured, which is characterized by an exponentially decaying current with increasing path length.[33, 43] However, at length scales of device geometries resonant transport is the dominant mechanism. Unfortunately, the risk of current-induced defect formation in STM-based conductance experiments makes it difficult to apply voltages beyond the band gap and access resonant transport without destruction of the junction, particularly at lower tip heights. Furthermore, the intrinsic features of GNRs involved in electronic transport are obscured as molecular states hybridize with metallic states of the substrate.[47, 48] In addition, nanoribbons in contact with a metallic substrate may accumulate a (partial) charge or be subject to correlation effects.[47, 48, 49] Therefore, although lifting experiments provide a way to access the conductance of single nanoribbons, the influence of the metal substrate can be detrimental for a detailed analysis of the intrinsic resonant transport properties.

It has been demonstrated that molecules can be electronically decoupled from a metal substrate by introducing an intercalating layer of an insulating material such as NaCl.[49, 50] Similarly, electronic decoupling of GNRs has been achieved by transfer onto a NaCl monolayer.[21, 47, 36] Unlike smaller



molecules, GNRs cannot directly be deposited onto intercalating layers by means of evaporation. Instead, transfer should be performed in situ, using the tip of an STM. This technique relies on the methodology of Koch *et al.*[43] to lift the nanoribbons from the metal substrate, followed by lateral manipulation[51] and deposition (by means of a voltage pulse).[47] Probe-controlled transfer has initially been used on 7-acGNRs on Au(111), but has since then also been applied to zigzag-type nanoribbons²¹ and metal-semiconductor heterojunctions composed of laterally fused 7-acGNRs.[36] Large molecular wires have been transferred to NaCl by using a higher coverage of the intercalant. This may be a complementary method to transfer GNRs onto thin insulating films.[50, 52]

Our aim in this work is to perform a detailed investigation of the electronic transport through different types of graphene nanoribbons, using the decoupling effect induced by NaCl intercalation to research the inherent, unperturbed conductance properties. Besides electronically decoupling the GNRs from the metal substrate, the introduction of an NaCl layer provides an additional tunnel barrier which dampens the current through the molecular junction. This allows us to probe resonant transport at low tip heights, while simultaneously reducing the risk of destruction of the junction through inelastic processes that were found to become more pronounced at high currents.[43]

We have selected two distinct types of nanoribbons, namely 7-acGNRs and 3,1-cGNRs, the latter of which have recently emerged as the surprising product of nanoribbon synthesis from bianthryl-type molecules on Cu(111).[23, 25, 26] Pure 7-acGNRs have experimentally been characterized as wide-band gap semiconductors.[47, 48, 53, 54] cGNRs on the other hand, are expected to host a band of topological edge states close to the Fermi level due to the partial zigzag structure of their edges.[29, 55, 56] Even though a detailed investigation on Au(111) has not revealed a pronounced edge-localized character of the low-bias states, it has been shown that for 3,1-cGNR these states reside at a significantly lower energy than the frontier states of 7-acGNR.[57]

Although a detailed investigation of the electronic structure of 7-acGNR on NaCl has been performed[47], decoupling of 3,1-cGNRs has not yet been reported. Therefore, we first characterize the nature of the frontier states of 3,1-cGNR after transfer onto NaCl by means of scanning tunneling spectroscopy (STS) and differential conductance mapping.[50] Next, we focus on the transport properties of GNRs as a function of tip height (length of the junction) and bias voltage, providing conductance maps in two-dimensional (V, z)-space.

Finally, we study the length-dependent current decay as a function of voltage by means of double modulation spectroscopy, where the tip height is modulated using a lock-in amplifier in addition to the one used to monitor the conductance. Specifically, the exponential current decay parameter

β was recorded as a function of voltage. This parameter characterizes the nature of the charge transport: (quasi-)ballistic transport (zero or small β) or non-resonant (large β).[46] The double modulation spectroscopy technique described in this work is applicable to graphene nanoribbons, but can equally well be applied to other types of molecular junctions.

6.2 Results

6.2.1 Characterization of 3,1-cGNR on NaCl

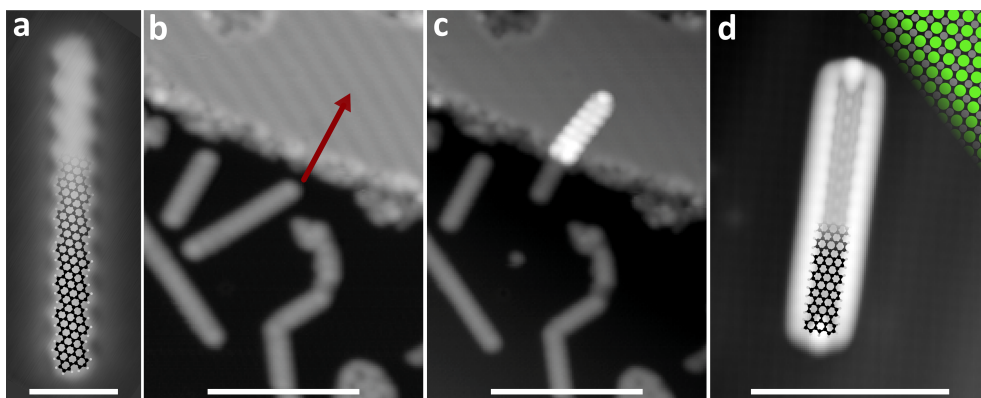
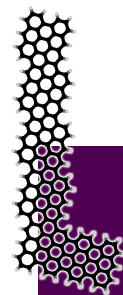


Fig. 6.1 Transfer of graphene nanoribbons onto sodium chloride. a) STM scan ($V = -1.8$ V, $I = 20$ pA) of a 10-monomer long 3,1-cGNR on Cu(111). The overlay shows a model of the atomic geometry. Scale bar: 2 nm. b) STM scan ($V = -1.8$ V, $I = 20$ pA) of a 3,1-cGNR before being transferred onto a patch of sodium chloride. Scale bar: 10 nm. c) STM scan ($V = -1.8$ V, $I = 20$ pA) showing the same nanoribbon after partial transfer onto the sodium chloride. Scale bar: 10 nm. d) STM scan ($V = -1.8$ V, $I = 20$ pA) of a 7-acGNR on NaCl. A model of the atomic geometry is overlaid, as well as a model of the underlying sodium chloride. Scale bar: 5 nm.

3,1-cGNRs were grown on Cu(111) using 10,10'-dichloro-9,9'-bianthryl (DCBA) as described before.[26] After ribbon growth, a sub-monolayer of NaCl was deposited onto the same substrate and the sample was transferred into a low-temperature STM housed in the same vacuum system. We transferred 3,1-cGNRs onto NaCl as described using the method described by Wang *et al.*[47] STM scans of a chiral nanoribbon on Cu(111), both before and after being partially dragged onto a NaCl patch, are shown in Fig. 6.1a-c. For comparison, Fig. 6.1d shows an STM scan of a 7-acGNR that has been transferred onto NaCl. Similar to what has been reported for 7-acGNRs, the electronic decoupling of 3,1-cGNRs from the surface due to intercalation immediately presents itself as a large increase in the apparent height, and in the appearance of nodal planes.[50] This is true as long as the bias voltage is sufficiently



high for resonant tunneling into states of the nanoribbon; the ribbons were found to be highly mobile while scanning in-gap, underlining the weak interaction between the GNR and NaCl.

Fig. 6.2a shows dI/dV spectra recorded on different positions of a 6-monomer long 3,1-cGNR, where the inset shows an STM scan on the ribbon and the crosses indicate the positions at which the spectra have been recorded. A spectrum recorded on the middle of the nanoribbon (green curve) shows resonances at -1.7 V, -1.3 V, 0.5 V and 0.9 V. Additional peaks at -1.4 V, 0.7 V, 1.2 and 1.4 V are observed in spectra recorded on different points on the ribbon (orange, blue and purple curves).

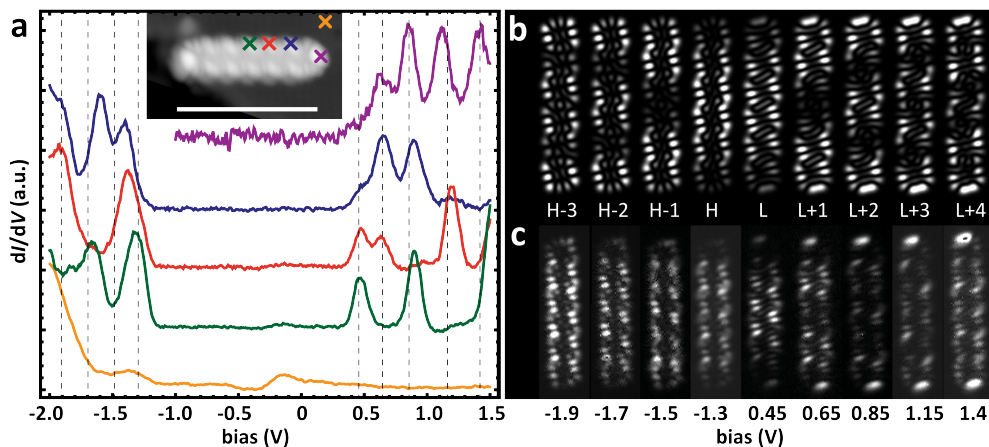


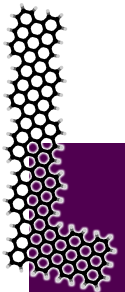
Fig. 6.2 Differential conductance spectroscopy on a decoupled 3,1-cGNR. a) dI/dV spectra acquired on a 6-monomer long 3,1-cGNR on NaCl. The inset shows an STM scan ($V = -1.8$ V, $I = 20$ pA) of the nanoribbon. The crosses indicate the positions where the spectra were acquired. Scale bar: 5 nm. b) Simulated differential conductance maps corresponding to the frontier orbitals of the 3,1-cGNR. “H” indicates the highest occupied molecular orbital (HOMO); “L” indicates the lowest unoccupied molecular orbital (LUMO). c) Differential conductance maps recorded on the 3,1-cGNR, with the respective bias voltages indicated underneath. The bias voltages correspond to the successive peaks in the spectra over the ribbon and should therefore be correlated to the successive states in b.

In order to establish the nature of the frontier states, differential conductance maps were recorded at the energetic positions of the peaks in the dI/dV spectroscopy, and compared to simulated maps as obtained from tight-binding calculations. From the theoretical perspective, it is clear that infinitely long 3,1-cGNRs have a relatively small band gap compared to 7-acGNRs, with low-energy bands that have a pronounced edge-localized character. Calculations performed on the hexameric 3,1-cGNR return molecular orbitals around the Fermi energy that have a pronounced edge-localized character. Fig. 6.2b shows simulated differential conductance maps of the states from HOMO - 4 to LUMO + 5 obtained from this model. Experimental differential conductance

maps on the 6-monomer long 3,1-cGNR are shown in Fig. 6.2c. Nine states could be accessed at different bias voltages, and the corresponding maps reveal the respective orbital shapes in detail. In particular, the edge-localized character is immediately apparent for all energy states. At positive bias voltage, the maps have distinct nodal plane structures along the length of the nanoribbons. States at negative bias feature some overlap due to their broadening, and therefore some superposition is seen in the successive differential conductance maps that obscures the pattern for individual orbitals. Nevertheless, the simulated and experimental maps of the molecular orbitals are in good agreement. We note that, in comparison with 3,1-cGNRs on Au(111), a more pronounced localization of the orbitals on the edges is observed.[57] This result is analogous to the decoupling of zigzag end-localized states in 7-acGNRs and edge-localized states in zigzag-type nanoribbons on NaCl.[21, 47, 50]

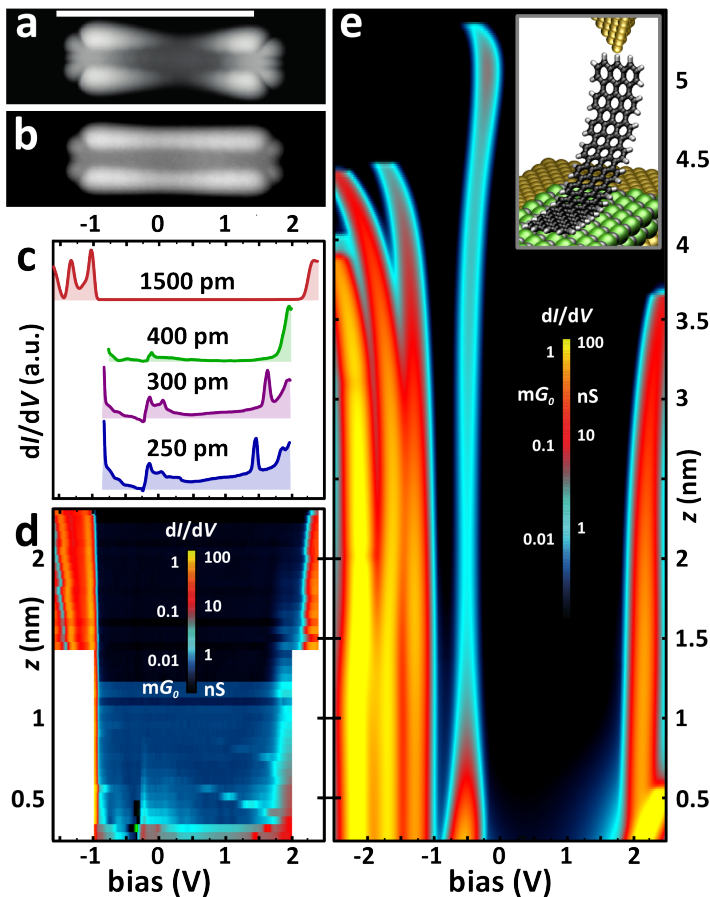
6.2.2 Conductance mapping of 7-acGNR

Now, we turn to the charge transport properties of graphene nanoribbons. The GNR to be studied was lifted from the substrate by approaching the tip to the middle of one zigzag terminus of the GNR, contacting the nanoribbon (as evidenced by a jump in the current), and moving the tip vertically. During the lifting process, the opposite end is expected to remain nearly flat on the surface. We will initially discuss the conductance experiments on 7-acGNRs. These were synthesized from 10,10'-dibromo-9,9'-bianthryl, following the procedure of Cai *et al.*[17] Vertical and subsequent horizontal transfer onto NaCl was performed, and by acquiring $I(V)$ spectra for a range of tip heights we obtained $dI/dV(V, z)$ maps of the conductance of 7-acGNR on NaCl on Au(111). This technique was applied to the 7-acGNR shown in Fig. 6.3a-b (where it is imaged on sodium chloride). A few individual $dI/dV(V)$ spectra at different heights are shown in Fig. 6.3c. Fig. 6.3d shows a two-dimensional contour plot of the conductance as a function of bias voltage and tip-sample distance (horizontal and vertical axis, respectively). A model of the nanoribbon being lifted off the NaCl by the tip is shown in the inset of Fig. 6.3e. It is clearly seen that the energy gap, where the conductance is essentially zero, is flanked by sharp onsets of resonant transport. Here, the conductance reaches values of over 100 nS, corresponding to approximately 2 per mille of the conductance quantum. This value is significantly lower than unimpeded molecular conductance as a result of the tunneling resistance of the NaCl. When the tip is retracted by more than 1.5 nm, peaks in the current transport are observed at approximately -1.0 V, -1.3 V and 2.3 V. For very low tip heights, off-resonant transport is visible inside the gap, becoming negligible for a tip height of approximately 1.5 nm. For increasing tip heights, the energy gap becomes larger, with the transport resonances shifting away from the Fermi level. We find that



the maximum currents these junctions can sustain are of the order of 100 nA; larger currents typically result in destruction of the junction. This limits the experimentally accessible bias voltage window. The main features of the maps are well reproduced in conductance experiments on various 7-acGNRs. Discontinuities are occasionally observed in successive spectra, which may originate from lateral relaxations of the segment of the nanoribbon in contact with the surface with increasing tip height - a stick-slip effect. Nevertheless, the peak positions and conductance values remain relatively well-behaved. In addition to the differential conductance, determination of the current and its gradient in (V, z) -space allows numerous transport quantities to be obtained. Fig. 6.4 shows the map of the current $I(V, z)$ and the resistance $R(V, z)$, as well as traces of the current, current decay dI/dz , conductance $G = I/V$, differential conductance, resistance $R = V/I$, and differential resistance dV/dI for the 7-acGNR of Fig. 6.3. Notably, the resistance takes on values in the T Ω range in the energy gap, but drops to the M Ω range upon reaching the resonant regime.

Fig. 6.3 Conductance mapping of 7-acGNR on NaCl. a) STM scan ($V = -1.0$ V, $I = 20$ pA) of a 5-monomer long 7-acGNR on NaCl on Au(111). Scale bar: 5 nm. b) STM scan of the same ribbon as panel a, at $V = -1.8$ V, $I = 20$ pA. c) $dI/dV(V)$ spectra (cross-sections of the map in panel d) on the 5-monomer long 7-acGNR for different values of the tip height z . d) Conductance map $dI/dV(V, z)$. e) Simulated conductance map $dI/dV(V, z)$ for the 5-monomer long 7-acGNR on NaCl on Au(111). The inset shows a model of the ribbon being lifted off the NaCl by the tip.



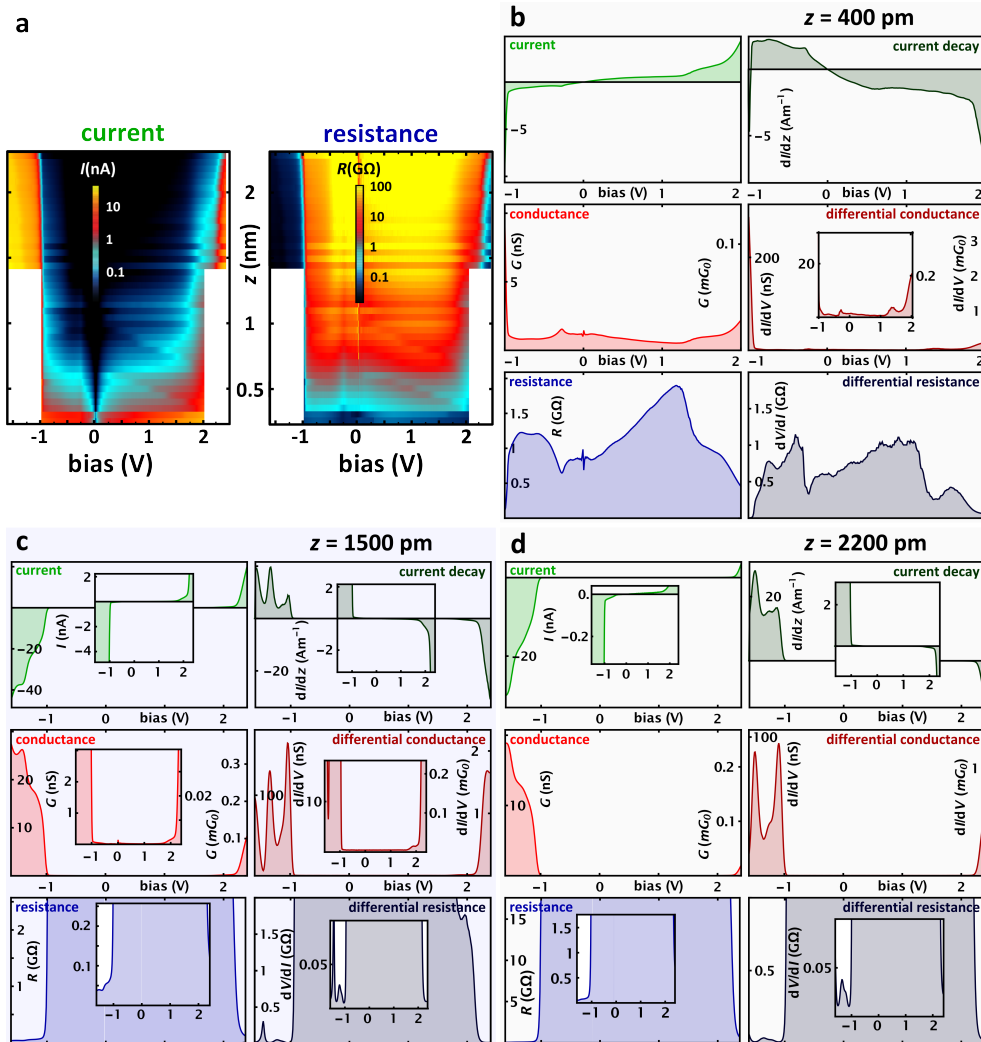


Fig. 6.4 Additional data from the experiment on the 7-acGNR. a) Current (I) and resistance ($R = V/I$) maps. For the current, absolute values are shown, but the sign of the current is negative for negative bias. b) Traces of the current, current decay (dI/dz), conductance (I/V), differential conductance (dI/dV), resistance (V/I), and differential resistance (dV/dI) at a tip height of 400 pm. c) Same as b, but at 1500 pm. d) Same as b, but at 2200 pm.

The energy values corresponding to the onset of resonant transport are in quantitative agreement with the values found in spectroscopy experiments.[47] We therefore assume that the transport is mediated by the corresponding frontier orbitals. At the same time, this suggests that attaching the tip to the ribbon does not strongly affect the frontier states of the nanoribbon. This is



in agreement with earlier work showing that the electronic structure of the ribbons is not significantly affected by contacting to a metallic lead.[58] The widening of the energy gap with increasing tip height can be understood in terms of capacitive effects. When the tip is lifted from the surface, the nanoribbon loses contact with the substrate, lowering the coupling of the nanoribbon to the substrate. This causes the relative coupling of the nanoribbon to the tip in comparison with the coupling to the surface to become more pronounced. By considering the double-junction system composed of tip, substrate and nanoribbon as a capacitive voltage divider[59, 60, 61], it is evident that the voltage of the nanoribbon becomes more capacitively coupled to the voltage of the tip. Now a larger bias voltage needs to be applied to reach resonance, explaining the opening of the energy gap with increasing tip height.

6.2.3 Conductance experiment simulations

To corroborate this picture, we performed transport simulations on GNRs within the framework of the non-equilibrium Green's function technique (NEGF) and the tight-binding model. In this model, the vacuum orbital energies are capacitively shifted from the vacuum energies by an amount given by the ratio of coupling to tip and surface. The model works by employing the following steps.

- The tight-binding Hamiltonian of the graphene nanoribbon is appended with self-energies to model the effect of coupling to the tip and substrate (the values are given in the Experimental methods section). The tip-induced self-energies are only present in the carbon atoms in contact with the tip. The metal substrate-induced self-energies are present in the carbon atoms in contact with the substrate. A model is used where the self-energy terms due to the substrate are reduced to zero along the long axis of the ribbon (using a spatial Fermi-Dirac-type function) to mimic the lifting from the surface. The surface-induced self-energy of atom i at position x_i is given by

$$\Sigma_{s,i} = \frac{\Lambda_i + i\gamma_i}{1 + e^{-\kappa x_i}}$$

Here, the decay parameter κ gives the inverse characteristic length over which the coupling strength of the individual carbon atoms along the length of the nanoribbon with the underlying metal substrate drops to zero. This parameter should therefore be related to the spatial extent over which the ribbon curves away from the surface - the “lift-off regime”. In our calculations, we set $\kappa = 4 \text{ nm}^{-1}$, noting that the precise value



should be extracted from geometric considerations. Models of nanoribbons being lifted from the surface and self-energy parametrizations are given in Fig. 6.5.

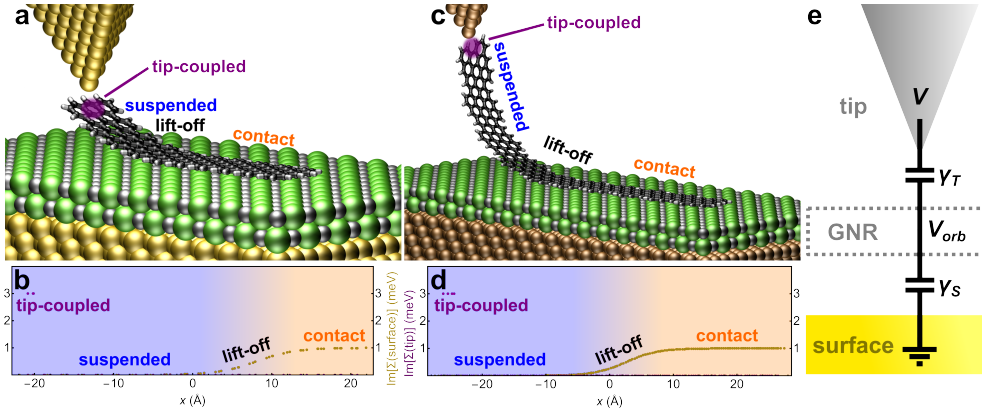


Fig. 6.5 Models and self-energy parameters of the graphene nanoribbons in lifting geometry. a) Model of a 5-monomer long 7-acGNR lifted by the tip from a NaCl monolayer on Au(111). Atoms that are coupled to the tip highlighted in purple. b) Self-energy values due to coupling to the tip (purple) and coupling to the surface (brown) for the 5-monomer long 7-acGNR. The suspended part of the nanoribbon (blue), the contacted part (orange) and the lift-off regime are indicated. c) Model of an 8-monomer long 3,1-cGNR, with atoms that are coupled to the tip highlighted in purple. d) Self-energy values due to coupling to the tip (purple) and coupling to the surface (brown) for an 8-monomer long 3,1-cGNR. The suspended part of the nanoribbon (blue), the contacted part (orange) and the lift-off regime are indicated. e) Equivalent circuit model (capacitive voltage divider) of the double barrier junction composed of tip, GNR and surface.

- The Hamiltonian is diagonalized to obtain the conductance orbitals and the eigenenergies.

$$\mathbf{E} = \mathbf{C}^{-1}(\mathbf{H} + \Sigma_s + \Sigma_t)\mathbf{C}$$

$$\mathbf{E}_{ij} = (\epsilon_i + i\gamma_i)\delta_{ij}$$

The diagonal eigenenergy matrix is the Hamiltonian matrix written in the eigenbasis of conductance orbitals.

- To include the charging energy - the energy difference between hole tunneling and electron tunneling - an empirical charging energy of 1.8 eV for 7-acGNR and 1.4 eV for 3,1-cGNR is used based on the size of the HOMO-LUMO gaps observed in spectroscopy[47, 62] in comparison to the tight-binding vacuum energies. After diagonalization, the occupied (valence band) states are downshifted and the unoccupied (conduction



band) states are upshifted by half this energy to transform the vacuum eigenenergies in charging-corrected eigenenergies.

- The next step in the model is to translate the charging-corrected eigenenergies to resonance energies in the transport model. To this end, the coupling matrices $\Gamma_{t/s}$ which are the anti-Hermitian parts of the self-energy matrices are transformed into the basis of molecular orbitals using a similarity transformation with the expansion coefficient matrices

$$\Gamma_{t/s,m} = \mathbf{C}^{-1}\Gamma_{t/s}\mathbf{C}$$

The coupling matrices in the basis of conductance orbitals are used to calculate the resonance energies. We assume that for each conductance orbital localized on the nanoribbon, there is an associated bias drop over the tip-nanoribbon junction and over the tip-sample junction. Therefore, the bias voltage at which the orbital resides is calculated by the relative capacitances of this “capacitive voltage divider”. This is shown schematically in Fig. 6.5e. We assume that each molecular orbital has a coupling γ_t to the tip and a coupling γ_s to the surface, where γ is the diagonal element of the coupling matrix in the basis of molecular orbitals. Setting the voltage of the substrate to zero, the energy of the orbital will shift with the applied bias to the tip V as [30, 60, 61, 49]

$$\epsilon(V) = \epsilon(0) + \frac{\gamma_t}{\gamma_t + \gamma_s}eV$$

The resonance condition is met when $\epsilon(V)$ enters the bias window which happens (at forward bias) at

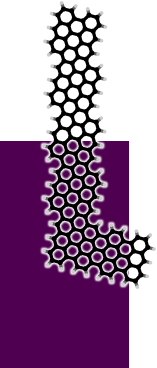
$$\epsilon = \frac{\gamma_t + \gamma_s}{\gamma_s}\epsilon(0)$$

This equation turns the vacuum energies into resonance energies.

- Now, we construct the (diagonal) Greens function matrix in the basis of conductance orbitals by inversion of the eigenenergy matrix.

$$\mathbf{G}_{m(ij)} = \frac{\delta_{ij}}{E - \epsilon_i}$$

The transmission is obtained using the Landauer formula in the conductance orbitals basis utilizing the retarded and advanced Greens function and using the coupling matrices in this basis. Since the trace is basis-independent, this is equivalent to calculating the transmission in the basis of the atomic sites of the graphene nanoribbon. Application of the



Landauer formula using the wide band limit has also been performed in [33].

$$T(E) = \frac{e^2}{\hbar} \text{tr} (\Gamma_{s,m} \mathbf{G}_m \Gamma_{t,m} \mathbf{G}_m^*)$$

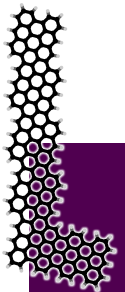
Under the assumption that, at the low temperatures of the experiment ($T = 4.5$ K), the Fermi-Dirac distribution function approximately takes the form of a step function, the differential conductance is approximately equal to the transmission. The simulated differential conductance maps are therefore maps of the transmission as a function of voltage and tip height.

Fig. 6.3e shows a simulated conductance map on the nanoribbon of Fig. 6.3a-d. There is a strong resemblance between the simulated and the experimental map. In particular, the opening of the band gap with increasing tip height is well reproduced. We note that the “phantom” transport channel near zero bias that arises in the simulation but not in the experiment is related to the end states of the nanoribbon, which are degenerate in the tight-binding model due to absence of explicit electron-electron interactions. In reality, these states are affected by coupling to the tip, lifting the degeneracy. In addition, they may be localized on either end and therefore not contribute to transport.[43, 62]

6.2.4 Conductance mapping of 3,1-cGNR

Having established the conductance characteristics of 7-acGNRs, we turned to the 3,1-cGNRs to apply the same methodology. In the same fashion as described above for 7-acGNRs, various 3,1-cGNRs were transferred onto NaCl and conductance measurements were performed by recording $I(V)$ and $dI/dV(V)$ spectra for a range of tip heights z , again resulting in two-dimensional maps of the conductance in (V, z) -space. Fig. 6.6a shows a conductance map of a 3,1-cGNR. Cross-sections of the map ($dI/dV(V)$, $dI/dz(V)$ and $I(V)$ spectra corresponding to two different tip heights) are shown in Fig. 6.6b.

For the 3,1-cGNR, the onsets of resonant transport occur at -1.3 V and 0.3 V. Similar to the case of 7-acGNRs, these values are in agreement with the energetic position of the HOMO and LUMO as obtained from spectroscopy measurements (see Fig. 6.2a). We can therefore again draw the conclusion that the perturbing effect of the tip on the frontier states is relatively small, and assume that the current transport at the resonant onsets is mediated by these orbitals. This shows that conductance maps of different nanoribbons immediately return transport characteristics that can be directly related to the electronic structure of the corresponding structures. The conductance maps consistently show onsets of conductance at the same bias voltages, the



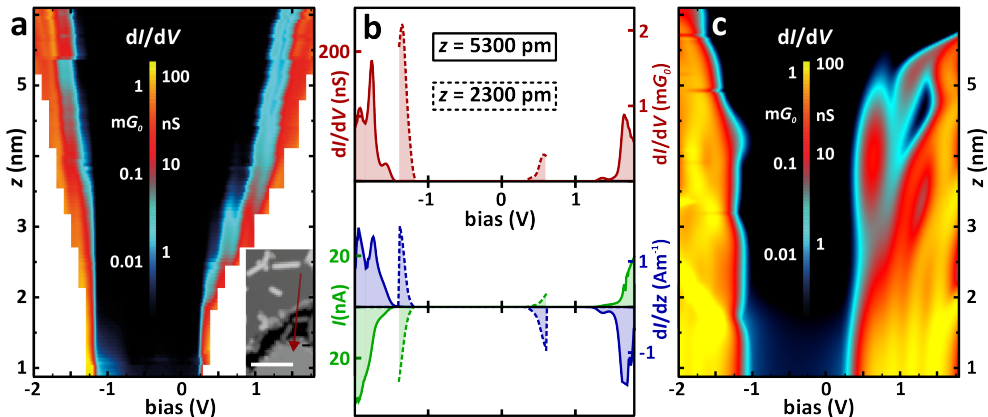


Fig. 6.6 Conductance mapping of 3,1-cGNR on NaCl. a) Conductance map $dI/dV(V, z)$. The inset shows an STM scan ($V = -1.8$ V, $I = 20$ pA) of the 3,1-cGNR before manipulation onto the NaCl (manipulation indicated with the red arrow). Scale bar: 10 nm. b) $dI/dV(V)$ spectra (red), $I(V)$ spectra (green) and dI/dz curves (blue) of the 3,1-cGNR at two different tip heights. The dashed curves (smaller bias window) correspond to the ribbon lifted to a height of 2300 pm, whereas the solid curves correspond to a tip height of 5300 pm. c) Simulated conductance map $dI/dV(V, z)$ for the 3,1-cGNR on NaCl on Cu(111).

same magnitude of the (differential) conductance, and the same qualitative features and opening of the energy gap, regardless of tip apex shape or ribbon length.

For increasing tip heights, the energy gap widens, similar to the effect of 7-acGNRs on NaCl on Au(111). This effect is also observed in the simulation, as shown in Fig. 6.6c. Although there is a qualitative agreement between the experimental and simulated conductance maps, the shifting of the transport resonances away from the Fermi energy is more uniform in the experiment than in the calculations. Moreover, we find that the energy gap widening with increasing tip height is almost independent of ribbon length. This hints towards a similar magnitude of capacitive coupling of conductance orbitals to the surface in short and long nanoribbons. We tentatively propose that the orbitals that play a role in transport are more strongly localized on the part of the nanoribbon between tip and surface due to their bent geometry[43] and possibly an internal bias drop[63], limiting the proportion of the orbitals in capacitive connection to the surface to a relatively short segment close to the point where the nanoribbon curves up from the surface. The simple tight-binding-based transport model used here does not take these effects into account. We expect more accurate models to yield a more quantitative resemblance. The above results show that the conductance profiles of different ribbons can be understood and simulated in terms of the different electronic

structures of the respective ribbons and capacitive effects due to coupling to tip and substrate.

For both 7-acGNRs and 3,1-cGNRs, we also measured conductance maps on the bare metal surface. Although the onsets of resonant transport could be observed, it was found that the large currents involved prevented us from increasing the bias voltage sufficiently far to be able to properly observe peaks related to resonant transport. Attempts to do so were repeatedly met with destruction of the junction. Furthermore - and especially in the case with 3,1-cGNRs - significant discontinuities are observed between successive spectra, likely originating from a severe stick-slip effect of the segment of the nanoribbon in contact with the surface, due to the strong interaction of the GNR with the metal. This underlines the necessity of intercalation in conductance experiments.

6.2.5 Double modulation spectroscopy

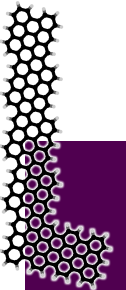
The final result relates to our further development of the conductance mapping methodology. In addition to the current I and the differential conductance dI/dV , another quantity of interest is the current decay with increasing tip height dI/dz . More specifically, an important parameter in the context of transport is the current decay parameter β , which is the proportionality constant in the exponential decay of current with tip height.

$$I(V, z) = I(V, z_0)e^{-\beta(z-z_0)}$$

For ballistic transport in the resonant regime, the current does not decay with junction length: β should vanish. However, the bent geometry of the ribbon in the junction can result in a non-zero value of the decay parameter, also during resonant transport.[43] Measurements of β have been instrumental in conductance measurements on GNRs.[33] Usually, β is extracted by fitting a $\ln(I)$ vs z plot. However, since β is a function of voltage, but may even depend on tip height (for example in the multi-exponential decay in GNR heterojunctions[33]), a technique to measure $\beta(V, z)$ locally is desirable. The differential conductance dI/dV can efficiently be obtained using a lock-in amplifying technique, where a modulation signal is added to the bias voltage. In the same spirit, in order to measure dI/dz , we subjected the z -piezoelectric element of the tip to a modulation signal from a second lock-in amplifier. The resulting current through the junction can be described as

$$I(t) = I_0 + V_{\text{mod}} \frac{dI}{dV} e^{i\omega_V t} + z_{\text{mod}} \frac{dI}{dz} e^{i\omega_z t}$$

where I_0 is the discrete component of the tunnel current, V_{mod} and ω_V the modulation amplitude and frequency of the voltage modulation, and z_{mod} and



ω_z the amplitude and frequency of the tip-height modulation. After conversion of the tunnel current signal to a voltage by the control unit (CU), this signal can be distributed to the respective lock-in amplifiers, with each lock-in amplifier “selecting” the current component according to frequency. A schematic image of this set-up is shown in Fig. 6.7a. Finally, β is calculated as

$$\beta(V, z) = -\frac{\partial \ln I(V, z)}{\partial z} = -\left(\frac{1}{I(V, z)}\right) \frac{\partial I(V, z)}{\partial z}$$

The value of I is simply the discrete (or time-averaged) value of the tunnel current, and dI/dz is extracted from the tip-height modulating lock-in amplifier. The absence of cross-talk between the dI/dV and dI/dz signals was established by recording spectra on a 7-acGNR on NaCl on Au(111) with the separate lock-in signals switched on and off.

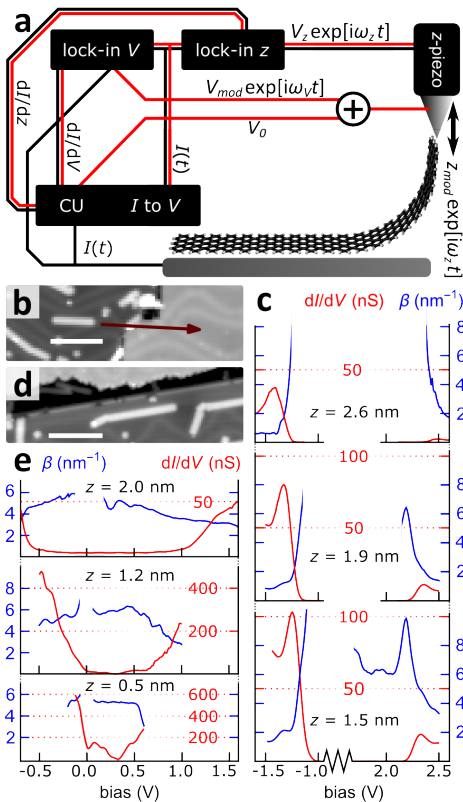


Fig. 6.7 Conductance decay measurements using the double modulation technique. a) Schematic set-up of the lock-in amplifiers to modulate the bias voltage and tip height and record dI/dV and dI/dz simultaneously. b) STM scan ($V = -1.8$ V, $I = 20$ pA) of a 7-acGNR which was subjected to double modulation spectroscopy experiments after transfer to NaCl (transfer indicated with the red arrow). c) Conductance (red) and current decay (blue) for the ribbon of panel b, on NaCl. d) STM image of a 7-acGNR which was subjected to double modulation spectroscopy on Au(111). e) Conductance (red) and current decay (blue) for the ribbon of panel d, on Au(111).

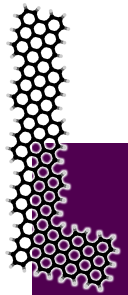
This technique was used to simultaneously measure dI/dV and dI/dz on a 7-acGNR suspended between the tip and NaCl/Au(111) surface. Fig. 6.7b shows an STM scan of a ribbon that was picked up and dragged onto a NaCl patch. Fig. 6.7c shows spectra of the conductance (red) and the current decay parameter β (blue) at different tip-sample distances. As can clearly be seen,

β is large inside the gap region (it diverges as the current becomes essentially zero) and decreases when resonant tunneling become accessible. At 2.63 nm, β is seen to decrease to values as low as 0.5 nm^{-1} (at voltages corresponding to tunneling through the HOMO), down from 2 nm^{-1} for the same transport channel at $z = 1.5 \text{ nm}$. The faster decay of the transport channel on the positive bias side compared to the channel on the negative bias side manifests itself in a consistently higher value of β at the energies corresponding to the resonance found in the dI/dV . The fact that the conductance decay goes to zero for the HOMO resonance indicates that it obtains an increasingly ballistic character, and after an initial decrease in the conductance possibly due to the curvature of the nanoribbon as the junction is in the formation stage[43] further increase of the junction results does not suppress the current anymore. This suggests that the HOMO could contribute to long-range transport.[46]

As a further validation of this technique and in order to compare with established results, an experiment was carried out on the ribbon shown in Fig. 6.7d, which was not dragged onto NaCl. Fig. 6.7e shows dI/dV and dI/dz spectra, focusing on the low-bias regime at low tip heights. Similar to earlier studies, the value of β becomes 5 nm^{-1} for low bias, or off-resonant transport. In addition to this off-resonant decay value, it can be seen that β diminishes when approaching onsets of resonance in the differential conductance, again in agreement with earlier experiments.[43] In contrast with earlier literature results, β can now be determined in a single continuous spectrum, rather than recording numerous $I(z)$ spectra and extracting a value through fitting. Moreover, β can be determined for precisely defined tip heights, even when the current decay with tip height is multi-exponential due to the nanoribbons being segmented or transport resonances shifting in energy capacitively. We conclude that the double modulation spectroscopy technique allows for a voltage- and junction length dependent measurement of the current decay parameter, where the degree of ballistic transport can be found as a function of tip height and voltage in a single measurement.

6.3 Conclusions

We demonstrated successful electronic decoupling of different types of GNRs by STM-mediated transfer onto an intercalating layer of NaCl. STS measurements on electronically decoupled 3,1-cGNRs revealed the existence of edge-localized frontier states at low bias voltages. The spectroscopic analysis provided a benchmark for the electronic structure for comparison with conductance experiments. The conductance of individual GNRs was measured in lifting geometry, using the methodology developed by Koch *et al.*[43] Besides electronic decoupling, the monolayer of NaCl acts as an additional



tunnel barrier, minimizing the risk of current-induced defect formation and thereby facilitating the characterization of resonant transport along the long GNR axis. Too high currents can result in defective GNRs, presumably due to dehydrogenation of the edges and carbon-carbon bond cleavage, as well as ejection of tip material onto the surface/GNR. We mapped out the conductance of 7-acGNRs and 3,1-cGNRs in (V, z) -space and observed transport through multiple resonant channels. The $dI/dV(V, z)$ maps provide detailed information on the conductance properties. The height-dependence of the conductance can be explained in terms of the electronic structures of the specific types of GNRs and capacitive coupling to tip and substrate. Specifically, the widening of the band gap with increasing tip height can be understood in terms of a decreasing coupling of molecular orbitals with the surface compared to the tip. This explanation was corroborated by transport calculations.

Finally, we demonstrated the feasibility of double modulation spectroscopy simultaneously measuring the differential conductances dI/dV and dI/dz by making use of two separate lock-in amplifiers. The double modulation spectroscopy technique allowed for the simultaneous measurement of $I(V, z)$ and its gradient $\nabla I(V, z)$, from which the current decay β can readily be extracted. This parameter was shown to give a “degree” of resonance of transport, with $\beta = 5 \text{ nm}^{-1}$ returned as the well-known off-resonant transport value for 7-acGNRs on Au(111) and values decreasing to 0.5 nm^{-1} indicating the transport channel obtaining a more ballistic character.

6.4 Experimental methods

6.4.1 Conductance mapping

After lifting the GNRs to the desired height z and laterally manipulating to the desired position, $I(V, z)$ current measurements were performed by recording $I(V)$ spectra for a series of tip heights z . Here, $z = 0$ corresponds to the lowest tip height that was used, where the tunnel current between the tip and metal surface, without a contacted nanoribbon, is 400 pA at a bias voltage of 10 mV. Each single $I(V)$ curve was followed by a tip height increment/decrement Δz of 20-100 pm. All measurements are performed at a resolution of $\Delta V = 10 \text{ mV}$ per point, regardless of bias range, and with an integration time of 50 ms per point. $dI/dV(V)$ spectra were obtained using a 819 Hz oscillating signal of amplitude 5 mV RMS, and 50 ms integration time per point. Numerical values of the differential conductance were obtained by scaling the dI/dV data to give the least-squares fit to the differential conductance obtained through numerically differentiating the $I(V)$ spectra. It was found that during the course of measurements, there is always a chance of drop-down (detachment from the tip), pick-up (irreversible attachment to

the tip), tip crash or current-induced destruction of single nanoribbons. In order to prevent the latter, the bias voltage range was dynamically adjusted during the course of measurements (where in our experience, currents larger than approximately 100 nA give rise to an increased risk of detachments or defect formation due to inelastic processes). Following an experiment that takes around 2 or 3 hours, going back to the feedback set-point revealed that the total drift is of the order of 100 pm. This is small in comparison with the range of the conductance maps.

6.4.2 Double modulation spectroscopy

The tip height was modulated with a 20 pm (peak-to-peak) oscillation amplitude at a frequency of 121 Hz, by application of the appropriate modulation voltage to the z -piezo of the STM.

6.4.3 Tight-binding calculations

The simulated differential conductance maps were obtained by diagonalizing a tight-binding Hamiltonian containing on-site energies ϵ_0 and nearest-neighbor hopping parameters t . We employed a 12 percent increase of the hopping integral t for carbon atoms on the edge, so that $t_{ij}(\text{edge}) = 1.12 t$ whenever atom i or j is bonded to at least one hydrogen atom. The simulated maps correspond to pure eigenstates, the orbitals of which are convolved with a Gaussian-shaped tip of width 1.2 Å to simulate the finite size of the STM tip.

6.4.4 Conductance map simulations

For the simulated conductance maps, the non-equilibrium Greens function technique was applied in the wide-band limit[33, 64] (J. M. Thijssen, personal communication), in conjunction with the aforementioned tight-binding model. Here, we use a nearest-neighbor interaction parameter $t = -2.7$ eV[65], and an on-site energy of $\epsilon_0 = 0.8$ eV for 7-acGNRs on Au(111) and $\epsilon_0 = 0.2$ eV for 3,1-cGNRs on Cu(111), reflecting the Fermi energy difference of graphene *in vacuo* with respect to that of gold and copper.[66, 67, 68, 69, 70] We employ an empirical charging energy (difference between hole tunneling and electron tunneling) of 1.8 eV for 7-acGNRs and 1.4 eV for 3,1-cGNRs based on the size of the HOMO-LUMO gaps observed in spectroscopy[47, 59] in comparison to the vacuum energies found from tight-binding. The self-energies due to the substrate are $\sigma_{sub} = \Lambda + 1i$ meV and those due to the tip are $\sigma_{tip} = \Lambda + 3i$ meV. The self-energies due to the substrate are spatially modulated to zero to simulate lifting. The real parts of the self-energies are $\Lambda = -0.6$ eV for 7-acGNRs on Au(111) and $\Lambda = -0.4$ eV for 3,1-cGNRs on Cu(111). The parametrization is schematically shown in Fig. 6.5. Broadening - primarily due



to interaction with phonons in the NaCl - is taken into account by convolving the conductance map with a Gaussian peak of width 100 meV, similar to the peak widths observed in spectroscopy.[49]

Bibliography

- [1] K. S. Novoselov, A. K. Geim, S. V. Morozov, D. Jiang, Y. Zhang, S. V. Dubonos, I. V. Grigorieva, and A. A. Firsov, *Science* **306**, pp. 666–669 (2004).
- [2] A. K. Geim and K. S. Novoselov, *Nature Materials* **6**, pp. 183–191 (2007).
- [3] A. H. Castro Neto, F. Guinea, N. M. R. Peres, K. S. Novoselov, and A. K. Geim, *Reviews of Modern Physics* **81**, pp. 109–162 (2009).
- [4] K. Nakada, M. Fujita, G. Dresselhaus, and M. S. Dresselhaus, *Physical Review B* **54**, pp. 17954–17961 (1996).
- [5] Y. W. Son, M. L. Cohen, and S. G. Louie, *Physical Review Letters* **97**, pp. 216803 (2006).
- [6] L. Yang, C. H. Park, Y. W. Son, M. L. Cohen, and S. G. Louie, *Physical Review Letters* **99**, pp. 186801 (2007).
- [7] K. Wakabayashi, K.-I. Sasaki, T. Nakanishi, and T. Enoki, *Science and Technology of Advanced Materials* **11**, pp. 054504 (2010).
- [8] A. Narita, X. Feng, and K. Müllen, *Chemical Record* **15**, pp. 295–309 (2015).
- [9] A. Narita, X.-Y. Wang, X. Feng, and K. Müllen, *Chem. Soc. Rev.* **44**, pp. 6616–6643 (2015).
- [10] R. Lindner and A. Kühnle, *ChemPhysChem* **16**, pp. 1582–1592 (2015).
- [11] Q. Shen, H.-Y. Gao, and H. Fuchs, *Nano Today* **13**, pp. 77–96 (2017).
- [12] G. D. Nguyen, F. M. Toma, T. Cao, Z. Pedramrazi, C. Chen, D. J. Rizzo, T. Joshi, C. Bronner, Y. C. Chen, M. Favaro, S. G. Louie, F. R. Fischer, and M. F. Crommie, *Journal of Physical Chemistry C* **120**, pp. 2684–2687 (2016).
- [13] R. R. Cloke, T. Marangoni, G. D. Nguyen, T. Joshi, D. J. Rizzo, C. Bronner, T. Cao, S. G. Louie, M. F. Crommie, and F. R. Fischer, *Journal of the American Chemical Society* **137**, pp. 8872–8875 (2015).
- [14] S. Kawai, S. Saito, S. Osumi, S. Yamaguchi, A. S. Foster, P. Spijker, and E. Meyer, *Nature Communications* **6**, pp. 8098 (2015).
- [15] L. Talirz, H. Söde, T. Dumslaff, S. Wang, J. R. Sanchez-Valencia, J. Liu, P. Shinde, C. A. Pignedoli, L. Liang, V. Meunier, N. C. Plumb, M. Shi, X. Feng, A. Narita, K. Müllen, R. Fasel, and P. Ruffieux, *ACS Nano* **11**, pp. 1380–1388 (2017).
- [16] A. Kimouche, M. M. Ervasti, R. Drost, S. Halonen, A. Harju, P. M. Joensuu, J. Sainio, and P. Liljeroth, *Nature Communications* **6**, pp. 10177 (2015).
- [17] J. Cai, P. Ruffieux, R. Jaafar, M. Bieri, T. Braun, S. Blankenburg, M. Muoth, A. P. Seitsonen, M. Saleh, X. Feng, K. Müllen, and R. Fasel, *Nature* **466**, pp. 470–473 (2010).
- [18] H. Zhang, H. Lin, K. Sun, L. Chen, Y. Zagryarski, N. Aghdassi, S. Duhm, Q. Li, D. Zhong, Y. Li, K. Müllen, H. Fuchs, and L. Chi, *Journal of the American Chemical Society* **137**, pp. 4022–4025 (2015).
- [19] A. Basagni, F. Sedona, C. A. Pignedoli, M. Cattelan, L. Nicolas, M. Casarin, and M. Sambri, *Journal of the American Chemical Society* **137**, pp. 1802–1808 (2015).
- [20] Y. C. Chen, D. G. De Oteyza, Z. Pedramrazi, C. Chen, F. R. Fischer, and M. F. Crommie, *ACS Nano* **7**, pp. 6123–6128 (2013).
- [21] P. Ruffieux, S. Wang, B. Yang, C. Sanchez-Sanchez, J. Liu, T. Dienel, L. Talirz, P. Shinde, C. A. Pignedoli, D. Passerone, T. Dumslaff, X. Feng, K. Müllen, and R. Fasel, *Nature* **531**, pp. 489–492 (2016).

- [22] J. Liu, B.-W. Li, Y.-Z. Tan, A. Giannakopoulos, C. Sanchez-Sanchez, D. Beljonne, P. Ruffieux, R. Fasel, X. Feng, and K. Müllen, *Journal of the American Chemical Society* **137**, pp. 6097–6103 (2015).
- [23] P. Han, K. Akagi, F. Federici Canova, H. Mutoh, S. Shiraki, K. Iwaya, P. S. Weiss, N. Asao, and T. Hitosugi, *ACS Nano* **8**, pp. 9181–9187 (2014).
- [24] P. Han, K. Akagi, F. Federici Canova, R. Shimizu, H. Oguchi, S. Shiraki, P. S. Weiss, N. Asao, and T. Hitosugi, *ACS Nano* **9**, pp. 12035–12044 (2015).
- [25] C. Sánchez-Sánchez, T. Dienel, O. Deniz, P. Ruffieux, R. Berger, X. Feng, K. Müllen, and R. Fasel, *ACS Nano* **10**, pp. 8006–8011 (2016).
- [26] F. Schulz, P. H. Jacobse, F. F. Canova, J. Van Der Lit, D. Z. Gao, A. Van Den Hoogenband, P. Han, R. J. Klein Gebbink, M. E. Moret, P. M. Joensuu, I. Swart, and P. Liljeroth, *Journal of Physical Chemistry C* **121**, pp. 2896–2904 (2017).
- [27] D. G. De Oteyza, A. García-Lekue, M. Vilas-Varela, N. Merino-Díez, E. Carbonell-Sanromà, M. Corso, G. Vasseur, C. Rogero, E. Guitián, J. I. Pascual, J. E. Ortega, Y. Wakayama, and D. Peña, *ACS Nano* **10**, pp. 9000–9008 (2016).
- [28] M. Fujita, K. Wakabayashi, K. Nakada, and K. Kusakabe, *Journal of the Physical Society of Japan* **65**, pp. 1920–1923 (1996).
- [29] C. Tao, L. Jiao, O. V. Yazyev, Y. C. Chen, J. Feng, X. Zhang, R. B. Capaz, J. M. Tour, A. Zettl, S. G. Louie, H. Dai, and M. F. Crommie, *Nature Physics* **7**, pp. 616–620 (2011).
- [30] Z. Jiang and Y. Song, *Physica B: Condensed Matter* **464**, pp. 61–67 (2015).
- [31] A. R. Carvalho, J. H. Warnes, and C. H. Lewenkopf, *Physical Review B - Condensed Matter and Materials Physics* **89**, pp. 245444 (2014).
- [32] L. Sun, P. Wei, J. Wei, S. Sanvito, and S. Hou, *Journal of Physics Condensed Matter* **23**, pp. 425301 (2011).
- [33] P. H. Jacobse, A. Kimouche, T. Gebraad, M. M. Ervasti, J. M. Thijssen, P. Liljeroth, and I. Swart, *Nature Communications* **8**, pp. 119 (2017).
- [34] S. Blankenburg, J. Cai, P. Ruffieux, R. Jaafar, D. Passerone, X. Feng, K. Müllen, R. Fasel, and C. A. Pignedoli, *ACS Nano* **6**, pp. 2020–2025 (2012).
- [35] Y. C. Chen, T. Cao, C. Chen, Z. Pedramrazi, D. Haberer, D. G. De Oteyza, F. R. Fischer, S. G. Louie, and M. F. Crommie, *Nature Nanotechnology* **10**, pp. 156–160 (2015).
- [36] S. Wang, N. Kharche, E. Costa Girão, X. Feng, K. Müllen, V. Meunier, R. Fasel, and P. Ruffieux, *Nano Letters* **17**, pp. 4277–4283 (2017).
- [37] C. Bronner, R. A. Durr, D. J. Rizzo, Y.-L. Lee, T. Marangoni, A. M. Kalayjian, H. Rodriguez, W. Zhao, S. G. Louie, F. R. Fischer, and M. F. Crommie, *ACS Nano* **12**, pp. 2193–2200 (2018).
- [38] J. Cai, C. A. Pignedoli, L. Talirz, P. Ruffieux, H. Söde, L. Liang, V. Meunier, R. Berger, R. Li, X. Feng, K. Müllen, and R. Fasel, *Nature Nanotechnology* **9**, pp. 896–900 (2014).
- [39] G. D. Nguyen, H. Z. Tsai, A. A. Omrani, T. Marangoni, M. Wu, D. J. Rizzo, G. F. Rodgers, R. R. Cloke, R. A. Durr, Y. Sakai, F. Liou, A. S. Aikawa, J. R. Chelikowsky, S. G. Louie, F. R. Fischer, and M. F. Crommie, *Nature Nanotechnology* **12**, pp. 1077–1082 (2017).
- [40] B. Huang, Q. M. Yan, Z. Y. Li, and W. H. Duan, *Frontiers of Physics in China* **4**, pp. 269–279 (2009).
- [41] P. B. Bennett, Z. Pedramrazi, A. Madani, Y. C. Chen, D. G. De Oteyza, C. Chen, F. R. Fischer, M. F. Crommie, and J. Bokor, *Applied Physics Letters* **103**, pp. 253114 (2013).
- [42] J. P. Llinas, A. Fairbrother, G. Borin Barin, W. Shi, K. Lee, S. Wu, B. Yong Choi, R. Braganza, J. Lear, N. Kau, W. Choi, C. Chen, Z. Pedramrazi, T. Dumslaff, A. Narita, X. Feng, K. Müllen, F. Fischer, A. Zettl, P. Ruffieux, E. Yablonovitch, M. Crommie, R. Fasel, and J. Bokor, *Nature Communications* **8**, pp. 1–15 (2017).



- [43] M. Koch, F. Ample, C. Joachim, and L. Grill, *Nature Nanotechnology* **7**, pp. 713–717 (2012).
- [44] L. Lafferentz, F. Ample, H. B. Yu, S. Hecht, C. Joachim, and L. Grill, *Science* **323**, pp. 1193–1197 (2009).
- [45] C. Nacci, F. Ample, D. Blegler, S. Hecht, C. Joachim, and L. Grill, *Nature Communications* **6**, pp. 7397 (2015).
- [46] G. Kuang, S. Z. Chen, W. Wang, T. Lin, K. Chen, X. Shang, P. N. Liu, and N. Lin, *Journal of the American Chemical Society* **138**, pp. 11140–11143 (2016).
- [47] S. Wang, L. Talirz, C. A. Pignedoli, X. Feng, K. Müllen, R. Fasel, and P. Ruffieux, *Nature Communications* **7**, pp. 11507 (2016).
- [48] O. Deniz, C. Sánchez-Sánchez, T. Dumsflaff, X. Feng, A. Narita, K. Müllen, N. Khariche, V. Meunier, R. Fasel, and P. Ruffieux, *Nano Letters* **17**, pp. 2197–2203 (2017).
- [49] J. Repp, G. Meyer, S. M. Stojković, A. Gourdon, and C. Joachim, *Physical Review Letters* **94**, pp. 26803 (2005).
- [50] C. Bombis, F. Ample, L. Lafferentz, H. Yu, S. Hecht, C. Joachim, and L. Grill, *Angewandte Chemie - International Edition* **48**, pp. 9966–9970 (2009).
- [51] S. Kawai, A. Benassi, E. Gnecco, H. Söde, R. Pawlak, X. Feng, K. Müllen, D. Passerone, C. A. Pignedoli, P. Ruffieux, R. Fasel, and E. Meyer, *Science* **351**, pp. 957–961 (2016).
- [52] J. Björk, S. Stafström, and F. Hanke, *J. Am. Chem. Soc.* **133**, pp. 14884–14887 (2011).
- [53] P. Ruffieux, J. Cai, N. C. Plumb, L. Patthey, D. Prezzi, A. Ferretti, E. Molinari, X. Feng, K. Müllen, C. A. Pignedoli, and R. Fasel, *ACS Nano* **6**, pp. 6930–6935 (2012).
- [54] H. Söde, L. Talirz, O. Gröning, C. A. Pignedoli, R. Berger, X. Feng, K. Müllen, R. Fasel, and P. Ruffieux, *Physical Review B - Condensed Matter and Materials Physics* **91**, pp. 045429 (2015).
- [55] A. R. Akhmerov and C. W. J. Beenakker, *Physical Review B* **77**, pp. 85423 (2008).
- [56] M. Wimmer, A. R. Akhmerov, and F. Guinea, *Physical Review B* **82**, pp. 45409 (2010).
- [57] N. Merino-Díez, J. Li, A. Garcia-Lekue, G. Vasseur, M. Vilas-Varela, E. Carbonell-Sanromà, M. Corso, J. E. Ortega, D. Peña, J. I. Pascual, and D. G. De Oteyza, *Journal of Physical Chemistry Letters* **9**, pp. 25–30 (2018).
- [58] J. van der Lit, M. P. Boneschanscher, D. Vanmaekelbergh, M. Ijäs, A. Uppstu, M. Ervasti, A. Harju, P. Liljeroth, and I. Swart, *Nature Communications* **4**, pp. 2023 (2013).
- [59] I. Swart, L. Gross, and P. Liljeroth, *Chemical Communications* **47**, pp. 9011 (2011).
- [60] G. V. Nazin, S. W. Wu, and W. Ho, *Proceedings of the National Academy of Sciences of the United States of America* **102**, pp. 8832–8837 (2005).
- [61] A. Nitzan and M. A. Ratner, *Science* **300**, pp. 1384–1389 (2003).
- [62] M. Ijäs, M. Ervasti, A. Uppstu, P. Liljeroth, J. van der Lit, I. Swart, and A. Harju, *Physical Review B - Condensed Matter and Materials Physics* **88**, pp. 75429 (2013).
- [63] G. C. Liang, A. W. Ghosh, M. Paulsson, and S. Datta, *Physical Review B - Condensed Matter and Materials Physics* **69**, pp. 115302 (2004).
- [64] H. Haug and A.-P. Jauho, “Quantum kinetics in transport and optics of semiconductors, Volume 6” (2008).
- [65] R. Kundu, *Modern Physics Letters B* **25**, pp. 163–173 (2011).
- [66] G. A. Haas and R. E. Thomas, *Journal of Applied Physics* **48**, pp. 86–93 (1977).
- [67] D. Pescia and F. Meier, *Surface Science* **117**, pp. 302–309 (1982).
- [68] J. Sławińska, I. Wlasny, P. Dabrowski, Z. Klusek, and I. Zasada, *Physical Review B - Condensed Matter and Materials Physics* **85**, pp. 235430 (2012).
- [69] V. Barone, J. E. Peralta, J. Uddin, and G. E. Scuseria, *J. Chem. Phys.* **124**, pp. 24709 (2006).
- [70] H. Ishii, H. Oji, E. Ito, N. Hayashi, D. Yoshimura, and K. Seki, *Journal of Luminescence* **87**, pp. 61–65 (2000).

Appendix



The summary in Dutch in this chapter is adapted from
Tunneldiodes en metaal-halfgeleiderverbindingen van grafeen-nanodraden
Peter H. Jacobse, Ingmar Swart
NEVAC BLAD 56 (June), pp. 6-10 (2018)

7.1 Samenvatting in het Nederlands

Grafeen-nanodraden zijn smalle strookjes van grafeen die - in tegenstelling tot het bulkmateriaal - een bandkloof kunnen hebben, een eigenschap waardoor ze interessante kandidaten zijn voor toekomstige nanoelektronica. De aanwezigheid en grootte van deze bandkloof is sterk afhankelijk van de breedte en structuur van de draden. Met behulp van oppervlaktesynthese in ultrahoogvacuüm (UHV) kunnen met atomaire precisie verschillende typen nanodraden gemaakt worden en bovendien heterostructuren zoals metaal-halfgeleiderverbindingen direct in individuele draden ingebouwd worden. De elektronische en geometrische structuren van de draden kunnen in kaart gebracht worden met rastertunnelmicroscopie en atoomkrachtmicroscopie, ook in UHV. Bovendien kan de geleiding gemeten worden door de grafeen-nanodraden op te tillen aan de tip. Deze metingen laten zien hoe verschillende armchair- en chirale nanodraden zich gedragen en laten karakteristieken zien van elektronische componenten in een enkele draad, zoals een tunnelbarrière. De combinatie van chemische synthese, oppervlaktesynthese en elektronische karakterisatie ligt aan de basis van het experimentele werk beschreven in dit proefschrift. In toevoeging daarop is er ook theoretisch werk gebaseerd op het gebied van tight-binding, een praktische methode om de quantummechanische structuur van grafeen-nanodraden te berekenen en derhalve de elektronische eigenschappen te kunnen deduceren.

De behoefte van de moderne mens aan steeds snellere en compactere elektronica, aan steeds krachtiger gadgets en smartphones en steeds meer dataopslag lijkt eindeloos. Om aan deze behoefte tegemoet te komen is het van belang dat elektronische componenten zoals geheugencellen en logische poorten steeds kleiner worden. Deze continue inspanning om elektronica steeds verder te miniaturizeren heeft het reeds mogelijk gemaakt om transistors en diodes van kleiner dan 10 nanometer te maken (10 miljoenste van een millimeter). Derhalve is het vandaag de dag mogelijk om het equivalent van meer dan 80 high-definition videos op te slaan op een USB-stick van slechts 7,5 centimeter.

Helaas heeft het er alle schijn van dat de miniaturisatie van elektronica in de nabije toekomst tegen een aantal grenzen aan zal lopen. Een belangrijke barrière is dat het lithografieproces, waarmee de baantjes met behulp van licht op siliciumchips worden geprint - vanwege de inherente diffractielimiet van elektromagnetische straling en thermische effecten in de chips - bij nog kleinere lengteschalen niet meer zal werken. De onvermijdelijke vraag is hoe lang we deze methodes nog kunnen aanwenden voor onze elektronica.

Bottom-up methodes, waarbij elektronisch functionele componenten ge-

assembleerd worden uit kleinere structuren in plaats van ze te definiëren in bulkmaterialen - hebben de potentie om in het veld van nanoelektronica een revolutie te veroorzaken. Dit is de hoofdgedachte achter het nieuwe veld van moleculaire elektronica: om de elektronica van morgen uit moleculen op te bouwen in plaats van in microchips te branden. Om koolstof te gebruiken in plaats van silicium. Om transistors, diodes en chips op te bouwen uit de kleinst mogelijke structuren.

Naast de belofte die de moleculaire approach met zich meebrengt voor komende generaties van nanoelektronica moet ook grafeen genoemd worden. Sinds de ontdekking van grafeen in 2004 wordt het materiaal gezien als een wondermateriaal voor de toekomst. Niet alleen heeft het atomair dunne honingraatrooster van koolstof (zie Fig. 7.1) ongeëvenaarde mechanische eigenschappen, maar bovenal is aangetoond dat het elektronen vele malen beter kan geleiden dan metalen zoals koper en goud. Grafeen heeft daarom óók de potentie het materiaal te zijn waarop een volgende generatie van nog snellere microchips wordt gebouwd.

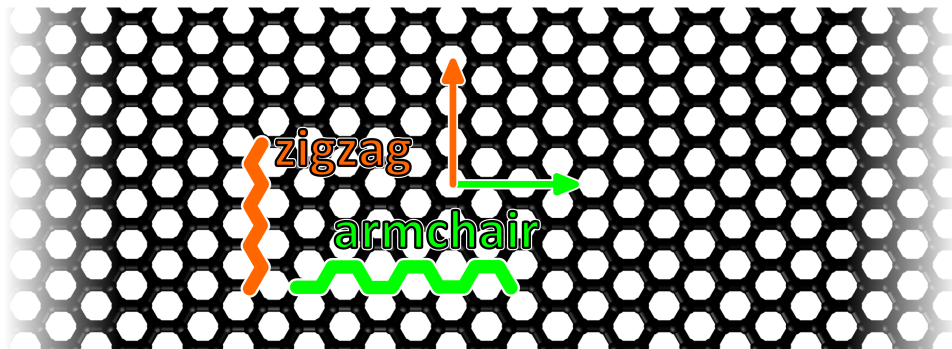


Fig. 7.1 Model van grafeen. Hierin zijn de zigzagrichting en de *armchair*-richting aangegeven.

Ondanks de goede geleidingseigenschappen is grafeen zelf niet het perfecte materiaal voor toepassing in elektronische componenten zoals transistors en diodes. Het materiaal heeft namelijk geen bandkloof (Engels: *band gap*). Een bandkloof zorgt ervoor dat een materiaal halfgeleidend wordt: geleidend in een elektrisch veld maar isolerend zonder. Dit maakt het mogelijk om de geleiding naar keuze aan- en uit te schakelen - een principe dat cruciaal is voor de werking van transistors. Wereldwijd onderzoeken verschillende groepen hoe een bandkloof gecontroleerd in grafeen aangebracht kan worden zodat het materiaal haar potentie als bouw materiaal voor elektronische componenten van de microchips van morgen waar zal kunnen maken (toegegeven: “morgen” zou best enkele tientallen jaren in de toekomst kunnen liggen).

Een interessante benadering is het toepassen van het quantumopsluitings-

appendix

effect (Engels: *quantum confinement*). Door grafeen “uit te stansen” in strookjes met een breedte van enkele nanometers worden grafeen-nanodraden (GNRs) verkregen. Dit zijn structuren die veel van de gunstige geleidingseigenschappen van het grafeen overnemen maar daarnaast - vanwege de quantummechanische kwantisatie van elektrongolven - een bandkloof kunnen hebben. De exacte grootte van deze kloof is sterk afhankelijk van de breedte van de stroken en kan ook enorm variëren met de structuur van de rand. Afhankelijk van hoe het materiaal gesneden wordt zijn er in principe twee verschillende soorten randen, de zogenoemde zigzag- en *armchair*-rand (zie Fig. 7.1).

Juist vanwege de gevoeligheid van de elektronische structuur met betrekking tot de geometrische structuur van de nanodraad is het erg lastig een draad te verkrijgen met exact de gewenste eigenschappen. Draden die niet met de grootst mogelijke precisie vervaardigd kunnen worden zullen erg vatbaar zijn voor variaties in de bandkloof over de lengte van de draad, hetgeen verstrooiing van elektronen in de hand werkt. Dit zal hypothetische elektronische nanoribboncomponenten inefficiënt maken.

Gelukkig zijn er recentelijk methodes ontwikkeld om de benodigde atomaire precisie te kunnen verkrijgen. Dit zijn bottom-upmethodes. Met behulp van oppervlaktesynthese (Engels: *on-surface synthesis*) kunnen de nanodraden gegroeid worden uit chemische stoffen. Hier smelten de vakgebieden van moleculaire elektronica en grafeenelektronica samen. De vorming van grafeen-nanodraden gebeurt door moleculen, die worden gesynthetiseerd in het scheikundelaboratorium, aan te brengen op een metaaloppervlak en polymerisatiereacties en andere koppelingen uit te voeren. De chemische methode levert nanodraden met atomaire precisie en vaak zonder ook maar een enkel defect in de draad te introduceren. Dit in tegenstelling tot de eerder ontwikkelde top-downmethodes waarin grafeen-nanodraden werden uitgesneden met behulp van lithografie, of koolstof nanobuisjes werden “opengeritst”. Een ander belangrijk voordeel van de bottom-upmethode is dat de uiteindelijke structuur van de draad is “ingebakken” in het uitgangsmolecuul. Door verschillende moleculen te maken en gebruiken kunnen dus draden van verschillende breedte en randstructuur worden gemaakt (zie Fig. 7.2). Dit maakt het mogelijk om vele verschillende types van nanodraden te synthetiseren - elk met hun eigen elektronische eigenschappen. Dit is de gedachte achter het onderzoek dat is uitgevoerd door de auteur. Onderzoek dat de synthese van uitgangsstoffen voor nanodraden omvat, maar ook de synthese van de nanodraden zelf, en bovendien de elektronische karakterisatie daarvan behelst.

De oppervlaktesynthese begint met het schoonmaken van een éénkristal van een metaal in een preparatiekamer van onze UHV-opstelling (zie kader). Hierna worden moleculen opgedampt op het metaaloppervlak en zodra de gewenste bedekking is bereikt (ruwweg een kwart van een (oppevlakbedekkende) monolaag) kunnen de oppevlaktesynthetische reacties uitgevoerd

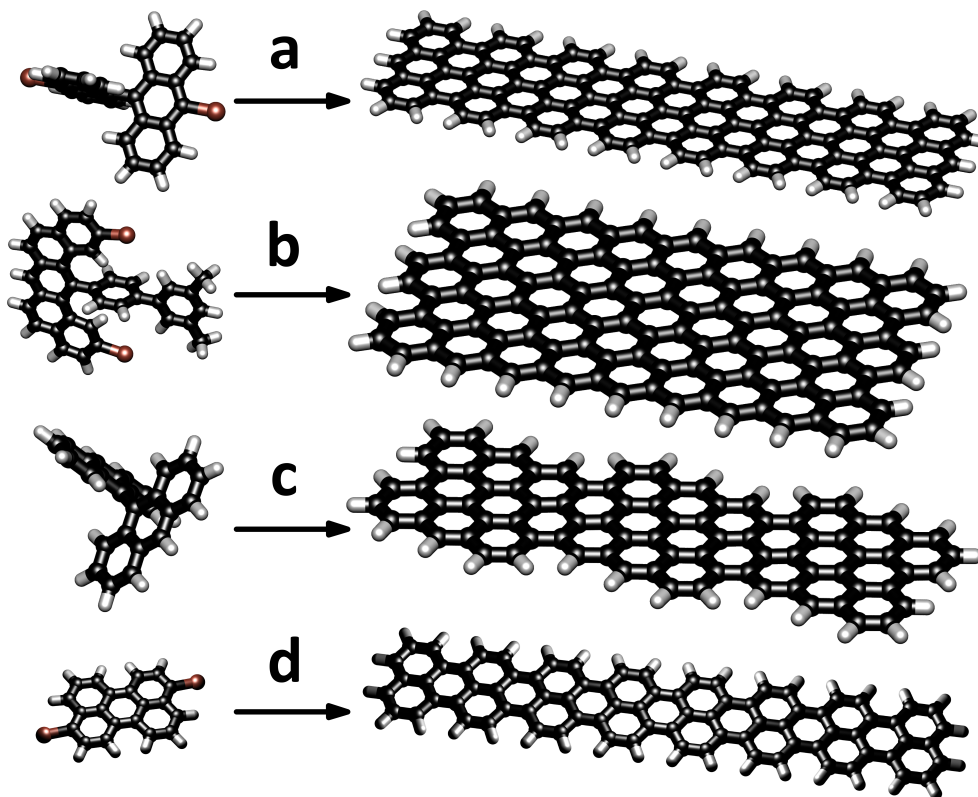


Fig. 7.2 Verschillende moleculen geven verschillende nanodraden. a) 10,10'-dibroom-9,9'-bianthryl reageert op goud tot *armchair* nanodraden.[1] b) Zigzag nanodraden worden gemaakt met 1-(3,5-dimethylfenyl)-4-(di-(3-broom)benz[a,j]-9'-anthracenyl)benzeen.[2] c) Chirale draden kunnen gemaakt worden met 9,9'-bianthryl.[3, 4, 5] d) *armchair* nanodraden met een breedte van 5 atomen worden vervaardigd met 3,9-dibroomperyleen.[6]

worden. Hiertoe wordt het metaalkristal simpelweg verhit. De reacties die daardoor plaatsvinden zijn dehalogenatiereacties (reacties waarbij in de moleculen een koolstof-halogeenbinding wordt verbroken en daarmee het koolstof geactiveerd wordt voor koppelingsreacties), polymerisaties (reacties waarbij moleculen met elkaar koppelen tot lange ketens) en cyclodehydrogenaties (reacties waarbij koolstof-koolstofbindingen worden gevormd onder verlies van waterstof om extra ringen te vormen en waarbij de structuur plat wordt). Door steeds exact de juiste temperatuur aan te houden gedurende de juiste tijd en vervolgens verder te verhitten naar de volgende temperatuur kunnen de verschillende reacties opeenvolgend uitgevoerd worden.

De UHV-opstelling

Alle rastertunnelmicroscopie- (STM) en atoomkrachtmicroscopiemetingen (AFM) worden uitgevoerd in ultrahog vacuüm (UHV, $p \approx 10^{-10}$ mbar) bij een temperatuur van 4,5 K (-268,5 °C). Bij deze gecontroleerde, koude condities kan de AFM in non-contact mode gebruikt worden, wat nodig is om de atomaire structuur van de nanodraden in kaart te brengen. In dezelfde behuizing zit een preparatiekamer waar metaalkristallen kunnen worden schoongemaakt (zie Fig. 7.3). Dit gebeurt door verscheidene cycli van sputteren (het verwijderen van de bovenste lagen door het te beschieten met een plasma van hoogenergetische argonionen) en annealen (het verhitten tot het punt waarop de metaal-atomen aan het oppervlak mobiel genoeg worden om zich netjes te rangschikken in atomair vlakke “terrassen”). Zodra dit is gebeurd wordt een zogenaamde molecuulverdamer (een klein houdertje waarin enkele korrels van de chemische uitgangsstof zitten) verhit tot het punt dat de moleculen sublimeren. Stabiele molecuulsublimatie is af te lezen aan een drukverhoging, meestal in de orde van $5 \cdot 10^{-9}$ mbar vanaf een basisdruk die een orde van grootte lager ligt. De moleculen worden op het metaaloppervlak gedampt waarna de oppervlaktesynthese kan worden uitgevoerd.

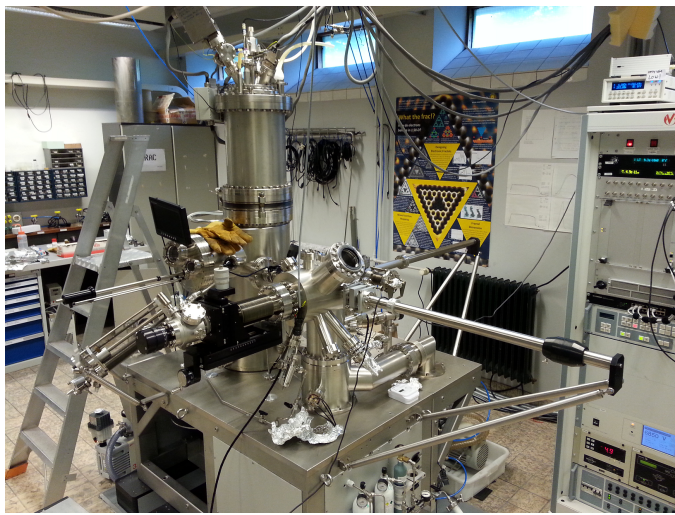


Fig. 7.3 **Onze UHV-opstelling.** Op de voorgrond is de preparatiekamer te zien, en daarachter (de verticale cylinder) de rastertunnel- en atoomkrachtmicroscop.

De moleculen die we vaak gebruiken zijn dihalobianthryllen: organische verbindingen met zes benzeenringen en twee halogeenatomen. De halogeenatomen zijn ofwel chlooratomen ofwel broomatomen. Deze moleculen geven *armchair*-nanodraden met een breedte van 7 atomen[1] (Fig. 7.2a): nanodraden met een significante bandkloof van ongeveer 2,4 eV. Verassend genoeg werkt de oppervlaktechemie op koper anders dan op een goudkristal. Hier vindt een ander type reactie plaats dan de gebruikelijke polymerisatie, met als

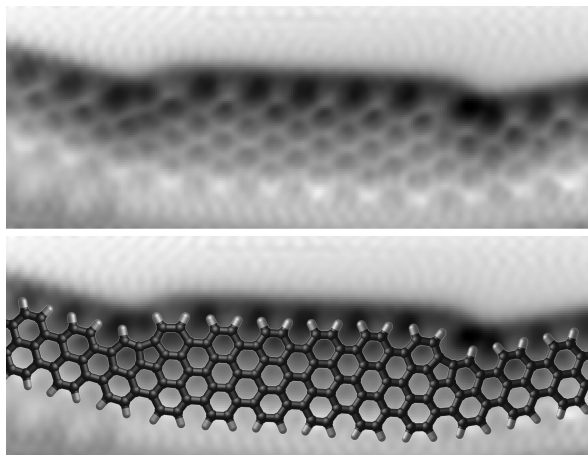
resultaat draden met een “chirale” rand - een gemengde *armchair*-/zigzagrand, zie Fig. 7.2c.[7, 4, 5] De chirale draden hebben een veel kleinere bandkloof dan de *armchair*-nanodraden wat grotendeels komt door elektronische toestanden die aan de randen zijn gelokaliseerd. Een derde type draad dat we kunnen synthetiseren is de 5 atomen brede *armchair*-nanodraad (Fig. 7.2d).[6] In tegenstelling tot de andere draden heeft deze een bandkloof die naar nul afneemt met toenemende lengte: de nanodraad kan als een metaal worden beschouwd.

Karakterisatie van de draden vindt plaats in onze gecombineerde rastertunnel- en atoomkrachtmicroscopie (STM en AFM) die ingebouwd is in dezelfde UHV-opstelling waar preparatie wordt uitgevoerd (zie kader). STM en AFM zijn op een fundamenteel ander principe gebaseerd dan optische microscopen en elektronenmicroscopen. In deze zogenaamde *scanning probe* methodes wordt het oppervlak afgetast met een extreem scherpe naald, die met een precisie van enkele picometers (een picometer is een miljardste van een millimeter en kleiner dan de diameter van een atoom) bewogen kan worden. In AFM wordt de trillingsfrequentie van de tip gemonitord, die - op een resonantiefrequentie van ongeveer 20000 Hertz - enkele Hertz kan veranderen als gevolg van krachten tussen tip en oppervlak. In STM wordt er een spanning aangelegd tussen tip en oppervlak en wordt het aantal elektronen dat door het vacuüm tussen tip en oppervlak (een afstand van ruwweg een nanometer of een miljoenste van een millimeter) springt gemonitord. Door de tip tijdens het scannen van het oppervlak zo te bewegen dat deze parameters (frequentieverhuiving of tunnelstroom) constant blijven, en wel door continu de hoogte van de tip aan te blijven passen, kan een beeld worden gevormd van het oppervlak en alles wat daarop ligt.

Met behulp van STM kan niet alleen een beeld van de structuur van de draden op het oppervlak verkregen worden, maar ook van de elektronische structuur in de draden zelf. Dit komt doordat de spanning naar wens aangepast kan worden en er bij verschillende spanningen resonant tunnelen kan plaatsvinden in de elektronische toestanden van de grafeen-nanodraden (bijvoorbeeld in de valentie- en geleidingsband). In tegenstelling tot STM kan met AFM de geometrische structuur van de nanodraad zichtbaar gemaakt worden. Fig. 7.4 toont een AFM-scan van een grafeen-nanodraad met segmenten die 5 en 7 atomen breed zijn.

Dit proefschrift omvat de synthese van uitgangsmoleculen voor de synthese van nanodraden, het bestuderen van de vormingsmechanismen van de nanodraden op metaaloppervlakken en de karakterisatie van de aldus gevormde structuren. **Hoofdstukken 1** tot en met **3** concentreren zich op de chemie die plaatsvindt op het oppervlak bij de vorming van GNRs. De betrokken processen, de mechanismen en vooral de karakterisering van producten en tussenproducten met rastertunnel- en atoomkrachtmicroscopie (STM en AFM) komen aan de orde. Deze hoofdstukken beschrijven in detail het fa-

Fig. 7.4 AFM-scan van een grafeen-nanodraad met ingebouwde metaal-halfgeleiderverbindingen. Het onderste paneel toont een model van de atomaire geometrie.



bricageproces dat twee belangrijke stappen omvat. De eerste stap is de synthese van uitgangsmoleculen in het chemielaboratorium, met behulp van synthetisch organische chemie. In de tweede stap worden de moleculen onder UHV-omstandigheden op metalen éénkristallen aangebracht en onderworpen aan thermisch geïnduceerde reacties. Deze oppervlaktechemische reacties zijn intermoleculaire koppelingsreacties en intramoleculaire cyclisatiereacties die uiteindelijk resulteren in grafeen-nanodraden.

Hoofdstuk 1 geeft een gedetailleerde inleiding in non-contact atoomkrachtmicroscopie (nc-AFM), alsook in het jonge veld van oppervlaktesyntese. Recente ontwikkelingen in de structuurbepaling van afzonderlijke moleculen op oppervlakken worden besproken, en het werk beschreven in **hoofdstukken 2** en **3** - waarin de mechanismes in de vorming van verschillende nanografenen en nanodraden worden beschreven - wordt geïntroduceerd. **Hoofdstuk 2** beschrijft de nanografeenvorming van 10,10'-dichloor-9,9'-bianthryl (DCBA) op een goudoppervlak. Dit molecuul is een chlooranaloog van 10,10'-dibroom-9,9'-bianthryl (DBBA) - een molecuul dat eerder is gebruikt in de synthese van *armchair* nanodraden.[1] Hier wordt opgehelderd hoe de aard van het halogeen een sleutelrol speelt in de volgorde van verschillende inter- en intramoleculaire reacties, en hoe de gebromeerde en gechloreerde moleculen enorm verschillende nanografenen geven. In **hoofdstuk 4** wordt de vorming van GNRs op een koperoppervlak onderzocht. Verrassenderwijs is de structuur van de draden volledig anders dan zou worden verwacht op basis van de structuur van de uitgangsstoffen. Het koperoppervlak katalyseert een specifieke C-H-splitsing en faciliteert de vorming van chirale nanodraden, die een gemengde *armchair*-zigzagrand hebben.

De daaropvolgende hoofdstukken hebben een sterkere nadruk op elektronische structuur in plaats van vormingsmechanisme en derhalve bevatten deze

hoofdstukken meer elektronische metingen. Deze metingen worden aangevuld met elektronische structuurberekeningen, op basis van zowel dichtheidsfunctionaaltheorie als *tight-binding*. **Hoofdstuk 4** gaat in op de kwantummechanische eigenschappen van GNRs zoals berekend kan worden met *tight-binding*. Dit hoofdstuk presenteert het *Mathematica*-pakket dat is ontwikkeld om de berekeningen uit te voeren, genaamd MathemaTB. Dit pakket kan niet slechts gebruikt worden voor berekeningen aan nanodraden, maar is toepasbaar op een grote variëteit aan moleculaire systemen (Hückel-berekeningen) alsook periodieke structuren. **Hoofdstuk 5** beschrijft de synthese en karakterisering van metaal-halfgeleiderverbindingen in grafeen-nanodraden, waarbij een copolymerisatie van twee verschillende uitgangsmoleculen wordt gebruikt om structuren met metalen en halfgeleidende segmenten te vervaardigen. Naast de nc-AFM-karakterisering van deze structuren wordt een meer gedetailleerd onderzoek naar de elektronische eigenschappen van de draden gepresenteerd aan de hand van rastertunnelspectroscopie (STS). Niet alleen worden de draden gekarakteriseerd op het metaaloppervlak, maar door ze met de naald van de STM op te pakken van het oppervlak en omhoog te tillen kan ook de geleiding door de lengte van de draden worden onderzocht. Deze geleidingsmetingen vormen de basis voor **hoofdstuk 6**, waar de elektronische eigenschappen van de draden nog gedetailleerder worden onderzocht. Hiertoe worden de nanodraden na optillen verslept op een ultradunne isolerende laag natriumchloride om storende effecten, die het metaaloppervlak in de nanodraden induceert, tegen te gaan.

Samenvattend wordt er in dit proefschrift een verzameling aan werk op het gebied van synthese en karakterisatie van grafeen-nanodraden gepresenteerd. Om hun potentie als kandidaten voor moleculaire elektronische componenten te gaan vervullen is het belangrijk om de structuur met de grootst mogelijke precisie te controleren. Hiertoe wordt de bottom-up methode gebruikt, die organische synthese en oppervlaktesynthese behelst. De oppervlaktesynthese en alle mechanismen daarin wordt bestudeerd met AFM en STM, en van de gevormde nanodraden worden de elektronische eigenschappen gemeten en berekend. Dit onderzoek heeft geresulteerd in de synthese van verschillende types van grafeen-nanodraden, begrip over hun vorming en eigenschappen, en bovendien heterostructuren van grafeen-nanodraden die elektronische functionaliteit bezitten. Aldus beschrijft het onderzoek in dit proefschrift stappen voorwaarts in grafeen-nanodraadgebaseerde moleculaire elektronica alsook in methodologiën in elektronische structuurbepaling en oppervlaktesynthese, iets wat van significant belang is in het voortschrijdend onderzoek naar de elektronica van morgen.

Bibliography

- [1] J. Cai, P. Ruffieux, R. Jaafar, M. Bieri, T. Braun, S. Blankenburg, M. Muoth, A. P. Seitsonen, M. Saleh, X. Feng, K. Müllen, and R. Fasel, *Nature* **466**, pp. 470–473 (2010).
- [2] P. Ruffieux, S. Wang, B. Yang, C. Sanchez-Sanchez, J. Liu, T. Dienel, L. Talirz, P. Shinde, C. A. Pignedoli, D. Passerone, T. Dumlaff, X. Feng, K. Müllen, and R. Fasel, *Nature* **531**, pp. 489–492 (2016).
- [3] P. Han, K. Akagi, F. Federici Canova, R. Shimizu, H. Oguchi, S. Shiraki, P. S. Weiss, N. Asao, and T. Hitosugi, *ACS Nano* **9**, pp. 12035–12044 (2015).
- [4] C. Sánchez-Sánchez, T. Dienel, O. Deniz, P. Ruffieux, R. Berger, X. Feng, K. Müllen, and R. Fasel, *ACS Nano* **10**, pp. 8006–8011 (2016).
- [5] F. Schulz, P. H. Jacobse, F. F. Canova, J. Van Der Lit, D. Z. Gao, A. Van Den Hoogenband, P. Han, R. J. Klein Gebbink, M. E. Moret, P. M. Joensuu, I. Swart, and P. Liljeroth, *Journal of Physical Chemistry C* **121**, pp. 2896–2904 (2017).
- [6] A. Kimouche, M. M. Ervasti, R. Drost, S. Halonen, A. Harju, P. M. Joensuu, J. Sainio, and P. Liljeroth, *Nature Communications* **6**, pp. 10177 (2015).
- [7] P. Han, K. Akagi, F. Federici Canova, H. Mutoh, S. Shiraki, K. Iwaya, P. S. Weiss, N. Asao, and T. Hitosugi, *ACS Nano* **9**, pp. 3404–3405 (2015).

7.2 Publications

2013

- S. K. Hamalainen, M. P. Boneschanscher, **P. H. Jacobse**, I. Swart, K. Pussi, W. Moritz, J. Lahtinen, P. Liljeroth, J. Sainio. Structure and local variations of the graphene moire on Ir(111). *Physical Review B - Condensed Matter and Materials Physics* **88** (20), p. 201406

2015

- J. van der Lit, **P. H. Jacobse**, D. A. M. Vanmaekelbergh, I. Swart. Bending and buckling of narrow armchair graphene nanoribbons *via* STM manipulation. *New Journal of Physics* **17** (053013), p. 53013
- S. G. Stuij, **P. H. Jacobse**, V. Juricic, C. Morais Smith. Tuning edge state localization in graphene nanoribbons by in-plane bending. *Physical Review B - Condensed Matter and Materials Physics* **92** (7), pp. 75424-75425

2016

- J. van der Lit, J. L. Marsman, R. S. Koster, **P. H. Jacobse**, S. den Hartog, D. A. M. Vanmaekelbergh, R. J. M. Klein Gebbink, L. Filion, I. Swart. Modeling the Self-Assembly of Organic Molecules in 2D Molecular Layers with Different Structures. *The Journal of Physical Chemistry C* **121** (5), pp. 2896-2904
- **P. H. Jacobse**, A. van den Hoogenband, M.-E. Moret, R. J. M. Klein Gebbink, I. Swart. Aryl Radical Geometry Determines Nanographene Formation on Au(111). *Angewandte Chemie International Edition* **55** (42), pp. 13052-13055

2017

- F. Schulz, **P. H. Jacobse**, F. F. Canova, J. van Der Lit, D. Z. Gao, A. van Den Hoogenband, P. Han, R. J. M. Klein Gebbink, M.-E. Moret, P. M. Joensuu, I. Swart, P. Liljeroth. Precursor Geometry Determines the Growth Mechanism in Graphene Nanoribbons. *The Journal of Physical Chemistry C* **121** (5), pp. 2896-2904
- M. R. Slot, T. S. Gardenier, **P. H. Jacobse**, G. C. P. van Miert, S. N. Kempkes, S. J. M. Zevenhuizen, C. de Morais Smith, D. A. M. Vanmaekelbergh, I. Swart. Experimental realization and characterization of an electronic Lieb lattice. *Nature Physics* **13** (7), pp. 672-676

appendix

- **P. H. Jacobse**, A. Kimouche, T. Gebraad, M. M. Ervasti, J. M. Thijsen, P. Liljeroth, I. Swart. Electronic components embedded in a single graphene nanoribbon. *Nature Communications* **8** (1), p. 119
- **P. H. Jacobse**, M.-E. Moret, R. J. M. Klein Gebbink, I. Swart. Tracking On-Surface Chemistry with Atomic Precision. *Synlett* **28** (19), pp. 2509-2516

2018

- (popular) **P. H. Jacobse**, I. Swart. Tunneldiodes en metaal-halfgeleiderverbindingen van grafeen-nanodraden. *NEVAC BLAD* **56** (June), pp. 6-10
- **P. H. Jacobse**, M. J. J. Mangnus, S. J. M. Zevenhuizen, I. Swart. Mapping the Conductance of Electronically Decoupled Graphene Nanoribbons. *ACS Nano* **12** (7), pp. 7048-7056
- **P. H. Jacobse**, K. A. Simonov, M. J. J. Mangnus, G. I. Svirskiy, A. V. Generalov, A. S. Vinogradov, A. Sandell, N. Mørtensson, A. Preobrajenski, I. Swart. Influence of Substrate and Halogen in the Synthesis of Graphene Nanoribbons from Dihalobianthryls. *Manuscript in preparation*
- **P. H. Jacobse**. MathemaTB, a *Mathematica* package for tight-binding calculations. *Manuscript in preparation*

7.3 About the author

Peter Jacobse was born in Emmen as the youngest of three children, and raised in Leek, near the city of Groningen, the Netherlands. He attended the Praedinius Gymnasium in Groningen, and subsequently studied chemistry and physics at the University of Groningen. Here he was active in the students association ‘T. F. V. Professor Francken’.

After completing his BSc (2012), he moved to Utrecht, continuing in the field of nanoscience. He quickly realized that the STM and AFM research in the group of Ingmar Swart was totally his cup of tea. He decided to append, to the curriculum provided in Utrecht, courses on nano-electronics and molecular electronics, as provided at the technical universities of Twente and Delft.

He obtained his MSc (honors, *cum laude*) from Utrecht University in 2014. His research proposal on advancing the study of graphene nanoribbons was awarded a grant from the Debye Institute for Nanomaterials Science. This resulted in him initiating his PhD research at Utrecht University, but not before spending two months teaching English and mathematics in rural Nepal.

Peter has done a fair share of teaching, giving tutorials, but also helping secondary school students to pass their exams (privately and at the Ichtus College in Veenendaal) and helping out as a student assistant at the university of Groningen.

In addition to serious stuff, Peter likes to spend time (and banter) with friends. Playing the trumpet and playing golf are two passions of his, as is traveling to and exploring beautiful places. Peter really enjoys rafting, mountain biking and hiking in the mountains. A passion that he picked up during the time of his PhD is squash, which he enjoys thoroughly every week.



7.4 Acknowledgments

In this section I would like to acknowledge all the people who have played a role of importance during my time as a PhD in Utrecht.

First of all I want to thank the people who have made my PhD possible. These are of course my supervisors. Most of my work was done under *Ingmar Swart*, and he deserves most credits of everyone. He has turned me from a master student into an STM wizard, and has been outstanding in his teaching and guiding role. Of course, numerous work discussions, syntheses and presentations were also done in the David de Wied building, where *Marc-Etienne Moret* and *Bert Klein Gebbink* took on their roles of supervisors. Marc-Etienne, you've seen my fume hood after a Skraup reaction and a white phosphorus accident but still you kept your confidence in me as a chemist. And thanks to Bert for your active role in steering the direction of our research! The three of you are accomplished mentors, and each of you has helped me a lot to find my way in the academic world at this start of my PhD. Thanks you for being great supervisors!

Daniel Vanmaeckelbergh, you were not formally my supervisor or promotor but you are always really involved. But what I like most about you is that you simply share your enthusiasm whenever I've found something interesting. That is really motivating! Someone who also supported me (with plenty of nice discussions) was my roommate *Harold de Wijn*. Of course, I would also like to acknowledge *Celso de Mello-Donaga*, *Andries Meijerink* and *Leo Jenneskens*. *Adri van den Hoogenband*, I don't think I have ever met anyone as humble as you are. You used your years of experience in the chemistry lab to come to the rescue when my syntheses were failing, and then you're even giving me the credit when you make it work! It was great working with you!

I've had my fair share of students and they all deserve an acknowledgement! *Tom Konings*, *Victor van Wessel*, thanks for exploring the 5/7-junctions (and catching mice in the basement)! *Sam Borman*, *Margriet van Riggelen*, thanks for lifting nanoribbons with me! There are very few people on this planet who can do that. *Noor ten Veen* and *Luuk Goode*, thank you for exploring chiral and armchair nanoribbons on silver with me! *Daniel de Bruin*, *Casper Silvis*, *Robbin Kroes* and *Nora Mulder*, thanks for synthesizing diazaanthanthrene with me and bringing some color to the chemistry lab! *Janine Deou*, thanks for the DFT calculations and the involvement with the bianthryls and teranthryls! Thanks to all the synthesis and ester project students. It was fun teaching you about chemistry!

Two students should be mentioned for their contributions in terms of literature theses. These are *Cecilia Jespers*, from organic chemistry and catalysis, and *Ellenor Geraffy*, from condensed matter and interfaces. You've both did some really nice work in studying the literature and bringing it all together in

reports that have been very instructive for me and for yourselves. *Iris Teune*, although there have been some frustrating times when experiments worked out differently than we anticipated, your perseverance is admirable. You have been a very good student! *Mark Mangnus* and I were, as a team, able to lift, drag, transfer, stack and vibrate ribbons on metal surfaces and sodium chloride: likely among the most difficult and involved experiments ever performed with a scanning tunneling microscope. Thanks for being a great apprentice!

My collaborators also deserve some acknowledgement. Together with *Jos Thijssen*, I jointly supervised *Marienne Faro* and *Tim Gebraad* in performing transport calculations on graphene nanoribbons. This resulted in two bachelor theses, one master thesis, one *Nature Communications* paper, and an increased knowledge on graphene nanoribbons in Delft and knowledge on transport calculations in Utrecht. More collaborators that deserve a mention are *Fabian Schulz* and *Peter Liljeroth*, with whom I worked on the chiral nanoribbons. Together with *Amina Kimouche* I managed to make heterojunction nanoribbons, and we had two very productive weeks together in the summer of 2016. I would also like to thank *Gleb Svirskiy*, *Alexander Generalov*, *Alexei Preobrajenski*, and *Konstantin Simonov*. After meeting Konstantin in San Sebastian and confronting him with AFM images that proved that the ribbons that he thought were armchair-edged were in fact chiral, we set up a plan to resolve nanoribbon formation on silver. At the BESSY II synchrotron in Berlin (after a few initial setbacks), we eventually celebrated our succesful week (with numerous night shifts) with Dutch stroopwafels and wine from Kaufland. More collaboration took place with *Marijn van Huis* and *Somil Gupta*. Thank you for the DFT efforts!

Doing work in a laboratory is impossible without the people who know how to keep everything running. *Henk Kleijn*, *Jord van Schaik*, *Johann Jas-trzebski*, *Thomas Ran*, *Stephan Zevenhuizen*, *Hans Ligthart*, *Peter van den Beld*, thank you for all your efforts! Then I would also like to thank the managers: *Milka Westbeek*, *Thea Pozzi* and *Linda Kumeling*. People with whom I enjoyed the collaboration on the theoretical end of the spectrum and should be acknowledged for their discussions and support are *Simon Stuij*, *Guido van Miert*, *Sander Kempkes*, *Vladimir Juričić* and *Cristiane Morais Smith*.

Work without nice colleagues is like playing golf without a nineteenth hole! Especially the people who joined me in the basement: *Joost van der Lit*, *Mark Boneschanscher*, *Stephan den Hartog*, *Jaco Geuchies*, *Kiane de Kleijne*, *Nadine van der Heijden*, *Thomas Gardenier*, *Daniël Smith*, *Benedikt Klein*, *Lisanne Knijff*, *Jos Mulkens*, *Pascal Vermeeren*, *Jan Jurre Harsveld van der Veen*, *Jesper Moes*, *Saoirsé Freeney* and *Christiaan Post*!

Finally, I would like to acknowledge the rest of CMI and OCC, where I will resort to first names because of the number of people. Thanks to my CMI colleagues *Maryam*, *Anne*, *Joren*, *Annelies*, *Annalisa*, *Sophia*, *John K.*,

appendix

Zachar, Jeppe, Serena, Tim P., Tim S., Bas, Riande, Federico, Saydi, Matt, Arend, Kelly, Patrick, Luke, Veerle, Ward, Joep, Mathijs, Pedro, Francesca, Chenghui, Allan, Wenjin, Ting, Winston, Kelly S., Christa, Jacobine, Elleke, Carlo, Robin and Freddy. John, Jur, Daniele, it was an honor to be part of the table football gang. And of course my colleagues from OCC: *Jacco, Emily, Léon, Charl, Suresh, Pradip, Emma, Jianming, Richard, Matthias, Marc, Yoni, Desmond, Dirk-Jan, Stella, Eduard, Serhii, Martine, Jing, Raoul, Sam, Maxime, Alessio, Richt, Bas, Bart, Laurens B., Laurens V., Rohald and Cody*. Thank you all for being amazing colleagues, at the bowling alley, at blow karting, at glow golf Houten, at the tea house in Rhijnauwen, in the sea somewhere between Lauwersoog and Ameland, in the sea in Egmond, but most of all in the office and in the laboratory!

A big thanks to the people who have supported me in a more personal rather than professional way. The Francken members, the squashies, the golfies, the people from secondary school with whom I've never parted ways! And apart from friends, there's also family. Thanks *mum* and *dad*, thanks *Annemieke*, my dearest sister and your novel family, and *Rob*, the one who set up the weekly bro-day when I was in need of a bro-day. Thanks to the cousins and nieces and nephews an uncles and aunts and all the family I haven't listed here yet.

Tot *Slot, Marlou*. We celebrated our good times and cheered each other up (with Indian food) whenever we were down. That is special to me, so I only dropped your super promising sample twice in the UHV set-up. Thanks for everything!